The Zebrafish: A Preclinical Screening Model for the Optimization of Nanomedicine Formulations

Inauguraldissertation

zur

Erlangung der Würde eines Doktors der Philosophie

vorgelegt der

Philosophisch-Naturwissenschaftlichen Fakultät

der Universität Basel

von

Sandro Sieber

aus Widnau, SG

Basel, 2019

Genehmigt von der Philosophisch-Naturwissenschaftlichen Fakultät

Auf Antrag von

Prof. Dr. Jörg Huwyler

Prof. Dr. Markus Affolter

Basel, den 24. April 2018

Prof. Dr. Martin Spiess (Dekan)

“Science never solves a problem without creating ten more.”

George Bernard Shaw

TABLE OF CONTENTS

ZUSAMMENFASSUNG FÜR LAIEN 1

SUMMARY 3

INTRODUCTION 5

AIM OF THE THESIS 9

RESULTS 10

- Chapter I-I 11
- Chapter II-I 29
- Chapter II-II 42
- Chapter III-I 55
- Chapter IV-I 69
- Chapter IV-II 135
- Chapter IV-III 146

DISCUSSION AND OUTLOOK 159

- Systemic Clearance Mechanisms 159
- Blood Circulation Properties 163
- Macromolecular Basis of Nano-Bio-Interactions 167
- Passive and Active Targeting 172
- Enzyme Activity 173

CONCLUSION 176

ABBREVIATIONS 178

BIBLIOGRAPHY 180

ACKNOWLEDGMENT 185

CURRICULUM VITAE 187

ZUSAMMENFASSUNG FÜR LAIEN

Wenn einem Patienten Medikamente, zum Beispiel für eine Krebstherapie, in die Blutbahn injiziert werden, verteilen sie sich im ganzen Körper. Da hierbei allerdings nicht nur Krebszellen, sondern auch gesunde Zellen angegriffen werden, können zum Teil schwere Nebenwirkungen entstehen. Um dieses Problem zu lösen, versucht man mithilfe von Nanopartikeln die Medikamente gezielt zu ihrem Wirkungsort, z.B. dem Tumor, zu dirigieren. Die Kunst dabei ist es, die Nanopartikel so herzustellen, dass sie nicht sofort vom Immunsystem als fremdartig erkannt und zerstört werden oder von Filtrationsorganen wie der Leber und Niere ausgeschieden werden. Die grundlegende Idee für zielgerichtete Medikamente wurde schon vor über hundert Jahren von Paul Ehrlich beschrieben. Nach einer langen Zeit der intensiven Grundlagenforschung wurde dann Ende der 90er Jahre das erste auf Nanopartikeln basierende Krebsmedikament, namentlich Doxil, von den Behörden zugelassen. Nicht erst durch diesen Erfolg erfuhr das Feld der Nanomedizin einen riesigen Aufschwung. Unsummen an Forschungsgeldern wurden investiert auf der Suche nach einer neuen und besseren Generation von Krebsmedikamenten. Verglichen mit der Anzahl der wissenschaftlichen Publikationen und der darin enthaltenen Versprechungen schafften es leider nur relativ wenige Nanomedikamente bis zur definitiven Anwendung im Patienten. Dies hat in den letzten Jahren dazu geführt, dass kritische Stimmen laut wurden und einige zweifelten bereits an der allgemeinen Anwendbarkeit solcher Medikamente. Trotz der zum Teil berechtigten Kritik gibt es immer mehr auf Nanopartikeln basierende Medikamente in klinischen Studien (also kurz vor der Zulassung) oder solche, welche bereits zugelassen sind. Es wäre also falsch zu behaupten, dass sich das Forschungsfeld in einer grundlegenden Krise befände. Nichtsdestotrotz stimmt es, dass die Entwicklung der genauen Zusammensetzung eines solchen Nanopartikels extrem schwierig und mühsam ist. Dies hat auch damit zu tun, dass neue Nanopartikel in Zellkulturen getestet werden müssen, da eine grosse Anzahl von Tierversuchen in Ratten und Mäusen teuer, aufwändig und nicht zuletzt ethisch fragwürdig sind. Allerdings sind Zellkulturen nicht fähig, komplexe biologische Vorgänge eines Lebewesens genau darzustellen. Darum passiert es oft, dass, basierend auf den Ergebnissen aus Zellkulturstudien, Nanopartikel für weitere Experimente in Nagern ausgewählt werden, welche nicht genügend unter realistischen biologischen

Bedingungen optimiert werden konnten. Das Ziel dieser Doktorarbeit war es, diese Lücke zwischen Zellkultur und Nagetieren zu schliessen. Dafür wurden frühe Entwicklungsstadien des Zebrafisches als ideale Lösung identifiziert, da sie gegenüber Versuchen in Nagetieren zahlreiche Vorteile aufweisen. Die verwendeten Zebrafischjungtiere sind klein, günstig in der Haltung, extrem gut verfügbar (ca. 200 Stück pro Zebrafischpaar und Woche) und durchsichtig. Zudem ist keine ausführliche Bewilligung durch die Tierversuchsbehörden nötig, da Experimente in diesem Entwicklungsstadium nicht offiziell als Tierversuche gelten. In einem ersten Teil dieser Arbeit wurde das neue Zebrafischmodell getestet und mit bekannten Daten aus Nagetieren wie Mäusen oder Ratten verglichen. Es wurde gezeigt, dass aufgrund der Resultate aus einem Zebrafischversuch tatsächlich Vorhersagen über das Verhalten von Nanopartikeln in Wirbeltieren gemacht werden können. Im zweiten Teil dieser Arbeit wurden dann direkte Anwendungen am Zebrafischmodell getestet. Dabei war es möglich, neu entwickelte Nanopartikel mithilfe des Zebrafisches zu optimieren und unter realistischen biologischen Bedingungen zu testen. Aufgrund der erzielten Erfolge werden in Zukunft einige dieser Projekte weitergeführt werden, welche unter anderem die Entwicklung eines neuen Nanopartikel basierten Medikamentes zur Behandlung von Infektionskrankheiten einschliessen. Zusammenfassend konnte gezeigt werden, dass der Zebrafisch vielversprechende Möglichkeiten für die Optimierung von Nanopartikeln bietet und hoffentlich in der Lage sein wird, die Anzahl der erfolgreich in Patienten eingesetzten Nanomedikamente zu erhöhen.

SUMMARY

Nanomedicines are a valuable option to achieve drug accumulation specifically in diseased cells or tissues and therefore reduce side effects. Since the introduction of the revolutionary concept called the magic bullet for such sophisticated treatments more than 100 years ago, a lot of hope and expectations were placed into the field of nanoparticulate drug delivery. Initial forms of nanoparticles such as liposomes were described and extensively characterized which finally resulted in the FDA approval of the first cancer nanomedicine, namely Doxil, in 1996. This early success fueled the already gold-rush like atmosphere and resulted in a huge amount of time and money invested in nanomedicine research and development. As it is often the case for such a much-noticed field of medicinal research, the number of approved and clinically applied nanomedicines was not able to keep up with the unrealistic expectations resulting from the exponential increase of nanomedicine related publications. This triggered a lot of criticism questioning basic principles such as the enhanced permeability and retention effect or even the general use of nanomedicines. Despite the fact that the raised points are legitimate to a certain degree, the field of nanomedicine is far away from suffering from a general crisis, underlined by the steadily (but slowly) increasing number of approved formulations. Nevertheless, it cannot be denied that nanomedicine development is a cumbersome process suffering from a lot of drop-outs during very early phases of clinical trials. Among other things, this is due to the fact that formulation design and optimization is mainly based on *in vitro* studies, which are not able to fully mimic complex biological conditions. Moreover, only a selected number of formulations can subsequently be assessed in rodent *in vivo* experiments, since such studies are expensive, time consuming and suffer from ethical concerns. Obviously, there is a huge gap between *in vitro* cell culture and rodent *in vivo* studies, which makes the selection of potentially successful nanomedicine formulations extremely difficult. In addition, this situation does not allow a thorough formulation design and optimization under complex biological conditions and hampers a detailed understanding of basic nanomedicine interactions with biological environments at a macromolecular level. Therefore, this PhD thesis aimed to introduce the zebrafish as a complementary and easy accessible *in vivo* model in order to bridge the gap between *in vitro* and rodent *in vivo* studies during nanomedicine

development. In the first part (Chapters I-I to III-I), the current nanomedicine development process prior to rodent *in vivo* studies was reviewed and the zebrafish model was set-up, validated, and further characterized. Briefly, already described formulation effects on nanomedicine pharmacokinetics were reproduced and the predictive power of the zebrafish model system was verified. Thereby, a special focus was put on two main nanomedicine clearance mechanisms, namely phagocytosis by macrophages as a part of the mononuclear phagocytic system and scavenger receptors expressed on cells, which belong to the reticuloendothelial system. Based on the successful completion of the first part, the zebrafish model was used for the development of sophisticated nanoparticulate delivery systems (Chapter IV). For example, the optimal ligand density for an actively targeted nanoparticle was established in the zebrafish model and verified in a subsequent rodent biodistribution experiment. In addition, two different nanoparticle-enzyme systems were tested regarding their stability, biocompatibility, and functionality in this living biological system, i.e. zebrafish. During this thesis, general advantages of the zebrafish model such as large clutch size, optical transparency, availability of many transgenic lines, the possibility to screen a large number of formulations, and relatively low regulatory requirements became evident. All parameters were adapted to the purpose of nanomedicine formulation design and optimization. The promising findings will be further pursued in detailed follow-up studies regarding the development of an accurate and quantitative pharmacokinetic model, the elucidation of exact formulation dependent nanomedicine cell uptake and trafficking mechanisms under *in vivo* conditions, or to support the formulation design and optimization of nanomedicines for infectious diseases. Altogether, the presented zebrafish model showed to be a valuable and promising tool for several applications in the field of nanomedicine development and will hopefully foster the successful translation of further nanomedicines from bench to bedside.

INTRODUCTION

In 1907, Paul Ehrlich introduced the visionary concept of the magic bullet [1] which marked the beginning of a new medicinal concept called targeted drug delivery. In the following decades, drug loaded nanoparticles (nanomedicines) made of different materials [2,3] were investigated as therapeutic options for several diseases [4], but mainly cancer treatment [5,6]. Based on the discovery of liposomes in the early 60's by Bangham et al. [7], liposomal formulated doxorubicin (Doxil) became the first commercially available nanomedicine formulation approved by the FDA in 1995 [8]. Inspired by this early success, a lot of hope and expectations were placed into this revolutionary therapeutic concept and huge investments in the field of nanomedicine were made. This gold-rush like atmosphere resulted in a vast amount of publications, describing the synthesis and characterization of increasingly sophisticated nanomedicines. Nevertheless, only a very limited number of these systems showed to be useful for any clinical application [9]. In parallel, the enhanced permeability and retention effect (EPR), which served as a rational for almost every cancer targeted nanomedicine, was found to be less conserved between different cancer types as generally assumed [10]. To this end, a lot of studies were able to demonstrate passive accumulation of various long circulating nanomedicines in rodent tumor models, but again, only a minority of these formulations were successful in later clinical trials [11,12]. Moreover, Wilhelm et al. questioned the general validity of targeted nanomedicines by underlining that less than 0.7 % of the administered dose can be found in the targeted tumor [13]. Altogether, nanomedicines seem to suffer from a very poor translation from bench to bedside, which affects the trust of patients, the healthcare systems, and investors in the research field. On the other hand, the picture changes looking at the described concerns from a different angle. Lately, various forms of complex targeted or stimuli-responsive nanoparticles for controlled drug release were published in increasing numbers of articles [14,15]. However, these systems are highly sophisticated and often prepared and characterized under very controlled conditions, which do not reflect any biological environment [9]. Being realistic, such systems are often designed and promoted to attract funding and to be published in high impact journals rather than to be clinically applied in the near future. This negatively affects overall nanomedicine translation to clinics at the first glance. For example, to

overcome the issue of heterogenic EPR effect, patient stratification would increase the clinical success. This is already done for other therapies such as HER2 receptor positive breast cancer therapy [16]. The emerging field of nanoparticle based theranostics could further help to select patients, which will really benefit from nanomedicines [17]. Regarding the low targeting efficiency, one could argue that antibodies for cancer treatment, which are commercially very successful, do not target tumors more efficiently [18]. Interestingly, a slightly increased accumulation in target tissue in parallel to a decreased accumulation in off-target tissue can already result in patients' benefit which justifies the application of a nanomedicine formulation. In addition, considering the raising number of nanomedicines which are already approved or tested in clinical trials [19] indicates a lot of progress which has been made during the last years and does not confirm the picture of a research field suffering from a general crisis.

Nevertheless, progressing to clinical trials is a cumbersome and often difficult venture also originating from the up to date unsatisfying nanomedicine development process. Nanomedicines interact differently with biological environments such as cells or whole organisms, depending on their formulation (i.e. material, surface modifications) and their physicochemical properties (i.e. size, surface charge) [20]. Due to the high number of possible combinations, formulation design and optimization is usually performed based on empirical knowledge and by using *in vitro* systems which are suitable for screening approaches. Subsequently, a smaller number of formulations is selected and subjected to further rodent *in vivo* studies. This procedure represents a classical drug development process and has also become standard for the development process of nanomedicines [21], without reflecting their inherent complexity. Obviously, there is a huge gap between cell culture and living animals, which makes the selection of promising lead formulations difficult, leading to a lot of drop-outs during these early development phases [22]. Altogether, a cost- and time-effective *in vivo* model which can be used to screen large numbers of nanomedicine formulations prior to rodent *in vivo* studies is desperately needed in order to facilitate the optimization and selection of potentially successful formulations under complex biological conditions.

Caenorhabditis elegans (nematode), *Drosophila melanogaster* (fruit fly), and *Danio rerio* (zebrafish) are among the most extensively characterized animal models in life sciences. Nematodes and fruit flies (invertebrates) can be considered as initial models for developmental biology while zebrafish entered this field at a later stage due to the desire to study fundamental biological processes in a vertebrate animal model sharing more similarities with mammalians [23,24]. Moreover, chicken embryos featuring the relatively easy accessible chorioallontoic membrane (CAM) have been applied in biomedical research as tumor models [25], to investigate drug delivery [26], and to assess the toxicity of anti-cancer drugs [27]. However, the zebrafish model has many advantageous properties such as large clutch size and low husbandry costs making it applicable for screening processes. Furthermore, a broad spectrum of established and characterized genetic tools is available [28], allowing the generation of transgenic zebrafish lines expressing fluorescent proteins in specific cell types. Combined with its optical transparency at early developmental stages (embryo/larvae), this offers the possibility to observe physiological processes at a cellular or even macromolecular level using high-resolution imaging techniques such as fluorescent confocal microscopy. Consequently, the zebrafish became an emerging animal model for biomedical research and is widely applied as a tool for drug discovery [29], as a cancer [30] or disease model [31], and recently also for nanomedicine development [32]. Introducing the zebrafish model as a complementary tool to design, optimize, and preselect nanomedicine formulations for subsequent rodent *in vivo* experiments raises the question about the conservation and predictive value of such experimental results. Therefore, a detailed validation and characterization of the emerging zebrafish model is heavily required. Importantly, formulation effects which have already been described in established *in vivo* models (i.e. rats, mice) have to be confirmed.

In this regard, liposomes are the best characterized and clinically most successful form of nanomedicines [5]. Already from the beginning, rodent models have extensively been used to describe liposome formulation effects such as size [33], lipid composition [34], PEGylation [35] amount of cholesterol [36], or injected dose [37] on pharmacokinetic parameters such as clearance, area under the curve (AUC), or half-life ($t_{1/2}$) [38]. Using liposomes as a reference offers the possibility to assess

the zebrafish model regarding its ability to predict correctly the influence of minor formulation changes on later *in vivo* experiments in mice and rats. Once validated and characterized, the zebrafish model can also be used to assess the *in vivo* behavior (i.e. biodistribution, functionality, stability) of novel nanoparticulate systems as well as the optimization of sophisticated drug delivery systems such as targeted nanomedicines.

AIM OF THE THESIS

As outlined above, nanomedicine formulation design and optimization is mainly based on physicochemical characterization and *in vitro* studies which are not able to fully reflect the complex biological conditions as they are present *in vivo*. As a consequence, the design, optimization and selection of promising nanomedicine lead formulations for subsequent rodent *in vivo* studies represents a major bottleneck in nanomedicine development. Therefore, the aim of this PhD thesis was to establish and validate the zebrafish as an early and easy accessible *in vivo* tool for nanomedicine formulation design and optimization, finally bridging the gap between *in vitro* and rodent *in vivo* studies. To achieve this objective, four major work packages were defined as followed:

- **Evaluation of current zebrafish applications during nanomedicine formulation design and optimization (Chapter I)**
    - How can advantageous zebrafish features be optimally exploited during nanomedicine formulation design and optimization in order to close the *in vitro* – *in vivo* gap?
- **Set-up and validation of the zebrafish model for nanomedicine development (Chapter II)**
    - Is it possible to reproduce already known nanomedicine formulation effects in the zebrafish model?
    - Are findings from zebrafish studies predictable for rodent *in vivo* studies?
- **Mechanistic studies on cellular nanoparticle clearance in the zebrafish model (Chapter III)**
    - Which are the receptors involved in nanomedicine clearance in zebrafish?
    - What is the corresponding mechanism in mammalians?
- **Application of the established zebrafish model (Chapter IV)**
    - Can the zebrafish model be applied during the development of active targeted nanomedicines?
    - Is it possible to assess nanoparticle based enzyme systems under *in vivo* conditions using the zebrafish model?

RESULTS

The presented PhD project consist of four major working packages (Chapters I to IV) and has led to seven publications. Each of these publications is assigned to one of the four chapters as a subproject, which is separately presented.

Chapter I:

I) *Zebrafish as a preclinical in vivo screening model for nanomedicines*

Chapter II:

I) *Zebrafish as a predictive screening model to assess macrophage clearance of liposomes in vivo*

II) *Zebrafish as an early stage screening tool to study the systemic circulation of nanoparticulate drug delivery system in vivo*

Chapter III:

I) *Directing Nanoparticle Biodistribution through Evasion and Exploitation of Stab2-Dependent Nanoparticle Uptake*

Chapter IV:

I) *Optimization-by-Design of Hepatotropic Lipid Nanoparticles Targeting the Sodium-Taurocholate Cotransporting Polypeptide*

II) *Immobilization of Enzymes on PLGA Sub-Micrometer Particles by Crosslinked Layer-by-Layer Deposition*

III) *Biomimetic artificial organelles with in vitro and in vivo activity triggered by reduction in microenvironment*

Chapter I-I

Zebrafish as a preclinical in vivo screening model for nanomedicines

Sandro Sieber, Philip Grossen, Jeroen Bussmann, Frederick Campbell, Alexander Kros, Dominik Witzigmann, Jörg Huwyler

Manuscript: Advanced Drug Delivery Reviews (2019) [39]

Highlights: The zebrafish as an emerging model in biomedical research is a promising tool to close the gap between *in vitro* experiments and subsequent rodent *in vivo* studies. This review article summarizes current applications of the zebrafish during nanomedicine development (i.e. nanotoxicity, biodistribution, cancer targeting). Advantageous zebrafish features in combination with critical experimental parameters are discussed in order to further promote the successful application of this emerging model system during nanomedicine formulation design and optimization.

Advanced Drug Delivery Reviews xxx (2019) xxx

Contents lists available at ScienceDirect

Advanced Drug Delivery Reviews

journal homepage: www.elsevier.com/locate/addr

Zebrafish as a preclinical *in vivo* screening model for nanomedicines

Sandro Sieber [a], Philip Grossen [a], Jeroen Bussmann [b], Frederick Campbell [b], Alexander Kros [b], Dominik Witzigmann [a,c,*], Jörg Huwyler [a,*]

[a] Division of Pharmaceutical Technology, Department of Pharmaceutical Sciences, University of Basel, Basel, Switzerland
[b] Department of Supramolecular and Biomaterials Chemistry, Leiden Institute of Chemistry, Leiden University, Leiden, The Netherlands
[c] Department of Biochemistry and Molecular Biology, University of British Columbia, Health Sciences Mall, Vancouver, British Columbia, Canada.

ARTICLE INFO

Article history:
Received 6 November 2018
Received in revised form 23 December 2018
Accepted 2 January 2019
Available online xxxx

Keywords:
Nanomedicine
Preclinical screening
Drug development
Zebrafish
In vivo
Nanoparticle
Formulation optimization
Experimental parameters

ABSTRACT

The interactions of nanomedicines with biological environments is heavily influenced by their physicochemical properties. Formulation design and optimization are therefore key steps towards successful nanomedicine development. Unfortunately, detailed assessment of nanomedicine formulations, at a macromolecular level, in rodents is severely limited by the restricted imaging possibilities within these animals. Moreover, rodent *in vivo* studies are time consuming and expensive, limiting the number of formulations that can be practically assessed in any one study. Consequently, screening and optimisation of nanomedicine formulations is most commonly performed in surrogate biological model systems, such as human-derived cell cultures. However, despite the time and cost advantages of classical *in vitro* models, these artificial systems fail to reflect and mimic the complex biological situation a nanomedicine will encounter *in vivo*. This has acutely hampered the selection of potentially successful nanomedicines for subsequent rodent *in vivo* studies. Recently, zebrafish have emerged as a promising *in vivo* model, within nanomedicine development pipelines, by offering opportunities to quickly screen nanomedicines under *in vivo* conditions and in a cost-effective manner so as to bridge the current gap between *in vitro* and rodent studies. In this review, we outline several advantageous features of the zebrafish model, such as biological conservation, imaging modalities, availability of genetic tools and disease models, as well as their various applications in nanomedicine development. Critical experimental parameters are discussed and the most beneficial applications of the zebrafish model, in the context of nanomedicine development, are highlighted.

Contents

1. Introduction . . . 0
2. Important zebrafish features for nanomedicine research . . . 0
3. Critical parameters of zebrafish experiments . . . 0
4. Applications of the zebrafish in nanomedicine development . . . 0
   4.1. Toxicity assessment of nanoparticulate drug delivery systems . . . 0
   4.2. Biodistribution and systemic circulation of nanomedicines . . . 0
   4.3. Nanomedicines targeting macrophage resident pathogens . . . 0
   4.4. *In vivo* evaluation of advanced functional nanomedicines . . . 0
      4.4.1. Stimuli responsive nanomedicines . . . 0
      4.4.2. Enzyme and protein delivery . . . 0
      4.4.3. Gene therapy . . . 0
   4.5. Nanomedicines for cancer therapy . . . 0
      4.5.1. Zebrafish cancer models . . . 0
      4.5.2. Zebrafish and rodents as complementary model organisms in cancer research . . . 0
      4.5.3. Screening of cancer nanomedicines . . . 0
5. Discussion and conclusion . . . 0

* Correspondence authors at: Division of Pharmaceutical Technology, Department of Pharmaceutical Sciences, University of Basel, Klingelbergstrasse 50, 4056 Basel, Switzerland.
E-mail addresses: dominik.witzigmann@unibas.ch (D. Witzigmann), joerg.huwyler@unibas.ch (J. Huwyler).

https://doi.org/10.1016/j.addr.2019.01.001
0169-409X/

Acknowledgements . . . 0
References. . . . 0

1. Introduction

Drug delivery using nanoparticulate carrier systems (*i.e.* nanomedicines) is an effective way to enhance drug concentrations within specific target tissues and minimize side effects in off-target organs [1]. To effectively exploit these unique pharmacokinetic features of nanomedicines, the physicochemical properties of the underlying nanoparticles need to be optimized. Ideally nanomedicines should demonstrate low cytotoxicity, stability in biological environments, controlled blood circulation half-life, cell/tissue specificity and efficacy/functionality under *in vivo* conditions. To this end, nanomedicine formulations are designed and optimized according to almost endlessly tunable parameters. These include chemical composition, size, shape, surface charge or surface modification. Therefore, the preclinical development and evaluation of nanomedicines typically follows the same route taken as for traditional drug development, namely physicochemical characterization, *in vitro* experiments and finally rodent *in vivo* studies [2]. During this development pipeline, the number of investigated nanomedicine candidates decreases with each step, due to increasing experimental costs and complexity. However, as recently outlined by Dai *et al.*, nanomedicine performance is heavily affected by biological features which are mimicked during specific experimental set-ups [3]. In particular, the presence of serum and/or extracellular matrix proteins, heterogeneous cell populations (including cells of the immune system) and dynamic blood flow, particularly varying levels of shear stress, have all been shown to be critical to nanomedicine performance. Despite the vast battery of well characterized and increasingly sophisticated *in vitro* models, there remains a huge gap between cell culture experiments and rodent *in vivo* studies in terms of accurately mimicking the full complexity of a living animal. In light of this, significant efforts have been made in recent years to increase the predictive value of *in vitro* experiments through the development of 3D cell (co-) cultures and/or organ-on-a-chip set-ups [4–7]. However, the reproducible generation and characterization of these sophisticated cell culture models remains extremely challenging [8]. In the case of organs with a complex architecture such as the liver, accurate cell culture models are still missing, among other things due to notoriously difficult cultivation of liver sinusoidal endothelial cells. Furthermore, cell-based systems are often more sensitive in terms of nanomedicine toxicity, as they suffer from poor particle distribution and the inability to compensate stresses *via* homeostatic balances [9].

The absence of early and easy accessible *in vivo* screening tools to assess the effects of various nanomedicine formulation parameters under complex biological conditions has hindered effective nanomedicine formulation design and optimization (*e.g.* accurately tailoring the composition). This has resulted in a high rate of drop-outs during early phases of nanomedicine development [10] and limited understanding of nanomedicines' *in vivo* behaviour [11]. Alternative vertebrate animal models that are available in large numbers, easy to handle, cheap to house and maintain, and applicable to nanomedicine formulation screening approaches, are therefore of great interest to bridge the gap between *in vitro* and rodent *in vivo* studies.

Over time, different *in vivo* model systems such as nematodes (*Caenorhabditis elegans*), frogs (*Xenopus laevis*), chicken embryos, and zebrafish[1] (*Danio rerio*) have been introduced to answer various biological questions related to nanoparticles and nanomedicines [12–14]. While zebrafish are well established as a model system in developmental biology [15–20], increasingly these organisms are being used as *in vivo* models in biomedical research, most prominently as platforms for high throughput screens of small molecule drug candidates either in target- or phenotype-based approaches [21–25]. Critical experimental parameters when using zebrafish for biomedical screening (*i.e.* zebrafish age, sample size, concentrations, wild type versus transgenic lines) have been summarized by Rennkamp et al. [21]. The popularity of these biomedical screens has been further boosted by the development of several partially automated readout technologies (*e.g.* light/dark preference test, open field test, visual motor response test)[26]. Given the current empirical approach to nanomedicine design and optimization, and the almost endless variations in potential nanomedicine composition, shape, size, surface charge and surface modification, nanomedicines could potentially benefit significantly from this emerging *in vivo* model. Indeed, recent studies have demonstrated the potential of the zebrafish as an early and easily accessible *in vivo* tool during nanomedicine development [27,28].

To this end, this review focuses on applications of the emerging zebrafish model (Fig. 1) to facilitate nanomedicine formulation design and optimization prior to rodent studies. Zebrafish characteristics which are of special interest for biomedical research, such as the conservation of key biological features, imaging modalities and the availability of genetic tools and disease models are discussed in detail. Assessment of important nanomedicine characteristics including toxicity, *in vivo* stability and functionality, biodistribution and blood circulation properties, and targeting efficiency within the zebrafish are described and the most suitable experimental set-ups are emphasized. Since comparability and standardization of such experiments are of great importance, critical experimental parameters are also highlighted and discussed.

2. Important zebrafish features for nanomedicine research

Zebrafish larvae have several advantageous properties over adult zebrafish or rodents, which makes them attractive to screen nanomedicines. Firstly, the costs of zebrafish husbandry are low (compared to mice or rats) and larvae are available in large numbers and develop external from the mother. This allows for high-throughput screening set-ups under *in vivo* conditions. Secondly, information networks such as ZFIN (zfin.org), combined with the fact that embryos or frozen sperm can be easily transferred between labs, guarantee fast and easy access to specific transgenic zebrafish lines. Thirdly, the optical transparency of zebrafish larvae, which can be chemically prolonged up to several days (*e.g.* using 1-phenyl-2-thiourea (PTU) to inhibit melanogenesis [29]), enables high resolution (fluorescence) imaging of specific biological events in real time and across entire the living organism. Alternatively to PTU treatment, a transparent zebrafish line (*i.e.* Casper) has been generated which still lacks pigmentation in the adult stage [30]. Finally, numerous molecular and biological tools are available to create new genetically modified zebrafish lines. These include TILLING [31], morpholino oligonucleotides [32], zinc-finger nucleases [33], TALENs [34], and CRISPR/Cas [35], Tol2 transposons combined with bacterial artificial chromosomes [36], and in situ hybridization [37]. Using these tools, many zebrafish lines with particular relevance to nanomedicine development have been generated and are summarized in Table 1. The availability of transparent zebrafish larvae, fluorescent reporter lines and sophisticated imaging techniques, such as confocal or light sheet microscopy, are key factors that enable the investigation of nanomedicine behavior *in vivo* at a macromolecular level.

[1] Developmental stages of zebrafish described as follows: zebrafish = no specific developmental stage, zebrafish embryo = until 48 h post fertilization (hpf), zebrafish larvae = 48 hpf – 3 week post fertilization, adult zebrafish = >3 weeks post fertilization.

Please cite this article as: S. Sieber, P. Grossen, J. Bussmann, et al., Zebrafish as a preclinical *in vivo* screening model for nanomedicines, Adv. Drug Deliv. Rev., https://doi.org/10.1016/j.addr.2019.01.001

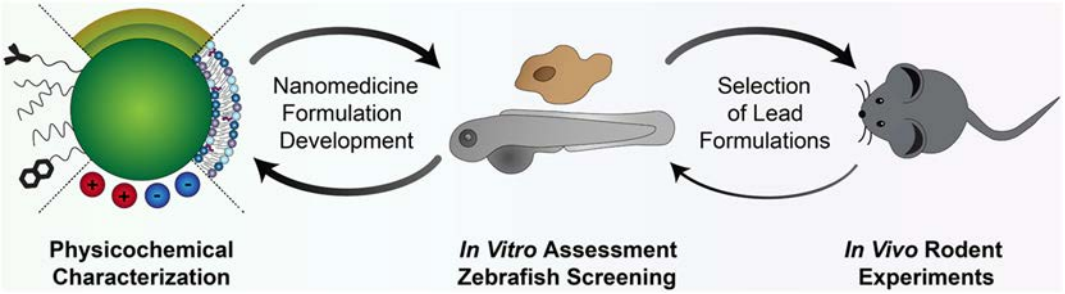

Fig. 1. Schematic representation of nanomedicine formulation design and optimization including the emerging zebrafish model. The complementary application of classical *in vitro* systems and the zebrafish model offers the possibility to screen the effects of varying nanomedicine formulations and physicochemical properties under complex biological conditions. This facilitates the selection of promising lead formulations for subsequent rodent *in vivo* studies.

Proposing the zebrafish as an *in vivo* tool for nanomedicine characterisation raises immediate questions regarding the conservation of relevant biological features and the accuracy of translating findings to mammals. At the genomic level, 76% of human genes (82% of disease-related genes) have orthologues in zebrafish, compared to 80% and 84% in chicken and mice, respectively [47]. Epigenetic markers, which regulate conserved genes between these species, are highly consistent [48]. Zebrafish anatomy and physiology are well described [49–52] and physiological parameters and organ systems of particular interest in terms of nanomedicine toxicity and biodistribution, such as the vascular system [53–55], blood composition [56,57], immune system [58,59] including a lymphatic system [60], blood-brain barrier [61–63] and liver [64,65] have been extensively studied and share many important physiological homologies with their mammalian equivalents [66]. The rapid development of the zebrafish embryo results in a compartmentalized brain and the presence of eyes, ears and internal organs after one day post fertilization (dpf) [29,67,68]. However, maturation of some key organs, particularly the adaptive immune systems, occurs at later developmental stages. When considering a zebrafish study, developmental stage is therefore a critical experimental parameter as discussed in Section 3.

As a key cell type of the mononuclear phagocyte system (MPS), macrophages are among the first cell types that respond to administered nanomedicines [9]. Importantly, early embryonic macrophages have been found to be present and functional at very early stages of zebrafish development (30 h post fertilization, hpf) [69]. In addition, other key cell types defining the mammalian MPS, including monocytes and dendritic cells, are present in adult zebrafish [70]. Macrophage polarization is reported to change from M1 to M2 upon tumor tissue infiltration. This is an important feature of tumor growth and progression [71] and conversion of M1 to M2 macrophages has been demonstrated in larval zebrafish to highlight the diversity and plasticity of zebrafish macrophages as well as similarities to their human counterparts [42]. The rapid development of zebrafish immune cells again highlights the importance of choosing an appropriate zebrafish developmental stage.

Interactions of nanomedicines with cells are heavily dependent on the adsorbed protein corona. In the case of intravenously (*i.v.*) administered nanomedicines, the protein corona comprises blood serum components [72]. In general, zebrafish and human plasma proteomes share striking similarities, in particular regarding the conservation of apolipoproteins and complement factors [73]. Surface opsonization *via* complement factors C3, C4, and C5 is an important initial step towards nanoparticle recognition by macrophages [74] and these proteins are highly conserved in zebrafish, including conservation of respective signalling pathways [75]. Likewise immunoglobulins (Igs), such as IgG and IgM, are known to tag nanoparticles as "foreign" material in the body, again initiating nanomedicine clearance by macrophages [76,77]. As in humans, zebrafish Igs are composed of a light- and heavy-chains, bearing variable V, D, and J segments that are generated through recombination. Junctional diversity and hypermutation further amplify variety of the antibody repertoire. In contrast to humans, where five classes of Igs are known, zebrafish possess only three different Ig isotypes: IgM, IgZ and IgD [78]. Moreover, different cells express varying types of apolipoprotein receptors, which greatly affects the biodistribution of apolipoprotein coated nanoparticles [79–81]. Otis *et al.* characterised the zebrafish as a suitable model for apolipoprotein biology [82], finding a generally conserved physiological role of apolipoproteins despite low genetic sequence similarity. Abundant serum proteins such as albumin, fibrinogen, and transferrin [83] are major components of the characterized protein corona of nanoparticles in mammals [77]. Whereas fibrinogen and transferrin are present in zebrafish [73], a coding gene for the albumin- paralogue, vitamin D binding protein, but not albumin itself, has been found [84].

Regarding the investigation of organ pathology the zebrafish has shown to be a valid tool [85–88]. Zebrafish disease models at varying developmental stages for the cardiovascular system [89–91], liver [92,93], kidney [94,95] and immune system, including the spleen [96–99], are available. Notably, all these organs can significantly influence nanomedicine biodistribution and clearance.

Table 1
Overview of zebrafish lines with particular value for the *in vivo* characterization of nanomedicines. Various promoters and fluorescent reporter proteins can be combined in almost any way. An exemplary selection of existing zebrafish lines is highlighted here together with their specific characteristics and possible applications in nanomedicine formulation development and optimization.

Zebrafish line	Reference	Specific characteristic	Possible application
Casper	[30]	Transparent adults	Long term tumor models, fluorescence imaging of adult zebrafish
Tg(flk1:EGFP)	[38]	Fluorescent vasculature	Blood circulation behavior
Tg(lyve1:EGFP)	[39]	Fluorescent lymphatic system	Lymphatic uptake and distribution
Tg(zmpo:GFP)	[40]	Fluorescent neutrophils	Immune systems interaction
Tg(mpeg1:mCherry)	[41]	Fluorescent macrophages	Immune systems interaction
Tg(tnfa:EGFP-F)	[42]	Fluorescent M1 macrophages	Immune systems interaction
Tg(l-fabp:DBP-EGFP)	[43]	Fluorescent Vitamin D binding protein	Binding to albumin paralogue
TgBAC(cldn5a:EGFP)	[44]	Fluorescent brain endothelial cells	Brain delivery
Stab2 mutant	[28]	No stabilin 2 receptors	Scavenger receptor interactions
LDLR mutant	[45]	Low density lipoprotein receptor deficiency	LDLR dependent biodistribution, hepatocyte or brain targeting
Apoc2 mutant	[46]	Apolipoprotein loss of function	Apoc2 dependent biodistribution

Please cite this article as: S. Sieber, P. Grossen, J. Bussmann, et al., Zebrafish as a preclinical *in vivo* screening model for nanomedicines, Adv. Drug Deliv. Rev., https://doi.org/10.1016/j.addr.2019.01.001

Beside the aforementioned advantageous features of the zebrafish model, there are practical limitations, primarily due to the small size of the experimental system. Firstly, blood sampling from zebrafish larvae and even adult zebrafish is difficult. Secondly, only low amounts of biomolecules, *e.g.* proteins, are available for further analysis due to the small size of zebrafish larvae or respective tumor burden (see Section 4.5). These challenges often require pooling several zebrafish larvae for analysis, which excludes the possibility to observe differences between individual animals, as it is for example possible in rodent *in vivo* studies. However, analysis of high numbers of zebrafish larvae increases the statistical power. In addition, there are technical limitations compared to *in vitro* models. Protocols including the inhibition and fluorescent staining of specific cellular uptake and trafficking mechanisms are mostly designed for *in vitro* set-ups [100,101] and still need to be optimized in order to routinely apply them in zebrafish. Furthermore, generating stable transgenic zebrafish lines expressing fluorescent proteins or specific targeting receptors requires several months, which can be an experimental constraint, especially when compared to simply transfecting cells *ex vivo*. Overall, zebrafish-based test systems have to be validated carefully by comparing them to established protocols. This will ultimately increase acceptance in the scientific community and facilitate the use of the zebrafish model during preclinical screening of nanomedicine formulations.

3. Critical parameters of zebrafish experiments

The success and reproducibility of nanomedicine zebrafish studies is affected by several experimental parameters which are discussed in the following section (Fig. 2). Developmental stage and experimental timing are the first parameters that must be carefully defined when planning a zebrafish study. The stages of zebrafish embryonic development and the presence of major vertebrate organ systems are well described and easy to predict [67,102]. As already indicated, zebrafish development including the gradual loss of transparency, organ maturation and the development of the immune system occurs over relatively short time frames (hours to days) and may influence experimental outcomes. Depending on the study objective, different stages of development are recommended as start point. For example, generation of genetically modified zebrafish lines using mutagens, such as *N*-Ethylnitrosourea (ENU), are performed on adult zebrafish whereas genetic constructs/systems, such as capped mRNA, expression plasmids or CRISPR-Cas, are preferentially injected at the single-cell stage [103]. Exploiting the optical transparency of the zebrafish larvae, fluorescently labeled nanomedicine injections are often coupled with fluorescence-based imaging. Importantly, the injection time points of different nanomedicine formulations, required controls and replicates should be planed carefully to ensure consistent intervals between injection and imaging.

Various administration routes of nanomedicines into the zebrafish have been used. These include, for example, oral administration, simple addition to the zebrafish media and both *i.v.* and intraperitoneal (*i.p.*) injections. Choosing a suitable administration route is partly dependent on the required dosing accuracy and zebrafish developmental stage. Oral administration by gavage has been performed in adult zebrafish [104,105], as well as in larvae [106], but will not be further discussed given the very few reports of orally administered nanomedicines. Injecting nanomedicines into blood circulation is often performed *via* the easily accessible duct of Cuvier, a comparatively large blood vessel of the embryonic zebrafish that continuously remodels and reduces in size until 120 hpf [107]. Alternatively, local CNS (*i.e.* brain ventricle) [108], retro-orbital [109] or *i.p.* injections [110] have been described. These injections are generally performed at later developmental stages. Finally, direct injection into the blood island/caudal hematopoietic tissue (CHT) is often used in infection models within the embryonic fish.

Using a microinjector-system, precise injections of samples can be achieved. By adjusting air pressure and volume, injection volumes can be calibrated by injecting samples into mineral oil followed by drop size measurements with a scale included in the microscope ocular, the injection base [111] or using microscopy calibration slides. For injections *via* the duct of Cuvier, special care must be taken to avoid injection into the yolk sac. Material injected into the yolk will not enter circulation, leaving an unknown sample volume in circulation. The blood volume of a zebrafish larvae at 2 dpf is around 60 nl, therefore *i.v.* injected sample volumes should not exceed low nanoliter ranges (*i.e.* up to 3 nl) [112].

Experimental temperature is another critical factor. Incubation temperature, during early zebrafish developmental stages, affects the rate of development and the innate immune response of zebrafish larvae [113]. In general, it is known that zebrafish cope with stress (*i.e.* chemical exposure, pain) by choosing regions of higher water temperatures. Temperature dependent physiological processes (*e.g.* immune response) can in turn affect experimental results [114–116], meaning experimental temperature must be carefully selected and standardized, especially when assessing processes involving the zebrafish immune system (*e.g.* nanomedicine clearance by macrophages). Furthermore, physicochemical nanoparticle properties can also vary dependent on body temperature thereby influencing nanomedicine pharmacokinetics [27]. Of particular note here are lipids (*e.g.* DMPC) with phase transition temperatures between 28°C (zebrafish) and 37°C (mammalian) for which small variations in experimental temperature can become critical.

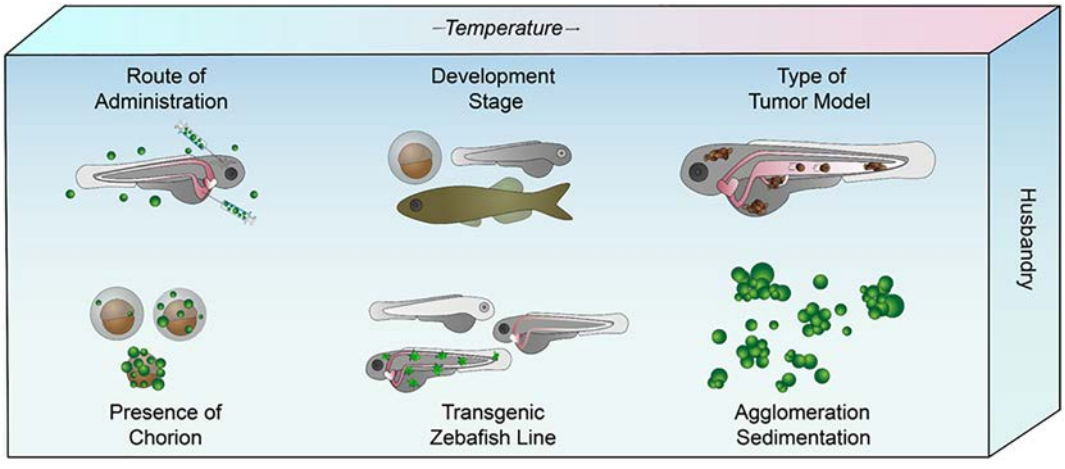

Fig. 2. Critical experimental parameters affecting the results of nanomedicine zebrafish studies. The appropriate selection of zebrafish developmental stage and the most suitable zebrafish line is crucial. In addition, the route of administration of nanomedicines, such as incubation in media or intravenous injection, strongly influences experimental results. Zebrafish husbandry and maintenance dictates many factors, such as water conductivity, pH, feeding, and fish density. They should be considered and controlled to guarantee consistent experimental conditions.

Please cite this article as: S. Sieber, P. Grossen, J. Bussmann, et al., Zebrafish as a preclinical *in vivo* screening model for nanomedicines, Adv. Drug Deliv. Rev., https://doi.org/10.1016/j.addr.2019.01.001

Notably, elevated temperatures over longer periods of time can affect physiological processes of the zebrafish, mediated by the presence of heat shock proteins [117,118]. Therefore, performing experiments under varying temperature conditions should be considered carefully, strictly controlled and exact conditions should be reported.

4. Applications of the zebrafish in nanomedicine development

Given the many advantages over rodent counterparts, zebrafish larvae are increasingly used as model systems during nanomedicine formulation development and optimization. Nanomedicine toxicity, biodistribution and systemic circulation, stability, functionality and targeting efficiency have all been successfully assessed within the complex biological, *in vivo* environment of a living zebrafish larvae (Fig. 3). Table 2 summarizes the experimental details of various nanomedicine studies using the zebrafish model. Since nanomedicines are most frequently developed as potential cancer therapies, the generation, compatibility (with well characterized mouse models [119–122]) and use of zebrafish cancer models will be discussed in Section 4.5 of this review.

4.1. Toxicity assessment of nanoparticulate drug delivery systems

Toxicological assessment of nanomedicines was one of the first applications to combine nanomedicines and zebrafish and is covered in several reviews [123–125]. In general, nanotoxicity studies involve exposing zebrafish embryos to nanoformulations *via* addition to the zebrafish media. This approach is, at the very least, questionable with respect to dosing accuracy, actual exposure and the stability of nanoparticles in zebrafish media. In testing the overall toxicity of nanomedicines, properties of the encapsulated drug will also affect experimental outcomes. Based on varying logP values, drugs permeate differently into zebrafish skin, a factor that will significantly affect the ability to control and standardize dosage and exposure [23]. Henn et al. showed that results of toxicological assays or drug screenings (*i.e.* chemical exposure), were differentially affected by the chorion surrounding the zebrafish embryo [126]. In a related study, Paatero et al. tested toxic effects of different nanoparticles following incubation with normal and dechorionated embryos, as well as injection of the same samples into 4 hpf embryos [127]. This study revealed differing abilities of nanoparticles to penetrate biological barriers, which significantly influenced toxicological profiles. To overcome this variable, the chorion can be removed by either enzyme supported- or mechanical dechorionation [126]. To standardize exposure of single zebrafish embryos in toxicological screens, the presence or absence of the chorion, assay volume, nanoparticle concentration and number of zebrafish/well has to be clearly stated. Going one step further, Pan et al. quantified nanoparticle uptake in individual zebrafish embryos through inductively coupled plasma mass spectrometry of digested zebrafish embryos/larvae obtained *via* an aqua regia-based microwave digestion protocol [128]. Although rigorous, this approach is time consuming which hampers its use for the screening of large nanomedicine libraries. Taken everything together, direct injection of nanomedicines into zebrafish larvae allows for a precise control of zebrafish exposure and should therefore be the method of choice. As an example, Vibe et al. assessed the toxicity of free and nanoparticle formulated drug upon injection into zebrafish larvae [129]. Thus, uncertainties regarding the actual drug exposure were excluded enabling the observation and analysis focused solely on nanoformulation effects. In contrast, simple addition of formulations to the fish water should be avoided since the amount of test substance taken up by the animal cannot be controlled. An exception are long-term exposure studies in the field of eco-nanotoxicology.

Nanoparticle aggregation and sedimentation are heavily affected by the suspension media. In contrast to cell culture media containing bicarbonate/CO_2 and buffering agents, sample addition to un- or only slightly buffered zebrafish media can induce pH changes (possibly resulting in false positive results) and should therefore be carefully monitored [128]. If nanoparticle toxicity is tested *via* addition to the zebrafish media, colloidal stability should also be assessed in that same media (*i.e.* E3 medium [130]) to ensure uniform exposure. Along these lines, Kiene *et al.* first determined the highest non-toxic nanoparticle concentration *in vitro* before proceeding to test their nanoparticles in a zebrafish embryo toxicology assay (mortality, morphology, hatching rate) with accompanying size and polydispersity measurements [131].

Toxicological readouts, such as survival or malformations, can be assessed in a controlled and relatively fast manner [132]. However, given the degree and severity of malformations is often subjective. In an attempt to improve comparability and reproducibility of these experimental outcomes semi-quantitative scoring systems have been

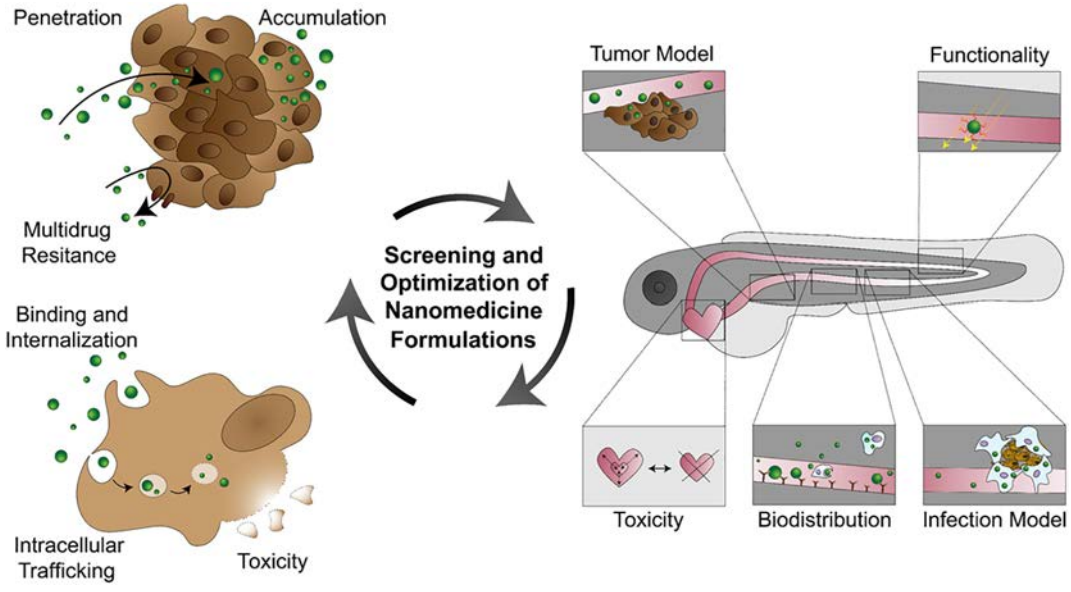

Fig. 3. Complementary application of *in vitro* and zebrafish model experimental set-ups for nanomedicine formulation design and optimization. The complementary application of classical 2-D (bottom left) and sophisticated 3-D (top left) *in vitro* systems and the zebrafish model (middle right) offers the possibility to assess nanomedicine interactions with biological environments under complex biological conditions. The availability of an optimized preclinical, *in vivo* screening platform increases the chance to identify potentially successful nanomedicine formulations prior to translation into rodent *in vivo* studies.

Please cite this article as: S. Sieber, P. Grossen, J. Bussmann, et al., Zebrafish as a preclinical *in vivo* screening model for nanomedicines, Adv. Drug Deliv. Rev., https://doi.org/10.1016/j.addr.2019.01.001

Table 2
Summary of nanomedicine studies using zebrafish to investigate toxicity, biodistribution, functionality and tumor treatment.

Application	Experimental readouts	Administration (nanomedicine/cancer cells)	Zebrafish line	Developmental stage	Reference
Nanotoxicology	Mortality, Blood flow, Tissue penetration	Incubation*/Injection	*Tg(kdrl:EGFP s843)*	6–24 hpf	[127]
	Morphology, Hatching, Mortality, Induction of Heat-Shock Protein	Incubation*	Wild-type, *Tg(hsp70:GFP)*	0 hpf	[128]
	Mortality, Swim bladder inflation, Yolk discoloration, Pericardial edemas	Injection	*Tg(nacre$^{-/-}$;roy$^{-/-}$)*	72 hpf	[129]
	Mortality, Morphology, Hatching	Incubation*	Wild-type (AB)	4 hpf	[131]
	Mortality	Injection	N.A.	1-cell stage	[132]
	Development, Morphology, Mortality	Incubation*	Wild-type (AB)	2 hpf	[133]
	Morphology, Mortality	Incubation*	Wild-type (AB)	0–2 hpf	[134]
	Development, Morphology, Apoptotic cell death, Heart functionality	Incubation*	Wild-type (AB), *Tg(cmlc2:EGFP)*	6–30 hpf	[136]
	Gill injury, Biochemical liver and kidney toxicity, Mortality	Incubation*	Wild-type	Adult	[138]
	Mortality, Morphology, Heart rate, Apoptotic cell death, Tissue distribution	Incubation*	N.A.	0 hpf	[139]
	Locomotion, Hatching, Morphology, Mortality, Body weight, Thyroid hormone levels	Incubation*	Wild-type (AB)	2 hpf	[140]
	Mortality, Morphology, Locomotion, Neuronal cell volume	Incubation*	Wild-type (AB), *Tg(lsl1:EGFP)*	48–96 hpf	[141]
Biodistribution	NP extravasation and blood circulation behavior	Injection *via* duct of Cuvier	*Tg(kdrl:GFP)*	48 hpf	[27]
	Scavenging receptor, macrophage and neutrophil mediated nanoparticle clearance	Injection *via* duct of Cuvier	*Tg(kdrl:GFP)^{s843}*, *Tg(kdrl:RFP-CAAX)^{s916}*, *Tg(mpeg:GFP)^{gl22}*, *Tg(mpeg:RFP-CAAX)^{ump2}*, *TG(flt1^{enh}:RFP)^{hu5333}*, *Tg(flt4^{BAC}:YFP)^{hu7135}*, *Tg(mpx:GFP)^{uwm1}*, CRISPR/Cas9 mutants	52–56 hpf	[28]
	Macrophage clearance	Injection *via* duct of Cuvier	*Tg(kdrl:EGFP)*, *Tg(mpeg1:Gal4;UAS:Kaede)*	48 hpf	(Sieber et al., manuscript in preparation)
	NP localization in blood vessels	Injection *via* heart	*Tg(kdrl:GFP)*, *Tg(gata1:DsRed)*	52 hpf	[149]
	Endothelial cell association, Tissue penetration	Injection *via* duct of Cuvier	*Tg(kdrl:GFP)*	52 hpf	[150]
	Endocytosis and stability	Injection *via* duct of Cuvier	*Tg(kdrl:GFP)*	52–56 hpf	[151]
	Transport across biological barriers	Incubation*	Wild-type	Embryo, Larvae, Adult	[153]
	Presence in whole body, brain, eye, and intestine, Intestinal absorption	Incubation*, Oral administration (gavage), Injection into intestine	Wild-type	24–168 hpf, Adult	[154]
	Ability to cross the BBB	Injection *via* heart	Wild-type	144 hpf	[155]
	Presence in brain, blood stream, and spinal cord	Injection *via* caudal vein, spinal cord, and brain	*Tg(-3mnxl:TagBFP)*, *Tg(isl1:GFP)*, *Tg(GFAP:EGFP)*, *Tg(fli1a:EGFP)*	96–144 hpf	[156]
	Uptake into infected and uninfected macrophages	Injection *via* caudal vein	Casper, *Tg(mpeg1:mcherry)*, *Tg(lyz:DsRed2)*, *Tg(fli1:EGFP)*	72–120 hpf	[163]
	Accumulation in tuberculosis granulomas	Injection *via* posterior caudal vein	*Tg(fli1a:EGFP)*, Wild-type	48-52hpf	[164]
Functionality	Photothermal triggered drug release	Injection *via* brain ventricle	N.A.	120 hpf	[170]
	Photothermal induction of ROS generation	Injection of cancer cell/NP mixture *via* duct of Cuvier	Casper	30 hpf	[171]
	Reduction of xenograft cell viability upon singlet oxygen generation	Injection *via* cardinal vein	N.A.	48 hpf	[172]
	Laser induced formation of plasmonic nanobubbles	N.A.	N.A.	Blastula stage	[173]
	Enzyme activity, Stability	Injection *via* duct of Cuvier	Wild-type (ABC/TU)	48 hpf	[174]
	Enzyme activity, Stability	Injection *via* duct of Cuvier	Wild-type (ABC/TU), *Tg(mpeg1:Gal4;UAS:Kaede)*	48 hpf	[175]
	Transfection efficiency	Injection into embryo interlayer	N.A.	1-cell stage	[180]
	mRNA delivery	Injection into yolk, *via* hindbrain ventricle, caudal vein, trunk, and pericardial cavity	Wild-type (AB)	1-cell stage, 24–48 hpf	[181]
	Gene silencing	Injection	*Tg(fli:EGFP)*	Sphere stage	[182]

Table 2 (*continued*)

Application	Experimental readouts	Administration (nanomedicine/cancer cells)	Zebrafish line	Developmental stage	Reference
Tumor Treatment	Tumor proliferation analysis	Cancer cell injection *via* the perivitelline space, NP *via* yolk	N.A	48–144 hpf	[229]
	Cancer cell targeting	Cancer cell injection *via* duct of Cuvier, NP *via* the caudal vein	*Tg(fli1:EGFP)*	48–53 hpf	[230]
	Tumor growth inhibition	Cancer cell injection *via* the perivitelline space, NP incubation*	*Tg(FLK-1:EGFP), Tg(FLK-1:mCherry)*	48 hpf	[231]
	Tumor growth inhibition, Tumor spreading	Injection of cancer cell/NP mixture into yolk	N.A.	96 hpf	[232]
	Tumor vascularization	Injection of cancer cell/NP mixture *via* perivitelline space	*Tg(fli1a:EGFP)*, Wild-type	48 hpf	[233]
	Tumor vascularization	Injection of cancer cell/NP mixture into yolk	Wild-type (AB)	48 hpf	[234]
	Metastasis	Pretreated cancer cell injection into yolk	Tg(kdrl:mCherry)	48 hpf	[235]
	NP tumor accumulation, Tumor growth, NP circulation, NP macrophage uptake	Cancer cell injection *via* duct of Cuvier, NP injection *via* caudal vein	Wild-type (AB), *Tg(fli1:EGFP)y1, Tg(mpeg1:mCherry)*^{UMSF001}	48–96 hpf	[236]
	Angiogenesis, Tumor growth, Metastasis	Cancer cell injection *via* perivitelline space, NP incubation*	*Tg(FLK-1:EGFP)*	48 hpf	[238]
	Tumor cell migration/invasion	Cancer cell *via* hindbrain ventricle, NP incubation*	5D tropical strain	48–96 hpf	[239]
	PCR analysis of VEGF RNA as a marker of cancer cell growth	Injection *via* common cardinal vein	*Tg(fli1:GFP)*	120 hpf	[240]
	PCR analysis of cancer cell specific RNA	Cancer cell injection into yolk,	Tübingen Wild-type	48–144 hpf	[241]
	Evaluation of optimal targeting ligand density	Cancer cell and NP injection *via* duct of Cuvier	*Tg(kdrl:EGFP), Tg(mpeg1:Gal4;UAS:Kaede)*	48 hpf	(Witzigmann et al., manuscript in preparation)

For each study, experimental readouts are included. Administration routes of nanomedicines and/or cancer cells (for the generation of zebrafish tumor models) are indicated as well as transgenic zebrafish lines used and zebrafish development stage during the course of experiments. References are sorted according to their application and listed in order of their appearance in the manuscript. It has to be noted that simple incubation of zebrafish with nanomedicines (*) is not recommended as exposure and dose cannot be controlled. NP = nanoparticle, hpf = hours post fertilization, N.A. = information not available.

proposed by different experts [133,134]. Accompanying these scoring systems are newly developed nanotoxicity readouts focusing on behavioral aspects of zebrafish larvae and aimed at greater automation and sample throughput. These include automated procedures for studying locomotion parameters such as swimming speed and depth [135].

Interestingly, nanomedicine toxicity can been visualized at a cellular level within zebrafish embryos/larvae [136]. For example, acridine orange staining of apoptotic cells and tissues is possible [137]. Furthermore, toxicological endpoints such as disruption of gill [138], skin [139], and the endocrine system [140], as well as complex toxicity mechanisms (*e.g.* immunotoxicity, genotoxicity, neurotoxicity, or reproductive toxicity) have all been reported [123]. Nasrallah et al. performed a locomotion assay in *Tg(Isl1:EGFP)* zebrafish larvae, stably expressing green fluorescent protein in motor neurons, following nanoparticle incubation [141]. Finally, a highly sensitive analysis of nanoparticle toxicity was recently proposed by Pan et al. [128], that takes advantage of the endogenous expression of heat shock proteins in response to toxic compounds [142]. Using a newly generated transgenic zebrafish line, expressing green fluorescent protein (GFP) under the control of a heat shock protein promoter, the authors were able to show nanoparticle toxicity induced GFP expression with 20-fold greater sensitivity as compared to a classical toxicology analysis in wild type zebrafish [128].

4.2. Biodistribution and systemic circulation of nanomedicines

Most *i.v.* administered nanomedicines aim to alter the biodistribution of their drug payload, prolong blood circulation lifetimes of drugs and/or promote passive accumulation of drugs in fenestrated solid tumors. Organ biodistribution, circulation half-life ($t_{1/2}$) and area under the curve (AUC) are therefore important pharmacokinetic parameters of nanomedicines that have been traditionally assessed in mice, rats or dogs [143,144]. These dynamic parameters can be assessed in zebrafish larvae, with the accompanying advantage of being able to extensively optimize nanomedicine formulations under realistic and complex *in vivo* conditions early in the development process and prior to first trials in higher animals.

Biodistribution is heavily affected by nanoparticles' propensity to be recognized and cleared by cells of the reticuloendothelial system (RES or MPS) [145–147]. By screening nanoparticles in zebrafish larvae, both the systemic circulation and the clearance of nanoparticles, primarily by macrophages and scavenger receptor expressing cells, can easily be assessed [27,28]. Correlating data ascertained in zebrafish embryos to higher order mammals. We recently demonstrated that zebrafish larvae are an accurate *in vivo* model to predict pharmacokinetic properties in rodents [27]. In this study, different lipid-based nanoparticle formulations demonstrated different binding affinities to venous tissues of the zebrafish larvae. Based on the analyzes of acquired confocal images, zebrafish extravasation and circulation factors were defined to enable semi-quantitative descriptions of nanoparticles' blood circulation. With this approach, investigational nanomedicine formulations can be compared to established and well-defined formulations (*e.g.* long circulating PEGylated liposomes). Here it is important to note that predictions of absolute pharmacokinetic parameters (allometric scaling from zebrafish to mice), such as $t_{1/2}$ or AUC, are not yet possible but are the subject of current investigations. To further elucidate the underlying biological mechanisms of nanoparticle clearance,

we uncovered the presence of the stabilin-2 scavenger receptor, expressed exclusively in the caudal vein (CV) and caudal hematopoietic tissue (CHT) of the zebrafish larvae [28]. Highly expressed on mammalian liver sinusoidal endothelial cells (LSECs) and other clearance organs [148], stabilin-2 is primarily responsible for the removal of macromolecular and colloidal waste from blood circulation. By injecting different nanoparticles in zebrafish larvae, we showed a preference of this receptor for all anionic nanoparticles, a finding which was verified in mice. Nanoparticle uptake by macrophages represents another important clearance mechanism of nanomedicines. Transgenic zebrafish expressing fluorescent proteins in all macrophages [41] are therefore a valuable tool to assess this important pharmacokinetic parameter. Our group has recently investigated macrophage clearance of liposomes of various sizes and surface modifications (*i.e.* PEGylation) in zebrafish embryos. Importantly, a good correlation between macrophage uptake in zebrafish larvae and liposome accumulation in the spleen of rats, a main reservoir of mammalian macrophages, was found (Sieber et al., manuscript in preparation).

To assess the ability to accurately mimic dynamic flow, Garcia et al. assessed various parameters including blood flow velocity, shear stress and flow disturbances in zebrafish larvae. It was found that depending on the vasculature architecture (*i.e.* branch points, curvature), and concomitant changes in velocity and shear stress, nanoparticle accumulation was strikingly altered. This study further highlights the value of the zebrafish larvae model when it comes to nanoparticle studies under dynamic conditions [149], a parameter which cannot be mimicked *in vitro* in such a detailed manner. Jiang et al. investigated the impact of surface charge on nanoparticle interactions with endothelial cells, under flow, in zebrafish larvae [150]. In this case, vessel diameter dependent changes of blood flow velocity as well as nanoparticle surface charge was found to influence nanoparticle binding to endothelial cells and penetration into surrounding tissue. Askes et al. investigated cellular uptake and trafficking of nanoparticles in cell culture and zebrafish larvae at various timepoints [151]. Here, nanoparticle endocytosis and lysosomal accumulation, including long-term stability in these cellular compartments, was demonstrated both *in vitro* and *in vivo*.

Biological barriers, such as the blood brain barrier (BBB), prevent nanomedicines reaching their site of action. The BBB is of particular interest, as effective drug delivery to the brain remains a major challenge in terms of drug delivery. Active targeting of nanomedicines to receptors (over-)expressed at the BBB is one popular approach taken to try and breach this biological barrier [152]. Li et al. successfully demonstrated this approach in larval zebrafish envisioned based on already described zebrafish features such as a functional BBB and the expression of tight junctions, transferrin receptors, and efflux transporters [153–155]. Furthermore, transgenic zebrafish lines expressing fluorescent proteins in neuronal cells or astrocytes have been used to examine brain accumulation of nanoparticles upon injection at different sites within zebrafish embryos [156]. However, it is important to note that current information on BBB development in the zebrafish is scarce and this topic remains controversial. Accurate descriptions of the functional development of the BBB in zebrafish larvae, determined using established protocols [157,158] and with appropriate control experiments, will be of great value to the zebrafish community. In the context of nanomedicines, BBB permeability is relevant and can be assessed using fluorescent dyes with different molecular weights [159].

4.3. Nanomedicines targeting macrophage resident pathogens

Nanomedicines are a promising therapeutic option to treat infectious diseases. Ideally, this should involve the preferential biodistribution of nanomedicines, and subsequent targeted drug delivery, to niches formed by bacteria. Interestingly, zebrafish larvae have emerged as more accurate model system for many infectious diseases. Mice often fail to replicate important features of human pathology which is particularly striking in the case of tuberculosis (TB) where compact granulomas, characteristic of human tuberculosis infections, are present in zebrafish embryo TB models [160,161] but absent from the most widely used mouse models [162]. Taking advantage of the high persistency of TB in macrophages, Fenaroli et al. were able to show rifampicin loaded nanoparticles, administered to zebrafish larvae and targeted to macrophages, resulted in increased survival rates and decreased bacterial load, whereas free rifampicin showed only a reduced efficacy [163]. Complementary to the transgenic macrophage fluorescent line, the authors also exploited established transgenic zebrafish lines expressing fluorescent proteins in neutrophils or in vascular endothelial cells, to precisely describe both the infection status and nanomedicine treatment process. In a follow up study, the authors investigated the possibility of macrophage independent nanomedicine-based delivery strategies to tuberculosis granulomas *via* an enhanced permeability and retention (EPR)-like process. Here, the versatility in experimental set-ups of zebrafish larvae enabled injection of *Mycobacterium marinum* into the neural tube of zebrafish larvae, resulting in the formation of tissue granuloma (*i.e.* model organism to study tuberculosis infection). Subsequent injection of PEGylated nanoparticles resulted in reduced clearance by macrophages and accumulation of nanoparticles within granulomas, supporting the authors' hypothesis [164].

4.4. In vivo evaluation of advanced functional nanomedicines

Nanomaterials are used in a broad range of applications including stimuli responsive systems, enzyme/protein delivery, and gene therapeutics [165–169]. Successfully developing such complex and sophisticated systems is heavily dependent on their stability and functionality under *in vivo* conditions. These parameters can often be ideally assessed in zebrafish.

4.4.1. Stimuli responsive nanomedicines

Nanoparticle drug delivery systems can be designed to release their cargo upon a specific trigger (*e.g.* pH changes, redox changes, photoirradiation). Yan et al. injected photo-responsive, curcumin loaded nanoparticles in zebrafish larvae [170] to demonstrate triggered drug release upon light irradiation or temperature increase (37 °C). Here, the inherent fluorescence of curcumin could be used as a reporter within the living embryo. In addition, curcumin released in the zebrafish larvae heart was able to improve heart function (*i.e.* heartbeat rate and cardio muscular contractility). Photoirradiation, in combination with nanoparticles, has also been used to generate reactive oxygen species (ROS) to kill tumor cells within zebrafish larvae [171,172]. Nanomedicines are also ideal candidates for combined diagnostic and therapeutic function, so-called theranostics. In zebrafish larvae, theranostic plasmonic nanobubbles, generated around gold nanoparticles, have been successfully used to both identify and kill xenografted cancer cells upon focused laser illumination and without harming surrounding tissue [173]. As a more general comment here, the small and transparent zebrafish larvae are, of course, an ideal proof-of-concept *in vivo* system to validate and optimize photo-responsive systems. However, the micrometer thick tissue of a transparent zebrafish larvae does not resemble clinically relevant tissue and, in taking these technologies forward into the clinic, significant challenges to efficiently deliver light into deep and opaque tissue must be additionally met.

4.4.2. Enzyme and protein delivery

For nanoparticle-mediated enzyme delivery, enzyme activity upon immobilization is a key question to be assessed. An important parameter for enzymatic activity is access to substrates and co-factors. This process can be affected by many factors *in vivo*, including blood flow, shear stress, cell interactions (*e.g.* immune cells) and protein adsorption. Using classical enzymatic activity assays, it is simply not possible to mimic all these complex and intertwined determinants.

Please cite this article as: S. Sieber, P. Grossen, J. Bussmann, et al., Zebrafish as a preclinical *in vivo* screening model for nanomedicines, Adv. Drug Deliv. Rev., https://doi.org/10.1016/j.addr.2019.01.001

Transparent zebrafish larvae are an ideal platform for initial *in vivo* assessment of enzyme delivery systems since many enzymes can process colorimetric or fluorescent substrates (a requirement for image-based analysis). Recently, enzyme loaded nanoparticles and free enzyme were injected into the blood circulation of zebrafish larvae followed by an enzyme activity assay [174]. Both enzyme preparations were shown to be active and neither elicited acute toxicity (*i.e.* seizures, heart failure, signs of denaturation). Interestingly, immobilized enzymes remained associated with particles after injection (distinct localized areas) in contrast to the very diffuse distribution of free enzyme throughout the zebrafish larvae. Qualitative analysis of staining patterns enabled assessment of both the stability and functionality of enzyme loaded particles *in vivo*. In this example, zebrafish larvae had to be euthanized prior to the enzyme activity assay, however this limitation can be overcome by choosing a suitable enzyme reaction, preferably one producing a fluorescent product, as demonstrated by Einfalt et al. [175]. In this study, polymer-based artificial organelles, containing protein gates and a model enzyme, were developed. After demonstrating functionality *in vitro*, zebrafish larvae were then used to demonstrate activity *in vivo*. In this case, fluorescently labeled artificial enzyme-containing organelles were injected into the blood circulation of zebrafish larvae. After successful uptake of artificial organelles by macrophages in the caudal region of the zebrafish larvae, the enzyme substrate was injected. Importantly, the formation of a fluorescent product demonstrated the intracellular functionality of the designed system in a complex *in vivo* environment.

4.4.3. Gene therapy

The past decades have seen significant progress in the development of non-viral vectors for gene therapy [169,176]. Typically, an excess of positively charged or ionizable lipids or polymers is required to efficiently complex polyanionic nucleic acids within discrete nanoparticle formulations. Since cationic nanoparticles are often highly cytotoxicity *in vitro* [177], much effort has been made to optimize formulation design, *e.g.* screening polymer/lipid to nucleic acid ratios, use of ionizable cationic lipids (with optimized pK_a values) and/or including helper lipids, to minimize cytotoxicity and other detrimental features (*e.g.* aggregation in serum) associated with cationic particles. These efforts have recently resulted in the clinical translation of the first non-viral RNAi therapeutic [178]. Many challenges however remain, perhaps most significant being the ability to efficiently target genes to cells beyond the liver. Once again, the ability to quickly screen many and varied gene delivery systems within realistic *in vivo* situations would hugely benefit the field [179]. Encouragingly, zebrafish embryos/larvae have already been used to show successful nanoparticle-mediated gene transfection [171,180,181] and gene silencing [182], highlighting the suitability of this model organism for the design and optimization of gene delivery systems.

4.5. Nanomedicines for cancer therapy

In the past 30+ years, very few nanomedicines have been granted market approval for the targeted treatment of solid tumors, although several are currently in clinical trials [183]. Successful translation of nanomedicines, from the preclinical setting to the clinic, therefore remains a persistent and major hurdle. The development of new *in vivo* platforms to quickly screen, analyse, and optimize large numbers of cancer nanomedicines has the potential to facilitate the selection of lead formulations and to accelerate their preclinical development. However, *in vivo* cancer models must be designed and applied with utmost care to avoid misleading conclusions as to the nanomedicines' efficacy, particularly given cancer is a pathophysiologically heterogeneous disease (*e.g.* varying tumor size, presence and extent of the extracellular matrix, specific cell types, location). In the following sections, existing zebrafish cancer models are described including comparisons to their rodent counterparts and their applications during nanomedicine development are discussed.

4.5.1. Zebrafish cancer models

Zebrafish can be used to study the pathophysiology of various cancers including melanoma, rhabdomyosarcoma and hepatoma [184–186]. Most tumor models generated in zebrafish are histologically comparable to human tumors and possess important hallmarks of cancer, such as genomic instability, invasiveness, transplantability, existence of cancer stem cells and conservation of tumor suppressor genes and oncogenes [185,187–189]. Furthermore, the availability of various genetically modified zebrafish lines such as Casper [30] (transparent at adult stage), *Tg(kdrl:eGFP)* [38] (fluorescent embryonic and early larvae vasculature), *Tg(mpx:eGFP)* [190] (fluorescent neutrophils), *Tg(mpeg1:eGFP)* [41] (fluorescent macrophages) and *Tg(cd41:eGFP)* [191] (fluorescent thrombocytes) facilitates detailed investigation of important cancer features such as angiogenesis, neutrophil-mediated metastasis, and immune responses, at a cellular level and in living organisms [192–194]. For example, Nicoli et al. injected cancer cells, loaded with fluorescent dye, into zebrafish larvae expressing GFP in their vascular endothelial cells, to dynamically assess tumor angiogenesis *in vivo* [195,196]. In another study, Feng *et al.* investigated host inflammatory response, upon cancer cell transplantation, making use of various transgenic fluorescent zebrafish lines [197].

Zebrafish cancer models can be created through embryo exposure to carcinogens, forward genetic screens, reverse genetic knockouts, transgene expression or xenotransplantation of mammalian cancer cells [185]. Carcinogenic chemicals, such as *N*-nitrosodimethylamine [198], 7,12-dimethylbenz(*a*)anthracene [199] or *N*-ethyl-*N*-nitrosourea [200], can be directly dissolved or dispersed into the zebrafish media, making this approach straightforward. Since many oncogenes and tumor suppressor genes are also important for tumor development, new cancer-related genes can be identified through forward genetic screens, including the selection of phenotypes with proliferation defects [201,202]. The creation of reverse genetic knockout enables creation of human-like cancer mutations through specific knockout of a gene known to be linked to cancer development, for example the tumor suppressor, *TP53* [203]. Here it is important to note that these methods are affected by an evolutionary gene duplication event in zebrafish [204], resulting in the presence of redundant genes that can compensate for engineered genetic mutations. Therefore, induction of tumors by transgenic expression of mammalian oncogenes, within single cell zebrafish embryos, is a frequently used approach. This also allows for the combination of human oncogenes and fluorescent markers to be co-expressed in specific tissues [205]. However, transgene expression is time consuming and laborious. As an alternative, zebrafish cancer models can be generated by xenografting human cancer cell lines or patient-derived tumor cells within zebrafish embryos [206,207]. The success and reproducibility of this approach is however strongly affected by different experimental parameters, such as developmental stage, site of injection and experimental temperature, and care must therefore be taken to ensure these parameters are strictly controlled. Most studies involving the generation of zebrafish xenografts report cancer cell injection at 2 dpf, as highlighted in different reviews [192,208–210]. At this time point, gastrulation is complete, the main anatomical organization of the zebrafish body is established, larvae are fully transparent and have not yet developed an adaptive immune system. As a result, injection of human cancer cells into zebrafish embryos does not require immunosuppression. Furthermore, zebrafish, at this developmental stage, feed exclusively from their yolk, minimizing fish-to-fish variations caused by differential diet.

The site of xenograft injection is critical in determining resultant tumor access to blood and/or vascularization. The yolk is commonly preferred as xenograft injection site, given its large size, the ability to carry large tumor burdens and the naturally nutrient rich environment that promotes tumor proliferation. The main limitation of xenograft

injections within the yolk is the subsequent restricted access to blood which limits tumor vascularization (*i.e.* blood vessels do not sprout to xenograft). Alternatively, cancer cells can be injected into the perivitelline space, resulting in spontaneous tumor vascularization *via* the ingrowing subintestinal vessels [196]. This approach is often used to test novel angiogenesis inhibiting compounds [211].

Direct cancer cell injections into blood circulation, *via* the duct of Cuvier [212] or the cardinal vein [213], have also been demonstrated. This approach gives less control over the ultimate site of tumor formation, however most *i.v.* administered cancer cells will tend to accumulate in the caudal part of the zebrafish larvae vasculature, due to the narrowed blood vessels and reduced blood flow velocity of this tissue, which guarantees blood access of the established xenograft.

In general, injecting mammalian cancer cells into zebrafish larvae presumes an accurate control of experimental temperature given mammalian cells require an optimal temperature of 37 °C whereas the optimal temperature for zebrafish husbandry is 28 °C. Fortunately, zebrafish larvae, from 2 dpf onwards, are able to survive and develop at temperatures up to 35 °C [214] for several days, while adult zebrafish can withstand water temperatures up to 38 °C [215]. As mentioned previously, in carrying out zebrafish experiments at elevated temperatures, the potential activation of heat shock protein pathways should also be carefully considered.

4.5.2. Zebrafish and rodents as complementary model organisms in cancer research

As stated previously, most tumor models generated in zebrafish are histologically comparable to human tumors and possess many important hallmarks of cancer. For both mice and zebrafish, genetic cancer models and xenotransplants are available. Each has its own advantages and disadvantages. Genetically induced tumors (*i.e.* gene knockout or knock-in) in zebrafish, for instance, suffer from later onset and lower incidence rates (close to 30%) compared to orthologue mouse models [185]. This can be somewhat compensated by working with larger numbers of zebrafish, given the fecundity and comparably cheap husbandry costs of zebrafish. In addition, most cancer models can be effectively exploited in zebrafish larvae as observed larval phenotypes are strongly predictive of adult phenotypes. Nevertheless, some zebrafish organs are anatomically less complex (*e.g.* kidney, pancreas) than their mammalian counterparts or indeed absent all together (*e.g.* mammary and prostate glands and lungs) [189]. This clearly hampers, or prevents, the generation of representative tumor models within these organs. In addition, tumor classification and characterization of zebrafish cancer models is often difficult given the lack of zebrafish-specific antibodies required for tissue staining, flow cytometry or western blots. Regarding the conservation of oncogenic pathways, for example high conservation of *BRAF* and *NRAS* oncogenes and absence of *BRCA1* and *INK4α/ARF* tumor suppressors, the inability to accurately characterize tumor pathology can be critical [47,216]. Upon cancer cell xenotransplantation, successful tumor formation often requires the addition of supplementary cytokines, such as growth factors. The use of solubilized tissue basement membrane matrices (*e.g.* Matrigel® or Cultrex®), containing transforming growth factor and fibroblast growth factor, has been shown to support tumor growth in both rodents and zebrafish xenograft models [196,217]. Addition of tissue-specific growth factors to the zebrafish media is possible but has yet to be established as standard protocol. Regarding xenograft rejection, the adaptive immune system of zebrafish is not fully functional until 1 month post fertilization, making common immunosuppression protocols used in rodents, redundant in zebrafish embryos [218]. For xenotransplantation in adult zebrafish, immunosuppression through irradiation or dexamethasone treatment is effective [30,219].

In general, xenograft cancer models in zebrafish have several advantageous features over their rodent counterparts. Due to the small size of zebrafish embryos, zebrafish xenografts require a relatively small number of transplanted tumor cells (max. 2000 cells/zebrafish compared to up to 1 million cells/mouse) [192,220]. This is particularly relevant in cases where human primary cells are to be xenografted, given these cells are difficult to obtain in large numbers. As such, the potential use of zebrafish cancer models towards personalized cancer therapy has not gone unnoticed [221]. Indeed, given the relatively short amount of time needed to generate patient-derived xenografts in zebrafish larvae, it is possible to assess the effectiveness of various patient treatment options under more realistic and predictive biological conditions in zebrafish larvae [222].

Assessment of tumor growth and tumor cell migration in zebrafish is generally done before and after treatment. By transplanting fluorescently labeled cancer cells, these two parameters can be determined dynamically in living organisms at cellular resolution and can even be quantified [214,223]. In contrast, imaging of transplanted cancer cells in rodents generally relies on luminescence measurements, which suffer from limited resolution [189]. High resolution live imaging of tumors is possible in rodents by intravital microscopy [224]. However, this procedure requires invasive surgical procedures.

4.5.3. Screening of cancer nanomedicines

Various xenograft cancer models used in rodents can be successfully translated to zebrafish, including models for metastasis [225]. At present, xenografting remains the method of choice for zebrafish-based drug discovery and development of cancer nanomedicines, as emphasized in specific reviews [209,226]. Key advantages of this approach include the ability to transplant hundreds of larvae a day, the ability of zebrafish to support relatively large tumor burdens, the observed rapid onset of cancer, transparent larvae (for live fluorescence imaging) and the use of human cancer cell lines, which are stained or genetically modified to express fluorescent markers [185,209]. In addition, Stoletov et al. were able to observe characteristic fenestrations in the tumor vasculature following transplantation of cancer cells overexpressing vascular endothelial growth factor into zebrafish embryos [219,227]. This may prove a valuable model for the characterization of nanomedicines designed to passively accumulate within solid tumors *via* the EPR effect. However, the generation of such an 'EPR zebrafish model' will require thorough characterization given the developing vasculature of zebrafish larvae is intrinsically leaky, as evidenced by the increased observed extravasation of long circulating nanoparticles into the tissues of healthy larvae [27]. In addition, the size of the xenografted tumor is a potentially critical parameter. On the one hand, tumors in zebrafish larvae are inherently limited in size, raising questions over the conservation of key characteristics of large tumors, such as functional tumor microenvironment or the presence of a hypoxic/necrotic core. On the other hand, as observed in rodent tumor models, the use of adult zebrafish to generate larger tumors could result in the overestimation of nanomedicine performance due to exaggerated tumor growth rates and disproportionally large tumors [228]. Moreover, by using adult zebrafish, the many advantages of zebrafish larvae, such as optical transparency and availability, are lost.

If carefully implemented, zebrafish larvae xenograft models can be a valuable tool to optimize specific aspects of nanomedicine performance under *in vivo* conditions. Gao et al. successfully used zebrafish larvae to generate tumor models using multidrug resistant cancer cells, since comparable models in mice often lose drug resistance over long experimental time periods [229]. Making use of the optical transparency of zebrafish larvae, injected cells can be pre-treated (with membrane dyes or genetically modified) to obtain fluorescent cancer cells or cells expressing specific proteins/receptors. Going one step further, Yang et al. injected transfected cancer cells, expressing a coiled coil forming peptide, into zebrafish larvae [230]. Through subsequent injection of nanoparticles decorated with a complementary coiled coil peptide, selective cancer cell delivery of fluorescent nanoparticle cargos, *via* membrane fusion, was demonstrated.

Several ways of applying nanomedicine formulations to zebrafish xenografts have been demonstrated, including addition to the zebrafish

Please cite this article as: S. Sieber, P. Grossen, J. Bussmann, et al., Zebrafish as a preclinical *in vivo* screening model for nanomedicines, Adv. Drug Deliv. Rev., https://doi.org/10.1016/j.addr.2019.01.001

media [231], direct co-injection of a nanomedicine/cancer cell mixture [232–234] or injection of pre-treated cancer cells [235]. While issues surrounding the addition of nanomedicines to zebrafish media have already been discussed in this review, as potential cancer therapies, neither co-injection nor pre-treatment of cancer cells with nanomedicines accurately reflect any realistic course of treatment. Moreover, these administration routes do not exploit a key advantage of using zebrafish larvae, namely the ability to assess blood circulation behavior, a key parameter of all clinically approved cancer nanomedicines. Ideally, zebrafish larvae xenografts should be established and characterized before nanomedicine injection into blood circulation, as described by Evensen et al. [236]. To the best of our knowledge, this latter study is the most extensive application of zebrafish xenografts with regards to nanoparticle characterization. In a separate study, Zhou et al. exploited an established zebrafish model of cancer metastasis [225,237] to investigate the role of TGF-β during cancer metastasis and demonstrated cytokine function in both zebrafish and human cancer cells. Based on these findings and extensive characterization of this cancer model, Zhou et al. were subsequently able to develop a nanomedicine formulation for the co-delivery of two drugs to cancer cells [235]. This study highlights the importance of using well-established zebrafish cancer models during nanomedicine development.

Various readouts to assess cancer nanomedicine efficacy in zebrafish cancer models are available. Many studies report antiangiogenic properties of nanomedicines [233,234,238] following reported protocols [196]. In addition, evaluation of tumor growth or metastasis have been reported, to various degrees of detail [229,231,232,238]. However, assessing such experimental readouts in a reproducible, robust, and representative way remains a major issue. To address this, Wehmas et al. developed imaging software protocols to reproducibly measure glioblastoma cell migration and invasion in zebrafish larvae following nanomedicine treatment [239]. Other groups have reported polymerase chain reaction (PCR) procedures to assess RNA levels of specific tumor markers, such as vascular endothelial growth factor (VEGF) [240,241], as a quantitative assessment of nanomedicine treatment efficacy.

5. Discussion and conclusion

The potential value of the zebrafish model for nanomedicine development has been demonstrated by many studies. In particular, zebrafish larvae are uniquely placed to bridge the gap between *in vitro* models and rodent *in vivo* studies given their availability in large numbers, their optical transparency, the availability of numerous transgenic fluorescent lines and the relatively low costs of husbandry and experimental set-ups. These features facilitate the rapid and cost-effective assessment of nanomedicines, under *in vivo* conditions and down to the macromolecular level. Nanomedicine assessment in whole living organisms is particularly important as nanomedicine-bio interactions are determined by a combination of biological processes, anatomical features and molecular mechanisms. Up to date, this dynamism and complexity simply cannot be accurately mimicked *in vitro* [242].

Zebrafish models can be used for formulation screening using reported experimental set-ups and conventional imaging technologies. Screening of up to 20 nanomedicine formulations per day, researcher, and microscope is feasible. Nevertheless, to reach high-throughput screening capabilities, fully automated injection, imaging, and analysis protocols will need to be developed. Towards this goal, significant progress has been made to fully automate zebrafish injections [243-247] using organ-targeted microinjection systems [248]. However, these systems remain highly customized and are not widely available. Furthermore, automated injection into zebrafish blood circulation, given the precision required, remains a major unmet challenge. Nevertheless, given the zebrafish model for biomedical applications is rapidly gaining interest, further technical developments to improve screening speed and accuracy are anticipated.

Zebrafish are not yet considered a standard model for nanomedicine research. Further studies are necessary to fully characterize the model, evaluate potential applications, and assess its predictive value for studies in higher animals. Prediction of therapeutic efficacy or exact pharmacokinetics requires precise characterisation of physiological features. As highlighted above, the protein corona has a strong effect on nanoparticle behavior in biological environments [249,250]. Several publications have demonstrated the source of serum proteins (*i.e.* sheep, rat, human, rabbit) differentially influences the extent to which nanoparticles aggregate as well as their targeting efficiencies [249,251]. Nevertheless, the importance of assessing nanoparticle formulations *in vivo*, with respect to the adsorbed protein corona, have been highlighted by Hadjidemetriou et al. Here, striking differences between protein corona compositions formed *in vitro* (plasma incubation) and those formed *in vivo* (rodent injection and recovery) were observed resulting in markedly different profiles of both nanoparticle receptor binding and cellular uptake [252].

Further research is therefore needed to investigate the protein composition of zebrafish plasma, which has not yet been fully characterized [73]. Similarly, there are still several fundamental biological unknowns of the zebrafish that need to be fully characterized, including presence or absence of Kupffer cells and blood-brain barrier integrity. In terms of experimental parameters, both the route of nanomedicine administration and the developmental stage of the zebrafish are critical. Nanoparticles should always be administered to zebrafish larvae *via* the same anticipated route used in higher order animals and ultimately patients. For example, incubation of nanoparticles in zebrafish media does not reveal toxicological information of the same formulation administered into blood circulation. With respect to development stage, it is critical to appreciate that zebrafish development is a very rapid process, especially during early developmental stages (up to larvae). The presence and maturation of different cells and organs during early development can change in the timeframe of hours and must be considered carefully, particularly with respect to timing of nanomedicine administration and imaging over different experimental days.

Despite these open questions and challenges, zebrafish models are highly predictive when it comes to the characterization of pharmacokinetic properties of nanoformulations. For example, disparities between *in vitro* and in vivo results have been demonstrated when determining the optimal ligand density of receptor targeted nanomedicines. *In vitro*, higher ligand densities often result in an increased cellular uptake. However, this often does not translate to rodent *in vivo* studies, where intermediate ligand densities are often optimal so as to balance circulation, targeting, and clearance profiles [253]. Witzigmann et al. used a zebrafish larvae xenograft model to optimize nanoparticle targeting ligand density. As expected, optimal ligand densities *in vitro* did not correlate with in zebrafish larvae studies. However, the latter was precisely predictive of subsequent rodent *in vivo* experiments (Witzigmann et al., manuscript in preparation).

The vast majority of nanomedicine research in zebrafish is performed in zebrafish larvae (see footnote[1]). This is primarily due to their easy availability and favorable imaging properties (dimension and transparency). These advantages diminish at later developmental stages. Zebrafish larvae are therefore ideal tools to assess nano-bio interactions occurring over short timeframes. This includes cell specific binding, clearance by cells of the innate immune system and functionality of advanced nanosystems (*i.e.* enzyme/gene delivery). Zebrafish models might not be well suited to assess long-term effects of nanomedicines (*e.g.* evaluation of chronic toxicity of nanomedicines following repeated administration).

In conclusion, formulation design and optimization of nanomedicines in complex biological environments are key steps prior to first rodent *in vivo* experiments. Due to the inherent complexity and diversity of physicochemical parameters of nanomedicines, selection of appropriate biological model systems during preclinical development of nanomedicines is crucial (Fig. 4). Several factors influence this

Please cite this article as: S. Sieber, P. Grossen, J. Bussmann, et al., Zebrafish as a preclinical *in vivo* screening model for nanomedicines, Adv. Drug Deliv. Rev., https://doi.org/10.1016/j.addr.2019.01.001

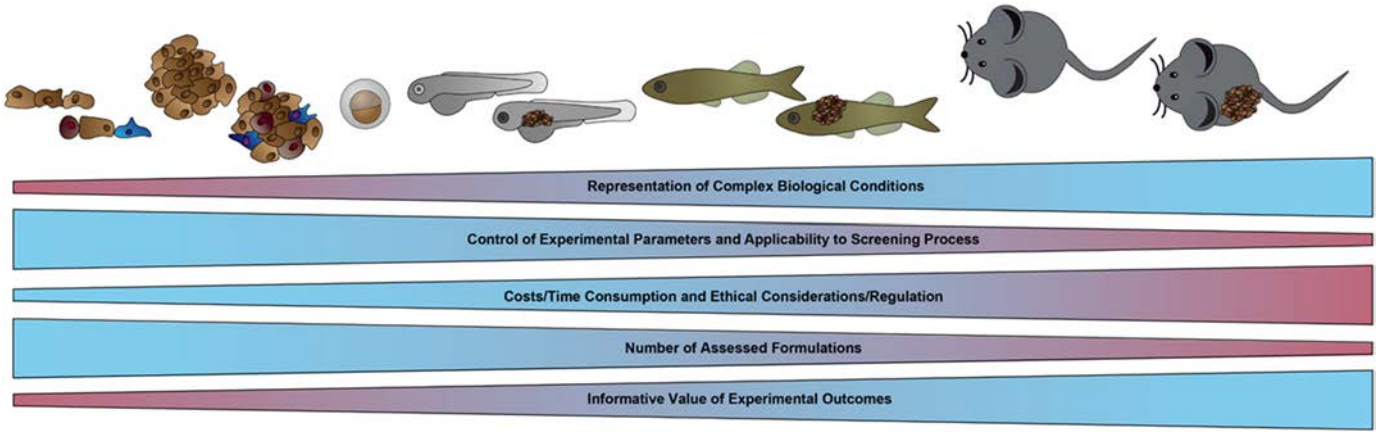

Fig. 4. Comparison of different preclinical models for nanomedicine development. Factors affecting the appropriate selection of a model system during nanomedicine formulation design and optimization are represented. Depending on the experimental complexity and rationale, each model system has its specific advantages and disadvantages. An optimized screening strategy relies on a smart combination of several available model systems and is key to success during clinical translation.

selection, including the extent to which complex biological conditions are mimicked, user control over experimental parameters, ability to screen appropriate numbers of samples, time, and costs. To this end, every available (*e.g.* 2D/3D cell culture) or emerging model system (zebrafish, organ-on-a-chip) has its own advantages and disadvantages. Ultimately, both *in vitro* and *in vivo* model systems (*i.e.* zebrafish) should be used to complement, enrich, and inform the design and optimization of nanomedicines prior to first injections in rodents. An approach, which aligns with reduce, replace and refine (3Rs) legislative guidelines concerning the ethical use of animals in research. With this arsenal of techniques, we may finally see the long awaited advance of many new nanomedicines from bench to bedside.

Acknowledgements

DW and JH have equally contributed to the present publication. The authors are thankful for financial support of the "Stiftung zur Förderung des pharmazeutischen Nachwuchses in Basel", the "Freiwillige Akademische Gesellschaft Basel", the Swiss National Science Foundation (SNF grants No. 174975 and No. 173057) and the EU Horizon 2020 project "NanoReg2" and declare no conflicts of interests. FC and AK are thankful for the financial support by M-Era.net (No. 732.016.101). In addition, AK is supported by the NWO*via* a VICI grant (No. 724.014.001)

References

[1] A. Wicki, D. Witzigmann, V. Balasubramanian, J. Huwyler, Nanomedicine in cancer therapy: challenges, opportunities, and clinical applications, J. Control. Release 200 (2015) 138–157, https://doi.org/10.1016/j.jconrel.2014.12.030.
[2] S. Mitragotri, T. Lammers, Y.H. Bae, S. Schwendeman, S. De Smedt, J.-C. Leroux, D. Peer, I.C. Kwon, H. Harashima, A. Kikuchi, Y.-K. Oh, V. Torchilin, W. Hennink, J. Hanes, K. Park, drug delivery research for the future: expanding the nano horizons and beyond, J. Control. Release 246 (2017) 183–184, https://doi.org/10.1016/j.jconrel.2017.01.011.
[3] Q. Dai, N. Bertleff-Zieschang, J.A. Braunger, M. Björnmalm, C. Cortez-Jugo, F. Caruso, Particle targeting in complex biological media, adv, Healthc. Mater. 7 (2018) https://doi.org/10.1002/adhm.201700575.
[4] Y.S. Zhang, A. Khademhosseini, Seeking the right context for evaluating nanomedicine: from tissue models in petri dishes to microfluidic organs-on-a-chip, Nanomedicine 10 (2015) 685–688, https://doi.org/10.2217/nnm.15.18.
[5] Y.S. Zhang, Y.-N. Zhang, W. Zhang, Cancer-on-a-chip systems at the frontier of nanomedicine, Drug Discov. Today 22 (2017) 1392–1399, https://doi.org/10.1016/j.drudis.2017.03.011.
[6] M. Ravi, V. Paramesh, S.R. Kaviya, E. Anuradha, F.D.P. Solomon, 3D cell culture systems: advantages and applications, J. Cell. Physiol. 230 (2015) 16–26, https://doi.org/10.1002/jcp.24683.
[7] V. van Duinen, S.J. Trietsch, J. Joore, P. Vulto, T. Hankemeier, Microfluidic 3D cell culture: from tools to tissue models, Curr. Opin. Biotechnol. 35 (2015) 118–126, https://doi.org/10.1016/j.copbio.2015.05.002.
[8] E.W. Esch, A. Bahinski, D. Huh, Organs-on-chips at the frontiers of drug discovery, Nat. Rev. Drug Discov. 14 (2015) 248–260, https://doi.org/10.1038/nrd4539.
[9] H.H. Gustafson, D. Holt-Casper, D.W. Grainger, H. Ghandehari, Nanoparticle uptake: the phagocyte problem, Nano Today 10 (2015) 487–510, https://doi.org/10.1016/j.nantod.2015.06.006.
[10] M. Mahmoudi, Debugging Nano-Bio Interfaces: Systematic Strategies to Accelerate Clinical Translation of Nanotechnologies, Trends Biotechnol 36 (2018) 755–769, https://doi.org/10.1016/j.tibtech.2018.02.014.
[11] D. Witzigmann, S. Hak, R. van der Meel, Translating nanomedicines: thinking beyond materials? A young investigator's reply to 'The Novelty Bubble, J. Control. Release 290 (2018) 138–140, https://doi.org/10.1016/j.jconrel.2018.10.011.
[12] L. Gonzalez-Moragas, P. Berto, C. Vilches, R. Quidant, A. Kolovou, R. Santarella-Mellwig, Y. Schwab, S. Stürzenbaum, A. Roig, A. Laromaine, In vivo testing of gold nanoparticles using the Caenorhabditis elegans model organism, Acta Biomater. 53 (2017) 598–609, https://doi.org/10.1016/j.actbio.2017.01.080.
[13] M. Giannaccini, A. Cuschieri, L. Dente, V. Raffa, Non-mammalian vertebrate embryos as models in nanomedicine, Nanomed. Nanotechnol. Biol. Med. 10 (2014) 703–719, https://doi.org/10.1016/j.nano.2013.09.010.
[14] A. Vargas, M. Zeisser-Labouèbe, N. Lange, R. Gurny, F. Delie, The chick embryo and its chorioallantoic membrane (CAM) for the in vivo evaluation of drug delivery systems, Adv. Drug Deliv. Rev. 59 (2007) 1162–1176, https://doi.org/10.1016/j.addr.2007.04.019.
[15] G. Streisinger, C. Walker, N. Dower, D. Knauber, F. Singer, Production of clones of homozygous diploid zebra fish (Brachydanio rerio), Nature 291 (1981) 293–296.
[16] C.B. Kimmel, Genetics and early development of zebrafish, Trends Genet. TIG. 5 (1989) 283–288.
[17] P. Haffter, M. Granato, M. Brand, M.C. Mullins, M. Hammerschmidt, D.A. Kane, J. Odenthal, F.J. van Eeden, Y.J. Jiang, C.P. Heisenberg, R.N. Kelsh, M. Furutani-Seiki, E. Vogelsang, D. Beuchle, U. Schach, C. Fabian, C. Nüsslein-Volhard, The identification of genes with unique and essential functions in the development of the zebrafish, Danio rerio, Dev. Camb. Engl. 123 (1996) 1–36.
[18] C. Nüsslein-Volhard, The identification of genes controlling development in flies and fishes (nobel lecture), Angew. Chem. Int. Ed. Eng. 35 (1996) 2176–2187, https://doi.org/10.1002/anie.199621761.
[19] C. Nüsslein-Volhard, The zebrafish issue of development, Dev. Camb. Engl. 139 (2012) 4099–4103, https://doi.org/10.1242/dev.085217.
[20] W. Driever, L. Solnica-Krezel, A.F. Schier, S.C. Neuhauss, J. Malicki, D.L. Stemple, D.Y. Stainier, F. Zwartkruis, S. Abdelilah, Z. Rangini, J. Belak, C. Boggs, A genetic screen for mutations affecting embryogenesis in zebrafish, Dev. Camb. Engl. 123 (1996) 37–46.
[21] A.J. Rennekamp, R.T. Peterson, 15 years of zebrafish chemical screening, Curr. Opin. Chem. Biol. 24 (2015) 58–70, https://doi.org/10.1016/j.cbpa.2014.10.025.
[22] R.T. Peterson, B.A. Link, J.E. Dowling, S.L. Schreiber, Small molecule developmental screens reveal the logic and timing of vertebrate development, Proc. Natl. Acad. Sci. U. S. A. 97 (2000) 12965–12969.
[23] C.A. MacRae, R.T. Peterson, Zebrafish as tools for drug discovery, Nat. Rev. Drug Discov. 14 (2015) 721–731, https://doi.org/10.1038/nrd4627.
[24] K. Strange, Drug discovery in fish, flies, and worms, ILAR J. 57 (2016) 133–143, https://doi.org/10.1093/ilar/ilw034.
[25] L.I. Zon, R.T. Peterson, In vivo drug discovery in the zebrafish, Nat. Rev. Drug Discov. 4 (2005) 35–44, https://doi.org/10.1038/nrd1606.
[26] S. Ali, D.L. Champagne, H.P. Spaink, M.K. Richardson, Zebrafish embryos and larvae: a new generation of disease models and drug screens, Birth Defects Res. Part C Embryo Today Rev. 93 (2011) 115–133, https://doi.org/10.1002/bdrc.20206.
[27] S. Sieber, P. Grossen, P. Detampel, S. Siegfried, D. Witzigmann, J. Huwyler, Zebrafish as an early stage screening tool to study the systemic circulation of nanoparticulate drug delivery systems in vivo, J. Control. Release 264 (2017) 180–191, https://doi.org/10.1016/j.jconrel.2017.08.023.
[28] F. Campbell, F.L. Bos, S. Sieber, G. Arias-Alpizar, B.E. Koch, J. Huwyler, A. Kros, J. Bussmann, Directing nanoparticle biodistribution through evasion and exploitation of Stab2-dependent nanoparticle uptake, ACS Nano 12 (2018) 2138–2150, https://doi.org/10.1021/acsnano.7b06995.

[29] J. Karlsson, J. von Hofsten, P.-E. Olsson, Generating transparent zebrafish: a refined method to improve detection of gene expression during embryonic development, Mar. Biotechnol. 3 (2001) 522–527, https://doi.org/10.1007/s1012601-0053-4.
[30] R.M. White, A. Sessa, C. Burke, T. Bowman, J. LeBlanc, C. Ceol, C. Bourque, M. Dovey, W. Goessling, C.E. Burns, L.I. Zon, Transparent adult zebrafish as a tool for in vivo transplantation analysis, Cell Stem Cell 2 (2008) 183–189, https://doi.org/10.1016/j.stem.2007.11.002.
[31] E. Wienholds, F. van Eeden, M. Kosters, J. Mudde, R.H.A. Plasterk, E. Cuppen, Efficient target-selected mutagenesis in zebrafish, Genome Res. 13 (2003) 2700–2707, https://doi.org/10.1101/gr.1725103.
[32] A. Nasevicius, S.C. Ekker, Effective targeted gene 'knockdown' in zebrafish, Nat. Genet. 26 (2000) 216–220, https://doi.org/10.1038/79951.
[33] Y. Doyon, J.M. McCammon, J.C. Miller, F. Faraji, C. Ngo, G.E. Katibah, R. Amora, T.D. Hocking, L. Zhang, E.J. Rebar, P.D. Gregory, F.D. Urnov, S.L. Amacher, Heritable targeted gene disruption in zebrafish using designed zinc-finger nucleases, Nat. Biotechnol. 26 (2008) 702–708, https://doi.org/10.1038/nbt1409.
[34] P. Huang, A. Xiao, M. Zhou, Z. Zhu, S. Lin, B. Zhang, Heritable gene targeting in zebrafish using customized TALENs, Nat. Biotechnol. 29 (2011) 699–700, https://doi.org/10.1038/nbt.1939.
[35] U. Irion, J. Krauss, C. Nüsslein-Volhard, Precise and efficient genome editing in zebrafish using the CRISPR/Cas9 system, Dev. Camb. Engl. 141 (2014) 4827–4830, https://doi.org/10.1242/dev.115584.
[36] J. Bussmann, S. Schulte-Merker, Rapid BAC selection for tol2-mediated transgenesis in zebrafish, Dev. Camb. Engl. 138 (2011) 4327–4332, https://doi.org/10.1242/dev.068080.
[37] C. Thisse, B. Thisse, High-resolution *in situ* hybridization to whole-mount zebrafish embryos, Nat. Protoc. 3 (2008) 59–69, https://doi.org/10.1038/nprot.2007.514.
[38] S.-W. Jin, D. Beis, T. Mitchell, J.-N. Chen, D.Y.R. Stainier, Cellular and molecular analyses of vascular tube and lumen formation in zebrafish, Development 132 (2005) 5199–5209, https://doi.org/10.1242/dev.02087.
[39] K.S. Okuda, J.W. Astin, J.P. Misa, M.V. Flores, K.E. Crosier, P.S. Crosier, lyve1 expression reveals novel lymphatic vessels and new mechanisms for lymphatic vessel development in zebrafish, Dev. Camb. Engl. 139 (2012) 2381–2391, https://doi.org/10.1242/dev.077701.
[40] J.R. Mathias, B.J. Perrin, T.-X. Liu, J. Kanki, A.T. Look, A. Huttenlocher, Resolution of inflammation by retrograde chemotaxis of neutrophils in transgenic zebrafish, J. Leukoc. Biol. 80 (2006) 1281–1288, https://doi.org/10.1189/jlb.0506346.
[41] F. Ellett, L. Pase, J.W. Hayman, A. Andrianopoulos, G.J. Lieschke, mpeg1 promoter transgenes direct macrophage-lineage expression in zebrafish, Blood 117 (2011) e49–e56, https://doi.org/10.1182/blood-2010-10-314120.
[42] M. Nguyen-Chi, B. Laplace-Builhe, J. Travnickova, P. Luz-Crawford, G. Tejedor, Q.T. Phan, I. Duroux-Richard, J.-P. Levraud, K. Kissa, G. Lutfalla, C. Jorgensen, F. Djouad, Identification of polarized macrophage subsets in zebrafish, elife 4 (2015) e07288, https://doi.org/10.7554/eLife.07288.
[43] J. Xie, E. Farage, M. Sugimoto, B. Anand-Apte, A novel transgenic zebrafish model for blood-brain and blood-retinal barrier development, BMC Dev. Biol. 10 (2010) 76, https://doi.org/10.1186/1471-213X-10-76.
[44] L.M. van Leeuwen, R.J. Evans, K.K. Jim, T. Verboom, X. Fang, A. Bojarczuk, J. Malicki, S.A. Johnston, A.M. van der Sar, A transgenic zebrafish model for the in vivo study of the blood and choroid plexus brain barriers using claudin 5, Biol. Open. 7 (2018) bio030494, https://doi.org/10.1242/bio.030494.
[45] C. Liu, Y.S. Kim, J. Kim, J. Pattison, A. Kamaid, Y.I. Miller, Modeling hypercholesterolemia and vascular lipid accumulation in LDL receptor mutant zebrafish, J. Lipid Res. 59 (2018) 391–399, https://doi.org/10.1194/jlr.D081521.
[46] C. Liu, K.P. Gates, L. Fang, M.J. Amar, D.A. Schneider, H. Geng, W. Huang, J. Kim, J. Pattison, J. Zhang, J.L. Witztum, A.T. Remaley, P.D. Dong, Y.I. Miller, Apoc2 loss-of-function zebrafish mutant as a genetic model of hyperlipidemia, Dis. Model. Mech. 8 (2015) 989–998, https://doi.org/10.1242/dmm.019836.
[47] K. Howe, M.D. Clark, C.F. Torroja, J. Torrance, C. Berthelot, M. Muffato, J.E. Collins, S. Humphray, K. McLaren, L. Matthews, S. McLaren, I. Sealy, M. Caccamo, C. Churcher, C. Scott, J.C. Barrett, R. Koch, G.-J. Rauch, S. White, W. Chow, B. Kilian, L.T. Quintais, J.A. Guerra-Assunção, Y. Zhou, Y. Gu, J. Yen, J.-H. Vogel, T. Eyre, S. Redmond, R. Banerjee, J. Chi, B. Fu, E. Langley, S.F. Maguire, G.K. Laird, D. Lloyd, E. Kenyon, S. Donaldson, H. Sehra, J. Almeida-King, J. Loveland, S. Trevanion, M. Jones, M. Quail, D. Willey, A. Hunt, J. Burton, S. Sims, K. McLay, B. Plumb, J. Davis, C. Clee, K. Oliver, R. Clark, C. Riddle, D. Elliot, D. Eliott, G. Threadgold, G. Harden, D. Ware, S. Begum, B. Mortimore, B. Mortimer, G. Kerry, P. Heath, B. Phillimore, A. Tracey, N. Corby, M. Dunn, C. Johnson, J. Wood, S. Clark, S. Pelan, G. Griffiths, M. Smith, R. Glithero, P. Howden, N. Barker, C. Lloyd, C. Stevens, J. Harley, K. Holt, G. Panagiotidis, J. Lovell, H. Beasley, C. Henderson, D. Gordon, K. Auger, D. Wright, J. Collins, C. Raisen, L. Dyer, K. Leung, L. Robertson, K. Ambridge, D. Leongamornlert, S. McGuire, R. Gilderthorp, C. Griffiths, D. Manthravadi, S. Nichol, G. Barker, S. Whitehead, M. Kay, J. Brown, C. Murnane, E. Gray, M. Humphries, N. Sycamore, D. Barker, D. Saunders, J. Wallis, A. Babbage, S. Hammond, M. Mashreghi-Mohammadi, L. Barr, S. Martin, P. Wray, A. Ellington, N. Matthews, M. Ellwood, R. Woodmansey, G. Clark, J.D. Cooper, J. Cooper, A. Tromans, D. Grafham, C. Skuce, R. Pandian, R. Andrews, E. Harrison, A. Kimberley, J. Garnett, N. Fosker, R. Hall, P. Garner, D. Kelly, C. Bird, S. Palmer, I. Gehring, A. Berger, C.M. Dooley, Z. Ersan-Ürün, C. Eser, H. Geiger, M. Geisler, L. Karotki, A. Kirn, J. Konantz, M. Konantz, M. Oberländer, S. Rudolph-Geiger, M. Teucke, C. Lanz, G. Raddatz, K. Osoegawa, B. Zhu, A. Rapp, S. Widaa, C. Langford, F. Yang, S.C. Schuster, N.P. Carter, J. Harrow, Z. Ning, J. Herrero, S.M.J. Searle, A. Enright, R. Geisler, R.H.A. Plasterk, C. Lee, M. Westerfield, P.J. de Jong, L.I. Zon, J.H. Postlethwait, C. Nüsslein-Volhard, T.J.P. Hubbard, H. Roest Crollius, J. Rogers, D.L. Stemple, The zebrafish reference genome sequence and its relationship to the human genome, Nature 496 (2013) 498–503, https://doi.org/10.1038/nature12111.
[48] H.K. Long, D. Sims, A. Heger, N.P. Blackledge, C. Kutter, M.L. Wright, F. Grützner, D.T. Odom, R. Patient, C.P. Ponting, R.J. Klose, Epigenetic conservation at gene regulatory elements revealed by non-methylated DNA profiling in seven vertebrates, elife 2 (2013) e00348, https://doi.org/10.7554/eLife.00348.
[49] A.L. Menke, J.M. Spitsbergen, A.P.M. Wolterbeek, R.A. Woutersen, Normal anatomy and histology of the adult zebrafish, Toxicol. Pathol. 39 (2011) 759–775, https://doi.org/10.1177/0192623311409597.
[50] J.P. Briggs, The zebrafish: a new model organism for integrative physiology, Am. J. Physiol.-Regul. Integr. Comp. Physiol. 282 (2002) R3–R9, https://doi.org/10.1152/ajpregu.00589.2001.
[51] P. Goldsmith, Zebrafish as a pharmacological tool: the how, why and when, Curr. Opin. Pharmacol. 4 (2004) 504–512, https://doi.org/10.1016/j.coph.2004.04.005.
[52] R.j. Roberts, A.e. Ellis, The anatomy and physiology of teleosts, in: R.J.R.B. FRSE (Glasgow), FRCVS, FRCPath, FSB (Ed.), Fish Pathol., Wiley-Blackwell (2012) 17–61, https://doi.org/10.1002/9781118222942.ch2.
[53] S. Isogai, M. Horiguchi, B.M. Weinstein, The vascular anatomy of the developing zebrafish: an atlas of embryonic and early larval development, Dev. Biol. 230 (2001) 278–301, https://doi.org/10.1006/dbio.2000.9995.
[54] L. Herwig, Y. Blum, A. Krudewig, E. Ellertsdottir, A. Lenard, H.-G. Belting, M. Affolter, Distinct cellular mechanisms of blood vessel fusion in the zebrafish embryo, Curr. Biol. 21 (2011) 1942–1948, https://doi.org/10.1016/j.cub.2011.10.016.
[55] E. Ellertsdóttir, A. Lenard, Y. Blum, A. Krudewig, L. Herwig, M. Affolter, H.-G. Belting, Vascular morphogenesis in the zebrafish embryo, Dev. Biol. 341 (2010) 56–65, https://doi.org/10.1016/j.ydbio.2009.10.035.
[56] A.T. Chen, L.I. Zon, Zebrafish blood stem cells, J. Cell. Biochem. 108 (2009) 35–42, https://doi.org/10.1002/jcb.22251.
[57] C. Thisse, L.I. Zon, Organogenesis–heart and blood formation from the zebrafish point of view, Science 295 (2002) 457–462, https://doi.org/10.1126/science.1063654.
[58] N.S. Trede, D.M. Langenau, D. Traver, A.T. Look, L.I. Zon, The use of zebrafish to understand immunity, Immunity 20 (2004) 367–379, https://doi.org/10.1016/S1074-7613(04)00084-6.
[59] C.j. Secombes, A.E. Ellis, The immunology of teleosts, in: R.J.R.B. FRSE (Glasgow), FRCVS, FRCPath, FSB (Ed.), Fish Pathol., Wiley-Blackwell (2012) 144–166, https://doi.org/10.1002/9781118222942.ch4.
[60] H.M. Jung, D. Castranova, M.R. Swift, V.N. Pham, M. Venero Galanternik, S. Isogai, M.G. Butler, T.S. Mulligan, B.M. Weinstein, Development of the larval lymphatic system in zebrafish, Dev. Camb. Engl. 144 (2017) 2070–2081, https://doi.org/10.1242/dev.145755.
[61] R.A. Umans, M.R. Taylor, Zebrafish as a model to study drug transporters at the blood-brain barrier, Clin. Pharmacol. Ther. 92 (2012) 567–570, https://doi.org/10.1038/clpt.2012.168.
[62] S.S. Kim, S.H. Im, J.Y. Yang, Y.-R. Lee, G.R. Kim, J.S. Chae, D.-S. Shin, J.S. Song, S. Ahn, B.H. Lee, J.C. Woo, J.H. Ahn, C.S. Yun, P. Kim, H.R. Kim, K.-R. Lee, M.A. Bae, Zebrafish as a Screening Model for Testing the Permeability of Blood–Brain Barrier to Small Molecules, Zebrafish 14 (2017) 322–330, https://doi.org/10.1089/zeb.2016.1392.
[63] Y. Li, T. Chen, X. Miao, X. Yi, X. Wang, H. Zhao, S.M.-Y. Lee, Y. Zheng, Zebrafish: a promising in vivo model for assessing the delivery of natural products, fluorescence dyes and drugs across the blood-brain barrier, Pharmacol. Res. 125 (2017) 246–257, https://doi.org/10.1016/j.phrs.2017.08.017.
[64] J. Chu, K.C. Sadler, New school in liver development: lessons from zebrafish, Hepatol. Baltim. Md. 50 (2009) 1656–1663, https://doi.org/10.1002/hep.23157.
[65] H.A. Field, P.D.S. Dong, D. Beis, D.Y.R. Stainier, Formation of the digestive system in zebrafish. II. Pancreas morphogenesis, Dev. Biol. 261 (2003) 197–208.
[66] G.J. Lieschke, P.D. Currie, Animal models of human disease: zebrafish swim into view, Nat. Rev. Genet. 8 (2007) 353–367, https://doi.org/10.1038/nrg2091.
[67] C. Nusslein-Volhard, R. Dahm, Zebrafish, OUP, Oxford, 2002.
[68] G. Kari, U. Rodeck, A.P. Dicker, Zebrafish: an emerging model system for human disease and drug discovery, Clin. Pharmacol. Ther. 82 (2007) 70–80, https://doi.org/10.1038/sj.clpt.6100223.
[69] P. Herbomel, B. Thisse, C. Thisse, Ontogeny and behaviour of early macrophages in the zebrafish embryo, Development 126 (1999) 3735–3745.
[70] V. Wittamer, J.Y. Bertrand, P.W. Gutschow, D. Traver, Characterization of the mononuclear phagocyte system in zebrafish, Blood 117 (2011) 7126–7135, https://doi.org/10.1182/blood-2010-11-321448.
[71] A. Mantovani, S. Sozzani, M. Locati, P. Allavena, A. Sica, Macrophage polarization: tumor-associated macrophages as a paradigm for polarized M2 mononuclear phagocytes, Trends Immunol. 23 (2002) 549–555, https://doi.org/10.1016/S1471-4906(02)02302-5.
[72] A.E. Nel, L. Mädler, D. Velegol, T. Xia, E.M.V. Hoek, P. Somasundaran, F. Klaessig, V. Castranova, M. Thompson, Understanding biophysicochemical interactions at the nano-bio interface, Nat. Mater. 8 (2009) 543–557, https://doi.org/10.1038/nmat2442.
[73] C. Li, X.F. Tan, T.K. Lim, Q. Lin, Z. Gong, Comprehensive and quantitative proteomic analyses of zebrafish plasma reveals conserved protein profiles between genders and between zebrafish and human, Sci. Rep. 6 (2016) 24329, https://doi.org/10.1038/srep24329.
[74] D.E. Owens, N.A. Peppas, Opsonization, biodistribution, and pharmacokinetics of polymeric nanoparticles, Int. J. Pharm. 307 (2006) 93–102, https://doi.org/10.1016/j.ijpharm.2005.10.010.
[75] S. Zhang, P. Cui, Complement system in zebrafish, Dev. Comp. Immunol. 46 (2014) 3–10, https://doi.org/10.1016/j.dci.2014.01.010.
[76] M. Lundqvist, J. Stigler, G. Elia, I. Lynch, T. Cedervall, K.A. Dawson, Nanoparticle size and surface properties determine the protein corona with possible implications for biological impacts, Proc. Natl. Acad. Sci. 105 (2008) 14265–14270, https://doi.org/10.1073/pnas.0805135105.

[77] P. Aggarwal, J.B. Hall, C.B. McLeland, M.A. Dobrovolskaia, S.E. McNeil, Nanoparticle interaction with plasma proteins as it relates to particle biodistribution, biocompatibility and therapeutic efficacy, Adv. Drug Deliv. Rev. 61 (2009) 428–437, https://doi.org/10.1016/j.addr.2009.03.009.
[78] N. Danilova, J. Bussmann, K. Jekosch, L.A. Steiner, The immunoglobulin heavy-chain locus in zebrafish: identification and expression of a previously unknown isotype, immunoglobulin Z, Nat. Immunol. 6 (2005) 295–302, https://doi.org/10.1038/ni1166.
[79] I. Lynch, K.A. Dawson, Protein-nanoparticle interactions, Nano Today 3 (2008) 40–47, https://doi.org/10.1016/S1748-0132(08)70014-8.
[80] S. Ritz, S. Schöttler, N. Kotman, G. Baier, A. Musyanovych, J. Kuharev, K. Landfester, H. Schild, O. Jahn, S. Tenzer, V. Mailänder, Protein corona of nanoparticles: distinct proteins regulate the cellular uptake, Biomacromolecules 16 (2015) 1311–1321, https://doi.org/10.1021/acs.biomac.5b00108.
[81] A.L. Barrán-Berdón, D. Pozzi, G. Caracciolo, A.L. Capriotti, G. Caruso, C. Cavaliere, A. Riccioli, S. Palchetti, A. Laganà, Time evolution of nanoparticle–protein corona in human plasma: relevance for targeted drug delivery, Langmuir 29 (2013) 6485–6494, https://doi.org/10.1021/la401192x.
[82] J.P. Otis, E.M. Zeituni, J.H. Thierer, J.L. Anderson, A.C. Brown, E.D. Boehm, D.M. Cerchione, A.M. Ceasrine, I. Avraham-Davidi, H. Tempelhof, K. Yaniv, S.A. Farber, Zebrafish as a model for apolipoprotein biology: comprehensive expression analysis and a role for ApoA-IV in regulating food intake, Dis. Model. Mech. 8 (2015) 295–309, https://doi.org/10.1242/dmm.018754.
[83] P.P. Karmali, D. Simberg, Interactions of nanoparticles with plasma proteins: implication on clearance and toxicity of drug delivery systems, Expert Opin. Drug Deliv. 8 (2011) 343–357, https://doi.org/10.1517/17425247.2011.554818.
[84] E.S. Noël, M. dos Reis, Z. Arain, E.A. Ober, Analysis of the Albumin/α-Fetoprotein/Afamin/Group specific component gene family in the context of zebrafish liver differentiation, Gene Expr. Patterns 10 (2010) 237–243, https://doi.org/10.1016/j.gep.2010.05.002.
[85] K. Dooley, L.I. Zon, Zebrafish: a model system for the study of human disease, Curr. Opin. Genet. Dev. 10 (2000) 252–256.
[86] S.A. Brittijn, S.J. Duivesteijn, M. Belmamoune, L.F.M. Bertens, W. Bitter, J.D. de Bruijn, D.L. Champagne, E. Cuppen, G. Flik, C.M. Vandenbroucke-Grauls, R.A.J. Janssen, I.M.L. de Jong, E.R. de Kloet, A. Kros, A.H. Meijer, J.R. Metz, A.M. van der Sar, M.J.M. Schaaf, S. Schulte-Merker, H.P. Spaink, P.P. Tak, F.J. Verbeek, M.J. Vervoordeldonk, F.J. Vonk, F. Witte, H. Yuan, M.K. Richardson, Zebrafish development and regeneration: new tools for biomedical research, Int. J. Dev. Biol. 53 (2009) 835–850, https://doi.org/10.1387/ijdb.082615sb.
[87] J.R. Goldsmith, C. Jobin, Think small: zebrafish as a model system of human pathology, J Biomed Biotechnol 2012 (2012) 817341, https://doi.org/10.1155/2012/817341.
[88] C.-H. Hsu, Z.-H. Wen, C.-S. Lin, C. Chakraborty, The zebrafish model: use in studying cellular mechanisms for a spectrum of clinical disease entities, Curr. Neurovasc. Res. 4 (2007) 111–120.
[89] T.J.A. Chico, P.W. Ingham, D.C. Crossman, Modeling cardiovascular disease in the zebrafish, Trends Cardiovasc. Med. 18 (2008) 150–155, https://doi.org/10.1016/j.tcm.2008.04.002.
[90] J. Bakkers, Zebrafish as a model to study cardiac development and human cardiac disease, Cardiovasc. Res. 91 (2011) 279–288, https://doi.org/10.1093/cvr/cvr098.
[91] J. Berman, K. Hsu, A.T. Look, Zebrafish as a model organism for blood diseases, Br. J. Haematol. 123 (2003) 568–576.
[92] A. Seth, D.L. Stemple, I. Barroso, The emerging use of zebrafish to model metabolic disease, Dis. Model. Mech. 6 (2013) 1080–1088, https://doi.org/10.1242/dmm.011346.
[93] W. Goessling, K.C. Sadler, Zebrafish: an important tool for liver disease research, Gastroenterology 149 (2015) 1361–1377, https://doi.org/10.1053/j.gastro.2015.08.034.
[94] S.J. Poureetezadi, R.A. Wingert, Little fish, big catch: zebrafish as a model for kidney disease, Kidney Int. 89 (2016) 1204–1210, https://doi.org/10.1016/j.kint.2016.01.031.
[95] I.A. Drummond, Kidney development and disease in the zebrafish, J. Am. Soc. Nephrol. 16 (2005) 299–304, https://doi.org/10.1681/ASN.2004090754.
[96] V. Torraca, S. Masud, H.P. Spaink, A.H. Meijer, Macrophage-pathogen interactions in infectious diseases: new therapeutic insights from the zebrafish host model, Dis. Model. Mech. 7 (2014) 785–797, https://doi.org/10.1242/dmm.015594.
[97] A.M. van der Sar, B.J. Appelmelk, C.M.J.E. Vandenbroucke-Grauls, W. Bitter, A star with stripes: zebrafish as an infection model, Trends Microbiol. 12 (2004) 451–457, https://doi.org/10.1016/j.tim.2004.08.001.
[98] N.D. Meeker, N.S. Trede, Immunology and zebrafish: spawning new models of human disease, Dev. Comp. Immunol. 32 (2008) 745–757, https://doi.org/10.1016/j.dci.2007.11.011.
[99] X. Xu, L. Zhang, S. Weng, Z. Huang, J. Lu, D. Lan, X. Zhong, X. Yu, A. Xu, J. He, A zebrafish (Danio rerio) model of infectious spleen and kidney necrosis virus (ISKNV) infection, Virology 376 (2008) 1–12, https://doi.org/10.1016/j.virol.2007.12.026.
[100] O. Faklaris, V. Joshi, T. Irinopoulou, P. Tauc, M. Sennour, H. Girard, C. Gesset, J.-C. Arnault, A. Thorel, J.-P. Boudou, P.A. Curmi, F. Treussart, Photoluminescent diamond nanoparticles for cell labeling: study of the uptake mechanism in mammalian cells, ACS Nano 3 (2009) 3955–3962, https://doi.org/10.1021/nn901014j.
[101] D. Hofmann, S. Tenzer, M.B. Bannwarth, C. Messerschmidt, S.-F. Glaser, H. Schild, K. Landfester, V. Mailänder, Mass spectrometry and imaging analysis of nanoparticle-containing vesicles provide a mechanistic insight into cellular trafficking, ACS Nano 8 (2014) 10077–10088, https://doi.org/10.1021/nn502754c.
[102] C.B. Kimmel, W.W. Ballard, S.R. Kimmel, B. Ullmann, T.F. Schilling, Stages of embryonic development of the zebrafish, Dev. Dyn. 203 (1995) 253–310, https://doi.org/10.1002/aja.1002030302.
[103] W.A. Sassen, R.W. Köster, A molecular toolbox for genetic manipulation of zebrafish, Adv. Genomics Genet. (2015)https://doi.org/10.2147/AGG.S57585.
[104] C. Collymore, S. Rasmussen, R.J. Tolwani, Gavaging adult zebrafish, J. Vis. Exp. JoVE. (2013)https://doi.org/10.3791/50691.
[105] S.D. Løvmo, M.T. Speth, U. Repnik, E.O. Koppang, G.W. Griffiths, J.P. Hildahl, Translocation of nanoparticles and Mycobacterium marinum across the intestinal epithelium in zebrafish and the role of the mucosal immune system, Dev. Comp. Immunol. (n.d.). doi:https://doi.org/10.1016/j.dci.2016.06.016.
[106] J.L. Cocchiaro, J.F. Rawls, Microgavage of zebrafish larvae, J. Vis. Exp. JoVE. (2013) https://doi.org/10.3791/4434.
[107] B.M. Weinstein, D.L. Stemple, W. Driever, M.C. Fishman, Gridlock, a localized heritable vascular patterning defect in the zebrafish, Nat. Med. 1 (1995) 1143–1147.
[108] J.H. Gutzman, H. Sive, Zebrafish brain ventricle injection, J. Vis. Exp. JoVE. (2009) https://doi.org/10.3791/1218.
[109] E.K. Pugach, P. Li, R. White, L. Zon, Retro-orbital injection in adult zebrafish, J. Vis. Exp. JoVE. (2009)https://doi.org/10.3791/1645.
[110] M.D. Kinkel, S.C. Eames, L.H. Philipson, V.E. Prince, Intraperitoneal injection into adult zebrafish, J. Vis. Exp. JoVE. (2010)https://doi.org/10.3791/2126.
[111] J.N. Rosen, M.F. Sweeney, J.D. Mably, Microinjection of zebrafish embryos to analyze gene function, J. Vis. Exp. JoVE. (2009)https://doi.org/10.3791/1115.
[112] M.P. Craig, S.D. Gilday, D. Dabiri, J.R. Hove, An optimized method for delivering flow tracer particles to intravital fluid environments in the developing zebrafish, Zebrafish (9) (2012) 108–119, https://doi.org/10.1089/zeb.2012.0740.
[113] Q. Zhang, M. Kopp, I. Babiak, J.M.O. Fernandes, Low incubation temperature during early development negatively affects survival and related innate immune processes in zebrafish larvae exposed to lipopolysaccharide, Sci. Rep. 8 (2018) 4142, https://doi.org/10.1038/s41598-018-22288-8.
[114] S. Rey, F.A. Huntingford, S. Boltaña, R. Vargas, T.G. Knowles, S. Mackenzie, Fish can show emotional fever: stress-induced hyperthermia in zebrafish, Proc. R. Soc. B 282 (2015) 20152266, https://doi.org/10.1098/rspb.2015.2266.
[115] S. Rey, V. Moiche, S. Boltaña, M. Teles, S. MacKenzie, Behavioural fever in zebrafish larvae, Dev. Comp. Immunol. 67 (2017) 287–292, https://doi.org/10.1016/j.dci.2016.09.008.
[116] S. Boltaña, S. Rey, N. Roher, R. Vargas, M. Huerta, F.A. Huntingford, F.W. Goetz, J. Moore, P. Garcia-Valtanen, A. Estepa, S. MacKenzie, Behavioural fever is a synergic signal amplifying the innate immune response, Proc. R. Soc. B 280 (2013) 20131381, https://doi.org/10.1098/rspb.2013.1381.
[117] J.M. Keller, J.F. Escara-Wilke, E.T. Keller, Heat stress-induced heat shock protein 70 expression is dependent on ERK activation in zebrafish (Danio rerio) cells, Comp. Biochem. Physiol. A. Mol. Integr. Physiol. 150 (2008) 307–314, https://doi.org/10.1016/j.cbpa.2008.03.021.
[118] C.M. Rabergh, S. Airaksinen, A. Soitamo, H.V. Bjorklund, T. Johansson, M. Nikinmaa, L. Sistonen, Tissue-specific expression of zebrafish (Danio rerio) heat shock factor 1 mRNAs in response to heat stress, J. Exp. Biol. 203 (2000) 1817–1824.
[119] N.E. Sharpless, R.A. DePinho, Model organisms: the mighty mouse: genetically engineered mouse models in cancer drug development, Nat. Rev. Drug Discov. 5 (2006) 741–754, https://doi.org/10.1038/nrd2110.
[120] D. Siolas, G.J. Hannon, Patient-derived tumor xenografts: transforming clinical samples into mouse models, Cancer Res. 73 (2013) 5315–5319, https://doi.org/10.1158/0008-5472.CAN-13-1069.
[121] S.E. Gould, M.R. Junttila, F.J. de Sauvage, Translational value of mouse models in oncology drug development, Nat. Med. 21 (2015) 431–439, https://doi.org/10.1038/nm.3853.
[122] D. Behrens, J. Rolff, J. Hoffmann, Predictive in vivo models for oncology, Handb. Exp. Pharmacol. 232 (2016) 203–221, https://doi.org/10.1007/164_2015_29.
[123] C. Chakraborty, A.R. Sharma, G. Sharma, S.-S. Lee, Zebrafish: a complete animal model to enumerate the nanoparticle toxicity, J. Nanobiotechnology. 14 (2016) 65, https://doi.org/10.1186/s12951-016-0217-6.
[124] E. Haque, A.C. Ward, Zebrafish as a model to evaluate nanoparticle toxicity, Nanomaterials. 8 (2018)https://doi.org/10.3390/nano8070561.
[125] C.S. Martinez, D.E. Igartúa, M.N. Calienni, D.A. Feas, M. Siri, J. Montanari, N.S. Chiaramoni, S. del V. Alonso, M.J. Prieto, Relation between biophysical properties of nanostructures and their toxicity on zebrafish, Biophys. Rev. 9 (2017) 775–791, https://doi.org/10.1007/s12551-017-0294-2.
[126] K. Henn, T. Braunbeck, Dechorionation as a tool to improve the fish embryo toxicity test (FET) with the zebrafish (Danio rerio), Comp. Biochem. Physiol. Part C Toxicol. Pharmacol. 153 (2011) 91–98, https://doi.org/10.1016/j.cbpc.2010.09.003.
[127] I. Paatero, E. Casals, R. Niemi, E. Özliseli, J.M. Rosenholm, C. Sahlgren, Analyses in zebrafish embryos reveal that nanotoxicity profiles are dependent on surface-functionalization controlled penetrance of biological membranes, Sci. Rep. 7 (2017) 8423, https://doi.org/10.1038/s41598-017-09312-z.
[128] Y. Pan, A. Leifert, M. Graf, F. Schiefer, S. Thoröe-Boveleth, J. Broda, M.C. Halloran, H. Hollert, D. Laaf, U. Simon, W. Jahnen-Dechent, High-sensitivity real-time analysis of nanoparticle toxicity in green fluorescent protein-expressing zebrafish, Small Weinh. Bergstr. Ger. 9 (2013) 863–869, https://doi.org/10.1002/smll.201201173.
[129] C.B. Vibe, F. Fenaroli, D. Pires, S.R. Wilson, V. Bogoeva, R. Kalluru, M. Speth, E. Anes, G. Griffiths, J. Hildahl, Thioridazine in PLGA nanoparticles reduces toxicity and improves rifampicin therapy against mycobacterial infection in zebrafish, Nanotoxicology 10 (2016) 680–688, https://doi.org/10.3109/17435390.2015.1107146.
[130] E3 medium (for zebrafish embryos), Cold Spring Harb Protoc (2011)https://doi.org/10.1101/pdb.rec066449 (2011) pdb.rec66449.
[131] K. Kiene, S.H. Schenk, F. Porta, A. Ernst, D. Witzigmann, P. Grossen, J. Huwyler, PDMS-b-PMOXA polymersomes for hepatocyte targeting and assessment of toxicity, Eur. J. Pharm. Biopharm. Off. J. Arbeitsgemeinschaft Pharm. Verfahrenstechnik EV. 119 (2017) 322–332, https://doi.org/10.1016/j.ejpb.2017.07.002.

Please cite this article as: S. Sieber, P. Grossen, J. Bussmann, et al., Zebrafish as a preclinical *in vivo* screening model for nanomedicines, Adv. Drug Deliv. Rev., https://doi.org/10.1016/j.addr.2019.01.001

[132] K. Peng, C. Cui, I. Tomatsu, F. Porta, A.H. Meijer, H.P. Spaink, A. Kros, Cyclodextrin/dextran based drug carriers for a controlled release of hydrophobic drugs in zebrafish embryos, Soft Matter 6 (2010) 3778–3783, https://doi.org/10.1039/C0SM00096E.
[133] T.C. King Heiden, E. Dengler, W.J. Kao, W. Heideman, R.E. Peterson, Developmental toxicity of low generation PAMAM dendrimers in zebrafish, Toxicol. Appl. Pharmacol. 225 (2007) 70–79, https://doi.org/10.1016/j.taap.2007.07.009.
[134] O. Bar-Ilan, R.M. Albrecht, V.E. Fako, D.Y. Furgeson, Toxicity assessments of multisized gold and silver nanoparticles in zebrafish embryos, Small 5 (2009) 1897–1910, https://doi.org/10.1002/smll.200801716.
[135] R.C. MacPhail, D.L. Hunter, T.D. Irons, S. Padilla, Locomotion and behavioral toxicity in larval zebrafish: background, methods, and data, in: P. McGrath (Ed.), Zebrafish, John Wiley & Sons, Inc. 2011, pp. 151–164, https://doi.org/10.1002/9781118102138.ch12.
[136] G.H. Jang, M.P. Hwang, S.Y. Kim, H.S. Jang, K.H. Lee, A systematic in-vivo toxicity evaluation of nanophosphor particles via zebrafish models, Biomaterials 35 (2014) 440–449, https://doi.org/10.1016/j.biomaterials.2013.09.054.
[137] C. Parng, N. Anderson, C. Ton, P. McGrath, Zebrafish apoptosis assays for drug discovery, Methods Cell Biol, Academic Press 2004, pp. 75–85, https://doi.org/10.1016/S0091-679X(04)76005-7.
[138] R.J. Griffitt, R. Weil, K.A. Hyndman, N.D. Denslow, K. Powers, D. Taylor, D.S. Barber, Exposure to copper nanoparticles causes gill injury and acute lethality in zebrafish (danio rerio), Environ. Sci. Technol. 41 (2007) 8178–8186, https://doi.org/10.1021/es071235e.
[139] P.V. Asharani, Y. Lian Wu, Z. Gong, S. Valiyaveettil, Toxicity of silver nanoparticles in zebrafish models, Nanotechnology 19 (2008) 255102, https://doi.org/10.1088/0957-4484/19/25/255102.
[140] W. Miao, B. Zhu, X. Xiao, Y. Li, N.B. Dirbaba, B. Zhou, H. Wu, Effects of titanium dioxide nanoparticles on lead bioconcentration and toxicity on thyroid endocrine system and neuronal development in zebrafish larvae, Aquat. Toxicol. Amst. Neth. 161 (2015) 117–126, https://doi.org/10.1016/j.aquatox.2015.02.002.
[141] G.K. Nasrallah, Y. Zhang, M.M. Zagho, H.M. Ismail, A.A. Al khalaf, R.M. Prieto, K.E. Albinali, A.A. Elzatahry, Y. Deng, A systematic investigation of the bio-toxicity of core-shell magnetic mesoporous silica microspheres using zebrafish model, Microporous Mesoporous Mater. (2019)https://doi.org/10.1016/j.micromeso.2018.02.008.
[142] S.C. Gupta, A. Sharma, M. Mishra, R.K. Mishra, D.K. Chowdhuri, Heat shock proteins in toxicology: How close and how far? Life Sci. 86 (2010) 377–384, https://doi.org/10.1016/j.lfs.2009.12.015.
[143] A.T. Lucas, L.B. Herity, Z.A. Kornblum, A.J. Madden, A. Gabizon, A.V. Kabanov, R.T. Ajamie, D.M. Bender, P. Kulanthaivel, M.V. Sanchez-Felix, H.A. Havel, W.C. Zamboni, Pharmacokinetic and screening studies of the interaction between mononuclear phagocyte system and nanoparticle formulations and colloid forming drugs, Int. J. Pharm. 526 (2017) 443–454, https://doi.org/10.1016/j.ijpharm.2017.04.079.
[144] N. Bertrand, P. Grenier, M. Mahmoudi, E.M. Lima, E.A. Appel, F. Dormont, J.-M. Lim, R. Karnik, R. Langer, O.C. Farokhzad, Mechanistic understanding of in vivo protein corona formation on polymeric nanoparticles and impact on pharmacokinetics, Nat. Commun. 8 (2017) 777, https://doi.org/10.1038/s41467-017-00600-w.
[145] L. Aschoff, Das reticulo-endotheliale System, Ergeb. Inn. Med. Kinderheilkd, Springer, Berlin, Heidelberg 1924, pp. 1–118, https://doi.org/10.1007/978-3-642-90639-8_1.
[146] A. Lasser, The mononuclear phagocytic system: A review, Hum. Pathol. 14 (1983) 108–126, https://doi.org/10.1016/S0046-8177(83)80239-1.
[147] K. Elvevold, B. Smedsrød, I. Martinez, The liver sinusoidal endothelial cell: a cell type of controversial and confusing identity, Am. J. Physiol.-Gastrointest. Liver Physiol. 294 (2008) G391–G400, https://doi.org/10.1152/ajpgi.00167.2007.
[148] C.M. Miller, A.J. Donner, E.E. Blank, A.W. Egger, B.M. Kellar, M.E. Østergaard, P.P. Seth, E.N. Harris, Stabilin-1 and Stabilin-2 are specific receptors for the cellular internalization of phosphorothioate-modified antisense oligonucleotides (ASOs) in the liver, Nucleic Acids Res. 44 (2016) 2782–2794, https://doi.org/10.1093/nar/gkw112.
[149] M.J. Gomez-Garcia, A.L. Doiron, R.R.M. Steele, H.I. Labouta, B. Vafadar, R.D. Shepherd, I.D. Gates, D.T. Cramb, S.J. Childs, K.D. Rinker, Nanoparticle localization in blood vessels: dependence on fluid shear stress, flow disturbances, and flow-induced changes in endothelial physiology, Nanoscale 10 (2018) 15249–15261, https://doi.org/10.1039/C8NR03440K.
[150] X.-Y. Jiang, C.D. Sarsons, M.J. Gomez-Garcia, D.T. Cramb, K.D. Rinker, S.J. Childs, Quantum dot interactions and flow effects in angiogenic zebrafish (Danio rerio) vessels and human endothelial cells, Nanomedicine Nanotechnol. Biol. Med. 13 (2017) 999–1010, https://doi.org/10.1016/j.nano.2016.12.008.
[151] S.H.C. Askes, N. Bossert, J. Bussmann, V.S. Talens, M.S. Meijer, R.E. Kieltyka, A. Kros, S. Bonnet, D. Heinrich, Dynamics of dual-fluorescent polymersomes with durable integrity in living cancer cells and zebrafish embryos, Biomaterials 168 (2018) 54–63, https://doi.org/10.1016/j.biomaterials.2018.03.037.
[152] P. Grossen, G. Québatte, D. Witzigmann, C. Prescianotto-Baschong, L.-H. Dieu, J. Huwyler, Functionalized solid-sphere peg-b-pcl nanoparticles to target brain capillary endothelial cells in vitro, J. Nanomater. (2016)https://doi.org/10.1155/2016/7818501.
[153] Y. Li, X. Miao, T. Chen, X. Yi, R. Wang, H. Zhao, S.M.-Y. Lee, X. Wang, Y. Zheng, Zebrafish as a visual and dynamic model to study the transport of nanosized drug delivery systems across the biological barriers, Colloids Surf. B: Biointerfaces 156 (2017) 227–235, https://doi.org/10.1016/j.colsurfb.2017.05.022.
[154] Y. Li, X. Song, X. Yi, R. Wang, S.M.-Y. Lee, X. Wang, Y. Zheng, Zebrafish: a visual model to evaluate the biofate of transferrin receptor-targeted 7peptide-decorated coumarin 6 micelles, ACS Appl. Mater. Interfaces 9 (2017) 39048–39058, https://doi.org/10.1021/acsami.7b12809.
[155] S. Li, Z. Peng, J. Dallman, J. Baker, A.M. Othman, P.L. Blackwelder, R.M. Leblanc, Crossing the blood-brain-barrier with transferrin conjugated carbon dots: a zebrafish model study, Colloids Surf. B: Biointerfaces 145 (2016) 251–256, https://doi.org/10.1016/j.colsurfb.2016.05.007.
[156] L. Chen, C. Watson, M. Morsch, N.J. Cole, R.S. Chung, D.N. Saunders, J.J. Yerbury, K.L. Vine, Improving the delivery of SOD1 antisense oligonucleotides to motor neurons using calcium phosphate-lipid nanoparticles, Front. Neurosci. (2017) 11, https://doi.org/10.3389/fnins.2017.00476.
[157] B.P. Eliceiri, A.M. Gonzalez, A. Baird, Zebrafish model of the blood-brain barrier: morphological and permeability studies, Methods Mol. Biol. Clifton NJ. 686 (2011) 371–378, https://doi.org/10.1007/978-1-60761-938-3_18.
[158] J.-Y. Jeong, H.-B. Kwon, J.-C. Ahn, D. Kang, S.-H. Kwon, J.A. Park, K.-W. Kim, Functional and developmental analysis of the blood–brain barrier in zebrafish, Brain Res. Bull. 75 (2008) 619–628, https://doi.org/10.1016/j.brainresbull.2007.10.043.
[159] A. Fleming, H. Diekmann, P. Goldsmith, Functional characterisation of the maturation of the blood-brain barrier in larval zebrafish, PLoS One 8 (2013) e77548, https://doi.org/10.1371/journal.pone.0077548.
[160] M.R. Cronan, D.M. Tobin, Fit for consumption: zebrafish as a model for tuberculosis, Dis. Model. Mech. 7 (2014) 777–784, https://doi.org/10.1242/dmm.016089.
[161] D.M. Tobin, L. Ramakrishnan, Comparative pathogenesis of Mycobacterium marinum and Mycobacterium tuberculosis, Cell. Microbiol. 10 (2008) 1027–1039, https://doi.org/10.1111/j.1462-5822.2008.01133.x.
[162] J.L. Flynn, Lessons from experimental Mycobacterium tuberculosis infections, Microbes Infect. 8 (2006) 1179–1188, https://doi.org/10.1016/j.micinf.2005.10.033.
[163] F. Fenaroli, D. Westmoreland, J. Benjaminsen, T. Kolstad, F.M. Skjeldal, A.H. Meijer, M. van der Vaart, L. Ulanova, N. Roos, B. Nyström, J. Hildahl, G. Griffiths, Nanoparticles as drug delivery system against tuberculosis in zebrafish embryos: direct visualization and treatment, ACS Nano 8 (2014) 7014–7026, https://doi.org/10.1021/nn5019126.
[164] F. Fenaroli, U. Repnik, Y. Xu, K. Johann, S. Van Herck, P. Dey, F.M. Skjeldal, D.M. Frei, S. Bagherifam, A. Kocere, R. Haag, B.G. De Geest, M. Barz, D.G. Russell, G. Griffiths, Enhanced permeability and retention-like extravasation of nanoparticles from the vasculature into tuberculosis granulomas in zebrafish and mouse models, ACS Nano 12 (2018) 8646–8661, https://doi.org/10.1021/acsnano.8b04433.
[165] S. Mura, J. Nicolas, P. Couvreur, Stimuli-responsive nanocarriers for drug delivery, Nat. Mater. 12 (2013) 991–1003, https://doi.org/10.1038/nmat3776.
[166] T.M.S. Chang, Therapeutic applications of polymeric artificial cells, Nat. Rev. Drug Discov. 4 (2005) 221–235, https://doi.org/10.1038/nrd1659.
[167] S. Ding, A.A. Cargill, I.L. Medintz, J.C. Claussen, Increasing the activity of immobilized enzymes with nanoparticle conjugation, Curr. Opin. Biotechnol. 34 (2015) 242–250, https://doi.org/10.1016/j.copbio.2015.04.005.
[168] S.A. Ansari, Q. Husain, Potential applications of enzymes immobilized on/in nano materials: a review, Biotechnol. Adv. 30 (2012) 512–523, https://doi.org/10.1016/j.biotechadv.2011.09.005.
[169] P.R. Cullis, M.J. Hope, Lipid nanoparticle systems for enabling gene therapies, Mol. Ther. J. Am. Soc. Gene Ther. 25 (2017) 1467–1475, https://doi.org/10.1016/j.ymthe.2017.03.013.
[170] H. Yan, C. Teh, S. Sreejith, L. Zhu, A. Kwok, W. Fang, X. Ma, K.T. Nguyen, V. Korzh, Y. Zhao, Functional mesoporous silica nanoparticles for photothermal-controlled drug delivery in vivo, Angew. Chem. Int. Ed. 51 (2012) 8373–8377, https://doi.org/10.1002/anie.201203993.
[171] C.M. Jimenez, D. Aggad, J.G. Croissant, K. Tresfield, D. Laurencin, D. Berthomieu, N. Cubedo, M. Rossel, S. Alsaiari, D.H. Anjum, R. Sougrat, M.A. Roldan-Gutierrez, S. Richeter, E. Oliviero, L. Raehm, C. Charnay, X. Cattoën, S. Clément, M.W.C. Man, M. Maynadier, V. Chaleix, V. Sol, M. Garcia, M. Gary-Bobo, N.M. Khashab, N. Bettache, J.-O. Durand, Porous porphyrin-based organosilica nanoparticles for NIR two-photon photodynamic therapy and gene delivery in zebrafish, Adv. Funct. Mater. 0 (2019) 1800235. doi:https://doi.org/10.1002/adfm.201800235.
[172] M. Poß, E. Zittel, C. Seidl, A. Meschkov, L. Muñoz, U. Schepers, C. Feldmann, Gd43+[AlPCS4]34− nanoagent generating 1O2 for photodynamic therapy, Adv. Funct. Mater. 28 (2018) 1801074, https://doi.org/10.1002/adfm.201801074.
[173] D.S. Wagner, N.A. Delk, E.Y. Lukianova-Hleb, J.H. Hafner, M.C. Farach-Carson, D.O. Lapotko, The in vivo performance of plasmonic nanobubbles as cell theranostic agents in zebrafish hosting prostate cancer xenografts, Biomaterials 31 (2010) 7567–7574, https://doi.org/10.1016/j.biomaterials.2010.06.031.
[174] S. Sieber, S. Siegrist, S. Schwarz, F. Porta, S.H. Schenk, J. Huwyler, Immobilization of enzymes on PLGA sub-micrometer particles by crosslinked layer-by-layer deposition, Macromol. Biosci. (2017) 17, https://doi.org/10.1002/mabi.201700015.
[175] T. Einfalt, D. Witzigmann, C. Edlinger, S. Sieber, R. Goers, A. Najer, M. Spulber, O. Onaca-Fischer, J. Huwyler, C.G. Palivan, Biomimetic artificial organelles with in vitro and in vivo activity triggered by reduction in microenvironment, Nat. Commun. 9 (2018) 1127, https://doi.org/10.1038/s41467-018-03560-x.
[176] J.A. Kulkarni, P.R. Cullis, R. van der Meel, Lipid nanoparticles enabling gene therapies: from concepts to clinical utility, Nucleic Acid Ther. 28 (2018) 146–157, https://doi.org/10.1089/nat.2018.0721.
[177] H. Lv, S. Zhang, B. Wang, S. Cui, J. Yan, Toxicity of cationic lipids and cationic polymers in gene delivery, J. Control. Release 114 (2006) 100–109, https://doi.org/10.1016/j.jconrel.2006.04.014.
[178] D. Adams, A. Gonzalez-Duarte, W.D. O'Riordan, C.-C. Yang, M. Ueda, A.V. Kristen, I. Tournev, H.H. Schmidt, T. Coelho, J.L. Berk, K.-P. Lin, G. Vita, S. Attarian, V. Planté-Bordeneuve, M.M. Mezei, J.M. Campistol, J. Buades, T.H. Brannagan, B.J. Kim, J. Oh, Y. Parman, Y. Sekijima, P.N. Hawkins, S.D. Solomon, M. Polydefkis, P.J. Dyck, P.J. Gandhi, S. Goyal, J. Chen, A.L. Strahs, S.V. Nochur, M.T. Sweetser, P.P. Garg, A.K. Vaishnaw, J.A. Gollob, O.B. Suhr, Patisiran, an RNAi therapeutic, for hereditary transthyretin amyloidosis, N. Engl. J. Med. 379 (2018) 11–21, https://doi.org/10.1056/NEJMoa1716153.

[179] K. Paunovska, C.D. Sago, C.M. Monaco, W.H. Hudson, M.G. Castro, T.G. Rudoltz, S. Kalathoor, D.A. Vanover, P.J. Santangelo, R. Ahmed, A.V. Bryksin, J.E. Dahlman, A direct comparison of in vitro and in vivo nucleic acid delivery mediated by hundreds of nanoparticles reveals a weak correlation, Nano Lett. (2018)https://doi.org/10.1021/acs.nanolett.8b00432.

[180] X. Zhou, F. Laroche, G.E.M. Lamers, V. Torraca, P. Voskamp, T. Lu, F. Chu, H.P. Spaink, J.P. Abrahams, Z. Liu, Ultra-small graphene oxide functionalized with polyethylenimine (PEI) for very efficient gene delivery in cell and zebrafish embryos, Nano Res. 5 (2012) 703–709, https://doi.org/10.1007/s12274-012-0254-x.

[181] C. Patton, G.H. Farr, D. An, P.G.V. Martini, L. Maves, Lipid nanoparticle packaging is an effective and nontoxic mRNA delivery platform in embryonic zebrafish, Zebrafish 15 (2018) 217–227, https://doi.org/10.1089/zeb.2017.1511.

[182] M. Cordeiro, L. Carvalho, J. Silva, L. Saúde, A.R. Fernandes, P.V. Baptista, Gold nanobeacons for tracking gene silencing in zebrafish, Nanomaterials. 7 (2017) 10, https://doi.org/10.3390/nano7010010.

[183] S. Hua, D. Matos, M.B. C, J.M. Metselaar, G. Storm, Current trends and challenges in the clinical translation of nanoparticulate nanomedicines: pathways for translational development and commercialization, Front. Pharmacol. 9 (2018). doi: https://doi.org/10.3389/fphar.2018.00790.

[184] C.J. Ceol, Y. Houvras, R.M. White, L.I. Zon, Melanoma biology and the promise of zebrafish, Zebrafish 5 (2008) 247–255, https://doi.org/10.1089/zeb.2008.0544.

[185] H. Feitsma, E. Cuppen, Zebrafish as a cancer model, Mol. Cancer Res. MCR. 6 (2008) 685–694, https://doi.org/10.1158/1541-7786.MCR-07-2167.

[186] S. Zhao, J. Huang, J. Ye, A fresh look at zebrafish from the perspective of cancer research, J. Exp. Clin. Cancer Res. 34 (2015) 80, https://doi.org/10.1186/s13046-015-0196-8.

[187] D.M. Langenau, M.D. Keefe, N.Y. Storer, J.R. Guyon, J.L. Kutok, X. Le, W. Goessling, D.S. Neuberg, L.M. Kunkel, L.I. Zon, Effects of RAS on the genesis of embryonal rhabdomyosarcoma, Genes Dev. 21 (2007) 1382–1395, https://doi.org/10.1101/gad.1545007.

[188] J.F. Amatruda, J.L. Shepard, H.M. Stern, L.I. Zon, Zebrafish as a cancer model system, Cancer Cell 1 (2002) 229–231, https://doi.org/10.1016/S1535-6108(02)00052-1.

[189] R. White, K. Rose, L. Zon, Zebrafish cancer: the state of the art and the path forward, Nat. Rev. Cancer 13 (2013) 624–636, https://doi.org/10.1038/nrc3589.

[190] S.A. Renshaw, C.A. Loynes, D.M.I. Trushell, S. Elworthy, P.W. Ingham, M.K.B. Whyte, A transgenic zebrafish model of neutrophilic inflammation, Blood 108 (2006) 3976–3978, https://doi.org/10.1182/blood-2006-05-024075.

[191] H.-F. Lin, D. Traver, H. Zhu, K. Dooley, B.H. Paw, L.I. Zon, R.I. Handin, Analysis of thrombocyte development in CD41-GFP transgenic zebrafish, Blood 106 (2005) 3803–3810, https://doi.org/10.1182/blood-2005-01-0179.

[192] M. Konantz, T.B. Balci, U.F. Hartwig, G. Dellaire, M.C. André, J.N. Berman, C. Lengerke, Zebrafish xenografts as a tool for in vivo studies on human cancer, Ann. N. Y. Acad. Sci. 1266 (2012) 124–137, https://doi.org/10.1111/j.1749-6632.2012.06575.x.

[193] C. Tulotta, S. He, W. van der Ent, L. Chen, A. Groenewoud, H.P. Spaink, B.E. Snaar-Jagalska, Imaging cancer angiogenesis and metastasis in a zebrafish embryo model, Adv. Exp. Med. Biol. 916 (2016) 239–263, https://doi.org/10.1007/978-3-319-30654-4_11.

[194] M. Roh-Johnson, A.N. Shah, J.A. Stonick, K.R. Poudel, J. Kargl, G.H. Yang, J. di Martino, R.E. Hernandez, C.E. Gast, L.R. Zarour, S. Antoku, A.M. Houghton, J.J. Bravo-Cordero, M.H. Wong, J. Condeelis, C.B. Moens, Macrophage-dependent cytoplasmic transfer during melanoma invasion in vivo, Dev. Cell 43 (2017) 549–562 , (e6) https://doi.org/10.1016/j.devcel.2017.11.003.

[195] S. Nicoli, D. Ribatti, F. Cotelli, M. Presta, Mammalian tumor xenografts induce neovascularization in zebrafish embryos, Cancer Res. 67 (2007) 2927–2931, https://doi.org/10.1158/0008-5472.CAN-06-4268.

[196] S. Nicoli, M. Presta, The zebrafish/tumor xenograft angiogenesis assay, Nat. Protoc. 2 (2007) 2918–2923, https://doi.org/10.1038/nprot.2007.412.

[197] Y. Feng, C. Santoriello, M. Mione, A. Hurlstone, P. Martin, Live imaging of innate immune cell sensing of transformed cells in zebrafish larvae: parallels between tumor initiation and wound inflammation, PLoS Biol. 8 (2010) e1000562, https://doi.org/10.1371/journal.pbio.1000562.

[198] I.V. Mizgireuv, I.G. Majorova, V.M. Gorodinskaya, V.V. Khudoley, S.Y. Revskoy, Carcinogenic effect of N-nitrosodimethylamine on diploid and triploid zebrafish (Danio rerio), Toxicol. Pathol. 32 (2004) 514–518, https://doi.org/10.1080/01926230490496311.

[199] J.M. Spitsbergen, H.W. Tsai, A. Reddy, T. Miller, D. Arbogast, J.D. Hendricks, G.S. Bailey, Neoplasia in zebrafish (Danio rerio) treated with 7,12-dimethylbenz[a]anthracene by two exposure routes at different developmental stages, Toxicol. Pathol. 28 (2000) 705–715, https://doi.org/10.1177/019262330002800511.

[200] L.G. Beckwith, J.L. Moore, G.S. Tsao-Wu, J.C. Harshbarger, K.C. Cheng, Ethylnitrosourea induces neoplasia in zebrafish (Danio rerio), Lab. Investig. J. Tech. Methods Pathol. 80 (2000) 379–385.

[201] J.L. Shepard, J.F. Amatruda, H.M. Stern, A. Subramanian, D. Finkelstein, J. Ziai, K.R. Finley, K.L. Pfaff, C. Hersey, Y. Zhou, B. Barut, M. Freedman, C. Lee, J. Spitsbergen, D. Neuberg, G. Weber, T.R. Golub, J.N. Glickman, J.L. Kutok, J.C. Aster, L.I. Zon, A zebrafish bmyb mutation causes genome instability and increased cancer susceptibility, Proc. Natl. Acad. Sci. 102 (2005) 13194–13199, https://doi.org/10.1073/pnas.0506583102.

[202] J.L. Shepard, J.F. Amatruda, D. Finkelstein, J. Ziai, K.R. Finley, H.M. Stern, K. Chiang, C. Hersey, B. Barut, J.L. Freeman, C. Lee, J.N. Glickman, J.L. Kutok, J.C. Aster, L.I. Zon, A mutation in separase causes genome instability and increased susceptibility to epithelial cancer, Genes Dev. 21 (2007) 55–59, https://doi.org/10.1101/gad.1470407.

[203] S. Berghmans, R.D. Murphey, E. Wienholds, D. Neuberg, J.L. Kutok, C.D.M. Fletcher, J.P. Morris, T.X. Liu, S. Schulte-Merker, J.P. Kanki, R. Plasterk, L.I. Zon, A.T. Look, tp53 mutant zebrafish develop malignant peripheral nerve sheath tumors, Proc. Natl. Acad. Sci. 102 (2005) 407–412, https://doi.org/10.1073/pnas.0406252102.

[204] M. Furutani-Seiki, J. Wittbrodt, Medaka and zebrafish, an evolutionary twin study, Mech. Dev. 121 (2004) 629–637, https://doi.org/10.1016/j.mod.2004.05.010.

[205] T.W. Chew, X.J. Liu, L. Liu, J.M. Spitsbergen, Z. Gong, B.C. Low, Crosstalk of Ras and Rho: activation of RhoA abates Kras-induced liver tumorigenesis in transgenic zebrafish models, Oncogene 33 (2014) 2717–2727, https://doi.org/10.1038/onc.2013.240.

[206] G. Gaudenzi, M. Albertelli, A. Dicitore, R. Würth, F. Gatto, F. Barbieri, F. Cotelli, T. Florio, D. Ferone, L. Persani, G. Vitale, Patient-derived xenograft in zebrafish embryos: a new platform for translational research in neuroendocrine tumors, Endocrine 57 (2017) 214–219, https://doi.org/10.1007/s12020-016-1048-9.

[207] L. Mercatali, F. La Manna, A. Groenewoud, R. Casadei, F. Recine, G. Miserocchi, F. Pieri, C. Liverani, A. Bongiovanni, C. Spadazzi, A. de Vita, G. van der Pluijm, A. Giorgini, R. Biagini, D. Amadori, T. Ibrahim, E. Snaar-Jagalska, L. Mercatali, F. La Manna, A. Groenewoud, R. Casadei, F. Recine, G. Miserocchi, F. Pieri, C. Liverani, A. Bongiovanni, C. Spadazzi, A. de Vita, G. van der Pluijm, A. Giorgini, R. Biagini, D. Amadori, T. Ibrahim, E. Snaar-Jagalska, Development of a patient-derived xenograft (PDX) of breast cancer bone metastasis in a zebrafish model, Int. J. Mol. Sci. 17 (2016) 1375, https://doi.org/10.3390/ijms17081375.

[208] J. Wertman, C.J. Veinotte, G. Dellaire, J.N. Berman, the zebrafish xenograft platform: evolution of a novel cancer model and preclinical screening tool, Adv. Exp. Med. Biol. 916 (2016) 289–314, https://doi.org/10.1007/978-3-319-30654-4_13.

[209] H.K. Brown, K. Schiavone, S. Tazzyman, D. Heymann, T.J. Chico, Zebrafish xenograft models of cancer and metastasis for drug discovery, Expert Opin. Drug Discovery 12 (2017) 379–389, https://doi.org/10.1080/17460441.2017.1297416.

[210] Y. Drabsch, B.E. Snaar-Jagalska, P.D. Ten, Fish tales: the use of zebrafish xenograft human cancer cell models, Histol. Histopathol. 32 (2017) 673–686, https://doi.org/10.14670/HH-11-853.

[211] K.M. Muthukumarasamy, K.L. Handore, D.N. Kakade, M.V. Shinde, S. Ranjan, N. Kumar, S. Sehrawat, C. Sachidanandan, D.S. Reddy, Identification of noreremophilane-based inhibitors of angiogenesis using zebrafish assays, Org. Biomol. Chem. 14 (2016) 1569–1578, https://doi.org/10.1039/C5OB01594D.

[212] M. de Boeck, C. Cui, A.A. Mulder, C.R. Jost, S. Ikeno, P. ten Dijke, Smad6 determines BMP-regulated invasive behaviour of breast cancer cells in a zebrafish xenograft model, Sci. Rep. 6 (2016) 24968, https://doi.org/10.1038/srep24968.

[213] M. Kanada, J. Zhang, L. Yan, T. Sakurai, S. Terakawa, Endothelial cell-initiated extravasation of cancer cells visualized in zebrafish, PeerJ. 2 (2014)https://doi.org/10.7717/peerj.688.

[214] M. Haldi, C. Ton, W.L. Seng, P. McGrath, Human melanoma cells transplanted into zebrafish proliferate, migrate, produce melanin, form masses and stimulate angiogenesis in zebrafish, Angiogenesis (9) (2006) 139–151, https://doi.org/10.1007/s10456-006-9040-2.

[215] R. Spence, G. Gerlach, C. Lawrence, C. Smith, The behaviour and ecology of the zebrafish, Danio rerio, Biol. Rev. 83 (2008) 13–34, https://doi.org/10.1111/j.1469-185X.2007.00030.x.

[216] M. Dovey, R.M. White, L.I. Zon, Oncogenic NRAS cooperates with p53 loss to generate melanoma in zebrafish, Zebrafish 6 (2009) 397–404, https://doi.org/10.1089/zeb.2009.0606.

[217] P. Mullen, The use of matrigel to facilitate the establishment of human cancer cell lines as xenografts, Methods Mol. Med. 88 (2004) 287–292, https://doi.org/10.1385/1-59259-406-9:287.

[218] S.H. Lam, H.L. Chua, Z. Gong, T.J. Lam, Y.M. Sin, Development and maturation of the immune system in zebrafish, Danio rerio: a gene expression profiling, in situ hybridization and immunological study, Dev. Comp. Immunol. 28 (2004) 9–28, https://doi.org/10.1016/S0145-305X(03)00103-4.

[219] K. Stoletov, V. Montel, R.D. Lester, S.L. Gonias, R. Klemke, High-resolution imaging of the dynamic tumor cell vascular interface in transparent zebrafish, Proc. Natl. Acad. Sci. U. S. A. 104 (2007) 17406–17411, https://doi.org/10.1073/pnas.0703446104.

[220] J. Wertman, C.J. Veinotte, G. Dellaire, J.N. Berman, the zebrafish xenograft platform: evolution of a novel cancer model and preclinical screening tool, Cancer Zebrafish, Springer, Cham 2016, pp. 289–314, https://doi.org/10.1007/978-3-319-30654-4_13.

[221] M. Astone, E.N. Dankert, S.K. Alam, L.H. Hoeppner, Fishing for cures: the alLURE of using zebrafish to develop precision oncology therapies, Npj Precis. Oncol. 1 (2017) 39, https://doi.org/10.1038/s41698-017-0043-9.

[222] V.L. Bentley, C.J. Veinotte, D.P. Corkery, J.B. Pinder, M.A. LeBlanc, K. Bedard, A.P. Weng, J.N. Berman, G. Dellaire, Focused chemical genomics using zebrafish xenotransplantation as a pre-clinical therapeutic platform for T-cell acute lymphoblastic leukemia, Haematologica 100 (2015) 70–76, https://doi.org/10.3324/haematol.2014.110742.

[223] D.P. Corkery, G. Dellaire, J.N. Berman, Leukaemia xenotransplantation in zebrafish – chemotherapy response assay in vivo, Br. J. Haematol. 153 (2011) 786–789, https://doi.org/10.1111/j.1365-2141.2011.08661.x.

[224] R.K. Jain, L.L. Munn, D. Fukumura, Dissecting tumour pathophysiology using intravital microscopy, Nat. Rev. Cancer 2 (2002) 266–276, https://doi.org/10.1038/nrc778.

[225] Y. Drabsch, S. He, L. Zhang, B.E. Snaar-Jagalska, P. ten Dijke, Transforming growth factor-β signalling controls human breast cancer metastasis in a zebrafish xenograft model, Breast Cancer Res. BCR. 15 (2013) R106, https://doi.org/10.1186/bcr3573.

[226] J. Barriuso, R. Nagaraju, A. Hurlstone, Zebrafish: a new companion for translational research in oncology, Clin. Cancer Res. Off. J. Am. Assoc. Cancer Res. 21 (2015) 969–975, https://doi.org/10.1158/1078-0432.CCR-14-2921.

Please cite this article as: S. Sieber, P. Grossen, J. Bussmann, et al., Zebrafish as a preclinical *in vivo* screening model for nanomedicines, Adv. Drug Deliv. Rev., https://doi.org/10.1016/j.addr.2019.01.001

[227] K. Stoletov, R. Klemke, Catch of the day: zebrafish as a human cancer model, Oncogene 27 (2008) 4509–4520, https://doi.org/10.1038/onc.2008.95.
[228] F. Danhier, To exploit the tumor microenvironment: Since the EPR effect fails in the clinic, what is the future of nanomedicine? J. Control. Release Off. J. Control. Release Soc. 244 (2016) 108–121, https://doi.org/10.1016/j.jconrel.2016.11.015.
[229] M. Gao, Y. Xu, L. Qiu, Sensitization of multidrug-resistant malignant cells by liposomes co-encapsulating doxorubicin and chloroquine through autophagic inhibition, J. Liposome Res. 27 (2017) 151–160, https://doi.org/10.1080/08982104.2016.1185731.
[230] J. Yang, Y. Shimada, R.C.L. Olsthoorn, B.E. Snaar-Jagalska, H.P. Spaink, A. Kros, Application of coiled coil peptides in liposomal anticancer drug delivery using a zebrafish xenograft model, ACS Nano 10 (2016) 7428–7435, https://doi.org/10.1021/acsnano.6b01410.
[231] X. Gao, S. Wang, B. Wang, S. Deng, X. Liu, X. Zhang, L. Luo, R. Fan, M. Xiang, C. You, Y. Wei, Z. Qian, G. Guo, Improving the anti-ovarian cancer activity of docetaxel with biodegradable self-assembly micelles through various evaluations, Biomaterials 53 (2015) 646–658, https://doi.org/10.1016/j.biomaterials.2015.02.108.
[232] S. Ahn, E. Seo, K. Kim, S.J. Lee, Controlled cellular uptake and drug efficacy of nanotherapeutics, Sci. Rep. 3 (2013) 1997, https://doi.org/10.1038/srep01997.
[233] J. Cheng, Y.-J. Gu, Y. Wang, S.H. Cheng, W.-T. Wong, Nanotherapeutics in angiogenesis: synthesis and in vivo assessment of drug efficacy and biocompatibility in zebrafish embryos, Int. J. Nanomedicine 6 (2011) 2007–2021, https://doi.org/10.2147/IJN.S20145.
[234] R. Harfouche, S. Basu, S. Soni, D.M. Hentschel, R.A. Mashelkar, S. Sengupta, Nanoparticle-mediated targeting of phosphatidylinositol-3-kinase signaling inhibits angiogenesis, Angiogenesis 12 (2009) 325–338, https://doi.org/10.1007/s10456-009-9154-4.
[235] Q. Zhou, Y. Li, Y. Zhu, C. Yu, H. Jia, B. Bao, H. Hu, C. Xiao, J. Zhang, X. Zeng, Y. Wan, H. Xu, Z. Li, X. Yang, Co-delivery nanoparticle to overcome metastasis promoted by insufficient chemotherapy, J. Control. Release 275 (2018) 67–77, https://doi.org/10.1016/j.jconrel.2018.02.026.
[236] L. Evensen, P.L. Johansen, G. Koster, K. Zhu, L. Herfindal, M. Speth, F. Fenaroli, J. Hildahl, S. Bagherifam, C. Tulotta, L. Prasmickaite, G.M. Mælandsmo, E. Snaar-Jagalska, G. Griffiths, Zebrafish as a model system for characterization of nanoparticles against cancer, Nanoscale 8 (2016) 862–877, https://doi.org/10.1039/c5nr07289a.
[237] S. He, G.E. Lamers, J.-W.M. Beenakker, C. Cui, V.P. Ghotra, E.H. Danen, A.H. Meijer, H.P. Spaink, B.E. Snaar-Jagalska, Neutrophil-mediated experimental metastasis is enhanced by VEGFR inhibition in a zebrafish xenograft model, J. Pathol. 227 (2012) 431–445, https://doi.org/10.1002/path.4013.
[238] Q. Wu, S. Deng, L. Li, L. Sun, X. Yang, X. Liu, L. Liu, Z. Qian, Y. Wei, C. Gong, Biodegradable polymeric micelle-encapsulated quercetin suppresses tumor growth and metastasis in both transgenic zebrafish and mouse models, Nanoscale 5 (2013) 12480–12493, https://doi.org/10.1039/C3NR04651F.
[239] L.C. Wehmas, R.L. Tanguay, A. Punnoose, J.A. Greenwood, Developing a novel embryo-larval zebrafish xenograft assay to prioritize human glioblastoma therapeutics, Zebrafish 13 (2016) 317–329, https://doi.org/10.1089/zeb.2015.1170.
[240] T. Yang, P. Martin, B. Fogarty, A. Brown, K. Schurman, R. Phipps, V.P. Yin, P. Lockman, S. Bai, Exosome delivered anticancer drugs across the blood-brain barrier for brain cancer therapy in Danio rerio, Pharm. Res. 32 (2015) 2003–2014, https://doi.org/10.1007/s11095-014-1593-y.
[241] F. Porta, D. Ehrsam, C. Lengerke, H.E. Meyer zu Schwabedissen, Synthesis and characterization of a PDMS-PMOXA based polymersomes sensitive to MMP-9 for application in breast cancer, Mol. Pharm. (2018)https://doi.org/10.1021/acs.molpharmaceut.8b00521.
[242] B. Yin, K.H.K. Li, L.W.C. Ho, C.K.W. Chan, C.H.J. Choi, Toward understanding in vivo sequestration of nanoparticles at the molecular level, ACS Nano 12 (2018) 2088–2093, https://doi.org/10.1021/acsnano.8b00141.
[243] W. Wang, X. Liu, D. Gelinas, B. Ciruna, Y. Sun, A fully automated robotic system for microinjection of zebrafish embryos, PLoS One 2 (2007) e862, https://doi.org/10.1371/journal.pone.0000862.
[244] J.N. Wittbrodt, U. Liebel, J. Gehrig, Generation of orientation tools for automated zebrafish screening assays using desktop 3D printing, BMC Biotechnol. 14 (2014) 36, https://doi.org/10.1186/1472-6750-14-36.
[245] M.F. Yanik, C.B. Rohde, C. Pardo-Martin, Technologies for Micromanipulating, Imaging, and Phenotyping Small Invertebrates and Vertebrates, Annu. Rev. Biomed. Eng. 13 (2011) 185–217, https://doi.org/10.1146/annurev-bioeng-071910-124703.
[246] R. Pulak, Tools for automating the imaging of zebrafish larvae, Methods 96 (2016) 118–126, https://doi.org/10.1016/j.ymeth.2015.11.021.
[247] D.T. White, A.U. Eroglu, G. Wang, L. Zhang, S. Sengupta, D. Ding, S.K. Rajpurohit, S.L. Walker, H. Ji, J. Qian, J.S. Mumm, ARQiv-HTS, a versatile whole-organism screening platform enabling *in vivo* drug discovery at high-throughput rates, Nat. Protoc. 11 (2016) 2432–2453, https://doi.org/10.1038/nprot.2016.142.
[248] T.-Y. Chang, P. Shi, J.D. Steinmeyer, I. Chatnuntawech, P. Tillberg, K.T. Love, P.M. Eimon, D.G. Anderson, M.F. Yanik, Organ-targeted high-throughput in vivo biologics screen identifies materials for RNA delivery, Integr. Biol. 6 (2014) 926–934, https://doi.org/10.1039/C4IB00150H.
[249] L.K. Müller, J. Simon, C. Rosenauer, V. Mailänder, S. Morsbach, K. Landfester, The transferability from animal models to humans: challenges regarding aggregation and protein corona formation of nanoparticles, Biomacromolecules 19 (2018) 374–385, https://doi.org/10.1021/acs.biomac.7b01472.
[250] G. Caracciolo, O.C. Farokhzad, M. Mahmoudi, Biological identity of nanoparticles in vivo: clinical implications of the protein corona, Trends Biotechnol. 35 (2017) 257–264, https://doi.org/10.1016/j.tibtech.2016.08.011.
[251] Q. Dai, Y. Yan, J. Guo, M. Björnmalm, J. Cui, H. Sun, F. Caruso, Targeting ability of affibody-functionalized particles is enhanced by albumin but inhibited by serum coronas, ACS Macro Lett. 4 (2015) 1259–1263, https://doi.org/10.1021/acsmacrolett.5b00627.
[252] M. Hadjidemetriou, Z. Al-Ahmady, M. Mazza, R.F. Collins, K. Dawson, K. Kostarelos, Vivo Biomolecule Corona around Blood-Circulating, Clinically Used and Antibody-Targeted Lipid Bilayer Nanoscale Vesicles, ACS Nano. 9, 2015 8142–8156, https://doi.org/10.1021/acsnano.5b03300.
[253] D. Shan, J. Li, P. Cai, P. Prasad, F. Liu, A.M. Rauth, X.Y. Wu, RGD-conjugated solid lipid nanoparticles inhibit adhesion and invasion of αvβ3 integrin-overexpressing breast cancer cells, drug deliv. Transl. Res. 5 (2015) 15–26. doi: https://doi.org/10.1007/s13346-014-0210-2.

Please cite this article as: S. Sieber, P. Grossen, J. Bussmann, et al., Zebrafish as a preclinical *in vivo* screening model for nanomedicines, Adv. Drug Deliv. Rev., https://doi.org/10.1016/j.addr.2019.01.001

Chapter II-I

Zebrafish as a predictive screening model to assess macrophage clearance of liposomes in vivo

Sandro Sieber, Philip Grossen, Philipp Uhl, Pascal Detampel, Walter Mier, Dominik Witzigmann, Jörg Huwyler

Manuscript: Nanomedicine: Nanotechnology, Biology and Medicine (2019) [40]

Highlights: Recognition and uptake by cells of the immune system (i.e. macrophages) is one of the major nanomedicine clearing mechanism and mainly affected by nanomedicine size and surface modification (i.e. PEGylation). In this study, differently sized liposomes modified with varying amounts and molecular weights of PEG were assessed regarding their clearance by macrophages following the traditional drug development process (preparation and physicochemical characterization, *in vitro*, *in vivo*). In addition, the zebrafish was used as a complementary *in vivo* screening model in order to design and optimize nanomedicine formulations under complex biological conditions. Finally, selected and most interesting findings were verified in a biodistribution study in rats, demonstrating the predictive power of the zebrafish model.

Nanomedicine: Nanotechnology, Biology, and Medicine
17 (2019) 82–93

nanomedicine
Nanotechnology, Biology, and Medicine

nanomedjournal.com

Zebrafish as a predictive screening model to assess macrophage clearance of liposomes *in vivo*

Sandro Sieber, PhD[a,1], Philip Grossen, PhD[a,1], Philipp Uhl, PhD[b], Pascal Detampel, PhD[a], Walter Mier, PhD[b], Dominik Witzigmann, PhD[a,c,*], Jörg Huwyler, PhD[a,*]

[a]*Division of Pharmaceutical Technology, Department of Pharmaceutical Sciences, University of Basel, Basel, Switzerland*
[b]*Department of Nuclear Medicine, University Hospital Heidelberg, Heidelberg, Germany*
[c]*Department of Biochemistry and Molecular Biology, University of British Columbia, Health Sciences Mall, Vancouver, British Columbia, Canada*

Revised 11 October 2018

Abstract

Macrophage recognition of nanoparticles is highly influenced by particle size and surface modification. Due to the lack of appropriate *in vivo* screening models, it is still challenging and time-consuming to characterize and optimize nanomedicines regarding this undesired clearance mechanism. Therefore, we validate zebrafish embryos as an emerging vertebrate screening tool to assess the macrophage sequestration of surface modified particulate formulations with varying particle size under realistic biological conditions. Liposomes with different PEG molecular weights (PEG350-PEG5000) at different PEG densities (3.0-10.0 mol%) and particle sizes between 60 and 120 nm were used as a well-established reference system showing various degrees of macrophage uptake. The results of *in vitro* experiments, zebrafish embryos, and *in vivo* rodent biodistribution studies were consistent, highlighting the validity of the newly introduced zebrafish macrophage clearance model. We hereby present a strategy for efficient, systematic and rapid nanomedicine optimization in order to facilitate the preclinical development of nanotherapeutics.

Key words: Nanoparticles; Liposomes; PEG; Cell uptake; Zebrafish screening model; Systemic clearance; Macrophage accumulation

Nanomedicines offer valuable therapeutic options by delivering drugs of interest to diseased tissues or organs. By modifying their physicochemical properties, interactions of nanomedicines with macrophages and other cells of the mononuclear phagocyte system (MPS) can be tailored to the intended application. On one hand, this can be exploited to treat various diseases. During inflammation and cancer for example, nanomedicines can be used to alter the polarization state of macrophages (*i.e.* M1, M2).[1–3] Furthermore, several infectious pathogens such as tuberculosis persist in macrophages and thus targeting these microbial reservoirs can dramatically decrease the disease progression.[4,5] On the other hand, most nanomedicine applications require a low uptake by the MPS to increase circulation half-life and ultimately enhance accumulation in target tissues.

In this regard, size and surface modification have been identified as crucial physicochemical characteristics of nanomedicines.[6] Consequently, the most advanced systems in clinics are based on liposomal formulations with long circulating properties, achieved by hydrophilic surface modification and a mean diameter of approximately 100 nm.[6,7] The state-of-the-art strategy to prevent

Conflicts of Interest: The authors declare no conflict of interest regarding the publication of this paper.

Acknowledgments: DW and JH have equally contributed to the present publication. The authors are thankful for support of the "Stiftung zur Förderung des pharmazeutischen Nachwuchses in Basel", the "Freiwillige Akademische Gesellschaft Basel", the Swiss National Science Foundation (SNF grants No. 174975 and No. 173057) and the EU Horizon 2020 project "NanoReg2". Prof. Dr. M. Affolter, Dr. H.G. Belting and N. Schellinx are acknowledged for providing zebrafish eggs and sharing their expertise.

*Corresponding authors at: Division of Pharmaceutical Technology, Department of Pharmaceutical Sciences, University of Basel, 4056 Basel, Switzerland.
E-mail addresses: dominik.witzigmann@unibas.ch, (D. Witzigmann), joerg.huwyler@unibas.ch. (J. Huwyler).
[1] These authors contributed equally to this work.

https://doi.org/10.1016/j.nano.2018.11.017

clearance from circulation by macrophages is modification of the liposome surface with polyethylene glycol (PEG), *i.e.* a hydrophilic polymer coating. In recent decades, various groups have analyzed the effect of key PEG characteristics such as chain length (*i.e.* molecular weight) and PEG concentration (*i.e.* surface density) on pharmacokinetics of nanoparticles *in vitro* and *in vivo*.[8–10] However, whereas some research groups report that circulation times are relatively independent of changes in PEG modifications, others report a PEG molecular weight and surface density dependent influence on liposome circulation.[8–10] Similarly, size differences of liposomes may have a major impact on their pharmacokinetics and clearance rate. For example, an upper particle size limit of 150 nm was proposed to avoid rapid hepatosplenic clearance whereas the lower size limit is set by the glomerular filtration size cut-off of around 6 nm to avoid renal elimination.[11] Nevertheless, many studies include particles with a large size range up to micrometer scale,[12] which is therefore in disagreement with the generally accepted size range for biomedical applications.[13,14]

A major challenge in the design of novel nanomedicines is the lack of appropriate screening models to optimize physicochemical properties of nanoparticles. So far, *in vitro* models can be used only to study cellular interactions with nanoparticles. It is not possible to predict from *in vitro* experiments to which degree small variations in physicochemical properties and surface modifications influence nanoparticle circulation properties *in vivo* and their accumulation in macrophage rich organs such as the spleen. Furthermore, novel nanomedicine components substituting PEG such as a broad range of various polymers,[15] polysarcosines,[16] hyperbranched polyether chains,[17] or polyglycerol derivatives[18] are continuously synthesized and require a thorough analysis. Such novel nanomedicine formulations have to be tested *in vivo* to account for the full complexity of a living animal including the presence of blood flow, shear stress, and serum proteins. In view of ethical considerations, high costs and limited throughput of animal experiments in higher vertebrates, zebrafish embryos have been proposed as a vertebrate screening model for nanomedicines. Recent studies show that the systemic circulation of nanoparticles can be assessed in a time-effective manner using this novel screening tool.[19–21]

Since the evolution of the adaptive immune system took place before the divergence of fish from other vertebrates, the innate and adaptive immune system of teleost (zebrafish) and mammals is highly conserved.[22] Early embryonic macrophages are present in zebrafish embryos already at 30 h post fertilization.[23] Furthermore, additional cells such as monocytes and dendritic cells, which define the mammalian MPS can be found in adult zebrafish.[24] Notably, polarized macrophages (M1, M2) are present in zebrafish embryos,[25] which are of special importance for nanomedicines intended to treat cancer or inflammatory disorders. Conclusively, the zebrafish offers the possibility to assess nanomedicine clearance by macrophages in a living animal under physiological conditions.

It was therefore the aim of the present study to validate the use of the zebrafish model to investigate nanoparticle clearance by macrophages. PEGylated liposomes were used as a well-established model system. The influence of various parameters such as PEG molecular weight (PEG350-PEG5000), PEG density (3 mol%-10 mol%) and liposome size (60-120 nm) on zebrafish macrophage clearance was assessed in a systematic zebrafish screening approach under live *in vivo* conditions.

Monodisperse liposome formulations with a physiologically relevant and well defined size range and different PEG modifications were prepared by a microfluidics Design-of-Experiment (DoE) approach, followed by physicochemical and *in vitro* characterization. Liposome clearance by macrophages was studied using transgenic zebrafish embryos with fluorescent macrophages in combination with fluorescently labeled liposomal formulations. The effects observed for the variation of liposome size and PEGylation were confirmed *in vivo* in rats using tissue distribution studies with a focus on unwanted nanoparticle accumulation in the spleen, *i.e.* the largest blood filter organ of the body.[26]

Methods

1,2-distearoyl-*sn*-glycero-3-phosphocholine (DSPC) and 1,2-distearoyl-*sn*-glycero-3-phosphoethanolamine-N-[methoxy (polyethylene glycol)-5000] (PEG5000) were purchased from Corden Pharma (Liestal, Switzerland). 1,2-distearoyl-*sn*-glycero-3-phosphoethanolamine-N-[methoxy(polyethylene glycol)-2000] (PEG2000) was obtained from Lipoid (Steinhausen, Switzerland). Cholesterol and 1,1′-Dioctadecyl-3,3,3′,3′-tetramethylindocarbocyanine perchlorate sterol (DiI) were purchased from Sigma-Aldrich (Buchs, Switzerland). 1,2-distearoyl-*sn*-glycero-3-phosphoethanolamine-N-[methoxy(polyethylene glycol)-350] (PEG350), 1,2-distearoyl-*sn*-glycero-3-phosphoethanolamine-N-[methoxy(polyethylene glycol)-750] (PEG750), and 1,2-distearoyl-sn-glycero-3-phosphoethanolamine-N-diethylenetriaminepentaacetic acid (DSPE-DTPA) were obtained from Avanti Polar Lipids (Alabaster, USA). $^{111}InCl_3$ was purchased from Mallinckrodt Pharmaceuticals (Hennef, Germany).

Preparation of fluorescent liposomes for zebrafish injections using a full factorial Design-of-Experiments (DoE)

Liposomes were prepared using microfluidics (NanoAssemblr Benchtop Instrument, Precision NanoSystems Inc., Vancouver, Canada) as described previously.[27] Briefly, microfluidics cartridges contained two separate inlets for the solvent (lipids in ethanol) and the aqueous (Dulbecco's phosphate buffered saline without calcium chloride and magnesium chloride, DPBS) phase. The herringbone mixing structure ensured optimal mixing of the two phases, resulting in liposome formation. To control liposome size, the flow rate ratio (FRR, ratio of aqueous and organic phase) of the two liquid phases was varied thereby influencing the speed of polarity change. To finally identify the optimal FRR for each lipid composition and to analyze the effects of PEG molecular weight and PEG density on liposome size and PDI, a full factorial DoE was used as described previously for various clinically approved liposome formulations.[28] Analysis of results and model fitting of the statistical DoE were performed using Stavex 5.2 software (Aicos Technologies AG, Basel, Switzerland). Lipids were dissolved in ethanol while the aqueous phase consisted of DPBS. The total flow rate (TFR) was kept constant at 10 mL/min while the flow rate ratio (FRR) between the solvent and aqueous stream was adjusted for each formulation. The liposome formulation was dialyzed overnight against H_2O using a dialysis membrane with a molecular weight cut-off of 12-14 kDa.

Preparation of radiolabeled liposomes for rat in vivo studies

Radioactive labeling of liposomes with ^{111}In was performed as described previously.[29] Liposomes with different sizes were prepared in citrate buffered saline pH 5.4 at a total lipid concentration of 60 mM including 3 mol% DSPE-DTPA. Liposomes were incubated immediately before injection with $^{111}InCl_3$ at 37°C for 45 min and purified using gel filtration chromatography (NAP® 5 columns, Pharmacia Biotech AB, Uppsala, Sweden). The outer buffer was exchanged to sterile saline.

Dynamic light scattering measurements

Size and polydispersity index (PDI) of liposome samples were determined by dynamic light scattering (DLS) using a Delsa Nano C Particle Analyzer (Beckman Coulter, Nyon, Switzerland) as described previously.[30] All measurements were performed at 10 mM lipid concentration in H_2O at room temperature.

Cell culture

Liver cancer-derived cell lines HepG2 and Sk-Hep1 were kindly provided by the cell depository of the Institute of Pathology, University Hospital of Basel, Switzerland. Cells were maintained in DMEM high glucose (4.5 g/L) containing 10% fetal calf serum (FCS) and 1% penicillin–streptomycin (P/S). THP-1 cells (ATCC, TIB-202) were cultured in Roswell Park Memorial Institute (RPMI-1640) medium containing 10% FCS, 1% P/S, 10 mM HEPES, 1% sodium pyruvate and 0.05 mM mercaptoethanol. All cells were cultured at 37 °C under 5% CO_2.[31,32]

Flow cytometry

In vitro uptake experiments were performed according to published protocols.[33,34] In brief, HepG2, Sk-Hep1 and THP1 cells were seeded at a density of 1×10^5 cells/cm^2 in a 12-well plate (TPP, Trasadingen, Switzerland). In order to induce differentiation of THP1 monocytes into macrophages, phorbol 12-myristate 13-acetate (PMA) at a final concentration of 100 nM was added to seeded THP-1 cells 72 h prior to the actual uptake experiment. For uptake experiments, cells (80% confluence) were washed with 37 °C DPBS and incubated with cell culture media at final lipid concentrations of 50, 100, and 200 mM, or corresponding volumes of DPBS as negative control. Uptake experiments were terminated 3 or 24 h post incubation by removal of liposome or DPBS containing cell medium and washing of cells with 1 mL of DPBS. Cells were detached with 0.25% Trypsin–EDTA at 37 °C for 8 (HepG2, SkHep1) or 10 (THP1) min. The trypsin reaction was stopped by adding 1 mL of ice-cold cell medium and the cells were collected by centrifugation for 5 min at 200 ×*g* and 4 °C. The cell pellet was washed with 1 mL ice cold DPBS, centrifuged and suspended in 500 μL FACS buffer (DPBS, 0.05% NaN_3, 1% FCS, 2.5 mM EDTA). Flow cytometry analysis was performed using a FACS Canto II (BD Bioscience, California, USA). DiI fluorescence was excited at 561 nm and detected using a 586/15 bandpass filter. Signals of 20,000 cells were analyzed using FlowJo analysis software version V9/X (Tree-Star, Oregon, USA). Cell doublets were excluded from analysis.

Zebrafish embryo culture and injection

Zebrafish embryos/larvae from adult Tg(kdrl:EGFP)[35] and Tg(mpeg1:Gal4;UAS:Kaede)[36,37] were raised at standard conditions at 28 °C in zebrafish culture media[38] containing 1-phenyl-2-thiourea (PTU) and in accordance with Swiss animal welfare regulations. Injections of liposome samples (10 mM) in zebrafish embryos (2 dpf) were performed as described previously.[19,39] Calibrated volumes of 1 nL were injected into the blood circulation *via* the common cardinal vein using a micromanipulator (Wagner Instrumentenbau KG, Schöffengrund, Germany), a pneumatic Pico Pump PV830 (WPI, Sarasota, Florida), and a Leica S8APO microscope (Leica, Wetzlar, Germany). Imaging of successful injected zebrafish embryos was performed 3 and 24 h post injection (hpi) using an Olympus FV-1000 inverted confocal laser scanning microscope (Olympus Ltd., Tokyo, Japan) equipped with a 10× UPlanSApo (NA 0.4) and 20× UPlanSApo (NA 0.75) objective.

Macrophage colocalization analysis

To analyze macrophage clearance of liposomes, transgenic zebrafish embryos were imaged using an Olympus FV-1000 inverted confocal laser scanning microscope equipped with a 20× UPlanSApo (NA 0.75) objective. For colocalization analysis of liposomes with macrophages, the overlap coefficient was used as implemented by the JaCoP plugin from Fiji ImageJ.[40,41] Overlap coefficients are given as fold change in colocalization as compared to PEG350 modified liposomes with a size of 90 nm.

Pharmacokinetic study in rats

Organ and tissue distribution profile of PEG350 and PEG2000 liposomes was analyzed in female Wistar rats (225-275 g body weight; Janvier Labs, Saint-Berthevin Cedex, France). Animal experiments were approved and carried out in accordance with local animal welfare regulations. ^{111}In-labeled liposomes, prepared using a chelating strategy based on DSPE-DTPA, were injected intravenously *via* the tail vein. The injection volume was 100-150 μL, the total activity was 10 MBq per rat, and the total lipid concentration was 30 mM. After 24 h, animals were euthanized, organs were collected and radioactivity associated with organs was measured with a Berthold LB 951G gamma counter (Berthold Technologies, Bad Wildbad, Germany) and expressed in terms of injected dose (%ID) per g tissue.

Results

Liposome preparation and physicochemical characterization

Since liposome PEGylation and particle size heavily influence liposome interactions with cells, a microfluidics-based formulation approach was selected to obtain liposomes of comparable sizes independent of PEG modification. Depending on the liposome composition, increasing FRR can result in larger or smaller liposomes. In order to accurately investigate the interplay between FRR and each liposome composition (*i.e.* PEG molecular weight, PEG density), a full factorial DoE was performed. At constant FRRs, increasing PEG molecular weight resulted in smaller liposomes (Figure 1). The FRR had a significant influence on

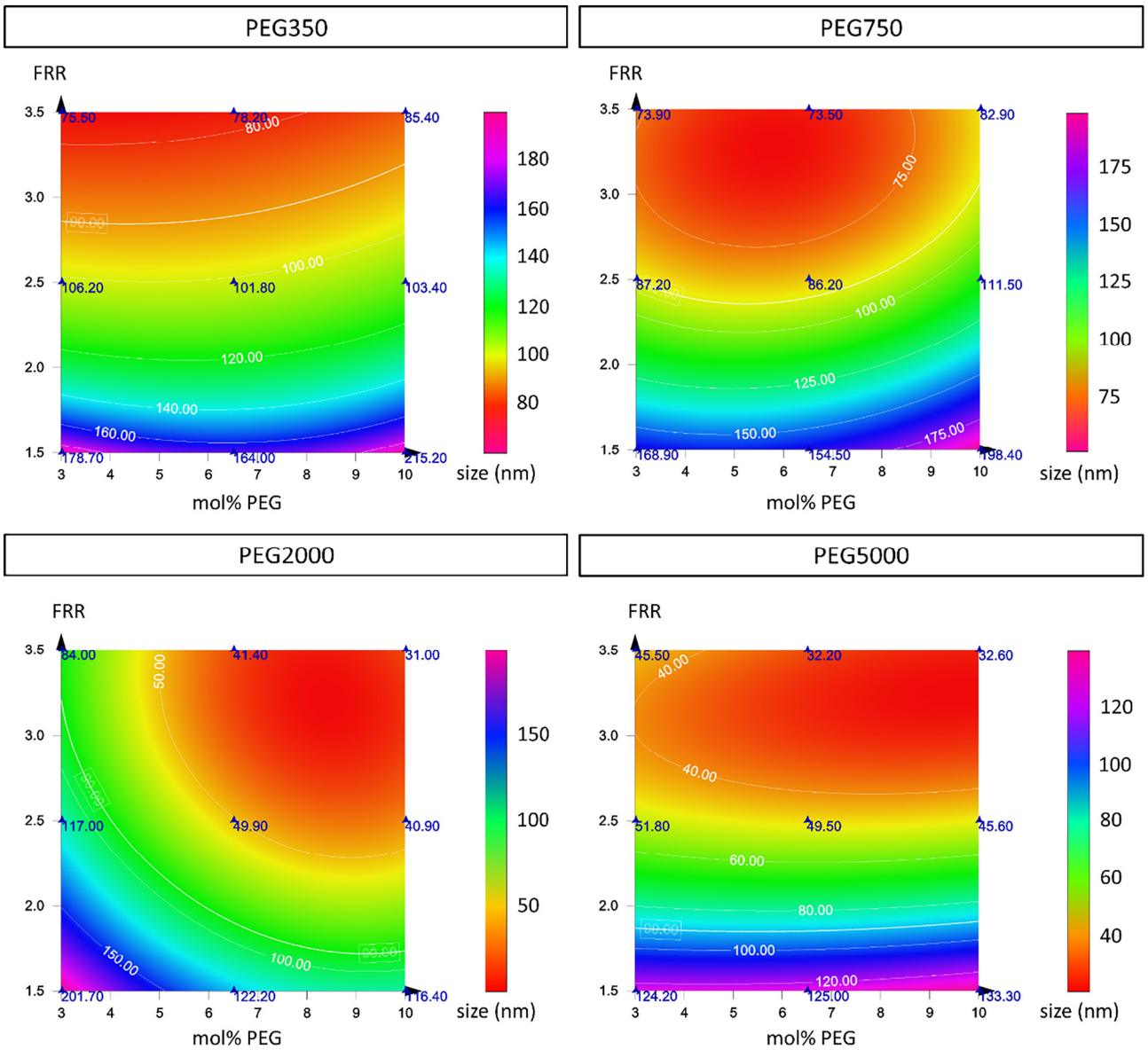

Figure 1. Preparation of PEGylated liposomes based on a Design-of-Experiment (DoE) approach. DSPC-cholesterol based liposomes with different PEG molecular weights and PEG densities were prepared using a microfluidics technology. Different flow rate ratios (FRRs) were used to adjust liposome size. The contour plots for each PEG chain length show the effect of different flow rate ratios and PEG densities on liposome size. r^2 of model fits = 0.988-0.998. Specific color legends represent liposome size (nm).

liposome size for all PEG molecular weights ($P \leq 0.001$). PEG density (mol%) had a variable influence on liposome size depending on PEG type ($0.001 \leq P \leq 0.259$). The size model fit for all PEG molecular weights was very good (r^2 = 0.988-0.998). Based on these findings, different types of PEGylated liposomes with a defined size and a narrow, monodisperse particle size distribution (*i.e.* a PDI < 0.15) were prepared by specifically adjusting FRR for each formulation. The exact size and PDI for each lipid composition using optimized FRRs are shown in Table 1. Fluorescent and radiolabeled liposome samples, which were injected into zebrafish or rats, were analyzed regarding their stability upon storage at 4 °C (Supplementary Tables S1 and S2). No significant changes of liposome size or PDI were observed for radiolabeled liposomes. One fluorescently labeled formulation showed a final PDI over 0.250 after one year of storage. Despite the high colloidal stability of the liposomal preparations, liposomes were used immediately after preparation.

In vitro characterization

Cellular interactions of the prepared liposome library with three human cell lines representative for hepatosplenic clearance were studied using a well-established *in vitro* screening assay (Figure 2, Supplementary Figure S1). HepG2 cells were used to mimic hepatocytes, SkHep1 cells are derived from liver sinusoidal epithelial cells, and THP1 cells represent macrophages. All cell

Table 1
Size and size distribution of different PEG liposome formulations.

Liposome Modification (mol% PEG MW)	Optimized FRR	Size (nm)	PDI
3.0 PEG350	2.85	91.6	0.142
6.5 PEG350	2.88	88.5	0.141
10.0 PEG350	3.19	83.7	0.041
3.0 PEG750	2.49	94.4	0.148
6.5 PEG750	2.39	94.2	0.077
10.0 PEG750	3.06	87.4	0.032
3.0 PEG2000	2.88	80.6	0.024
6.5 PEG2000	1.82	85.8	0.100
10.0 PEG2000	1.82	87.8	0.072
3.0 PEG5000	1.88	87.6	0.095
6.5 PEG5000	1.98	97.9	0.045
10.0 PEG5000	2.01	107.2	0.061

Based on a full factorial Design-of-Experiment (Figure 1), liposomes with various PEG molecular weights (MW) and PEG densities (mol%) were prepared using microfluidics with optimized flow rate ratios (FRR) to achieve a uniform size independent of lipid composition. Hydrodynamic size in nm and polydispersity index (PDI) were determined by dynamic light scattering.

lines were incubated for 3 and 24 h with DiI labeled liposomes and analyzed by flow cytometry to determine the fraction of DiI positive (DiI^+) cells (surface binding and/or internalization) and mean fluorescence intensity (MFI). Thus, the degree liposome interactions with cells characterized by a phagocytic or enhanced endocytic potential could be determined. After 3 h of incubation, phagocytic macrophages (THP1) showed a remarkably high liposome cell interaction compared to hepatocytes (HepG2) and liver sinusoidal epithelial cells (SkHep1). Notably, cellular interactions of liposomes increased over time for all cell lines. At both time points (*i.e.* 3 h and 24 h of incubation), an increased PEG molecular weight and PEG density resulted in a decreased liposome clearance. Liposomes modified with 3 mol% PEG showed a higher clearance as compared to liposomes with 6.5 mol % or 10 mol% PEG. PEG5000 decreased liposome clearance more efficiently than smaller PEG molecular weights.

Influence of PEGylation on liposome clearance in the zebrafish model

To assess the general clearance mechanisms of liposomes in the zebrafish model, two different non-pegylated liposome formulations (DSPC:cholesterol, 60:40 mol% and POPC:cholesterol 55:45 mol%) were initially injected into transgenic zebrafish lines expressing a green fluorescent protein in its vasculature (Supplementary Figure S2). As reported previously, liposome formulations composed of the high transition temperature lipid DSPC were mainly cleared *via* a scavenger receptor mediated mechanism.[19,20] However, this strong staining pattern does not allow a parallel assessment of liposome accumulation in macrophages, since the two signals are overlapping. To overcome this issue, low transition temperature lipids (*i.e.* POPC) can be used, as shown by a liposome formulation based on the clinically approved Myocet. The Myocet-based formulation was not cleared *via* scavenger receptors but resulted in distinct localized accumulations in the vasculature. Further investigations demonstrated that macrophages, but not neutrophils, were responsible for this clearance (Supplementary Figure S3). An alternative approach to decrease scavenger receptor clearance is the modification of liposomes using PEG. Since PEGylation can be varied regarding its molecular weight and density, this offers interesting perspectives for a library screening and was therefore further investigated. To this end, PEGylated liposomes were injected into blood circulation of 2-day-old zebrafish using a micro-injector device (Figure 3, *A*). A representative confocal image of a living zebrafish for each liposome formulation 24 h post injection (hpi) is shown in Figure 3, *B*. Fluorescent signal of DiI labeled PEGylated liposomes in the caudal vein and the caudal hematopoietic tissue was heavily influenced by variations of PEG molecular weight and PEG density on the liposome surface. To facilitate data evaluation, zebrafish embryos were analyzed 24 hpi since the number of liposome accumulations (representing macrophage clearance) increased over time. Consistent with the *in vitro* data shown above, an increase of liposomes accumulation in the posterior caudal vein was observed for liposomes with lower PEG density and lower PEG molecular weight. Semi-quantitative visual scores for liposome accumulation indicate that PEG5000 reduced the systemic clearance twofold as compared to PEG350.

Influence of PEGylation on macrophage blood clearance in transgenic zebrafish

Liposomes with a low degree of PEGylation showed and extensive uptake into THP1 *in vitro* as well as a high degree of agglomeration, most probably in macrophages, in the initial zebrafish screening. In order to verify this hypothesis, fluorescent (*i.e.* DiI labeled) liposomes containing 6.5 mol% of each PEG molecular weight were injected into genetically modified zebrafish, expressing green fluorescent KAEDE protein in their macrophages. Liposome clearance by macrophages was assessed qualitatively and quantitatively by confocal laser scanning microscopy followed by a colocalization analysis. With decreasing PEG molecular weight, we observed an increased colocalization of liposomes with macrophages resulting in a yellow signal, *i.e.* clearance of red fluorescent liposomes by green fluorescent macrophages (Figure 4, Supplementary Figure S4). In addition to the qualitative analysis, macrophage uptake was quantified by calculating the overlap colocalization coefficient of KAEDE (*i.e.* macrophages) and DiI (*i.e.* PEGylated liposomes). Macrophage clearance of liposomes decreased with increasing PEG molecular weight at both 3 hpi and 24 hpi leading to statistically significant differences between low and high PEG molecular weight formulations.

Influence of liposome size on macrophage clearance in the zebrafish

After successfully demonstrating PEGylation effects in the presented zebrafish model, the additional influence of liposome size was investigated. Based on *in vitro* and zebrafish data, liposomes modified with PEG5000 showed very little macrophage clearance irrespective of the PEG density. Therefore, the smaller and clinically used PEG2000 was used and compared to PEG350 in further studies. Consequently, liposomes containing either 6.5 mol% PEG2000 or 6.5 mol% PEG350 with sizes of 60, 90, and 120 nm were prepared and injected into zebrafish. After 24 h, confocal laser scanning microscopy was used to assess the systemic clearance of

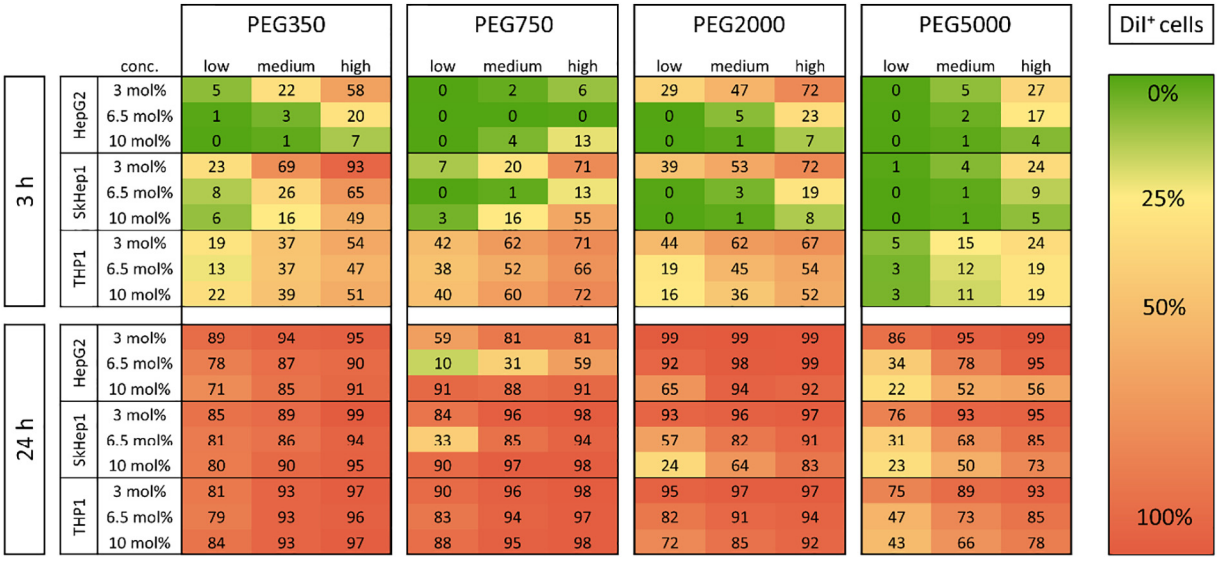

		conc.	PEG350 low	PEG350 medium	PEG350 high	PEG750 low	PEG750 medium	PEG750 high	PEG2000 low	PEG2000 medium	PEG2000 high	PEG5000 low	PEG5000 medium	PEG5000 high
3 h	HepG2	3 mol%	5	22	58	0	2	6	29	47	72	0	5	27
		6.5 mol%	1	3	20	0	0	0	0	5	23	0	2	17
		10 mol%	0	1	7	0	4	13	0	1	7	0	1	4
	SkHep1	3 mol%	23	69	93	7	20	71	39	53	72	1	4	24
		6.5 mol%	8	26	65	0	1	13	0	3	19	0	1	9
		10 mol%	6	16	49	3	16	55	0	1	8	0	1	5
	THP1	3 mol%	19	37	54	42	62	71	44	62	67	5	15	24
		6.5 mol%	13	37	47	38	52	66	19	45	54	3	12	19
		10 mol%	22	39	51	40	60	72	16	36	52	3	11	19
24 h	HepG2	3 mol%	89	94	95	59	81	81	99	99	99	86	95	99
		6.5 mol%	78	87	90	10	31	59	92	98	99	34	78	95
		10 mol%	71	85	91	91	88	91	65	94	92	22	52	56
	SkHep1	3 mol%	85	89	99	84	96	98	93	96	97	76	93	95
		6.5 mol%	81	86	94	33	85	94	57	82	91	31	68	85
		10 mol%	80	90	95	90	97	98	24	64	83	23	50	73
	THP1	3 mol%	81	93	97	90	96	98	95	97	97	75	89	93
		6.5 mol%	79	93	96	83	94	97	82	91	94	47	73	85
		10 mol%	84	93	97	88	95	98	72	85	92	43	66	78

Figure 2. *In vitro* clearance of liposomes with different PEG modification. Hepatocytes (HepG2), liver sinusoidal endothelial cells (SkHep1) and macrophages (THP1) were incubated with DiI labeled liposomes with a uniform size (Table 1). Different modifications (*i.e.* variation in PEG molecular weights and PEG densities) were tested for 3 and 24 h at different total lipid concentrations (50 mM: low, 100 mM: medium, and 200 mM: high). The percentage of DiI positive (DiI^+) cells is indicated and highlighted using a color code shown in the right panel from low clearance (green) to high clearance (red).

liposomes by macrophages (Figure 5, Supplementary Figure S5). As shown in Figure 5, PEG2000 modified liposomes showed a higher shielding effect as compared to PEG350 for all liposome sizes (*i.e.* normalized overlap coefficient always below 1 as compared to 90 nm sized PEG350 liposomes). Interestingly, PEG350 modified liposomes with a size above 90 nm showed a significantly higher macrophage clearance as compared to smaller liposomes. In sharp contrast, surface modification of liposomes using PEG2000 successfully decreased macrophage uptake of all liposomes independent of size. Even for liposomes with a size of 120 nm, no statistically significant difference in systemic macrophage clearance was observed. Thus, the zebrafish screening revealed a clear correlation between liposome size and PEG molecular weight on liposome shielding. Importantly, two groups have been identified by analyzing macrophage clearance: Liposomes with a size of 60-90 nm were shielded independent of PEG molecular weight whereas for liposomes with a size of 120 nm PEG2000 was needed to prevent macrophage clearance.

Influence of liposome size and PEGylation on splenic clearance in rats

To verify the combined influence of small changes in liposome size and PEGylation identified in the zebrafish model, a selection of two liposome sizes (70 nm *vs.* 120 nm) was injected into rats (Figure 6). Organ biodistribution was analyzed 24 hpi with a focus on clearance by the spleen, which contains a large number of tissue-resident macrophages.[42] As observed during our zebrafish experiments, liposome size strongly correlated with macrophage clearance (high accumulation in spleen). Systemic splenic clearance of 70 nm liposomes was low and increased PEG molecular weight (*i.e.* 6.5 mol% PEG2000) did not result in a beneficial *in vitro* biodistribution. Liposomes with an average size of 120 nm showed increased accumulation in the spleen. In contrast to small liposomes, surface modification of liposomes using PEG2000 was almost twice as effective in shielding as compared to PEG350.

Discussion

The physicochemical properties of nanomedicines such as size and surface charge heavily influence their pharmacokinetics and biodistribution. Thus, strategies to optimize these nanoparticle attributes and a valid prediction of these characteristics early in development under realistic biological conditions could increase the poor translation of promising preclinical results into effective therapeutics. Liposomes are the most advanced nanomedicines and well established in clinics[43] and can therefore be used to establish quantitative relationships between physicochemical characteristics and behavior *in vivo*.[44] Indeed, it was shown that varying particle size or single components can potentially affect the circulation properties of the final formulation.[19,45] Considering that advanced liposomal formulations can easily contain five or more (lipid) components as well as novel designed components such as PEG alternatives, optimization of these parameters remains complex. Therefore, nano-bio interactions should be investigated under dynamic conditions (*i.e.* blood flow and shear stress) in presence of plasma proteins including apolipoproteins or complement factors,[46,47] which are known to strongly influence interactions of liposomes with macrophages. To this end, Chang et al already introduced adult zebrafish as an animal model to study nanoparticle biodistribution prior to rodent *in vivo* studies. Nanoparticles prepared from different materials (*i.e.* polystyrene, titanium dioxide, dextran-sulfate, hyaluronic acid, and chitosan) were assessed and a high correlation between *in vitro* macrophage uptake and adult zebrafish liver accumulation was found.[48] Whereas adult zebrafish allow analysis of nanoparticle biodistribution and interaction with fully

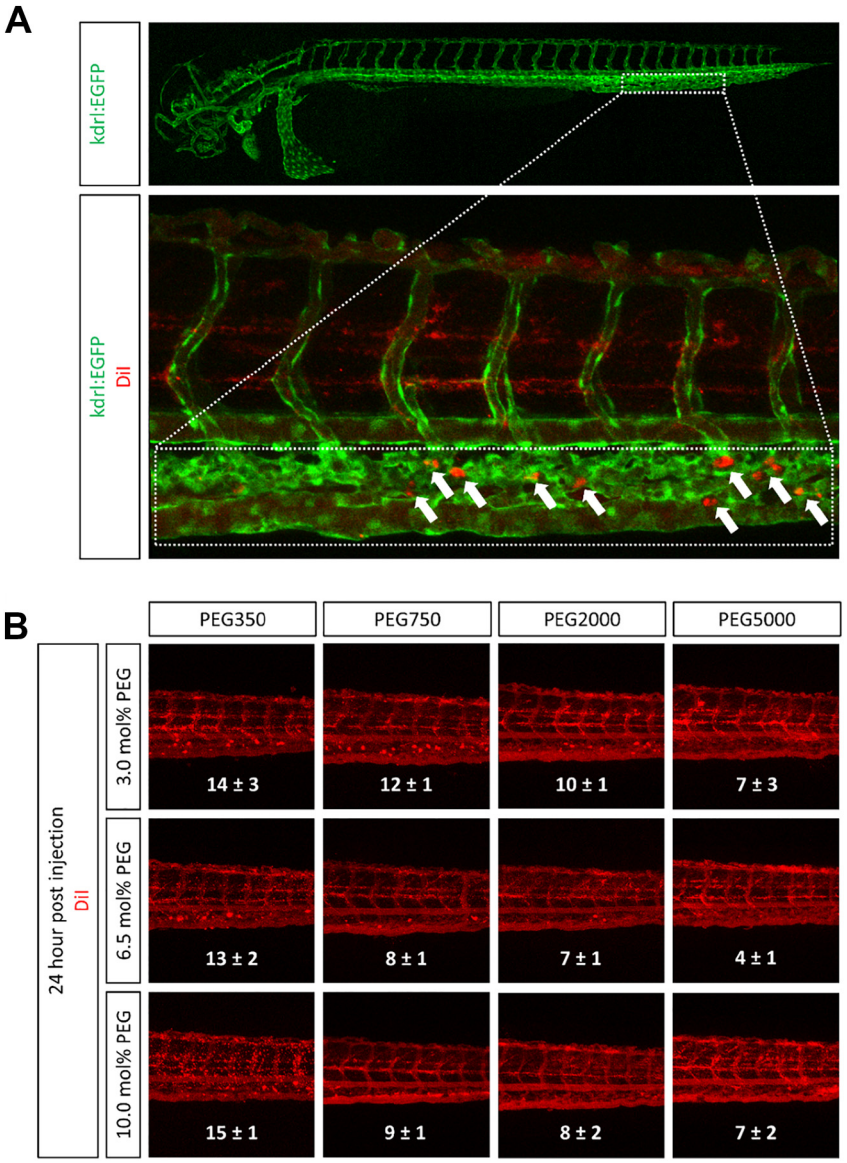

Figure 3. Influence of PEG modification on liposome accumulation in the zebrafish. DiI labeled Liposomes with various PEG molecular weights and PEG densities were injected into blood circulation of zebrafish 2 days post fertilization. (**A**) The indicated area (dotted box) of injected zebrafish representing part of the caudal vein and the caudal hematopoietic tissue was analyzed for liposome accumulates (white arrows) 24 h post injection. (**B**) Representative confocal images of the tail region for each liposome formulation are shown. The number of red dots (*i.e.* liposome accumulates) in the caudal vein was counted and is represented as mean ± SEM (n = 3).

matured organs, this approach is not applicable for screening. However, zebrafish embryos are easily available in large numbers and offer the possibility for spatio-temporal fluorescence imaging due to their optical transparency in combination with various transgenic fluorescent reporter lines. Altogether, we have therefore evaluated the potential of zebrafish embryos to serve as a vertebrate screening tool to optimize particulate drug formulations *in vivo*.[19] It was thus the primary goal of the present study to extend the use of the zebrafish model and to demonstrate that not only the systemic circulation but as well clearance of nanoparticles by macrophages can be evaluated by this tool and predicted for higher animals. A prerequisite for the present study was the availability of PEGylated liposomal formulations with a defined composition and precisely controlled size distribution as a reference system. As shown previously, PEG-lipids preferentially deposit on the liposome surface thereby increasing its relative polarity. The larger the molecular weight or molar ratio of PEG-lipids is, the smaller the resulting liposomes (*i.e.* PEG-lipid dictated liposome size).[49,50] Therefore, a systematic optimization of the scalable microfluidics technology using a DoE approach was used. Compared to extrusion trough filter membranes, where only a limited number of filter pore sizes are available, the microfluidics approach allowed a precise control of liposome size and PDI (independent of PEG modification) for the screening process. In agreement with previous studies, the flow rate ratio (FRR) of ethanolic lipid solution and aqueous buffer was thereby identified to determine liposome size.[28,51] This

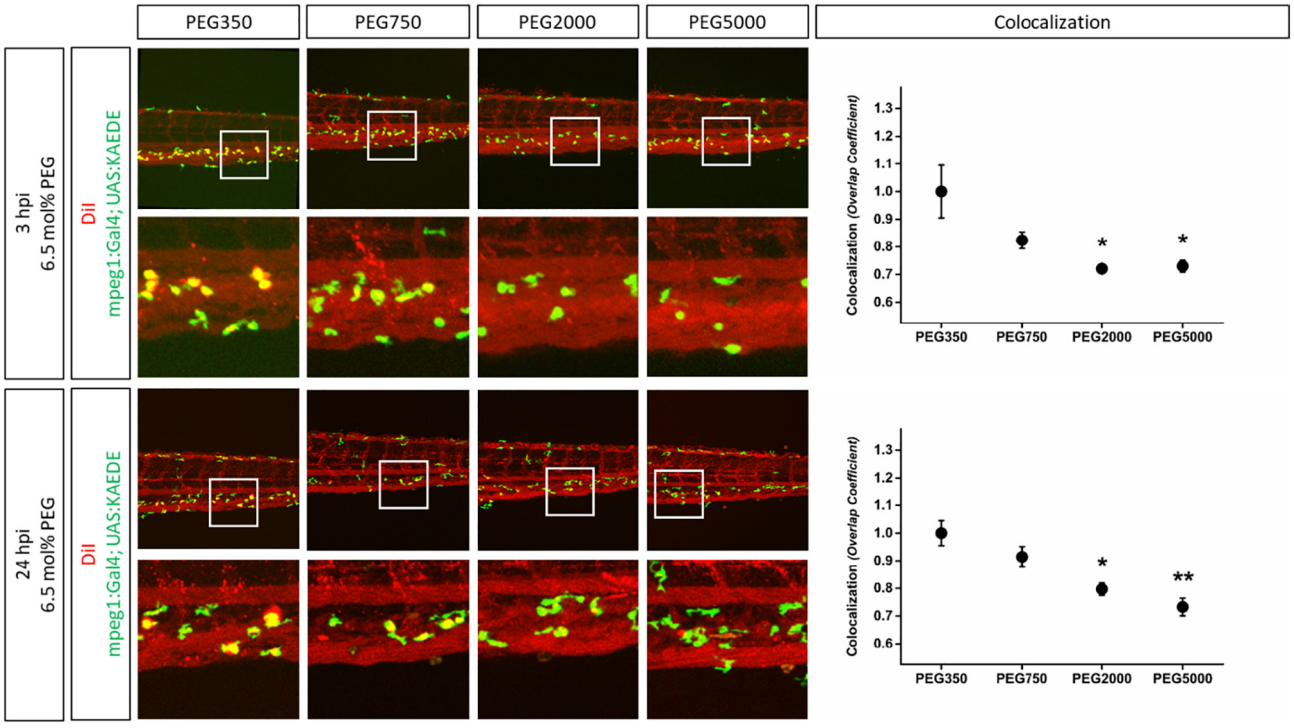

Figure 4. Influence of PEG modifications on macrophage clearance in transgenic zebrafish. DiI labeled liposomes modified with the indicated PEG molecular weights were injected into the blood circulation of zebrafish 2 days post fertilization. Confocal images were acquired 3 and 24 h post injection (hpi). Colocalization analysis of green fluorescent macrophages (KAEDE) and DiI labeled liposomes was performed based on normalized overlap colocalization coefficients. Values are means ± SEM, n = 3. *$P < 0.1$ or **$P < 0.05$ (multiple comparison using ANOVA assuming equal variance and Bonferroni correction) as compared to 90 nm sized PEG350 liposomes.

controlled manufacturing strategy enables to vary single characteristics of liposomal formulations (*e.g.* PEG molecular weight) while others remain constant (*e.g.* size).

Fluorescent labeling of the liposomes (*i.e.* lipophilic cationic indocarbocyanine dyes) or incorporation of a metal chelator (*i.e.* DSPE-DTPA needed for ^{111}In labeling) impaired neither size nor their storage stability. The latter observation is confirmed by studies, which demonstrated excellent *in vivo* properties of DSPE-DTPA liposomes.[29,52] It should be noted that active loading of liposomes with [^{3}H]doxorubicin using a pH- or ion-gradient did induce changes in liposome size, especially pronounced when small liposomes with a diameter below 90 nm were loaded. Consequently, protocols established previously by our team for systemic pharmacokinetics and tissue distribution studies[53] could not be used for the present study to evaluate the effect of small differences in liposome size on systemic clearance.

The traditional pattern of organization to screen interactions of nanoparticulate formulations with biological systems starts with *in vitro* experiments with cultured cells and progresses to investigations *in vivo* in rodents.[54] For *in vitro* experiments, nanoparticle uptake by cultured cells is analyzed mostly under static conditions. This experimental set-up allows a first characterization of nanoparticle interactions with living cells in a fast and controlled way. However, it has been shown that presence of plasma proteins[55] as well as dynamics of fluids and resulting shear stress[56,57] heavily influences the interaction of nanoparticle with cells, *e.g.* by altering the protein corona. Based on the design of the *in vitro* system, aggregation and subsequent sedimentation of liposomes can heavily influence cellular uptake results.[58] Our flow cytometry analysis revealed the highest clearance rate (number of DiI labeled liposome positive cells) for differentiated phagocytic THP1 cells, followed by liver sinusoidal endothelial cells (SkHep1) and hepatocytes (HepG2). This can be explained by the phagocytic nature of THP1 cells and high endocytic activity of SkHep1 cells.[59] Experiments performed after 24 h showed no or only minor differences between cell lines and liposomal formulations, probably due to saturation of liposome uptake and due to static cell culture conditions. Furthermore, liposomes containing PEG2000 showed a higher degree of interactions with different cells as compared to liposomes modified with PEG750. Similar phenomena have already been described previously and were linked to altered protein binding resulting in differences in the protein corona during *in vitro* assays.[60] Notably, flow cytometry analysis does not allow to clearly distinguish between liposomes which were internalized or simply bound to the cell surface. However, tedious washing steps and trypsinization of cells at the end of the uptake experiment decrease the amount of cell surface bound liposomes. In addition, reporting the number of DiI positive cells instead of the MFI can partially overcome this issue. Nevertheless, an additional liposome uptake study by confocal microscopy including a cell membrane staining would be required to completely answer such a question. This example demonstrates that a full and systematic assessment of nanoparticle uptake *in vitro* using different cell types is time-consuming and not suitable for a rapid screening process.

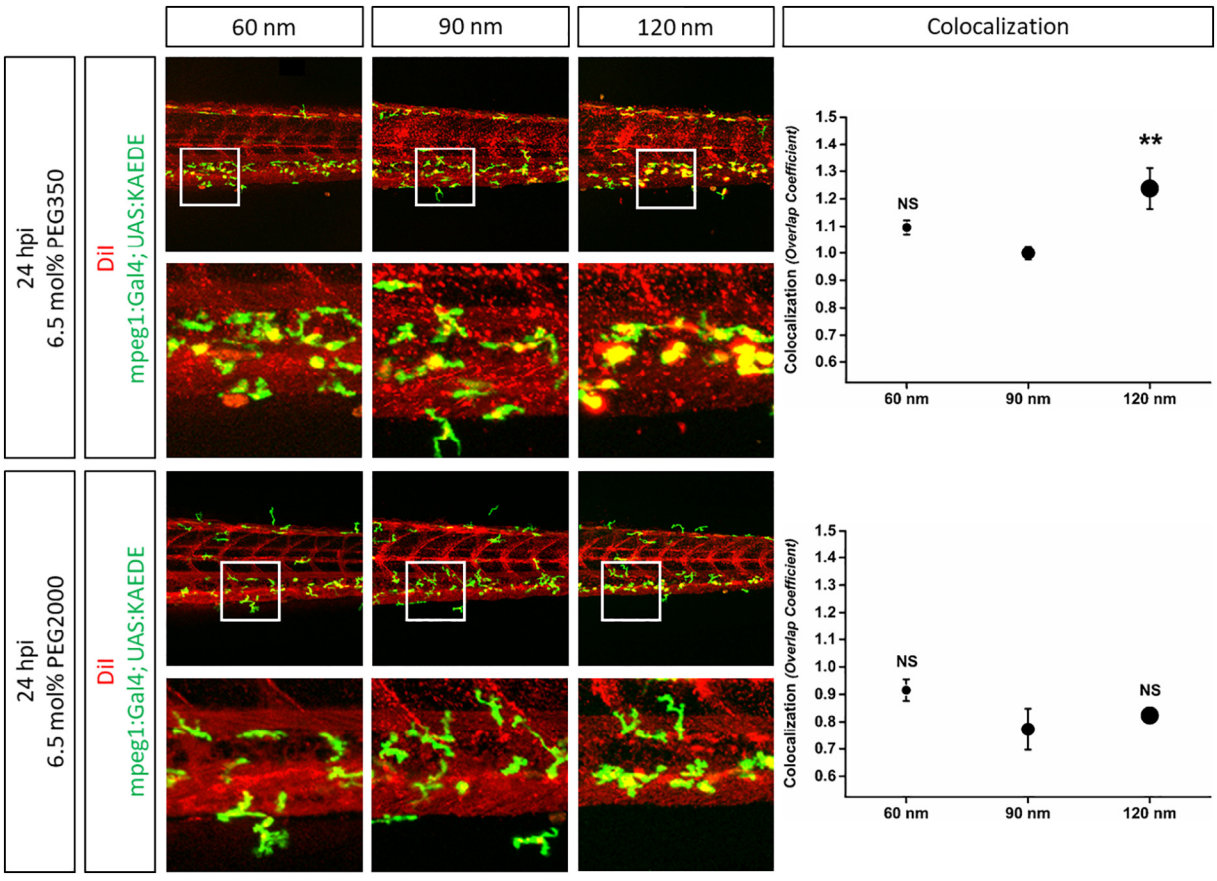

Figure 5. Influence of liposome size and different PEG modification on macrophage clearance in zebrafish. PEG350 or PEG2000 modified and DiI labeled liposomes with three different sizes (60 nm, 90 nm, and 120 nm) were injected into the blood circulation of zebrafish 2 days post fertilization. Confocal images were acquired 24 h post injection (hpi). Colocalization of green fluorescent macrophages (KAEDE) and DiI labeled liposomes was quantitated using normalized overlap colocalization coefficients. Values are means ± SEM, n = 5. not significant (NS) or $^{**}P < 0.05$ (ANOVA and Bonferroni correction) as compared to 90 nm sized liposomes.

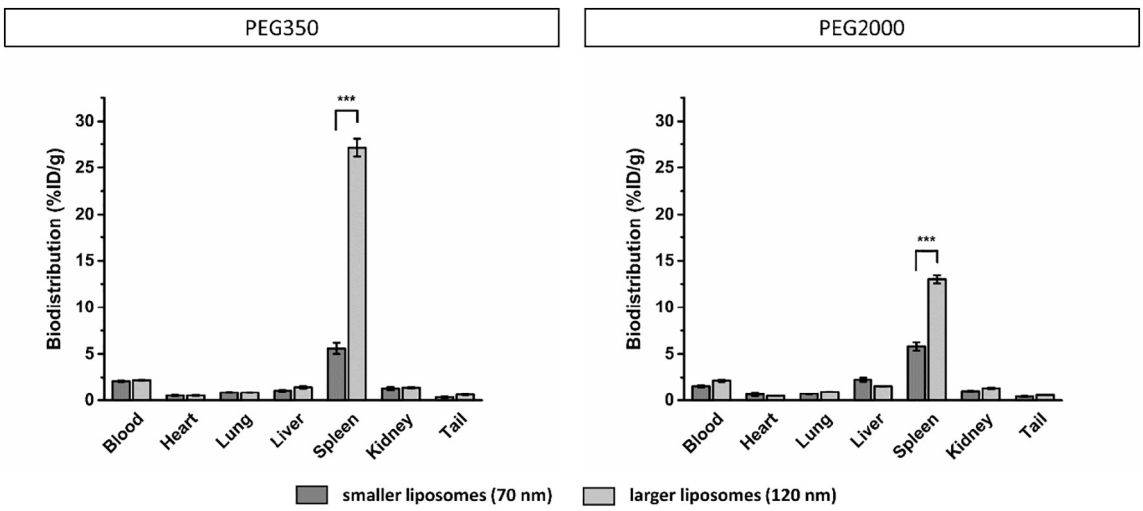

Figure 6. Influence of PEG modification and liposome size on splenic clearance in rats. ^{111}In labeled liposomes with 6.5 mol% of PEG350 or PEG2000 were injected into blood circulation of rats *via* the tail vein. Two size groups of liposomes, *i.e.* smaller liposomes (70 nm) and larger liposomes (120 nm), of each PEG molecular weight were tested. Organ distribution of radiolabeled liposomes 24 h post injection is shown. Values are means ± SEM, n = 3. $^{***}P < 0.001$ (ANOVA and Bonferroni correction).

In order to overcome shortcomings of static *in vitro* experiments, we injected the same lipid formulations into 2 day old zebrafish and analyzed liposome blood circulation behavior *in vivo* by live confocal imaging. This enables an assessment of PEG molecular weight and PEG density under *in vivo* conditions in a cost-effective and time-efficient manner. Analysis of nanoparticle biodistribution in zebrafish was facilitated using transgenic lines expressing fluorescent proteins in vasculature or macrophages. Increasing PEG molecular weights and densities efficiently decreased liposome clearance by macrophages as shown by semi-quantitative image analysis (*i.e.* colocalization studies). Interestingly, the high cellular uptake *in vitro* of PEG2000 liposomes was not observed in zebrafish experiments. In zebrafish embryos, phagocytosis by macrophages was reduced with increasing PEG chain length and PEG density (as known from numerous *in vivo* studies in higher vertebrates including human), underlining the importance of studying such phenomena under dynamic conditions *in vivo*. Encouraged by these results, the proposed zebrafish model was further validated regarding its ability to resolve small formulation differences such as size variations in the range of 30 nm. To this end, liposomes with a size of 60, 90, and 120 nm and modified with either PEG350 or PEG2000 were compared. Smaller liposomes with a medium PEG density (*i.e.* 6.5 mol%) and a size of 60 and 90 nm showed a decreased macrophage uptake as compared to their larger counterparts with a size of 120 nm. Interestingly, increasing the PEG molecular weight from 350 to 2000 Da was sufficient to mask this size dependent phenomenon.

To validate these findings and to analyze whether the data acquired in zebrafish embryos are predictive for rodents, we performed control experiments in rats. Previous studies in rodents have already shown high clearance rates for non- and low-PEGylated liposomes by the MPS which reached a plateau at 24 hpi.[33,61,62] Consequently, the experimental set-up was chosen accordingly to reduce the number of needed rats. Non-PEGylated liposomes were excluded from the study due to rapid clearance and organ biodistribution was analyzed 24 hpi. Liposomes with a size below and above the cut-off for macrophage uptake observed in zebrafish (*i.e.* 70 and 120 nm) modified with either 6.5 mol% of PEG350 or PEG2000 were radiolabeled with ^{111}In and injected intravenously. Biodistribution of liposomes was analyzed with a special focus on accumulation of liposomes in the spleen. This organ is ideally suited to study cellular clearance of particles (such as microorganisms but also nanoparticles) by macrophages due to its high blood filtration capacity, specific anatomical features and a high concentration of adapted macrophages.[26,42] Indeed, as shown in Figure 6, uptake in terms of %ID/g tissue was maximal for this organ. Liver tissue was not analyzed because this tissue consists of several cell types able to clear liposomes from blood circulation, *i.e.* parenchymal (*i.e.*, hepatocytes, 70%-80% of all liver cells)[63] and non-parenchymal liver cells including sinusoidal endothelial cells (LSEC, 10%-20%)[59] and hepatic macrophages (Kupffer cells, 10%-15% of the total liver cell population).[64] In fact, a recent publication by our team emphasized the cellular sequestration of nanoparticles by liver sinusoidal endothelial cells *via* the Stabilin-2 scavenger receptor.[20] These factors limit the reliable assessment of nanomedicine clearance by liver-resident macrophages (*i.e.* Kupffer cells). Thus, further studies are warranted focusing on the contribution of different liver cell types towards the clearance of nanomedicines. As demonstrated in zebrafish, liposome size was an important determinant for phagocytosis and modification of liposomes with high molecular weight PEG (*i.e.* PEG2000) was able to shield 120 nm liposomes and decrease macrophage uptake in the spleen. Thus, analysis of liposome clearance by macrophages in the zebrafish showed a high correlation with accumulation of liposomes in the spleen when injected intravenously in rats.

The development of nanomedicines from the preclinical situation to the human application is a time-consuming and challenging process, especially if novel nanomedicine components have to be tested. Thus, new strategies are needed to select promising nanoformulations and optimize their characteristics early in drug development. In this study, the zebrafish was successfully used and validated to assess macrophage clearance of nanoparticles using PEGylated liposomes as a reference system. Data obtained in zebrafish experiments correlated with *in vivo* experiments in rodents. Importantly, the zebrafish may serve as a bridging tool to mimic the complex situation *in vivo* with the advantage to screen a large number of nanoparticle samples in a time- and cost-effective manner. As a consequence, the presented zebrafish model could also be used for the optimization of nanomedicine-based therapies which take advantage of macrophage uptake (*i.e.* cancer, inflammation, infections). Notably, not all pharmacokinetic parameters such as metabolism or renal filtration can be assessed in zebrafish embryos. However, this vertebrate screening model has the potential to reduce the number of formulations needed to be tested in mammals and to serve as a predictive *in vivo* tool in early phases of the nanomedicine development process.

Appendix A. Supplementary data

Supplementary data to this article can be found online at https://doi.org/10.1016/j.nano.2018.11.017.

References

1. Binnemars-Postma KA, ten Hoopen HW, Storm G, Prakash J. Differential uptake of nanoparticles by human M1 and M2 polarized macrophages: protein corona as a critical determinant. *Nanomedicine* 2016;**11**:2889-902, https://doi.org/10.2217/nnm-2016-0233.
2. Jain S, Tran T-H, Amiji M. Macrophage repolarization with targeted alginate nanoparticles containing IL-10 plasmid DNA for the treatment of experimental arthritis. *Biomaterials* 2015;**61**:162-77, https://doi.org/10.1016/j.biomaterials.2015.05.028.
3. Fuchs A-K, Syrovets T, Haas KA, Loos C, Musyanovych A, Mailänder V, et al. Carboxyl- and amino-functionalized polystyrene nanoparticles differentially affect the polarization profile of M1 and M2 macrophage subsets. *Biomaterials* 2016;**85**:78-87, https://doi.org/10.1016/j.biomaterials.2016.01.064.
4. Fenaroli F, Westmoreland D, Benjaminsen J, Kolstad T, Skjeldal FM, Meijer AH, et al. Nanoparticles as drug delivery system against tuberculosis in zebrafish embryos: direct visualization and treatment. *ACS Nano* 2014;**8**:7014-26, https://doi.org/10.1021/nn5019126.
5. Fenaroli F, Repnik U, Xu Y, Johann K, Van Herck S, Dey P, et al. Enhanced permeability and retention-like extravasation of nanoparticles from the vasculature into tuberculosis granulomas in zebrafish and

mouse models. *ACS Nano* 2018;**12**:8646-61, https://doi.org/10.1021/acsnano.8b04433.
6. Duan X, Li Y. Physicochemical characteristics of nanoparticles affect circulation, biodistribution, cellular internalization, and trafficking. *Small* 2013;**9**:1521-32, https://doi.org/10.1002/smll.201201390.
7. Allen TM, Cullis PR. Liposomal drug delivery systems: from concept to clinical applications. *Adv Drug Deliv Rev* 2013;**65**:36-48, https://doi.org/10.1016/j.addr.2012.09.037.
8. Klibanov AL, Maruyama K, Beckerleg AM, Torchilin VP, Huang L. Activity of amphipathic poly(ethylene glycol) 5000 to prolong the circulation time of liposomes depends on the liposome size and is unfavorable for immunoliposome binding to target. *Biochim Biophys Acta* 1991;**1062**:142-8.
9. Litzinger DC, Buiting AM, van Rooijen N, Huang L. Effect of liposome size on the circulation time and intraorgan distribution of amphipathic poly(ethylene glycol)-containing liposomes. *Biochim Biophys Acta* 1994;**1190**:99-107.
10. Romberg B, Oussoren C, Snel CJ, Hennink WE, Storm G. Effect of liposome characteristics and dose on the pharmacokinetics of liposomes coated with poly(amino acid)s. *Pharm Res* 2007;**24**:2394-401, https://doi.org/10.1007/s11095-007-9393-2.
11. Moghimi SM, Hunter AC, Andresen TL. Factors controlling nanoparticle pharmacokinetics: an integrated analysis and perspective. *Annu Rev Pharmacol Toxicol* 2012;**52**:481-503, https://doi.org/10.1146/annurev-pharmtox-010611-134623.
12. Decuzzi P, Godin B, Tanaka T, Lee S-Y, Chiappini C, Liu X, et al. Size and shape effects in the biodistribution of intravascularly injected particles. *J Control Release* 2010;**141**:320-7, https://doi.org/10.1016/j.jconrel.2009.10.014.
13. Li S-D, Huang L. Pharmacokinetics and biodistribution of nanoparticles. *Mol Pharm* 2008;**5**:496-504, https://doi.org/10.1021/mp800049w.
14. Hoshyar N, Gray S, Han H, Bao G. The effect of nanoparticle size on in vivo pharmacokinetics and cellular interaction. *Nanomedicine* 2016;**11**:673-92, https://doi.org/10.2217/nnm.16.5.
15. Kierstead PH, Okochi H, Venditto VJ, Chuong TC, Kivimae S, Fréchet JMJ, et al. The effect of polymer backbone chemistry on the induction of the accelerated blood clearance in polymer modified liposomes. *J Control Release* 2015;**213**:1-9, https://doi.org/10.1016/j.jconrel.2015.06.023.
16. Weber B, Seidl C, Schwiertz D, Scherer M, Bleher S, Süss R, et al. Polysarcosine-based lipids: from lipopolypeptoid micelles to stealth-like lipids in Langmuir Blodgett monolayers. *Polymers* 2016;**8**:427, https://doi.org/10.3390/polym8120427.
17. Fritz T, Hirsch M, Richter FC, Müller SS, Hofmann AM, Rusitzka KAK, et al. Click modification of multifunctional liposomes bearing hyperbranched polyether chains. *Biomacromolecules* 2014;**15**:2440-8, https://doi.org/10.1021/bm5003027.
18. Abu Lila AS, Nawata K, Shimizu T, Ishida T, Kiwada H. Use of polyglycerol (PG), instead of polyethylene glycol (PEG), prevents induction of the accelerated blood clearance phenomenon against long-circulating liposomes upon repeated administration. *Int J Pharm* 2013;**456**:235-42, https://doi.org/10.1016/j.ijpharm.2013.07.059.
19. Sieber S, Grossen P, Detampel P, Siegfried S, Witzigmann D, Huwyler J. Zebrafish as an early stage screening tool to study the systemic circulation of nanoparticulate drug delivery systems in vivo. *J Control Release* 2017;**264**:180-91, https://doi.org/10.1016/j.jconrel.2017.08.023.
20. Campbell F, Bos FL, Sieber S, Arias-Alpizar G, Koch BE, Huwyler J, et al. Directing nanoparticle biodistribution through evasion and exploitation of Stab2-dependent nanoparticle uptake. *ACS Nano* 2018, https://doi.org/10.1021/acsnano.7b06995.
21. Evensen L, Johansen PL, Koster G, Zhu K, Herfindal L, Speth M, et al. Zebrafish as a model system for characterization of nanoparticles against cancer. *Nanoscale* 2016;**8**:862-77, https://doi.org/10.1039/c5nr07289a.
22. Meeker ND, Trede NS. Immunology and zebrafish: spawning new models of human disease. *Dev Comp Immunol* 2008;**32**:745-57, https://doi.org/10.1016/j.dci.2007.11.011.
23. Herbomel P, Thisse B, Thisse C. Ontogeny and behaviour of early macrophages in the zebrafish embryo. *Development* 1999;**126**:3735-45.
24. Wittamer V, Bertrand JY, Gutschow PW, Traver D. Characterization of the mononuclear phagocyte system in zebrafish. *Blood* 2011;**117**:7126-35, https://doi.org/10.1182/blood-2010-11-321448.
25. Nguyen-Chi M, Laplace-Builhe B, Travnickova J, Luz-Crawford P, Tejedor G, Phan QT, et al. Identification of polarized macrophage subsets in zebrafish. *Elife* 2015;**4**e07288, https://doi.org/10.7554/eLife.07288.
26. Mebius RE, Kraal G. Structure and function of the spleen. *Nat Rev Immunol* 2005;**5**:606-16, https://doi.org/10.1038/nri1669.
27. Kastner E, Verma V, Lowry D, Perrie Y. Microfluidic-controlled manufacture of liposomes for the solubilisation of a poorly water soluble drug. *Int J Pharm* 2015;**485**:122-30, https://doi.org/10.1016/j.ijpharm.2015.02.063.
28. Sedighi M, Sieber S, Rahimi F, Shahbazi M-A, Rezayan AH, Huwyler J, et al. *Rapid optimization of liposome characteristics using a combined microfluidics and design-of-experiment approach*; 2019, https://doi.org/10.1007/s13346-018-0587-4.
29. van der Geest T, Laverman P, Gerrits D, Franssen GM, Metselaar JM, Storm G, et al. Comparison of three remote radiolabelling methods for long-circulating liposomes. *J Control Release* 2015;**220**:239-44, https://doi.org/10.1016/j.jconrel.2015.10.043.
30. Witzigmann D, Sieber S, Porta F, Grossen P, Bieri A, Strelnikova N, et al. Formation of lipid and polymer based gold nanohybrids using a nanoreactor approach. *RSC Adv* 2015;**5**:74320-8, https://doi.org/10.1039/C5RA13967H.
31. Witzigmann D, Quagliata L, Schenk SH, Quintavalle C, Terracciano LM, Huwyler J. Variable asialoglycoprotein receptor 1 expression in liver disease: implications for therapeutic intervention. *Hepatol Res* 2016;**46**:686-96, https://doi.org/10.1111/hepr.12599.
32. Kettiger H, Sen Karaman D, Schiesser L, Rosenholm JM, Huwyler J. Comparative safety evaluation of silica-based particles. *Toxicol In Vitro* 2015;**30**:355-63, https://doi.org/10.1016/j.tiv.2015.09.030.
33. Detampel P, Witzigmann D, Krähenbühl S, Huwyler J. Hepatocyte targeting using pegylated asialofetuin-conjugated liposomes. *J Drug Target* 2013, https://doi.org/10.3109/1061186X.2013.860982.
34. Grossen P, Québatte G, Witzigmann D, Prescianotto-Baschong C, Dieu L-H, Huwyler J. Functionalized solid-sphere PEG-b-PCL nanoparticles to target brain capillary endothelial cells in vitro. *J Nanomater* 2016, https://doi.org/10.1155/2016/7818501.
35. Jin S-W, Beis D, Mitchell T, Chen J-N, Stainier DYR. Cellular and molecular analyses of vascular tube and lumen formation in zebrafish. *Development* 2005;**132**:5199-209, https://doi.org/10.1242/dev.02087.
36. Ellett F, Pase L, Hayman JW, Andrianopoulos A, Lieschke GJ. mpeg1 promoter transgenes direct macrophage-lineage expression in zebrafish. *Blood* 2011;**117**:e49-56, https://doi.org/10.1182/blood-2010-10-314120.
37. Scott EK, Mason L, Arrenberg AB, Ziv L, Gosse NJ, Xiao T, et al. Targeting neural circuitry in zebrafish using GAL4 enhancer trapping. *Nat Methods* 2007;**4**:323-6, https://doi.org/10.1038/nmeth1033.
38. Sieber S, Siegrist S, Schwarz S, Porta F, Schenk SH, Huwyler J. Immobilization of enzymes on PLGA sub-micrometer particles by cross-linked layer-by-layer deposition. *Macromol Biosci* 2017;**17**, https://doi.org/10.1002/mabi.201700015.
39. Weinstein BM, Stemple DL, Driever W, Fishman MC. Gridlock, a localized heritable vascular patterning defect in the zebrafish. *Nat Med* 1995;**1**:1143-7.
40. Bolte S, Cordelières FP. A guided tour into subcellular colocalization analysis in light microscopy. *J Microsc* 2006;**224**:213-32, https://doi.org/10.1111/j.1365-2818.2006.01706.x.
41. Manders EM, Stap J, Brakenhoff GJ, van Driel R, Aten JA. Dynamics of three-dimensional replication patterns during the S-phase, analysed by double labelling of DNA and confocal microscopy. *J Cell Sci* 1992;**103** (Pt 3):857-62.
42. Moghimi SM. Mechanisms of splenic clearance of blood cells and particles: towards development of new splenotropic agents. *Adv Drug Deliv Rev* 1995;**17**:103-15, https://doi.org/10.1016/0169-409X(95)00043-7.

43. Wicki A, Witzigmann D, Balasubramanian V, Huwyler J. Nanomedicine in cancer therapy: challenges, opportunities, and clinical applications. *J Control Release* 2015;**200**:138-57, https://doi.org/10.1016/j.jconrel.2014.12.030.
44. Barenholz Y. Doxil®—the first FDA-approved nano-drug: lessons learned. *J Control Release* 2012;**160**:117-34, https://doi.org/10.1016/j.jconrel.2012.03.020.
45. Kettiger H, Schipanski A, Wick P, Huwyler J. Engineered nanomaterial uptake and tissue distribution: from cell to organism. *Int J Nanomedicine* 2013;**8**:3255-69, https://doi.org/10.2147/IJN.S49770.
46. Otis JP, Zeituni EM, Thierer JH, Anderson JL, Brown AC, Boehm ED, et al. Zebrafish as a model for apolipoprotein biology: comprehensive expression analysis and a role for ApoA-IV in regulating food intake. *Dis Model Mech* 2015;**8**:295-309, https://doi.org/10.1242/dmm.018754.
47. Zhang S, Cui P. Complement system in zebrafish. *Dev Comp Immunol* 2014;**46**:3-10, https://doi.org/10.1016/j.dci.2014.01.010.
48. Chang H, Yhee JY, Jang GH, You DG, Ryu JH, Choi Y, et al. Predicting the in vivo accumulation of nanoparticles in tumor based on in vitro macrophage uptake and circulation in zebrafish. *J Control Release* 2016;**244**:205-13, https://doi.org/10.1016/j.jconrel.2016.07.025.
49. Belliveau NM, Huft J, Lin PJ, Chen S, Leung AK, Leaver TJ, et al. Microfluidic synthesis of highly potent limit-size lipid nanoparticles for in vivo delivery of siRNA. *Mol Ther Nucleic Acids* 2012;**1**e37, https://doi.org/10.1038/mtna.2012.28.
50. Chen S, Tam YYC, Lin PJC, Sung MMH, Tam YK, Cullis PR. Influence of particle size on the in vivo potency of lipid nanoparticle formulations of siRNA. *J Control Release* 2016;**235**:236-44, https://doi.org/10.1016/j.jconrel.2016.05.059.
51. Carugo D, Bottaro E, Owen J, Stride E, Nastruzzi C. Liposome production by microfluidics: potential and limiting factors. *Sci Rep* 2016;**6**srep25876, https://doi.org/10.1038/srep25876.
52. van der Geest T, Laverman P, Metselaar J, Boerman O. In vitro and in vivo properties of radiolabeled DSPE-DTPA liposomes. *J Nucl Med* 2015;**56**:1689.
53. Huwyler J, Yang J, Pardridge WM. Receptor mediated delivery of daunomycin using immunoliposomes: pharmacokinetics and tissue distribution in the rat. *J Pharmacol Exp Ther* 1997;**282**:1541-6.
54. Mitragotri S, Lammers T, Bae YH, Schwendeman S, De Smedt S, Leroux J-C, et al. Drug delivery research for the future: expanding the nano horizons and beyond. *J Control Release* 2017;**246**:183-4, https://doi.org/10.1016/j.jconrel.2017.01.011.
55. Ritz S, Schöttler S, Kotman N, Baier G, Musyanovych A, Kuharev J, et al. Protein corona of nanoparticles: distinct proteins regulate the cellular uptake. *Biomacromolecules* 2015;**16**:1311-21, https://doi.org/10.1021/acs.biomac.5b00108.
56. Caracciolo G, Farokhzad OC, Mahmoudi M. Biological identity of nanoparticles in vivo: clinical implications of the protein corona. *Trends Biotechnol* 2017;**35**:257-64, https://doi.org/10.1016/j.tibtech.2016.08.011.
57. Goodman TT, Ng CP, Pun SH. 3-D tissue culture systems for the evaluation and optimization of nanoparticle-based drug carriers. *Bioconjug Chem* 2008;**19**:1951-9, https://doi.org/10.1021/bc800233a.
58. Behzadi S, Serpooshan V, Tao W, Hamaly MA, Alkawareek MY, Dreaden EC, et al. Cellular uptake of nanoparticles: journey inside the cell. *Chem Soc Rev* 2017;**46**:4218-44, https://doi.org/10.1039/c6cs00636a.
59. Poisson J, Lemoinne S, Boulanger C, Durand F, Moreau R, Valla D, et al. Liver sinusoidal endothelial cells: physiology and role in liver diseases. *J Hepatol* 2017;**66**:212-27, https://doi.org/10.1016/j.jhep.2016.07.009.
60. Pozzi D, Colapicchioni V, Caracciolo G, Piovesana S, Capriotti AL, Palchetti S, et al. Effect of polyethyleneglycol (PEG) chain length on the bio-nano-interactions between PEGylated lipid nanoparticles and biological fluids: from nanostructure to uptake in cancer cells. *Nanoscale* 2014;**6**:2782-92, https://doi.org/10.1039/c3nr05559k.
61. van Rooijen N, Hendrikx E. Liposomes for specific depletion of macrophages from organs and tissues. *Methods Mol Biol* 2010;**605**:189-203, https://doi.org/10.1007/978-1-60327-360-2_13.
62. Samuelsson E, Shen H, Blanco E, Ferrari M, Wolfram J. Contribution of Kupffer cells to liposome accumulation in the liver. *Colloids Surf B Biointerfaces* 2017;**158**:356-62, https://doi.org/10.1016/j.colsurfb.2017.07.014.
63. Poelstra K, Prakash J, Beljaars L. Drug targeting to the diseased liver. *J Control Release* 2012;**161**:188-97, https://doi.org/10.1016/j.jconrel.2012.02.011.
64. Kolios G, Valatas V, Kouroumalis E. Role of Kupffer cells in the pathogenesis of liver disease. *World J Gastroenterol* 2006;**12**:7413-20.

Chapter II-II

Zebrafish as an early stage screening tool to study the systemic circulation of nanoparticulate drug delivery system in vivo

Sandro Sieber, Philip Grossen, Pascal Detampel, Salome Siegfried, Dominik Witzigmann, Jörg Huwyler

Manuscript: Journal of Controlled Release (2017) [41]

Highlights: Liposomes are the clinically most successful form of nanomedicines and therefore well characterized. However, liposomes can be composed of various lipids and different amounts of cholesterol, both influencing their pharmacokinetic behavior *in vivo*. In this study, different liposome formulations with reported pharmacokinetics in rodents were injected into the blood circulation of zebrafish embryos and investigated regarding their circulation and extravasation behavior. Qualitative and semi-quantitative zebrafish findings were evaluated and linked to known pharmacokinetic properties in rodents (i.e. long versus short circulating). Finally, the predictive power of the presented zebrafish model was demonstrated by assessing the so far unknown pharmacokinetic behavior of a specific liposome formulation first in zebrafish and finally in rats.

Journal of Controlled Release 264 (2017) 180–191

Contents lists available at ScienceDirect

Journal of Controlled Release

journal homepage: www.elsevier.com/locate/jconrel

Zebrafish as an early stage screening tool to study the systemic circulation of nanoparticulate drug delivery systems in vivo

Sandro Sieber, Philip Grossen, Pascal Detampel, Salome Siegfried, Dominik Witzigmann*,[1], Jörg Huwyler*,[1]

Division of Pharmaceutical Technology, Department of Pharmaceutical Sciences, University of Basel, Basel, Switzerland

ARTICLE INFO

Keywords:
Nanoparticles
Liposomes
Zebrafish
Screening model
Systemic circulation
Prediction

ABSTRACT

Nanomedicines have gained much attention for the delivery of small molecules or nucleic acids as treatment options for many diseases. However, the transfer from experimental systems to in vivo applications remains a challenge since it is difficult to assess their circulation behavior in the body at an early stage of drug discovery. Thus, innovative and improved concepts are urgently needed to overcome this issue and to close the gap between empiric nanoparticle design, in vitro assessment, and first in vivo experiments using rodent animal models.

This study was focused on the zebrafish as a vertebrate screening model to assess the circulation in blood and extravasation behavior of nanoparticulate drug delivery systems in vivo. To validate this novel approach, monodisperse preparations of fluorescently labeled liposomes with similar size and zeta potential were injected into transgenic zebrafish lines expressing green fluorescent protein in their vasculature. Phosphatidylcholine-based lipids differed by fatty acid chain length and saturation. Circulation behavior and vascular distribution pattern were evaluated qualitatively and semi-quantitatively using image analysis. Liposomes composed of lipids with lower transition temperature ($< 28\ ^{\circ}C$) as well as PEGylated liposomes showed longer circulation times and extravasation. In contrast, liposomes composed of lipids with transition temperatures $> 28\ ^{\circ}C$ bound to venous parts of the vasculature. This circulation patterns in the zebrafish model did correlate with published and experimental pharmacokinetic data from mice and rats.

Our findings indicate that the zebrafish model is a useful vertebrate screening tool for nanoparticulate drug delivery systems to predict their in vivo circulation behavior with respect to systemic circulation time and exposure.

1. Introduction

During the last decades, great expectations were placed on passively and actively targeted nanoparticles for the treatment of severe diseases including solid and metastatic tumors. The visionary concept of the magic bullet, introduced by Paul Ehrlich in 1907 [1], laid the foundation for a new age of cancer treatment. Liposomes, first described by Bangham et al. in 1965 [2], can be considered to be the by far most successfully used nanoparticles in clinical cancer care. Since the first approval of a liposomal anticancer product, namely Doxil/Caelyx in 1995, several lipid-based formulations have reached the market [3,4]. This milestone generated much hope for oncology-based nanoparticulate therapeutics resulting in an increased interest in cancer nanomedicines and a rapid growth of this research field [5].

Importantly, the physico-chemical properties of liposomal formulations have a direct impact on their pharmacokinetics and tissue distribution. Correspondingly, the efficacy and safety of the encapsulated drugs heavily depend on the used nanoparticulate drug delivery system. Recently, Lammers et al. highlighted that shifting the balance between off- and on-target accumulation is the most rational point for clinical use of nanomedicines [6]. Therefore, optimization of pharmacokinetics and biodistribution is of utmost importance for the success of nanomedicines. Unique nanoparticle properties combined with prolonged blood circulation characteristics result in decreased off-target effects and increased probability to reach the target side, e.g. via enhanced permeability and retention effect (EPR) in solid tumors.

The predictability of in vivo performance, however, remains a critical bottleneck in the development of nanoparticles and hampers the translation from in vitro to in vivo applications [3,7]. For example, the pharmacokinetic profile of liposomes can be influenced by multiple parameters

* Corresponding authors at: Division of Pharmaceutical Technology, Department of Pharmaceutical Sciences, University of Basel, Klingelbergstrasse 50, 4056 Basel, Switzerland.
E-mail addresses: dominik.witzigmann@unibas.ch (D. Witzigmann), joerg.huwyler@unibas.ch (J. Huwyler).
[1] Contributed equally.

http://dx.doi.org/10.1016/j.jconrel.2017.08.023
Received 8 June 2017; Received in revised form 20 August 2017; Accepted 21 August 2017
Available online 26 August 2017

including lipid composition, amount of cholesterol, PEGylation, or formulation methods as it is described in excellent reviews [8,9,4,10]. These parameters offer virtually endless possibilities for the optimization of nanoparticle formulations. Thus, liposome formulations are often designed empirically and based on physico-chemical properties but rarely optimized after the first in vivo experiments in mice and rats due to high costs and time consumption of in vivo studies. To overcome this issue and to advance the correlation between nanoparticle properties and in vivo performance, different attempts and suggestions have been described [3,7,11,12]. However, there is still an urgent need to incorporate improved pre-clinical test models for the assessment of nano-bio-interactions (e.g. with proteins, membranes, cells) in an early stage of development. This could help to predict the performance in higher animals, systematically pre-select promising nanomedicine formulations and thus facilitate the liposome formulation and development process.

In this study, we focused on the zebrafish as an early and easy accessible vertebrate model to evaluate the circulation behavior of lipid-based nanomedicines in vivo, thus bridging the gap between in vitro cell-based models and in vivo mammalian models. As compared to rodent in vivo models, the zebrafish offers unique advantages including high reproducibility, low husbandry and experimental costs, ethical considerations (3R principle), high level of genetic homology to humans, availability of transgenic lines, and most importantly optical transparency [13,14]. This enables in vivo imaging at spatio-temporal resolution (i.e. down to a cellular level and at various time points) [15]. Consequently, we combined a transgenic zebrafish line expressing green fluorescent protein (GFP) specifically in their vasculature with fluorescently labeled nanoparticles. This offers the possibility to gain advanced insights into the circulation behavior of nanoparticulate drug delivery systems [16]. In order to investigate the predictability of our approach, we have chosen the most established nanoparticulate drug delivery systems, i.e. liposomes. We have used a comprehensive and pioneering work by Semple et al., describing effects of fatty acid chain length, saturation of phosphatidylcholine-based lipids, and cholesterol content on liposome pharmacokinetics in mice [17]. First, we aimed to reproduce the results obtained in mice by Semple et al. in zebrafish embryos, in order to validate the zebrafish model as a sophisticated and early in vivo tool for nanoparticle screening and characterization. Second, we predicted the circulation behavior of a lipid formulation in rats after assessment in our zebrafish model. Finally, we analyzed the effect of cholesterol and PEGylation on the circulation behavior of liposomes in the zebrafish model in vivo.

This comprehensive study can provide the basis for a high-throughput screening platform to assess the circulation behavior of diverse nanoparticulate drug delivery approaches, thus offering a novel concept for nanomedicines development.

2. Material and methods

2.1. Material

1,2-Dimyristoyl-*sn*-glycero-3-phosphocholine (DMPC), 1,2-dioleoyl-*sn*-glycero-3-phosphocholine (DOPC), 1,2-dipalmitoyl-*sn*-glycero-3-phosphocholine (DPPC), 1,2 dioleoyl-3-trimethylammonium-propane (DOTAP), and 1,2-distearoyl-*sn*-glycero-3-phosphocholine (DSPC) were purchased from Corden Pharma Switzerland LLC (Liestal, Switzerland). 1,2-diarachidonoyl-*sn*-glycero-3-phosphocholine (DAPC 20:4), 1,2-diarachidoyl-*sn*-glycero-3-phosphocholine (DAPC 20:0), and 1,2-dioleoyl-*sn*-glycero-3-phosphoethanolamine-*N*-(lissamine rhodamine B sulfonyl) (ammonium salt) (Rhod-PE) were obtained from Avanti Polar Lipids (Alabaster, AL, USA). 1,2-distearoyl-*sn*-glycero-3-phosphoethanolamine-*N*-[methoxy(polyethylene glycol)-2000] (DSPE-PEG_{2000}) was provided by Lipoid (Steinhausen, Switzerland). Cholesterol, branched polyethylenimine Mw 25′000 (PEI), and Sulforhodamine B were purchased from Sigma-Aldrich (Buchs, Switzerland). 1,1′-dioctadecyl-3,3,3′,3′-tetramethylindocarbocyanine perchlorate (DiI) and 1,2-dihexadecanoyl-sn-glycero-3-phosphoethanolamine (Texas red) were purchased from Invitrogen (Basel, Switzerland). SolvableTM and Ultima GoldTM XR were purchased from PerkinElmer (Schwerzenbach, Switzerland).

2.2. Preparation of fluorescent liposomes

Liposomes were prepared as described previously [18]. Lipid and cholesterol stock solutions were prepared in chloroform/methanol (2:1, *v*/v). For the preparation of liposomes either pure phosphatidylcholine-based phospholipids, a combination of DSPC and an indicated mol% of cholesterol or a combination of DSPC/cholesterol and an indicated mol % of DSPE-PEG_{2000} were used [19]. Desired ratios of stock solutions were mixed at a total lipid concentration of 10 mM and dried overnight using nitrogen. Liposomes were fluorescently labeled using 1 mol% of fluorescent dye (as indicated). Dry lipid films were re-hydrated for 10 min at T_m + 10 °C using 0.4 mL of H_2O. For passive encapsulation of a hydrophilic fluorescent dye (i.e. sulforhodamine B), H_2O was replaced by a 1 mM aqueous solution of sulforhodamine B. The resulting multilamellar vesicles were equilibrated for 10 min at T_m + 10 °C and finally extruded 17 times through a polycarbonate membrane with a pore size of 100 nm (Avanti Polar-Lipids). Free hydrophilic dye was removed by size exclusion chromatography using a Sepharose CL-4B column (Sigma-Aldrich) and concentrated using a Millipore Amicon tube (Sigma-Aldrich) with a molecular cut off of 10 kDa (10 min, 4000 rcf).

2.3. Preparation of radioactive liposomes

Tritium labeled doxorubicin ([^{3}H]-doxorubicin) (Campro Scientific, Veenendaal, Netherlands) was encapsulated into DAPC 20:0- and DAPC 20:4-based liposomes using an active loading strategy (i.e. a pH gradient) as follows: Lipid films were re-hydrated using acetate buffer (0.3 M, pH 4.0) and extruded as described before. The external buffer phase was exchanged by PBS (0.01 M, pH 7.8) using gel filtration chromatography (Econo-Pac 10DG, Bio-Rad Laboratories AG, Cressier, Switzerland). [^{3}H]-doxorubicin in EtOH (15 μCi) was placed into a glass vial and EtOH was removed under nitrogen. Subsequently, [^{3}H]-doxorubicin was rehydrated in H_2O (20 μL) and liposome formulations were added. The mixtures were incubated at > T_m for 10 min. Free [^{3}H]-doxorubicin was removed by gel filtration chromatography using PBS (0.001 M, pH 7.4) as a mobile phase. Liposomes were immediately used for pharmacokinetic experiments in vivo in rats.

2.4. Dynamic and electrophoretic light scattering measurements

Dynamic and electrophoretic light scattering measurements for the determination of liposome size and zeta potential were conducted using a Delsa Nano C Particle Analyzer (Beckman Coulter, Nyon, Switzerland) as described previously [20,21]. All measurements were carried out at room temperature (RT) at a lipid concentration of 1 mM in H_2O. For size distribution analysis, the laser was adjusted to 658 nm and scattered light was detected at a 165° angle. Data was converted using CONTIN particle size distribution analysis. For zeta potential analysis, the measurement angle was 15° and data were converted using the Smoluchowski equation (Delsa Nano V3.73/2.30, Beckman Coulter Inc., Brea, CA).

2.5. Cryo transmission electron microscopy (Cryo-TEM)

Size and shape of liposomes were analyzed by Cryo-TEM using a Philips CM200-FEG electron microscope operated at an acceleration voltage of 200 kV as described previously [20]. In brief, liposomes were deposited onto glow-discharged carbon grids (Quantifoil, Jena, Germany), blotted with Whatman 1 filter papers, and vitrified in liquid nitrogen-cooled liquid ethane using a Vitrobot IV plunge-freezing device (FEI Company, Eindhoven, Netherland). Micrographs were recorded with a 4 k × 4 k TemCam-F416 CMOS camera (TVIPS, Gauting, Germany).

2.6. Zebrafish embryo nanotoxicity screening

Time and concentration dependent in vivo toxicity (i.e. viability) of injected liposome formulations was assessed following an adapted protocol [22–24]. In brief, fertilized zebrafish eggs at 4 h post fertilization were incubated in 24-well plates (5 zebrafish eggs/well) with different nanoparticle formulations at concentrations of 1 μM, 10 μM, 100 μM, and 1000 μM in zebrafish culture media. Standard liposomes (i.e. DOPC, DMPC, DPPS, DSPC, DAPC 20:0) were compared to DOTAP-based liposomes and PEI (polymeric nanomaterial) as positive controls. Viable embryos were counted after 24, 48, and 72 h post incubation using a Leica S8APO microscope (Leica Microsystems, Heerbrugg, Switzerland). Representative images at 24 h post incubation (i.e. timescale of pharmacokinetics experiments) were taken using an Olympus CKX41 microscope (Olympus Ltd., Tokyo, Japan).

2.7. Zebrafish embryo culture and injections

Zebrafish (*Danio rerio*) were maintained at standard conditions and in accordance with Swiss animal welfare regulations. Eggs from adult transgenic kdrl:EGFPs843 [25] zebrafishes were collected and kept in zebrafish culture media at 28 °C. In order to suppress pigment cell formation, 1-phenyl 2-thiourea (PTU) was added to the culture media 1-day post fertilization (dpf). Liposome samples were injected into zebrafish embryos (2 dpf) at a concentration of 1 mM. Injections were performed following an adapted protocol as described previously [26]. Anesthetized zebrafish embryos (0.01% tricaine, *w/v*) were embedded in 0.3% (*w/v*) agarose containing tricaine. Calibrated volumes of 1 nL were injected into the duct of Cuvier. Injections were performed using a micromanipulator (Wagner Instrumentenbau KG, Schöffengrund, Germany), a pneumatic Pico Pump PV830 (WPI, Sarasota, Florida), and a Leica S8APO microscope (Leica, Wetzlar, Germany). After successful liposome injection (i.e. exclusion of zebrafish embryos characterized by fluorescence accumulation in the yolk) zebrafish embryos were imaged using an Olympus FV-1000 inverted confocal laser scanning microscope equipped with a 10 × UPlanSApo (NA 0.4) and 20 × UPlanSApo (NA 0.75) objective. In addition to experiments at 28 °C, control injections at 37 °C were performed to relate the experiments to mammalian body temperature. Detailed procedures are provided in the Supplementary data.

2.8. Semi-quantitative image analysis

Image stacks were processed and analyzed using FIJI/ImageJ software 1.51 g [27,28]. For each z-stack a maximum intensity projection was created and a constant background was subtracted. For calculation of the circulation factor (CF), a mask of the vascular region was used and the mean intensity of bound ($\overline{I_{Bound}}$) from free particles ($\overline{I_{Free}}$) were discriminated by using the analyze particle function with a constant threshold. The mean fluorescence intensity of free particles was normalized by the vascular area (A_{Vasc}) after subtraction of the background (Eqs. (1) and (2)).

$$\overline{I_{Free}} = \overline{I_{Vasc}} - \overline{I_{Bound}} \quad (1)$$

$$CF = \frac{\overline{I_{Free}}}{A_{Vasc}} \quad (2)$$

For calculation of the extravasation factor (EF), mean fluorescence intensity of the vascular region ($\overline{I_{Vasc}}$) was divided by mean fluorescence intensity in the non-vascular region ($\overline{I_{Non\ Vasc}}$) after normalization by the corresponding area (Eq. 3).

$$EF = \frac{\overline{I_{Vasc}}}{A_{Vasc}} \frac{A_{Non\ Vasc}}{\overline{I_{Non\ Vasc}}} \quad (3)$$

It is important to note that EF values are fluorescence intensity ratios (i.e. absolute values) and therefore independent of instrument settings. In contrast, CF values are relative values and have been compared to a reference formulation in the same set.

2.9. Pharmacokinetic study in rats

Pharmacokinetic profiles of DAPC 20:0 or DAPC 20:4 liposomes were analyzed in female Wistar rats [250–280 g] (Janvier Labs, Saint-Berthevin Cedex, France) using [^{3}H]-doxorubicin as described earlier [29,30]. The protocol for animal experiments was approved by Swiss animal welfare authorities (authorization No. 2836) and all experiments were conducted in accordance with Swiss animal welfare regulations. Rats were anesthetized (isoflurane) and the jugular vein was cannulated. [^{3}H]-doxorubicin (4 μCi) encapsulated in DAPC 20:0 or DAPC 20:4 was injected via the catheter. Blood samples (200 μL) were collected at various time points via the catheter, mixed with EDTA (0.5 M, 10 μL), and centrifuged for 5 min at 1000 rcf and 4 °C to obtain plasma. The blood volume collected was replaced by saline containing heparin (100 U/mL). After 1 h, animals were sacrificed. Plasma aliquots (40 μL) were mixed with Solvable™ (200 μL) and solubilized by incubation for 4 h at 50 °C. Samples were bleached using 30% H_2O_2, mixed with 10 mL of Ultima-Gold™ XR scintillation cocktail and analyzed using liquid scintillation counting using a TriCarb 4910 TR Liquid Scintillation Analyzer (PerkinElmer, Schwerzenbach, Switzerland). Plasma-concentration time profiles were analyzed using PK solver [31]. Appropriate compartmental curve fitting models were chosen according to Akaike Information Criterion and Schwarz Criterion as described previously [32].

2.10. Statistical analysis

Statistical analysis was performed by one-way analysis of variance (ANOVA) followed by Bonferroni or Tukey post-hoc test using OriginPro 9.1 software (OriginLab Corporation; Northampton, MA). All zebrafish data represent at least $n \geq 4$ independent sets of experiments. Differences between groups were considered to be statistically significant at the indicated p-values ($^*p < 0.05$, $^{**}p < 0.01$ and $^{***}p < 0.001$).

3. Results

3.1. Physicochemical properties of liposomes

To validate the zebrafish as a screening tool, five different liposome formulations consisting of one single phosphatidylcholine-based lipid only were prepared. Vesicles had different main phase transition temperatures (T_m) depending on fatty acid chain length (DMPC 14:0, DPPC 16:0, DSPC 18:0, DAPC 20:0) or fatty acid saturation (DOPC 18:1) of the phospholipids (Table 1). Morphology, size, polydispersity index (PDI), and zeta potential of the different liposomal formulations were analyzed by Cryo-TEM or dynamic and electrophoretic light scattering analysis, respectively, as summarized in Fig. 1 and Table 1.

Table 1
Physico-chemical characteristics of different liposome formulations. Lipid transition temperature (T_m) was taken from Semple et al. [17]. Hydrodynamic size, polydispersity index (PDI), and zeta potential of different liposomes were analyzed using dynamic and electrophoretic light scattering. $n = 3$ independent experiments; values are means ± SD.

Liposome	Lipid T_m (°C)	Size (nm)	PDI	Zeta potential (mV)
DAPC 20:4	−70	106.1 ± 3.4	0.096 ± 0.043	−26.5 ± 5.8
DOPC	−22	116.8 ± 4.4	0.105 ± 0.031	−25.4 ± 7.7
DMPC	23	113.7 ± 3.2	0.075 ± 0.035	−19.6 ± 9.7
DPPC	41	105.9 ± 2.4	0.076 ± 0.015	−16.9 ± 4.0
DSPC	55	104.6 ± 2.3	0.062 ± 0.029	−16.6 ± 5.6
DAPC 20:0	66	110.7 ± 4.7	0.110 ± 0.037	−17.1 ± 6.6

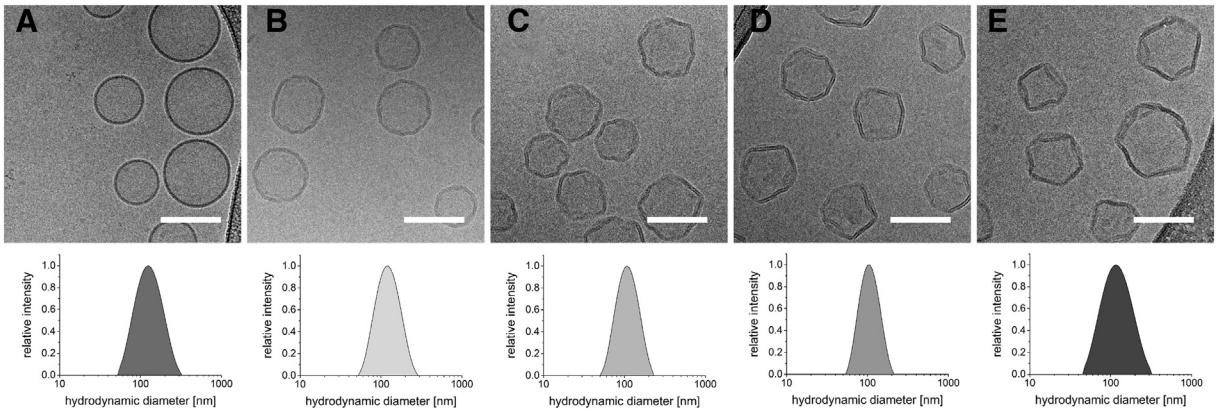

Fig. 1. Physico-chemical characterization of different liposome formulations. Liposomes were prepared using different phosphatidylcholine-based lipids and analyzed by Cryo-TEM and dynamic light scattering. Liposomes are selected based on Semple et al. [17] and ordered according to ascending main phase transition temperature T_m (Table 1), namely (A) DOPC, (B) DMPC, (C) DPPC, (D) DSPC, and (E) DAPC 20:0. A representative electron micrograph and intensity-based size distribution is shown for each liposome formulation. Scale bars represent 100 nm.

Each type of liposome showed an uniform and spherical vesicle morphology with an unilamellar lipid bilayer (Fig. 1). Liposomes composed of phospholipids with $T_m < 28$ °C (DOPC, DMPC) showed spherical geometries (Fig. 1A and B) whereas liposomes with $T_m > 28$ °C (DPPC, DSPC, DAPC 20:0) displayed irregular spherical shapes (Fig. 1C-E) on electron micrographs. Dynamic light scattering measurements confirmed the monodisperse size distribution of different liposome formulations (as indicated by a polydispersity index < 0.2) with an average hydrodynamic diameter of around 110 nm (Fig. 1 and Table 1). Zeta potential measurements revealed a negative zeta potential of all liposome formulations around − 20 mV.

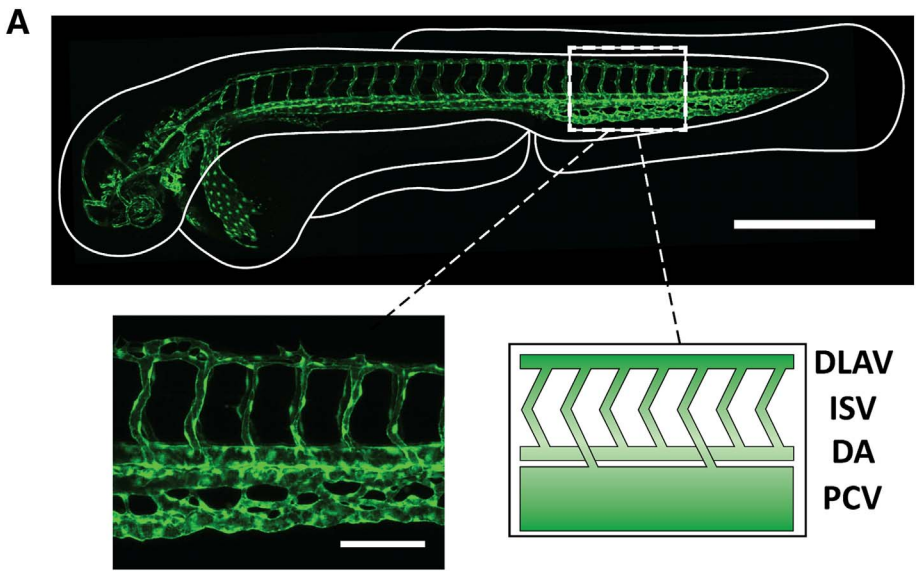

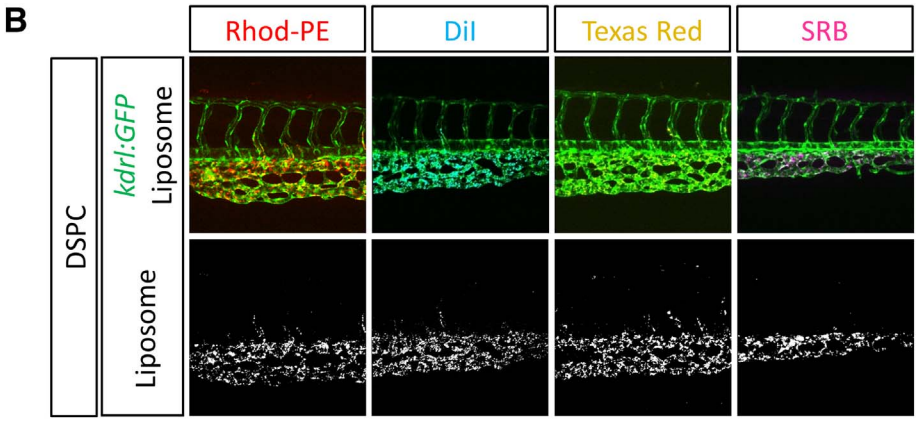

Fig. 2. Schematic representation of transgenic zebrafish embryo and influence of different fluorescent dyes on liposome circulation behavior. (A) Transgenic zebrafish embryo with fluorescent vasculature including the tail region which was used for imaging. Schematic representation of zebrafish vasculature with anatomical nomenclature. DLAV: dorsal longitudinal anastomotic vessel, ISV: intersegmental vessels, DA: dorsal aorta, PCV: posterior (caudal) cardinal vein. Scale bars represent 500 μm (overview) and 100 μm (insert). (B) Fluorescence distribution patterns of DSPC-based liposomes were analyzed 1 hpi using confocal microscopy. Liposomes contained either 1 mol% of a lipophilic dye, i.e. Rhod-PE, DiI, and Texas Red-DHPE, or 1 mM sulforhodamine B (SRB) as a hydrophilic payload. Representative images are shown for each setting.

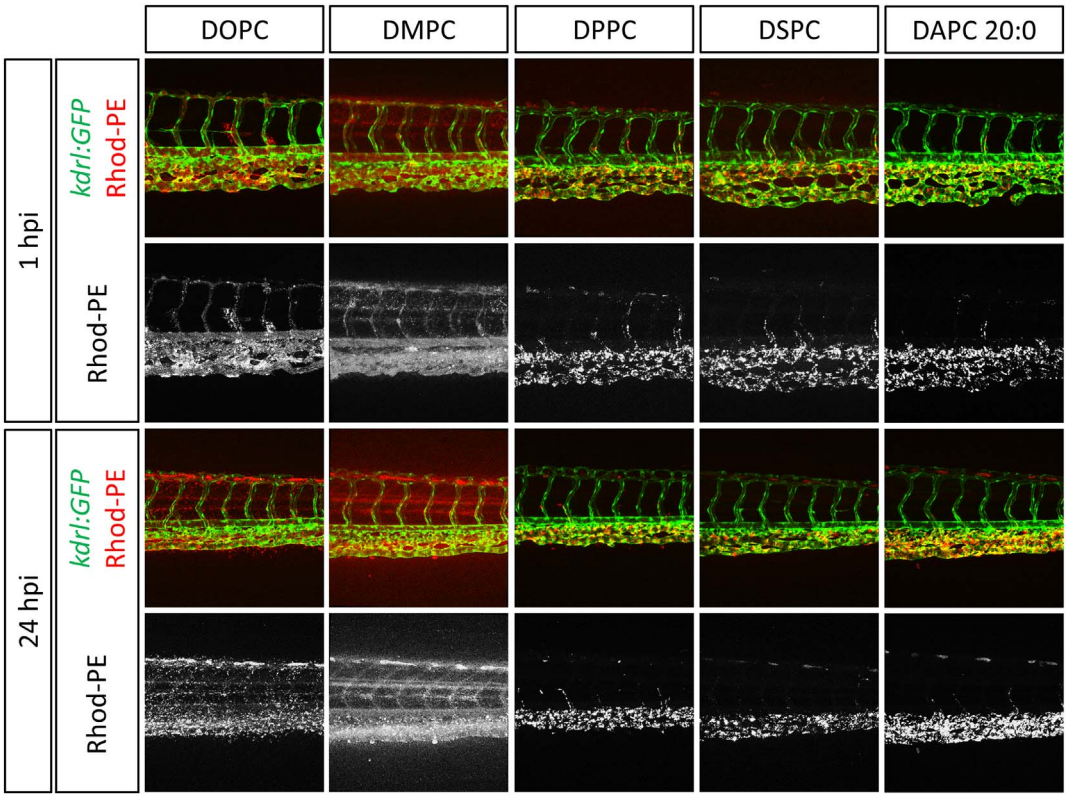

Fig. 3. Qualitative evaluation of liposome circulation behavior in vivo in the zebrafish model. Different liposome formulations composed of specific phosphatidylcholine-based lipids were injected into transgenic zebrafish embryo expressing green fluorescent protein in the vasculature endothelial cells. All liposome formulations contained 1 mol% Rhod-PE as a fluorescent marker. Confocal images were taken 1 and 24 hpi in the tail region (see Fig. 2A).

3.2. Nanotoxicity screening of liposomes

To investigate if the different liposome formulations exhibit toxic effects in vivo, we performed a nanotoxicity testing using the zebrafish embryo assay (Supp. Fig. 1). All single phosphatidylcholine-based liposomes were biocompatible and did not show any apparent toxic effects. In sharp contrast, positively charged lipid- (i.e. DOTAP) or polymer- (i.e. PEI) based nanomaterials showed strong toxic effects in zebrafish embryos.

3.3. Labeling strategy to study liposome circulation behavior

Fluorescently labeled liposomes were injected into the duct of Cuvier of 2 days old zebrafish embryos. After specific time points, the circulation behavior of different lipid formulations were imaged in the tail region using confocal laser scanning microscopy. A schematic representation of the zebrafish tail region including its vasculature nomenclature [33] is shown in Fig. 2A. To exclude an effect of the fluorescent dye on liposome circulation behavior, different labeling strategies were evaluated. Thereby, different fluorescent dyes were incorporated into DSPC-based liposomes (Fig. 2B). Three different lipophilic dyes and one hydrophilic dye were tested. Lipophilic dyes were used to label the phospholipid bilayer, i.e. the nanocarrier. Lipophilic Rhod-PE and Texas Red-DHPE were chosen as a head group-modified phospholipid analogs with large chromophore structures. The lipophilic and cationic indocarbocyanine dye DiI was chosen due to deep incorporation into the lipid bilayer and small chromophore structure. In order to investigate a hydrophilic payload, sulforhodamine B was encapsulated into the core of liposomes. As shown in Fig. 2B, different dyes did not influence the circulation behavior (i.e. fluorescence distribution patterns) of the DSPC-based lipid formulation. Therefore, Rhod-PE was chosen as fluorescent dye for all further experiments, due to its stable incorporation properties into the lipid bilayer, similar structure to phosphatidylcholine-based lipids used for the different formulations, and relatively small chromophore as compared to Texas Red.

3.4. Liposome circulation behavior in zebrafish embryos

In a next step, different liposome formulations consisting of specific phosphatidylcholine-based lipids were injected into the duct of Cuvier of zebrafish embryos and fluorescence signals in the tail region were analyzed at 1 h post injection (hpi) and 24 hpi (Fig. 3). Experiments were carried out at 28 °C. Confocal images revealed a different circulation behavior and staining pattern dependent on fatty acid chain length or saturation of phospholipids. Liposomes composed of DMPC (T_m 23 °C) or DOPC (T_m − 22 °C), which exist in the liquid crystalline state at experimental conditions, were evenly distributed in the whole vasculature at 1 hpi. In sharp contrast, liposomes containing lipids in the gel state, i.e. DPPC (T_m 41 °C), DSPC (T_m 55 °C), or DAPC 20:0 (T_m 66 °C), were mainly attached to the venous part of the vasculature (i.e. posterior cardinal vein, PCV). In addition, these lipid formulations showed a dotted staining pattern. In agreement to the observations at 1 hpi, a clear difference between the two groups, i.e. $T_m < 28$ °C or $T_m > 28$ °C, was also observed 24 hpi. Whereas lipids with a high transition temperature (DPPC, DSPC, DAPC 20:0) still mainly attached to the PCV, lipids with a low transition temperature (DOPC, DMPC) showed an evenly distributed staining pattern which was not restricted to the vascular structure, demonstrating extravasation into surrounding tissue (Fig. 3). Control experiments performed at 37 °C (i.e. mammalian body temperature) using a lipid formulation from each group (DSPC vs. DOPC) confirmed these results (Supp. Fig. 2). We observed the same staining patterns. In addition, zebrafish embryos developed normally and no change in zebrafish morphology could be detected up to 24 hpi.

Semi-quantitative parameters were calculated using computer-assisted image analysis to compare different lipid formulations. Two

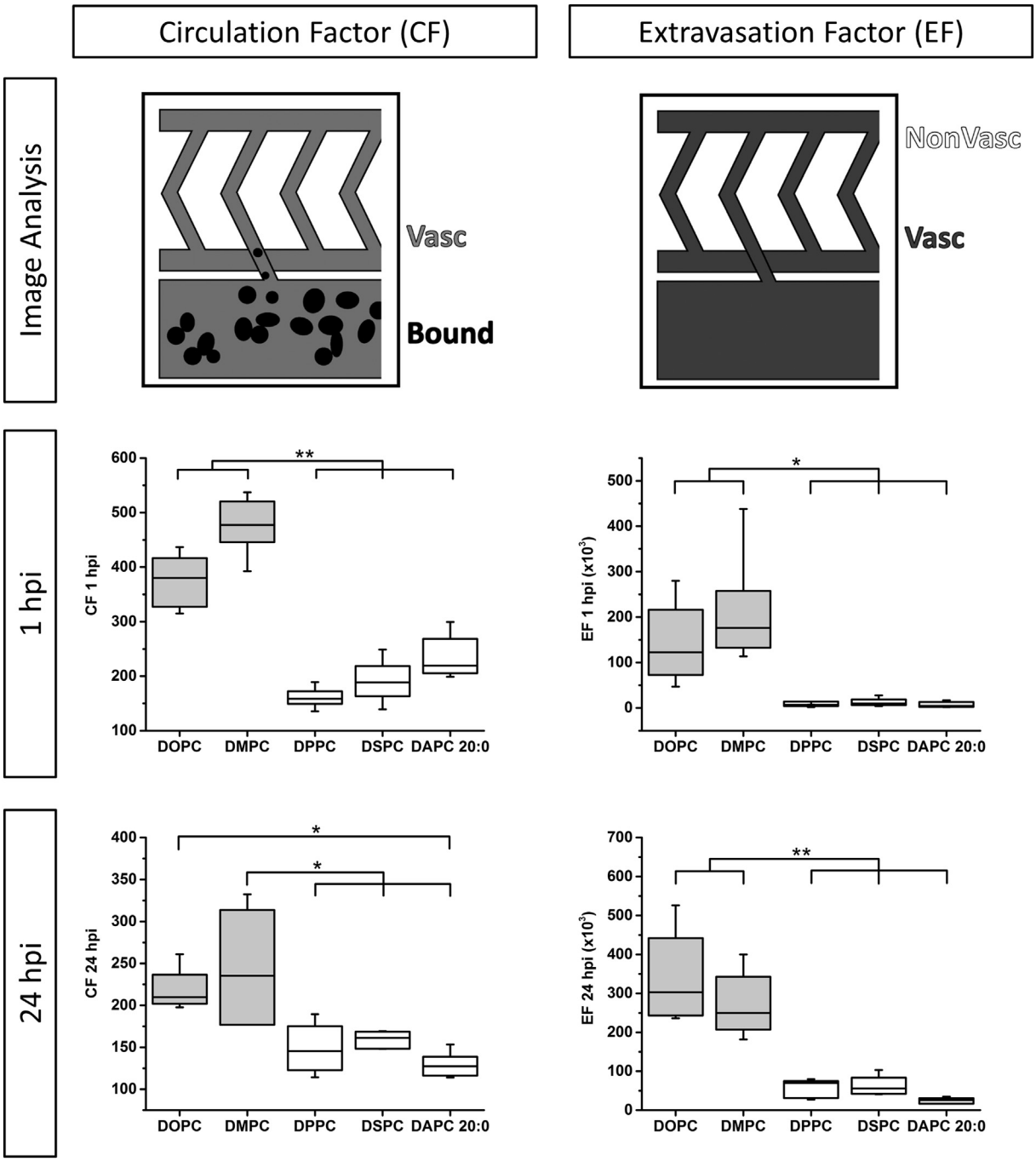

Fig. 4. Semi-quantitative analysis of liposome circulation behavior in vivo in the zebrafish model. Circulation (CF) and extravasation factors (EF) of each lipid composition were calculated 1 and 24 hpi based on fluorescence signal intensities of liposomes in specific regions as indicated by the respective colour coding. CF values correspond to freely circulating liposomes and represent the difference between total vascular (Vasc) and bound (Bound) liposome signals. EF values are based on ratios between vascular (Vasc) and nonvascular (NonVasc) signals. $n \geq 5$ experiments. Box plots represent median, third and first quantiles, minima and maxima, asterisks indicate statistically significant differences between phospholipids with a $T_m < 28$ °C (grey boxes) and a $T_m > 28$ °C (white boxes) (see Table 1). $^*p > 0.05$ or $^{**}p > 0.01$.

different factors characterizing the circulation behavior of liposomes in zebrafishes were defined (Fig. 4). First, fluorescence intensity of circulating liposomes was calculated and represented as circulation factor (CF). In this experiment, higher CF values (> 200) 24 hpi represent liposome formulations, which show an extended circulation time and reduced binding to vascular structures, i.e. PCV. Second, an extravasation factor (EF) was determined. The EF represents the ratio between liposomes located outside the vasculature and liposomes located inside the vasculature. Long circulating liposomes showed a higher tendency to extravasate 24 hpi (EF > 270), whereas short circulating lipid formulations had low extravasation values (EF < 70). As shown in Fig. 4, liposomes can be clearly differentiated into two groups (i.e. long and short circulating), based on their transition temperature, CF, and EF values. Table 2 shows the comparison of the plasma half-life ($t_{1/2}$) in mice reported by Semple et al. [17] and the calculated zebrafish factors for all used lipid formulations.

3.5. Effect of cholesterol on circulation behavior

To further verify the zebrafish model as efficient screening tool to assess multicomponent lipid formulations with minor differences and to confirm that the phase transition temperature T_m of phospholipid

Table 2
Circulation behavior of different liposome formulations in vivo in mice and zebrafishes. Plasma circulation half-life of liposomes in mice ($t_{1/2}$) were taken from Semple et al. [17]. Zebrafish circulation (CF) and extravasation factor (EF) are based on semi-quantitative image processing of fluorescence intensities 24 hpi. $n \geq 5$ independent zebrafish experiments; values are means ± SD.

Liposome	$t_{1/2}$ mice (min)	$CF_{zebrafish}$	$EF_{zebrafish}$ ($\times 10^3$)
DOPC	> 120	217.3 ± 25.1	334.5 ± 117.4
DMPC	74.0	243.3 ± 69.9	270.0 ± 81.7
DPPC	1.2	148.3 ± 28.8	56.3 ± 23.4
DSPC	0.9	159.0 ± 10.2	61.2 ± 25.2
DAPC 20:0	0.9	128.8 ± 14.4	24.7 ± 7.3

bilayers has a strong impact on systemic circulation of phosphatidylcholine-based liposomes, control experiments with DSPC liposomes containing increasing amounts of cholesterol (i.e. 10 to 50 mol%) were performed (Fig. 5). Cholesterol has been reported to have a strong impact on T_m in saturated phosphatidylcholine-based liposomes, subsequent protein binding and circulation lifetimes [17]. Indeed, an increase of circulating liposomes was observed with increasing amounts of cholesterol in the zebrafish model (Fig. 5A). The typical dotted and non-circulating staining pattern of pure DSPC liposomes in the PCV gradually changed towards the circulation behavior of circulating liposomes. Semi-quantitative image analysis confirmed the influence of cholesterol content on CF and EF (Fig. 5B). At 24 hpi striking

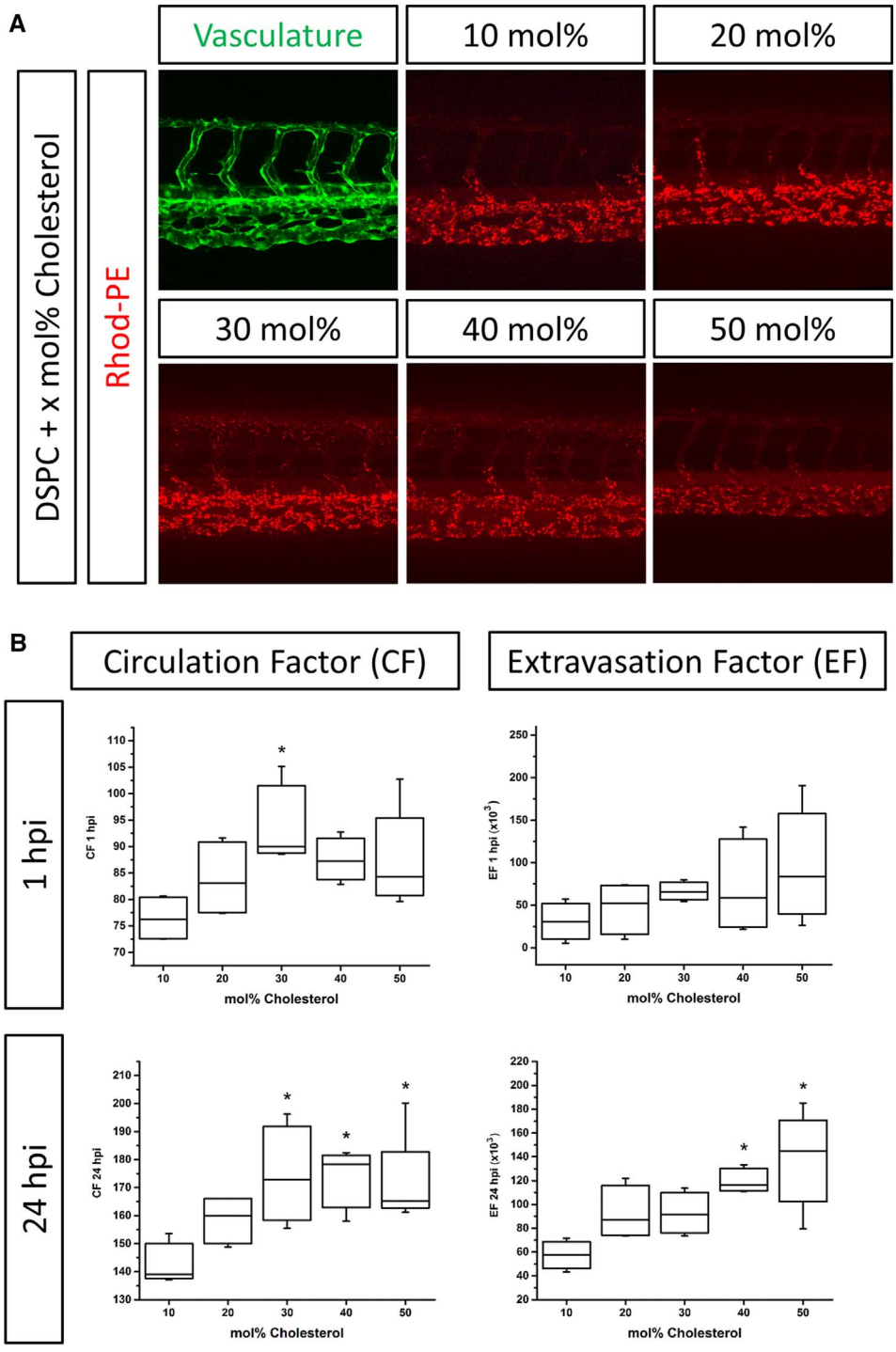

Fig. 5. Effect of cholesterol on circulation behavior of DSPC-based liposomes in vivo in the zebrafish model. (A) DSPC-based liposome formulations with increasing amounts of cholesterol were injected into transgenic zebrafish embryos and images were taken 1 hpi from the tail region. (B) Liposome circulation behavior was assessed semi-quantitatively. Circulation (CF) and extravasation factors (EF) of each lipid composition 1 and 24 hpi are given. $n \geq 4$ experiments. Box plots represent median, third and first quantiles, minima and maxima. *$p > 0.05$ as compared to control (10 mol% cholesterol).

differences in CF and EF for formulations containing higher amounts of cholesterol differences were observed.

3.6. Comparison of circulation behavior in the zebrafish model and rats

In a next step, a lipid formulation with unknown pharmacokinetic behavior was assessed in the zebrafish model and in rats as a proof-of-concept experiment to underline the validity of our proposed screening tool. Liposomes composed of the unsaturated DAPC 20:4 lipid were injected into zebrafish embryos and compared with already described DAPC 20:0-based liposomes (Fig. 6A). In contrast to non-circulating DAPC 20:0-based liposomes, the staining pattern of DAPC 20:4 matched to long-circulating liposomes consisting of lipids in the liquid crystalline state such as DMPC or DOPC. A statistically significant increased CF and EF for DAPC 20:4-based liposomes as compared to DAPC 20:0-based liposomes confirmed the qualitative observations. Subsequently, both lipid formulations were injected into rats and blood sampling was performed for 60 min (Fig. 6B). The predictive CF and EF (1 hpi) and the pharmacokinetic parameters from rat experiments are summarized in Table 3. As expected from the zebrafish experiments, DAPC 20:4-based liposomes injected into rats showed an approximately 5-fold increased circulation half-life ($t_{1/2}$) as well as a 10-fold increased area under the curve (AUC) as compared to DAPC 20:0-based liposomes.

3.7. Influence of PEGylation on liposome circulation

As a final proof-of-concept experiment to validate the zebrafish model, we assessed the effect of PEGylation on liposome circulation in the zebrafish model. Therefore, PEGylated liposomes containing increasing amounts of DSPE-PEG_{2000} were injected into zebrafish. As shown in Fig. 7, a clear correlation between increasing amounts of DSPE-PEG_{2000} and enhanced circulation behavior can be observed in the presented zebrafish model.

4. Discussion

Optimization of physicochemical and pharmacokinetic properties of liposomal formulations (or any other type of nanoparticulate drug delivery system) remains a challenge. Many factors including lipid composition, size, PDI, or surface charge can influence the pharmacokinetics of liposomes in vivo. Estimation or even prediction of liposome circulation behavior in vivo due to changes in lipid composition or physico-chemical characteristics is difficult and often based on empiric data. Therefore, the aim of the present study was to introduce and validate the zebrafish as an early stage vertebrate screening model closing the gap between in vitro and in vivo experiments in rodents. This could offer a possibility to change the predictable pattern of organization in nanoparticle research [11]. Interestingly, the zebrafish is an emerging model to study human diseases and some research groups have started to test the therapeutic efficacy of nanocarriers in these models [34–36]. The prediction value of the zebrafish model to study the circulation behavior of lipid-based nanoparticles in vivo was assessed in three steps. First, we compared the circulation behavior of liposomes in zebrafishes with data reported from mice experiments by Semple et al. Second, we evaluated a lipid formulation with unknown circulation properties in zebrafish embryos and compared these results to pharmacokinetic experiments which we have performed in rats. Finally, we investigated the effects of cholesterol or PEGylation as most widely used enhancer of liposome circulation [37,38] in the zebrafish model.

Inspired by the early publication of Semple et al., five different lipid formulations were chosen. Thus, the influence of lipid composition (length of fatty acid chain, saturation, amount of cholesterol, and consequently phase transition temperature) on liposome circulation behavior was assessed in vivo in zebrafishes and compared to reported findings in mice. All liposomes had comparable nanoparticle characteristics, i.e. size, PDI, and zeta potential, to increase comparability of different lipid formulations and thus minimize size-related effects. Importantly, the zebrafish model was also used to investigate the toxicological effects with respect to viability of the different liposomes in vivo. Estimating that a zebrafish embryo has a total blood volume of 60 nL [39], the final lipid concentration in blood circulation after injection of 1 nL liposomes is around 16 μM. Thus, none of the tested liposome formulations exhibited toxic effects in the concentration range used for zebrafish injections.

In a next step, different fluorescent dyes were incorporated into liposomes to validate our fluorescence microscopy-based approach. No influence on liposome circulation behavior was observed using low amounts of fluorescent label (i.e. 1 mol% of the final lipid composition for lipophilic dyes). The compatibility of lipophilic and hydrophilic dyes is an important prerequisite for further studies using the zebrafish model. Lipophilic dyes offer the possibility to exclusively follow the nanocarrier circulation in vivo, whereas the circulation of encapsulated, hydrophilic dyes is also influenced by the nanocarrier stability (i.e. encapsulated vs. free drug). Since the focus of the present study was to analyze the influence of lipid characteristics on nanocarrier circulation behavior, the fluorescent phospholipid analog Rhod-PE was used for all further experiments. After assessment of liposome circulation behavior at various time points post injection (data not shown), 1 and 24 hpi were chosen as suitable time points for image analysis. It has been shown that the 1 hpi time point offers the possibility of an almost immediate first assessment of blood circulation patterns. In addition, there is a good correlation with later (i.e. 24 hpi) time points. The 24 hpi time point is optimal to assess the extravasation factor of long circulating nanocarriers (i.e. evaluation of extravasation into vascular surrounding tissue). Furthermore, CF and EF show less variability for the same formulation 24 hpi due to smaller deviations in developmental stage of zebrafish.

Based on the qualitative observations and semi-quantitative image analysis, we propose following strategy for the assessment of different formulations: (I) Injection of reference samples with known pharmacokinetic properties and test samples of interest into the duct of Cuvier of zebrafish embryos 48 h post fertilization, (II) qualitative image analysis 1 hpi, and (III) qualitative and semi-quantitative image analysis 24 hpi. Following this strategy, the circulation behavior of novel nanocarriers can be determined relative to reference samples with known pharmacokinetic properties or due to gradual changes in the nanoparticle formulation (e.g. cholesterol amount). In our study using phosphatidylcholine-based lipids, the classification seems to be dependent on individual transition temperatures (which most probably influences subsequent protein binding in circulation) as reported by Semple et al. in mice [17]. It is therefore advisable to carefully control temperature (i.e. 28 °C) during the experiment. Interestingly, higher temperatures (e.g. 37 °C) can be used to extend the zebrafish model to temperature-sensitive drug delivery systems. However, it has to be kept in mind that in zebrafish embryos heat-shock proteins such as *hsp70* are activated at 37 °C [40,41]. In addition, Haldi et al. observed necrosis in the yolk after incubation for 2 days at 37 °C [42].

We observed that liposomes composed of lipids with lower transition temperature (i.e. DAPC 20:4 T_m −70 °C, DOPC T_m −22 °C, and DMPC T_m 23 °C) resulted in comparably higher CF and EF. In contrast, liposomes composed of lipids with higher transition temperatures (i.e. DPPC T_m 41 °C, DSPC T_m 55 °C, and DAPC 20:0 T_m 66 °C) resulted in low circulation factors and reduced extravasation.

Qualitatively, two main circulation patterns were observed in a defined tissue segment of the tail region of injected zebrafish embryos 1 hpi. Long circulating formulations evenly distributed into the whole vasculature whereas short circulating formulations attached to venous structures (e.g. PCV) almost immediately after injection.

Importantly, a clear distinction between fluorescent liposomes and endothelial structures was possible by using transgenic zebrafish embryos expressing GFP in endothelia cells. Thus, the unique properties of

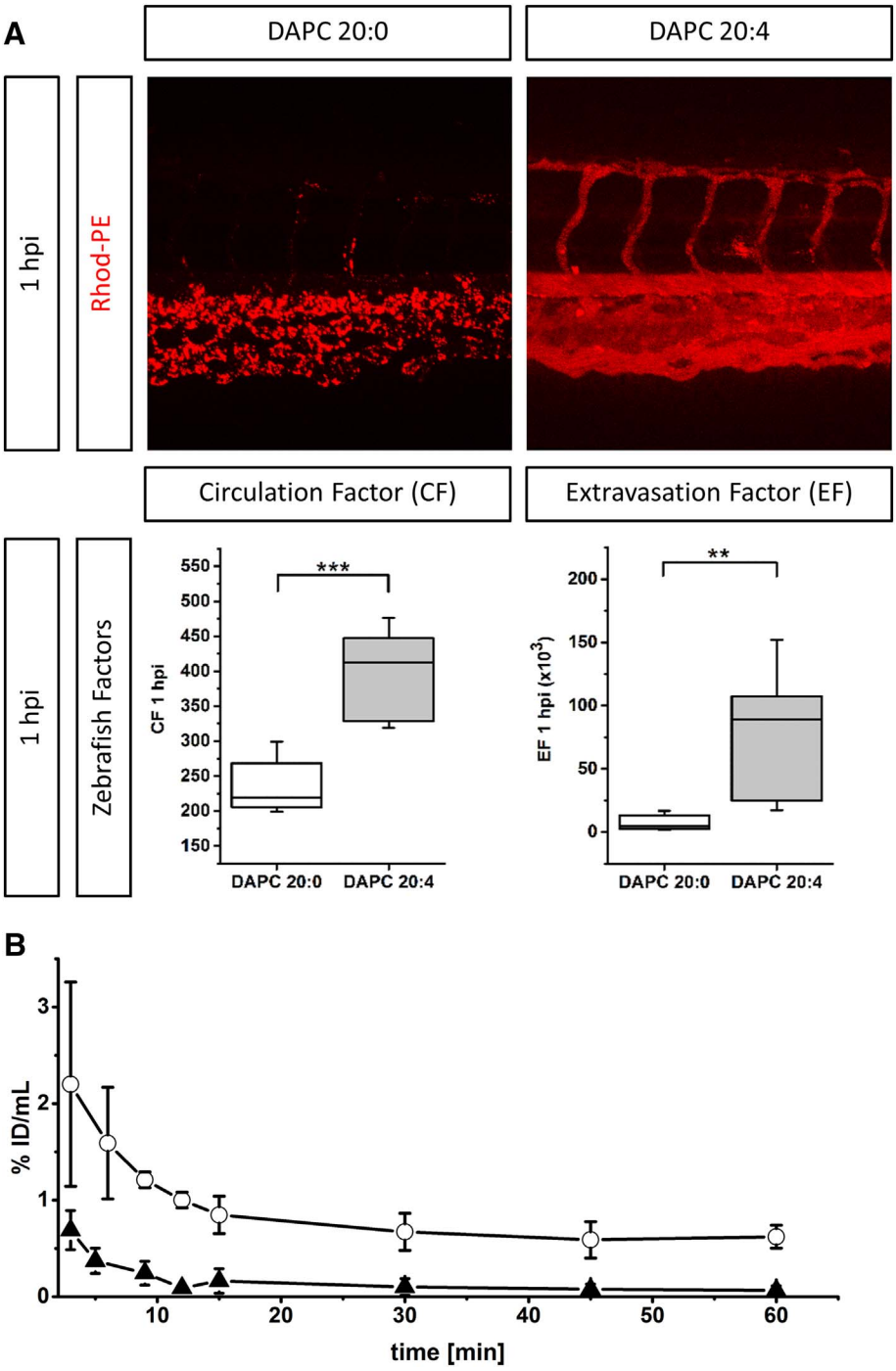

Fig. 6. Comparison of liposome circulation in zebrafishes and rats. Liposomes were prepared from saturated (DAPC 20:0) and unsaturated (DAPC 20:4) lipids. (A) Representative images of liposome distribution pattern and zebrafish circulation factor (CF) and extravasation factor (EF) 1 hpi are shown. $n \geq 5$ experiments. Box plots represent median, third and first quantiles, minima and maxima. $^{**}p > 0.01$ or $^{***}p > 0.001$. (B) Radiolabeled liposomes were intravenously injected into rats and plasma concentrations of encapsulated [^{3}H]-doxorubicin were analyzed at various time points over 1 h. $n \geq 3$ independent experiments. Values are means ± SD. Black triangles indicate DAPC 20:0-based liposomes. White open circles indicate DAPC 20:4-based liposomes. Pharmacokinetic parameters are summarized in Table 3.

Table 3
Summary of liposome circulation characteristics in vivo in zebrafishes and rats. DAPC 20:0- and DAPC 20:4-based liposomes were injected into zebrafishes and rats. The zebrafish circulation factor (CF), extravasation factor (EF), and pharmacokinetic factors in rats (terminal $t_{1/2}$, AUC_0^∞) were determined 1 hpi. $n \geq 3$ independent rat experiments; values are means ± SD. Data were evaluated using a 2-compartmental pharmacokinetic model.

Liposome	$CF_{zebrafish}$	$EF_{zebrafish}$ ($\times 10^3$)	$t_{1/2}$ $rat_{terminal}$ (min)	AUC_0^∞ rat (% ID ∗ mL/min)
DAPC 20:0	233.8 ± 38.2	7.0 ± 6.1	12.5 ± 10.1	19.6 ± 6.1
DAPC 20:4	398.2 ± 61.6	77.9 ± 49.4	54.4 ± 21.5	120.4 ± 31.9

the zebrafish embryo (i.e. transparency and availability of transgenic lines) allow for a clear distinction between nanoparticles located within or outside the vasculature. This feature was of special importance analyzing liposomes made of DOPC. Qualitatively, DOPC-based liposomes showed an intermediate circulation behavior (i.e. high fluorescence in circulation and strong signals in the PCV). However, long circulating properties should be observed for DOPC-based liposomes according to pharmacokinetic data reported in mice. Notably, an interesting phenomenon was observed for DOPC-based liposomes as compared to short circulating liposomes such as DSPC. Indeed, after injection, short circulating liposomes are attached to venous capillaries

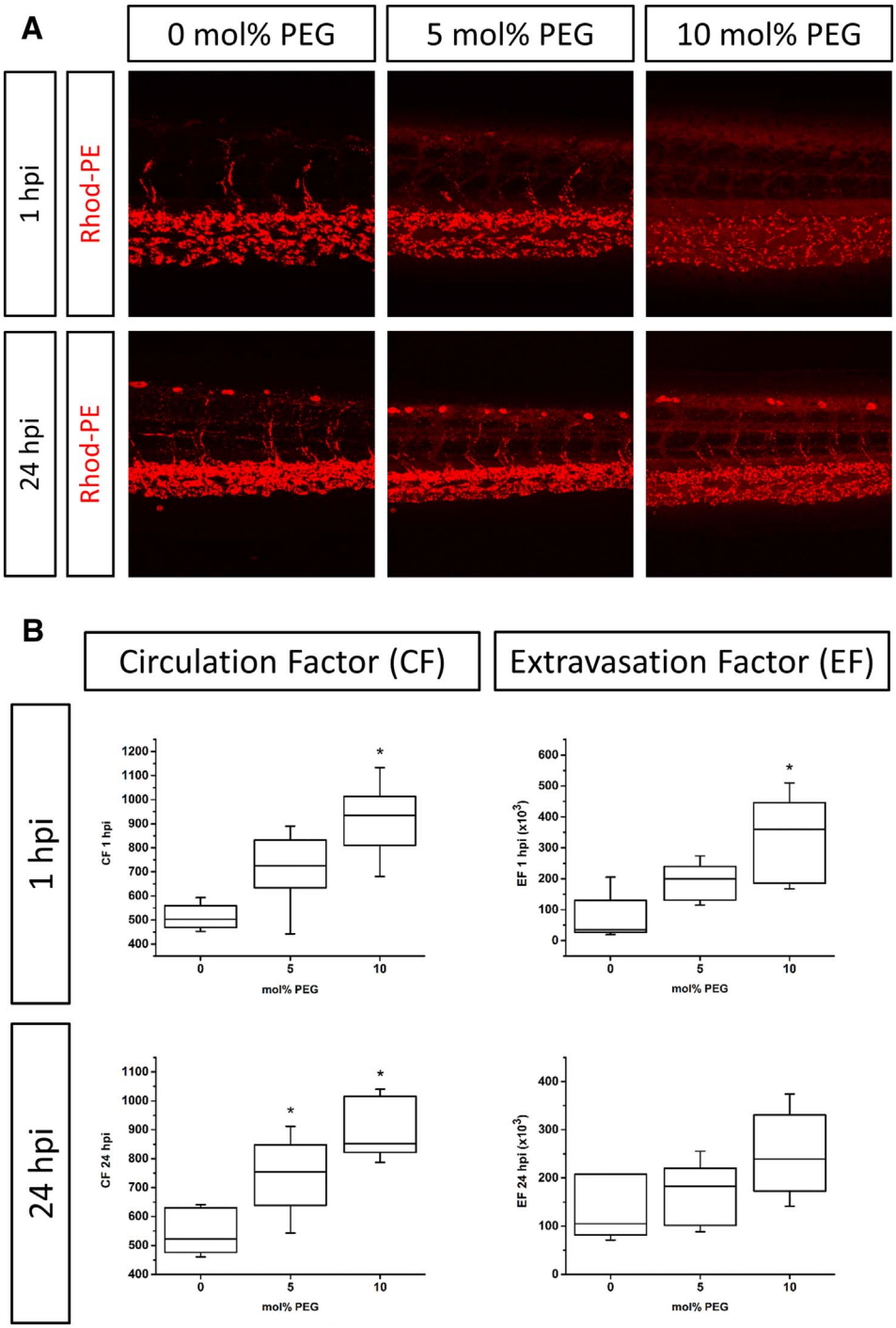

Fig. 7. Influence of PEGylation on liposome circulation in vivo in the zebrafish model. (A) Liposome formulations (DSPC/cholesterol with increasing amounts of DSPE-PEG_{2000}) were injected into transgenic zebrafish embryos and images were taken 1 and 24 hpi. (B) Circulation (CF) and extravasation factors (EF) of each lipid composition were calculated. $n \geq 5$ experiments. Box plots represent median, third and first quantiles, minima and maxima. *$p > 0.05$ as compared to control (0 mol% PEG).

inside the vasculature as can been visualized in merged fluorescence images of vasculature and liposomes. In sharp contrast, the strong fluorescence signals obtained for DOPC-based liposomes are located outside the vasculature. It is tempting to speculate that these extravascular signals result from extravasated liposomes accumulating in the perivascular space. DOPC-based liposomes have a low transition temperature (− 22 °C) which results in a fluid lipid bilayer at experimental conditions (28 °C). This characteristic might lead to an increased ability to diffuse through nanosized pores in the young and freshly formed vasculature of zebrafish embryos. The semi-quantitative assessment clearly showed, that DOPC-based liposomes belong to the group of long circulating formulations confirming published data in rodents.

In general, long circulating liposome formulations (DAPC 20:4, DOPC, DMPC) were still present in circulation 24 hpi and in addition showed a high degree of extravasation. In strong contrast, the circulation patter of short circulating liposomes (DPPC, DSPC, DAPC 20:0) was unaltered 24 hpi compared to 1 hpi. Therefore, obvious qualitative differences at specific time points allowed for a fast estimation of systemic circulation behavior, even without the proposed semi-quantitative analysis. However, if minor changes in the lipid composition have to be assessed and compared, qualitative differences of circulation behavior become less obvious.

To proof the validity of the zebrafish screening model to study such subtle phenomena, increasing amounts of cholesterol (up to 50 mol%) where incorporated into DSPC-based liposomes. It has been reported that incorporation of cholesterol increases liposome circulation half-life

and nanocarrier stability in mice [17,43]. In addition, cholesterol influences phospholipid dynamics and structure within bilayers and thereby has a strong impact on their phase transition temperature [44,45]. In agreement with our observation, concentration dependent modulation of phospholipid phase transition behavior led to a longer circulation time of liposomes containing cholesterol. It is tempting to speculate that cholesterol mediated effects such as membrane "fluidization" and reduced plasma protein binding [17] were responsible for the observed effect. Interestingly, the highest circulation factor was determined for DSPC-based liposomes with 30 mol% cholesterol. This plateau phenomenon was also observed by Semple et al. in mice. Successful assessment of these small changes in circulation behavior due to minor changes in liposome composition highlights the validity of the zebrafish model as sensitive and predictive screening tool.

After successful correlation and confirmation of published data from mice experiments in the zebrafish model, the zebrafish model was validated using a liposome formulation with unknown pharmacokinetic properties. Based on our previous findings in zebrafish embryos, that phosphatidylcholine-based lipids with a $T_m < 28$ °C show increased circulation properties, the unsaturated phospholipid DAPC 20:4 was selected. Liposomes composed of the previously tested long-chain saturated phospholipid DAPC 20:0 were selected as reference formulation. We expected that DAPC 20:4, which exists in the liquid crystalline state at 28 °C, increases the CF of liposomes in zebrafish embryos and finally circulation half-life in rodents as compared to DAPC 20:0. Indeed, based on the evaluation in zebrafish embryos, the pharmacokinetic properties of DAPC 20:4-based liposomes were successfully predicted in the rat using [^{3}H]-doxorubicin labeled formulations. In a final set of experiments, the effect of PEGylation was evaluated in the zebrafish model. In clinic, the encapsulation of doxorubicin into conventional (i.e. Myocet) or PEGylated liposomes (i.e. Doxil) increases the area under the curve (AUC) from 3.5 mg·h/L (free doxorubicin) to 19.4 mg·h/L or even 4082 mg·h/L, respectively and thus results in an improved therapeutic index [46]. As expected, Doxil-based formulations showed a significantly increased circulation behavior in the zebrafish. In addition, the zebrafish EF (i.e. extravasation of liposomes into adjacent tissue) was enhanced by PEGylation. All effects were concentration dependent and a function of the used amount of DSPE-PEG_{2000}.

Notably, ongoing experiments (manuscript in preparation) indicate that the proposed screening strategy can be applied to other types of nanoparticulate drug delivery systems such as polymer-based nanoparticles or super paramagnetic iron oxide nanoparticles (SPIONs). For example, a direct comparison of PEGylated liposomes and poly(ethylene glycol)-*b*-poly(ε-caprolactone) [PEG-PCL] micelles revealed similar circulation patterns in the zebrafish. Subsequent experiments in rats confirmed a long circulation behavior of these delivery systems. PEG-liposomes as well as PEG-PCL micelles increased the circulation half-life of the model drug doxorubicin by a factor of 42 and 60, respectively. Conclusively, pharmacokinetic properties of investigational as well as clinically approved nanoparticulate drug delivery systems can successfully be screened and verified in the zebrafish model.

5. Conclusion

In summary, a statistically significant difference in circulation behavior was observed for several different formulations starting from single- to multi-component lipid formulations. Furthermore, it was possible to study the effects of cholesterol and PEGylation and to predict the circulation behavior in mice and rats. Obtained results were indicative of a direct link between T_m, phospholipid bilayer fluidity, incorporation of surface coating and systemic circulation and extravasation. We conclude that the zebrafish model is a suitable screening tool to assess the influence of various parameters such as size, surface charge, encapsulation efficiency, targeting properties, and composition of nanoparticles on their circulation characteristics in vivo. Our proposed screening strategy is time- and cost-effective and can be used to optimize the circulation behavior of nanoparticulate drug delivery systems in a simple vertebrate model before moving to more complex pharmacokinetic studies in rodents. As compared to standard in vitro assays, nanoparticle formulations can be optimized under in vivo conditions including multiple factors simultaneously such as blood circulation, presence of various cell types, plasma protein binding and macrophage uptake. Its use as a screening model for the assessment of in vivo circulation behavior and toxicological effects during very early stages of drug discovery might therefore drastically reduce the amount of higher vertebrates needed for the pre-clinical assessment of nanoparticulate drug delivery systems in accordance to the 3R principle of animal welfare. In conclusion, this approach has the possibility to address an unmet pre-clinical need in the field of drug delivery and might facilitate the translation of the classical nanoparticle development process from an empirical approach, which is mainly based on optimization of physico-chemical characteristics, to an "optimization-by-design" concept.

Acknowledgements

DW and JH have equally contributed as senior authors. The authors are thankful for the financial support of the "Stiftung zur Förderung des pharmazeutischen Nachwuchses in Basel", "Freiwillige Akademische Gesellschaft Basel", "Novartis University Basel Excellence Scholarship for Life Sciences", the EU Horizon 2020 project "NanoReg2" (Swiss *SBF*I Nr. 15.0200-3) and the Swiss National Science Foundation (SNF grant No. 31003A_173057). The authors declare no conflicts of interests. Dr. M. Chami from the University of Basel, C-CINA, is acknowledged for Cryo-TEM experiments. We also thank Prof. Dr. M. Affolter, Dr. H.G. Belting and N. Schellinx for providing zebrafish eggs. Furthermore, we thank Prof. Dr. A. Kros, Dr. J. Bussmann, and Dr. F. Campbell from the University of Leiden for fruitful discussions and training regarding the handling of zebrafish embryos.

Appendix A. Supplementary data

Supplementary data to this article can be found online at http://dx.doi.org/10.1016/j.jconrel.2017.08.023.

References

[1] P. Ehrlich, Experimental Researches on Specific Therapy, on Immunity with Special Relationship between Distribution and Action of Antigens, Harben Lect., 1908.
[2] A.D. Bangham, M.M. Standish, J.C. Watkins, Diffusion of univalent ions across the lamellae of swollen phospholipids, J. Mol. Biol. 13 (1965) 238-IN27 http://dx.doi.org/10.1016/S0022-2836(65)80093-6.
[3] J.I. Hare, T. Lammers, M.B. Ashford, S. Puri, G. Storm, S.T. Barry, Challenges and strategies in anti-cancer nanomedicine development: an industry perspective, Adv. Drug Deliv. Rev. (n.d.). doi:http://dx.doi.org/10.1016/j.addr.2016.04.025.
[4] T.M. Allen, P.R. Cullis, Liposomal drug delivery systems: from concept to clinical applications, Adv. Drug Deliv. Rev. 65 (2013) 36–48, http://dx.doi.org/10.1016/j.addr.2012.09.037.
[5] A. Wicki, D. Witzigmann, V. Balasubramanian, J. Huwyler, Nanomedicine in cancer therapy: challenges, opportunities, and clinical applications, J. Control. Release 200C (2015) 138–157, http://dx.doi.org/10.1016/j.jconrel.2014.12.030.
[6] T. Lammers, F. Kiessling, M. Ashford, W. Hennink, D. Crommelin, G. Storm, Cancer nanomedicine: is targeting our target? Nat. Rev. Mater. 1 (2016), http://dx.doi.org/10.1038/natrevmats.2016.69.
[7] K.A. Whitehead, J. Matthews, P.H. Chang, F. Niroui, J.R. Dorkin, M. Severgnini, et al., In vitro–in vivo translation of lipid nanoparticles for hepatocellular siRNA delivery, ACS Nano 6 (2012) 6922–6929, http://dx.doi.org/10.1021/nn301922x.
[8] D.C. Drummond, O. Meyer, K. Hong, D.B. Kirpotin, D. Papahadjopoulos, Optimizing liposomes for delivery of chemotherapeutic agents to solid tumors, Pharmacol. Rev. 51 (1999) 691–744.
[9] D.C. Drummond, C.O. Noble, M.E. Hayes, J.W. Park, D.B. Kirpotin, Pharmacokinetics and in vivo drug release rates in liposomal nanocarrier development, J. Pharm. Sci. 97 (2008) 4696–4740, http://dx.doi.org/10.1002/jps.21358.
[10] B.S. Pattni, V.V. Chupin, V.P. Torchilin, New developments in liposomal drug delivery, Chem. Rev. 115 (2015) 10938–10966, http://dx.doi.org/10.1021/acs.chemrev.5b00046.
[11] S. Mitragotri, T. Lammers, Y.H. Bae, S. Schwendeman, S. De Smedt, J.-C. Leroux,

et al., Drug delivery research for the future: expanding the Nano horizons and beyond, J. Control. Release 246 (2017) 183–184, http://dx.doi.org/10.1016/j.jconrel.2017.01.011.
[12] B.J. Crielaard, A. Yousefi, J.P. Schillemans, C. Vermehren, K. Buyens, K. Braeckmans, et al., An in vitro assay based on surface plasmon resonance to predict the in vivo circulation kinetics of liposomes, J. Control. Release 156 (2011) 307–314, http://dx.doi.org/10.1016/j.jconrel.2011.07.023.
[13] C. Delvecchio, J. Tiefenbach, H.M. Krause, The zebrafish: a powerful platform for in vivo, HTS drug discovery, Assay Drug Dev. Technol. 9 (2011) 354–361, http://dx.doi.org/10.1089/adt.2010.0346.
[14] G.J. Lieschke, P.D. Currie, Animal models of human disease: zebrafish swim into view, Nat. Rev. Genet. 8 (2007) 353–367, http://dx.doi.org/10.1038/nrg2091.
[15] K. Howe, M.D. Clark, C.F. Torroja, J. Torrance, C. Berthelot, M. Muffato, et al., The zebrafish reference genome sequence and its relationship to the human genome, Nature 496 (2013) 498–503, http://dx.doi.org/10.1038/nature12111.
[16] L. Evensen, P.L. Johansen, G. Koster, K. Zhu, L. Herfindal, M. Speth, et al., Zebrafish as a model system for characterization of nanoparticles against cancer, Nano 8 (2016) 862–877, http://dx.doi.org/10.1039/c5nr07289a.
[17] S.C. Semple, A. Chonn, P.R. Cullis, Influence of cholesterol on the association of plasma proteins with liposomes, Biochemistry (Mosc) 35 (1996) 2521–2525, http://dx.doi.org/10.1021/bi950414i.
[18] P. Detampel, D. Witzigmann, S. Krähenbühl, J. Huwyler, Hepatocyte targeting using pegylated asialofetuin-conjugated liposomes, J. Drug Target. 22 (2014) 232–241, http://dx.doi.org/10.3109/1061186X.2013.860982.
[19] A. Gabizon, R. Catane, B. Uziely, B. Kaufman, T. Safra, R. Cohen, et al., Prolonged circulation time and enhanced accumulation in malignant exudates of doxorubicin encapsulated in polyethylene-glycol coated liposomes, Cancer Res. 54 (1994) 987–992.
[20] D. Witzigmann, S. Sieber, F. Porta, P. Grossen, A. Bieri, N. Strelnikova, et al., Formation of lipid and polymer based gold nanohybrids using a nanoreactor approach, RSC Adv. 5 (2015) 74320–74328, http://dx.doi.org/10.1039/C5RA13967H.
[21] D. Witzigmann, D. Wu, S.H. Schenk, V. Balasubramanian, W. Meier, J. Huwyler, Biocompatible polymer-peptide hybrid-based DNA nanoparticles for gene delivery, ACS Appl. Mater. Interfaces 7 (2015) 10446–10456, http://dx.doi.org/10.1021/acsami.5b01684.
[22] L.Y. Rizzo, S.K. Golombek, M.E. Mertens, Y. Pan, D. Laaf, J. Broda, et al., Vivo Nanotoxicity testing using the zebrafish embryo assay, J. Mater. Chem 1 (2013), http://dx.doi.org/10.1039/C3TB20528B.
[23] K. Kiene, S.H. Schenk, F. Porta, A. Ernst, D. Witzigmann, P. Grossen, et al., PDMS-b-PMOXA polymersomes for hepatocyte targeting and assessment of toxicity, Eur. J. Pharm. Biopharm. (2017) Verfahrenstechnik EV http://dx.doi.org/10.1016/j.ejpb.2017.07.002.
[24] Y.-L. Hu, W. Qi, F. Han, J.-Z. Shao, J.-Q. Gao, Toxicity evaluation of biodegradable chitosan nanoparticles using a zebrafish embryo model, Int. J. Nanomedicine 6 (2011) 3351–3359, http://dx.doi.org/10.2147/IJN.S25853.
[25] S.-W. Jin, D. Beis, T. Mitchell, J.-N. Chen, D.Y.R. Stainier, Cellular and molecular analyses of vascular tube and lumen formation in zebrafish, Development 132 (2005) 5199–5209, http://dx.doi.org/10.1242/dev.02087.
[26] B.M. Weinstein, D.L. Stemple, W. Driever, M.C. Fishman, Gridlock, a localized heritable vascular patterning defect in the zebrafish, Nat. Med. 1 (1995) 1143–1147.
[27] J. Schindelin, I. Arganda-Carreras, E. Frise, V. Kaynig, M. Longair, T. Pietzsch, et al., Fiji: an open-source platform for biological-image analysis, Nat. Methods 9 (2012) 676–682, http://dx.doi.org/10.1038/nmeth.2019.
[28] C.A. Schneider, W.S. Rasband, K.W. Eliceiri, NIH Image to ImageJ: 25 years of image analysis, Nat. Methods 9 (2012) 671–675.
[29] J. Huwyler, D. Wu, W.M. Pardridge, Brain drug delivery of small molecules using immunoliposomes, Proc. Natl. Acad. Sci. 93 (1996) 14164–14169.
[30] J. Huwyler, J. Yang, W.M. Pardridge, Receptor mediated delivery of daunomycin using immunoliposomes: pharmacokinetics and tissue distribution in the rat, J. Pharmacol. Exp. Ther. 282 (1997) 1541–1546.
[31] Y. Zhang, M. Huo, J. Zhou, S. Xie, PKSolver: an add-in program for pharmacokinetic and pharmacodynamic data analysis in Microsoft excel, Comput. Methods Prog. Biomed. 99 (2010) 306–314, http://dx.doi.org/10.1016/j.cmpb.2010.01.007.
[32] T.M. Ludden, S.L. Beal, L.B. Sheiner, Comparison of the Akaike Information Criterion, the Schwarz criterion and the F test as guides to model selection, J. Pharmacokinet. Biopharm. 22 (1994) 431–445.
[33] S. Isogai, M. Horiguchi, B.M. Weinstein, The vascular anatomy of the developing zebrafish: an atlas of embryonic and early larval development, Dev. Biol. 230 (2001) 278–301, http://dx.doi.org/10.1006/dbio. 2000.9995.
[34] S. Ahn, E. Seo, K. Kim, S.J. Lee, Controlled cellular uptake and drug efficacy of nanotherapeutics, Sci Rep 3 (2013) 1997, http://dx.doi.org/10.1038/srep01997.
[35] F. Fenaroli, D. Westmoreland, J. Benjaminsen, T. Kolstad, F.M. Skjeldal, A.H. Meijer, et al., Nanoparticles as drug delivery system against tuberculosis in zebrafish embryos: direct visualization and treatment, ACS Nano 8 (2014) 7014–7026, http://dx.doi.org/10.1021/nn5019126.
[36] C.B. Vibe, F. Fenaroli, D. Pires, S.R. Wilson, V. Bogoeva, R. Kalluru, et al., Thioridazine in PLGA nanoparticles reduces toxicity and improves rifampicin therapy against mycobacterial infection in zebrafish, Nanotoxicology 10 (2016) 680–688, http://dx.doi.org/10.3109/17435390.2015.1107146.
[37] A. Gabizon, F. Martin, Polyethylene glycol-coated (pegylated) liposomal doxorubicin, Drugs 54 (1997) 15–21, http://dx.doi.org/10.2165/00003495-199700544-00005.
[38] A.A. Gabizon, Y. Barenholz, M. Bialer, Prolongation of the circulation time of doxorubicin encapsulated in liposomes containing a polyethylene glycol-derivatized phospholipid: pharmacokinetic studies in rodents and dogs, Pharm. Res. 10 (1993) 703–708, http://dx.doi.org/10.1023/A:1018907715905.
[39] M.P. Craig, S.D. Gilday, D. Dabiri, J.R. Hove, An optimized method for delivering flow tracer particles to intravital fluid environments in the developing zebrafish, Zebrafish 9 (2012) 108–119, http://dx.doi.org/10.1089/zeb.2012.0740.
[40] S.R. Blechinger, T.G. Evans, P.T. Tang, J.Y. Kuwada, J.T. Warren, P.H. Krone, The heat-inducible zebrafish hsp70 gene is expressed during normal lens development under non-stress conditions, Mech. Dev. 112 (2002) 213–215, http://dx.doi.org/10.1016/S0925-4773(01)00652-9.
[41] R.J. Duszynski, J. Topczewski, E.E. LeClair, Simple, economical heat-shock devices for zebrafish housing racks, Zebrafish 8 (2011) 211–219, http://dx.doi.org/10.1089/zeb.2011.0693.
[42] M. Haldi, C. Ton, W.L. Seng, P. McGrath, Human melanoma cells transplanted into zebrafish proliferate, migrate, produce melanin, form masses and stimulate angiogenesis in zebrafish, Angiogenesis 9 (2006) 139–151, http://dx.doi.org/10.1007/s10456-006-9040-2.
[43] C. Kirby, J. Clarke, G. Gregoriadis, Effect of the cholesterol content of small unilamellar liposomes on their stability in vivo and in vitro, Biochem. J. 186 (1980) 591–598, http://dx.doi.org/10.1042/bj1860591.
[44] C.T. Boughter, V. Monje-Galvan, W. Im, J.B. Klauda, Influence of cholesterol on phospholipid bilayer structure and dynamics, J. Phys. Chem. B 120 (2016) 11761–11772, http://dx.doi.org/10.1021/acs.jpcb.6b08574.
[45] L. Redondo-Morata, M.I. Giannotti, F. Sanz, Influence of cholesterol on the phase transition of lipid bilayers: a temperature-controlled force spectroscopy study, Langmuir 28 (2012) 12851–12860, http://dx.doi.org/10.1021/la302620t.
[46] J. Huwyler, J. Drewe, S. Krähenbuhl, Tumor targeting using liposomal antineoplastic drugs, Int. J. Nanomedicine 3 (2008) 21–29.

Chapter III-I

Directing Nanoparticle Biodistribution through Evasion and Exploitation of Stab2-Dependent Nanoparticle Uptake

Frederick Campbell, Frank L. Bos, **Sandro Sieber**, Gabriela Arias-Alpizar, Bjørn E. Koch, Jörg Huwyler, Alexander Kros, Jeroen Bussmann

Manuscript: ACS Nano (2018) [42]

Highlights: In mammalians, macromolecular and colloidal waste is removed from blood circulation by scavenging receptors on liver sinusoidal endothelial cells, which are part of the reticuloendothelial system (RES). Interestingly, various nanoparticles were also found to bind to the caudal vein of zebrafish embryos resulting in their clearance from blood circulation. This article describes the identification and characterization of a specific orthologue zebrafish receptor, which is responsible for the observed nanoparticle binding pattern in zebrafish embryos. Different fluorescently labelled nanoparticles and various specific receptor binding molecules were injected in zebrafish and mice. As a result, the Stabilin-2 receptor has been discovered to scavenge nanoparticles from blood circulation in the caudal vein of zebrafish embryos/larvae and in the mammalian liver lined with liver sinusoidal endothelial cells. A zebrafish line lacking the Stabilin-2 receptor was generated via CRISPR/Cas9 mutagenesis in order to validate these findings. Finally, selective and functional nanoparticulate drug delivery via this receptor has been performed to demonstrate receptor mediated cellular uptake of bound nanomedicines.

ACS NANO

Cite This: ACS Nano XXXX, XXX, XXX−XXX

www.acsnano.org

ARTICLE

Directing Nanoparticle Biodistribution through Evasion and Exploitation of Stab2-Dependent Nanoparticle Uptake

Frederick Campbell,[*,†] Frank L. Bos,[‡,#,⊥] Sandro Sieber,[§,⊥] Gabriela Arias-Alpizar,[†,⊥] Bjørn E. Koch,[∥] Jörg Huwyler,[§] Alexander Kros,[*,†] and Jeroen Bussmann[*,†,∥]

[†]Department of Supramolecular and Biomaterials Chemistry, Leiden Institute of Chemistry (LIC), Leiden University, P.O. Box 9502, 2300 RA Leiden, The Netherlands

[‡]Hubrecht-Institute-KNAW and University Medical Centre and Centre for Biomedical Genetics, Uppsalalaan 8, 3584 CT Utrecht, The Netherlands

[§]Division of Pharmaceutical Technology, Department of Pharmaceutical Science, University of Basel, Klingelbergstrasse 50, Basel CH-4056, Switzerland

[∥]Department of Molecular Cell Biology, Institute Biology Leiden (IBL), Leiden University, P.O. Box 9502, 2300 RA Leiden, The Netherlands

Supporting Information

ABSTRACT: **Up to 99% of systemically administered nanoparticles are cleared through the liver. Within the liver, most nanoparticles are thought to be sequestered by macrophages (Kupffer cells), although significant nanoparticle interactions with other hepatic cells have also been observed. To achieve effective cell-specific targeting of drugs through nanoparticle encapsulation, improved mechanistic understanding of nanoparticle−liver interactions is required. Here, we show the caudal vein of the embryonic zebrafish (*Danio rerio*) can be used as a model for assessing nanoparticle interactions with mammalian liver sinusoidal (or scavenger) endothelial cells (SECs) and macrophages. We observe that anionic nanoparticles are primarily taken up by SECs and identify an essential requirement for the scavenger receptor, *stabilin-2* (*stab2*) in this process. Importantly, nanoparticle−SEC interactions can be blocked by dextran sulfate, a competitive inhibitor of *stab2* and other scavenger receptors. Finally, we exploit nanoparticle−SEC interactions to demonstrate targeted intracellular drug delivery resulting in the selective deletion of a single blood vessel in the zebrafish embryo. Together, we propose *stab2* inhibition or targeting as a general approach for modifying nanoparticle−liver interactions of a wide range of nanomedicines.**

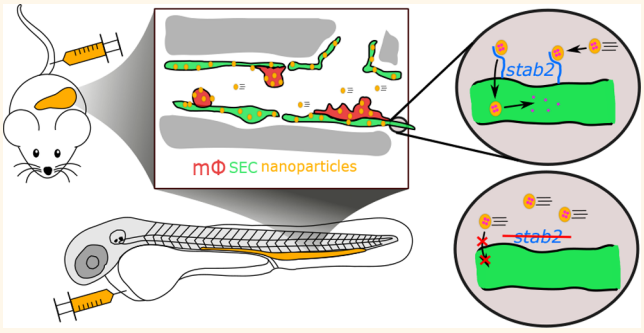

KEYWORDS: *endothelial cells, scavenger receptor, nanomedicine, liposomes, stabilin, zebrafish, targeted drug delivery*

Cell-type specific targeting is a common goal in nanoparticle drug delivery. However, the inability to efficiently target subpopulations of cells, beyond the macrophages and monocytes of the mononuclear phagocyte system (MPS), has stymied progress of these technologies into clinical use.[1−4] Up to 99% of systemically administered nanoparticles, of all shapes, sizes, and chemical compositions are cleared through the liver.[5] While it is generally accepted that nanoparticles are taken up by liver-resident macrophages (Kupffer cells (KCs)),[6] the principal cell type of the MPS in the liver, significant nanoparticle interactions with other hepatic cells, including liver sinusoidal endothelial cells (LSECs), hepatocytes, and hepatic B-cells, have also been observed.[7−10] In these instances however, the cell-specific mechanisms underpinning these interactions have not been elucidated. A detailed understanding of exactly where and how nanoparticles are sequestered and cleared within the liver is crucial for the effective optimization of nanoparticle-mediated drug delivery.

The principle function of the liver is to maintain homeostasis. This includes the removal ("scavenging") of macromolecular and colloidal waste and pathogens from the blood. Within the liver, scavenging function is primarily associated with the hepatic sinusoids,[11] specialized blood vessels connecting the

Received: October 2, 2017
Accepted: January 10, 2018
Published: January 10, 2018

DOI: 10.1021/acsnano.7b06995
ACS Nano XXXX, XXX, XXX−XXX

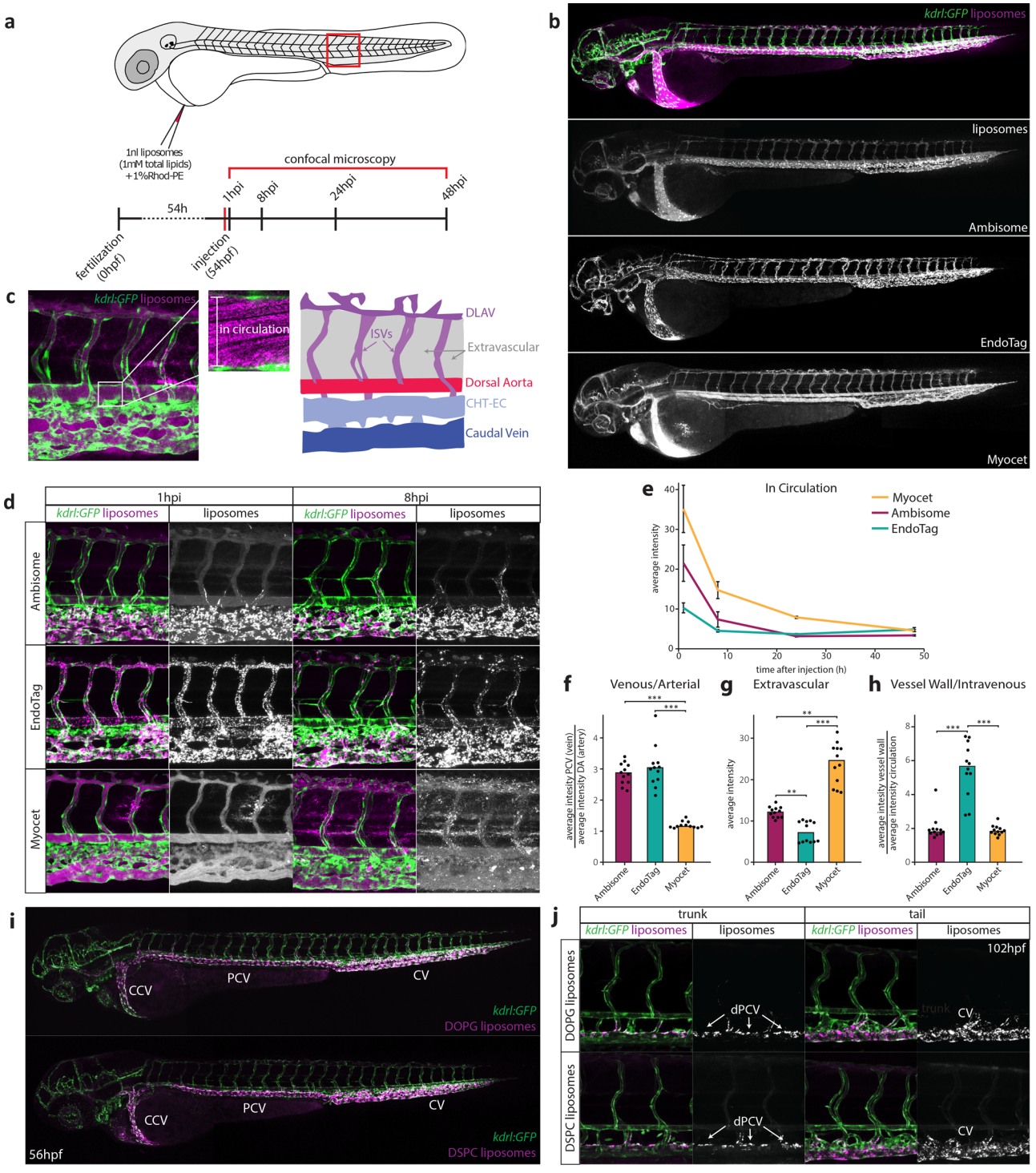

Figure 1. A zebrafish model for liposome biodistribution. (a) Schematic of liposome injection and quantification in zebrafish. Fluorescently labeled liposomes (1 mM total lipids containing 1 mol % Rhod-PE) were injected into the duct of Cuvier at 54 hpf. Confocal microscopy is performed in a defined region (boxed) caudal to the yolk extension at 1, 8, 24, and 48 h after injection. (b) Whole-embryo view of liposome distribution in *kdrl:GFP* transgenic embryos, 1 hpi with three different liposome formulations (AmBisome, EndoTAG-1, and Myocet). (c) High-resolution imaging allows quantification of liposomes in circulation (measured in the lumen of the dorsal aorta (white box)) and liposome association with different blood vessel types (see Supporting Information). CHT-EC: caudal hematopoietic tissue endothelial cells, DLAV: dorsal longitudinal anastomotic vessel. ISV: intersegmental vessel. (d) Tissue level view of liposome distribution in *kdrl:gfp* transgenic embryos, 1 h and 8 h after injection with three different liposome formulations and a single confocal section through the dorsal aorta (DA) at 1 h after injection. (e) Quantification of liposome levels in circulation based on mean rhodamine fluorescence intensity in the lumen of the dorsal aorta at 1, 8, 24, and 48 h after injection (error bars: standard deviation.) $n = 6$ individually injected embryos per formulation per time point (in two experiments). (f) Quantification of liposome levels associated with venous *vs* arterial endothelial cells based on rhodamine fluorescence intensity associated with caudal vein (CV) *vs* DA at 8 h after injection. (g) Quantification of extravascular liposome levels based on rhodamine fluorescence intensity outside of the vasculature between the DLAV and DA at 8 h after injection. (h) Quantification of liposome levels associated with the vessel wall based on rhodamine fluorescence intensity associated with all endothelial cells relative to

DOI: 10.1021/acsnano.7b06995
ACS Nano XXXX, XXX, XXX−XXX

Figure 1. continued

rhodamine fluorescence intensity in circulation at 1h after injection. (f–h) Bar height represents median values, dots represent individual data points, brackets indicate significantly different values (*: $p < 0.05$, **: $p < 0.01$, ***: $p < 0.001$) based on Kruskal–Wallis and Dunn's tests with Bonferroni correction for multiple testing. $n = 12$ individually injected embryos per group (in 2 experiments). (i) Whole-embryo view of liposome distribution in *kdrl:GFP* transgenic embryos, 1 h after injection with DOPG and DSPC liposomes. Liposome accumulation for both formulations is observed in the primitive head sinus (PHS), common cardinal vein (CCV), posterior cardinal vein (PCV), and caudal vein (CV). (j) Tissue level view of liposome distribution in *kdrl:GFP* transgenic embryos, 1 h after injection with DOPG and DSPC liposomes at 102 hpf. Liposome accumulation is observed in the entire caudal vein (CV), but only on the dorsal side of the PCV (dPCV, arrows).

hepatic artery and portal vein (incoming blood flow) with the central vein (outgoing blood flow). In these vessels, scavenging function is facilitated by a >10-fold decrease in blood flow velocity.[12] Hepatic sinusoids are primarily composed of LSECs (~70%) and KCs (~20%).[13] Together these cells comprise the hepatic reticuloendothelial system (RES), a term originally proposed in the early 20th century by Aschoff[14] to include specialized cells that accumulated vital stains. Since then, the term RES has been largely superseded by the MPS, which in the liver sinusoid includes KCs but not LSECs.

Cells with a scavenging function similar to mammalian LSECs have been identified in all vertebrates examined. However, in teleost fish, sharks, and lampreys these cells have not been found in the liver, but are identified in various other organs.[15] Collectively, these cells are known as scavenger endothelial cells (SECs), a specialized endothelial cell type functionally defined as the major clearance site of endogenous macromolecules such as oxidized low-density lipoprotein (oxLDL) and hyaluronic acid (HA) from the blood.[11] Mammalian LSECs have also been implicated in clearance of blood-borne viruses from circulation[16−18] and are important cell-types of both the innate and adaptive immune system.[19,20] In LSECs, clearance function is mediated through a relatively small number of pattern-recognition endocytosis receptors.[11] Given the wide variety of macromolecules, colloids, and pathogens sequestered by LSECs, these receptors are clearly promiscuous with respect to potential binding partners. However, what general physicochemical properties direct materials to LSECs, to what extent are individual endocytosis receptors involved, and the significance of these interactions in the clearance of nanoparticles from circulation are not clearly defined.

Here, we show a specific part of the zebrafish embryonic vasculature displays functional homology to the mammalian liver sinusoid and includes macrophages/monocytes and functional SECs. Using this model, we are able to study which general properties of nanoparticles result in their uptake by each of these cell types after intravenous injection. For SECs, we reveal an important molecular mechanism required for nanoparticle clearance, involving the transmembrane receptor *stabilin-2*, which can be both inhibited and exploited to guide cell-specific nanoparticle-mediated drug delivery.

RESULTS AND DISCUSSION

A Zebrafish Model for Liposome Biodistribution. Of the myriad nanoparticles reported as potential drug delivery vectors, liposomes are the most widely investigated and the major class of nanoparticles approved for clinical use.[21,22] So far, the ability to predict the fate of liposomes following intravenous injection based on lipid composition alone has been limited. Furthermore, the opacity of mammalian models precludes comprehensive assessment of the dynamic behavior of liposomes *in vivo*. Recent studies have shown that the small and transparent zebrafish embryo allows for the direct observation of circulating nanoparticles, including liposomes, and their interactions with cells.[23−26] These studies show key aspects of nanoparticle behavior, including uptake by the MPS, are conserved between zebrafish and mammals. We therefore selected this model to identify the influence of lipid composition on liposome biodistribution and the mechanisms of liposome uptake by cells.

Three liposome formulations, either approved for clinical use or under development (Myocet, EndoTAG-1, and AmBisome),[27−29] were initially selected for intravenous injection into zebrafish embryos. These formulations were specifically chosen to assess the influence of contrasting nanoparticle surface charge. Myocet is a neutral liposomal-doxorubicin formulation showing extravasation in tumors.[27] EndoTAG-1 is a positively charged liposomal-paclitaxel formulation targeting actively growing tumor blood vessels.[28] AmBisome is a negatively charged liposomal-amphotericin B formulation used to treat severe fungal infections.[29] Fluorescently labeled liposomes (~100 nm in diameter and without encapsulated drugs) based on the lipid composition of these formulations (Table S1) were injected intravenously into the duct of Cuvier of zebrafish embryos at 54 h post-fertilization (hpf), a stage at which most organ systems are established. Injected embryos were imaged using confocal microscopy at 1, 8, 24, and 48 h post-injection (hpi) (Figure 1a), and confocal micrographs were generated for the entire embryo (whole organism level) as well as from a region caudal to the cloaca (tissue level) (Figure 1b,d and Figure S1). We developed a quantification method to compare levels of circulating liposomes, extravasation, and accumulation in different blood vessel types between formulations (Figure 1c,e–h and Figure S2).

At 1 hpi, on a whole organism level, all three liposome formulations were found associated with the blood vasculature and over time, the fluorescence associated with freely circulating liposomes within the lumen of the dorsal aorta, decayed exponentially (Figure 1b,e). At the tissue level however, clear differences in liposome biodistribution were observed (Figure 1d). Consistent with their behavior in mammals, neutral Myocet liposomes were mostly seen circulating within the blood vessel lumen. At 1 hpi, liposome translocation through the vessel wall (extravasation) was already evident, and between 1 and 8 hpi, co-localization with plasma-exposed macrophages was observed (Figure 1d,g, Figure S3). Increasing the size of Myocet liposomes resulted in enhanced uptake by macrophages, whereas surface PEGylation—a strategy widely employed to limit nanoparticle clearance *in vivo*[30]—effectively inhibited phagocytotic uptake as described previously (Figure S3).[23,26]

For EndoTAG-1 and AmBisome, a large fraction of the injected dose was removed from circulation by 1 hpi and 8 hpi respectively, and these formulations were found associated with the vessel wall (Figure 1e,h). Strikingly however, anionic

DOI: 10.1021/acsnano.7b06995
ACS Nano XXXX, XXX, XXX–XXX

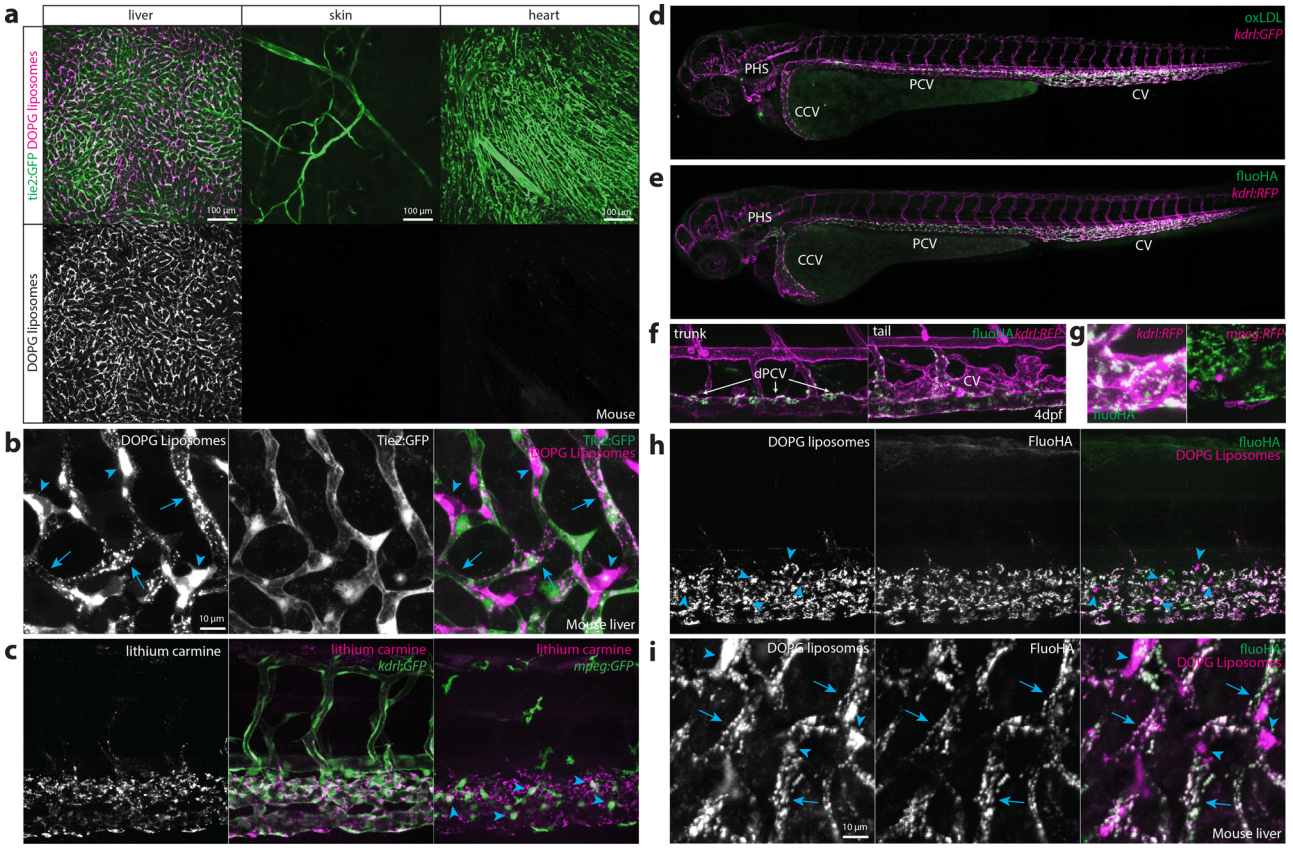

Figure 2. Identification of scavenger endothelial cells (SECs) in zebrafish embryos. (a, b) *Ex vivo* imaging of adult Tie2:GFP transgenic mouse organs, 1 h after injection with DOPG liposomes. (a) Liposome accumulation is observed in liver, but not in the ear skin or heart muscle. (b) Within the liver, DOPG liposomes are observed as punctae within Tie2:GFP$^+$ sinusoidal ECs (arrows) as well as sinusoid-associated cells which based on shape and position were identified as KCs (arrowheads). (c) Tissue level view of lithium carmine distribution in *kdrl:GFP* and *mpeg:GFP* transgenic zebrafish embryos, 1 h after injection. Lithium carmine (carminic acid) fluorescence co-localizes both with *kdrl:GFP*$^+$ endothelial cells in the caudal vein and *mpeg:GFP*$^+$ monocytes/macrophages (arrowheads) within the CHT. (d) Whole-embryo view of fluorescent oxLDL distribution in *kdrl:GFP* transgenic embryos, 1 h after injection. Accumulation of oxLDL is observed in the PHS, CCV, PCV, and CV. (e) Whole-embryo view of fluoHA distribution in *kdrl:RFP* transgenic embryos, 1 h after injection. Accumulation of fluoHA is observed in the PHS, CCV, PCV, and CV. (f) Tissue level view of fluoHA distribution in *kdrl:RFP* transgenic embryos, 1 h after injection at 102 hpf. FluoHA accumulation is observed in the entire caudal vein (CV), but only on the dorsal side of the PCV (dPCV, arrows). (g) Tissue level view of fluoHA in *kdrl:RFP* and *mpeg:RFP* transgenic embryos. Co-localization of RFP expression and fluoHA is observed only within *kdrl:RFP* endothelial cells, but not *mpeg:RFP* monocytes/macrophages. (h) Tissue level view of co-injected fluoHA and DOPG liposomes, 1 h after injection reveals co-localization in SECs. Monocytes/macrophages (arrowheads) take up DOPG but not fluoHA. (i) *Ex vivo* imaging of adult mouse liver, 1 h after injection with fluoHA and DOPG liposomes reveals widespread co-localization within sinusoidal ECs (arrows). KCs (arrowheads) take up DOPG liposomes only.

AmBisome liposomes associated only with ECs of a subset of blood vessels, namely the caudal vein (CV), the posterior and common cardinal veins (PCV and CCV), and the primary head sinus (PHS) as well as ECs within the caudal hematopoietic tissue (CHT-ECs) (Figure 1d,f–h).[31] These comprise the majority of venous ECs within the zebrafish embryo at this developmental stage.[32] Cationic EndoTAG-1 liposomes at 1 hpi associated with all ECs as expected[33] but at later time points remain associated only with venous ECs.

AmBisome, EndoTAG-1, and Myocet are each composed of various mixtures of (phospho)lipids and cholesterol. In these cases, lipid headgroup chemistries, fatty acid chain saturation and cholesterol content, will together combine to affect the overall physicochemical character of the formulated liposomes and consequently their *in vivo* fate. To limit potential variation in liposome membrane composition, we next formulated and injected ∼100 nm liposomes composed of the individual (phospho)lipids constituting AmBisome, EndoTAG-1, and Myocet (Figure S4 and Table S1). We also included liposomes composed of 1,2-dioleoyl-*sn*-glycero-3-phospho-(1′-*rac*-glycerol) (DOPG) and 1,2-dioleoyl-*sn*-glycero-3-phosphocholine (DOPC). In these experiments, injected cationic liposomes (measured zeta potential; >30 mV) initially associated with both arterial and venous ECs of the embryonic fish. All anionic liposomes (<−30 mV) associated with venous ECs alone, and the behavior of neutral liposomes was dependent on lipid fatty acid chain saturation, whereby "fluid" liposome membranes (for example, DOPC), rich in unsaturated lipids, are freely circulating, whereas those composed of 'rigid', saturated lipids (for example, 1,2-distearoyl-*sn*-glycero-3-phosphocholine (DSPC)) associated with venous ECs. Of these, liposomes composed of DSPC and DOPG associated with venous ECs of the CCV, PHS, PCV, CHT, and CV most strongly (Figure 1i, Figure S4a,d). Both these liposomes also accumulated in macrophages within the CHT and along the CCV (Figure S5).

Differential distribution of nanoparticles over blood vessel networks has previously been attributed to differences in flow patterns.[7,25] However, when injections were performed in 4

DOI: 10.1021/acsnano.7b06995
ACS Nano XXXX, XXX, XXX−XXX

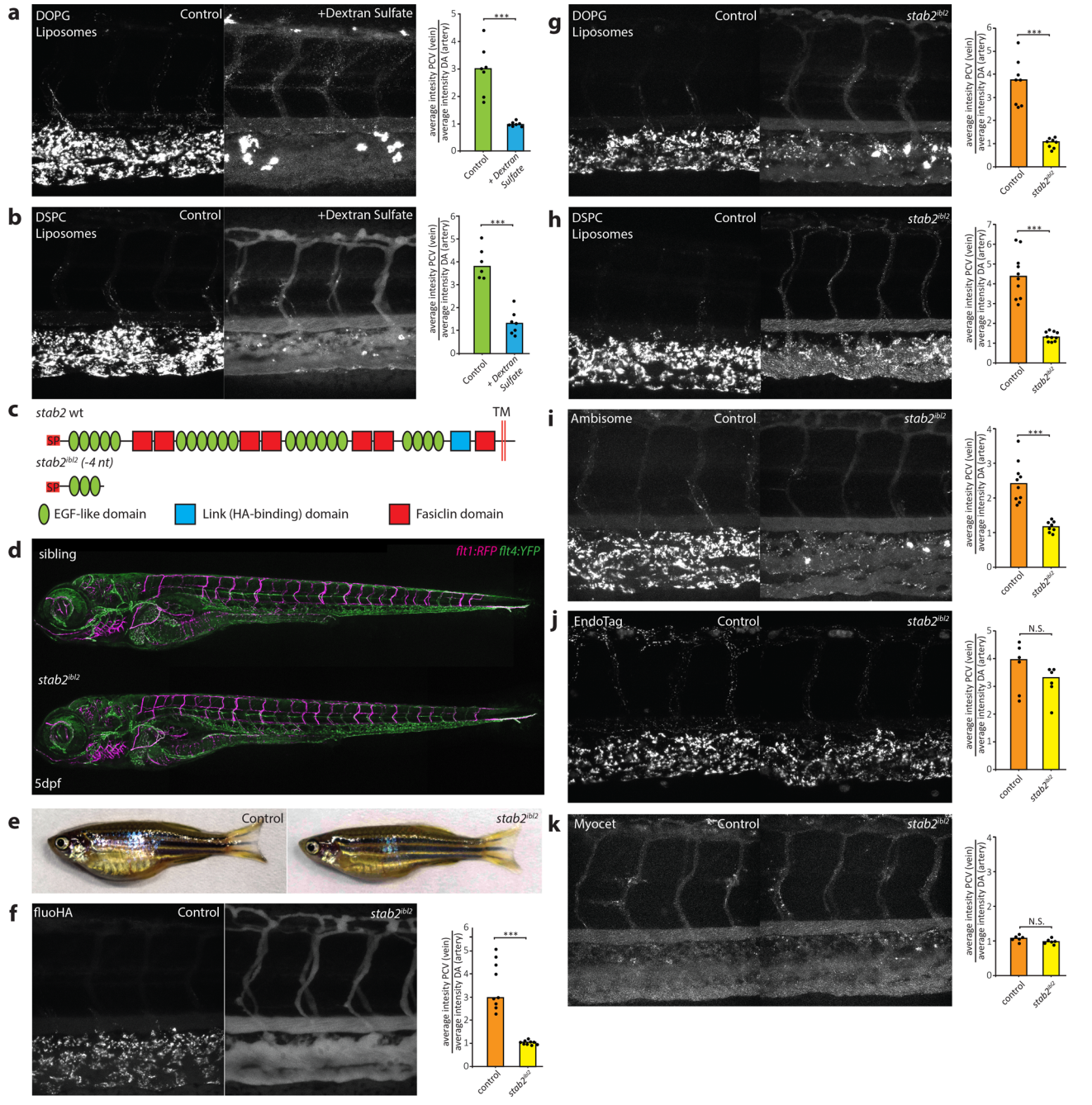

Figure 3. *stab2* is required for anionic liposome uptake by SECs. (a, b) Tissue level view of DOPG (a) and DSPC (b) liposome distribution at 1 hpi in control and dextran sulfate injected embryos, with quantification of liposome levels associated with venous *vs* arterial endothelial cells based on rhodamine fluorescence intensity associated with CV *vs* DA. (c) *stab2* domain structure predicted to be expressed from the wild-type *stab2* and the *stab2*^{ibl2} allele. (d) Whole-embryo view of *flt1:RFP, flt4:YFP* double transgenic embryos at 5 dpf to visualize blood vascular and lymphatic development. No defects were identified during (lymph)angiogenesis and vascular patterning in *stab2*^{ibl2} homozygous embryos compared to sibling controls. (e) Fertile adult females (*stab2*^{ibl2} homozygous and sibling controls) at 3 months post-fertilization. (f–k) Tissue level view of fluoHA (f) and DOPG (g), DSPC (h), AmBisome (i), EndoTAG-1 (j), and Myocet (k) liposome distribution at 1 hpi in *stab2*^{ibl2} and sibling control embryos, with quantification of liposome levels associated with venous *vs* arterial endothelial cells based on rhodamine fluorescence intensity associated with CV *vs* DA. (a, b, f–k) Bar height represents median values, dots represent individual data points, and brackets indicate significantly different values (*: $p < 0.05$, **: $p < 0.01$, ***: $p < 0.001$, N.S.: not significant) based on Mann–Whitney test. $n = 6–10$ per group (in two experiments).

day-old zebrafish embryos, both DOPG and DSPC liposomes preferentially associated with only a subset of venous ECs along the dorsal side of the PCV (dPCV) (Figure 1j). Liposome association with a subset of ECs in a single, straight blood vessel (where flow patterns are expected to be similar throughout) indicated dPCV ECs are a cell type distinct from ventral PCV (vPCV) ECs. Indeed, differentiation of dPCV and vPCV ECs has previously been observed during the induction of lymphatic differentiation and subintestinal vein angiogenesis,[34,35] suggesting dPCV differentiation may lead to the expression of specific receptors by these ECs which in turn

DOI: 10.1021/acsnano.7b06995
ACS Nano XXXX, XXX, XXX–XXX

could mediate the selective binding of DOPG and DSPC liposomes.

Identification of a Zebrafish EC Type Homologous to Mammalian LSECs. Selective association of liposomes with most venous ECs has not been observed in adult mammals. However, we hypothesized a more restricted subset of ECs in mammals could be functionally related to venous ECs of the embryonic zebrafish. To test this hypothesis, DOPG liposomes were injected intravenously into Tie2:GFP+ adult mice. In these mice, liposomes were removed from circulation within 1 hpi, and a striking accumulation was observed in the liver (Figure 2a). Within the liver, liposomes associated with Tie2:GFP+ sinusoidal ECs and with cells identified as KCs based on cell shape and intravascular localization (Figure 2b). No liposome accumulation was observed in hepatocytes or other analyzed organs. This suggested venous ECs and macrophages within the CHT and CV of the embryonic zebrafish were functionally homologous to LSECs and KCs of the mammalian liver and comprise the RES in zebrafish embryos. To confirm this, we injected colloidal lithium carmine (Li-Car), the most prominent vital stain originally used to define the mammalian RES, into zebrafish embryos. Making use of the inherent fluorescence of carminic acid,[36] we observed accumulation of this colloid in the same blood vessels (CV, CHT, PCV, and PHS) and subcellular structures within venous ECs and macrophages, in which DOPG and DSPC liposomes also accumulate (Figure 2c).

A small number of transmembrane receptors are selectively expressed in mammalian LSECs compared to other blood vascular ECs.[11] These include the scavenger receptors Stabilin-1 and -2[37] and the mannose receptor Mrc1. Analysis of the expression patterns of their orthologs (*stab1, stab2* and *mrc1a*) in zebrafish embryos confirmed their restricted expression in venous ECs of the PHS, PCV, CHT, and CV as described previously.[38,39] Importantly, expression of these genes becomes enriched in the dPCV, matching observed EC binding specificities of both DOPG and DSPC liposomes (Figure S6).

LSECs mediate the scavenging of macromolecular waste including oxLDL and HA through receptor-mediated endocytosis.[40] Therefore, we injected fluorescently labeled oxLDL and HA (fluoHA) and observed their rapid endocytosis, within the same subset of venous ECs (within the PHS, CCV, (d)PCV, and CV) (Figure 2d–f). Based on the conserved uptake of DOPG liposome, oxLDL, fluoHA, and Li-Car from circulation and expression of known LSEC markers by this venous EC subset in zebrafish embryos, we define them as SECs - homologous to mammalian LSECs.

In contrast to DSPC and DOPG liposomes and to oxLDL, fluoHA uptake was specific to SECs, and no uptake was observed in macrophages (Figure 2g). We next used fluoHA as a marker for endocytosis in SECs. Co-injection of fluoHA with DSPC or DOPG liposomes resulted in precise intracellular co-localization in all SECs of the embryonic fish, while in macrophages only liposome internalization was observed (Figure 2h, Figure S7). Intracellular co-localization in LSECs (but not KCs) of fluoHA and DOPG liposomes was conserved in the adult mouse liver (Figure 2i). These results demonstrated fluoHA endocytosis is a selective vital marker for SECs in vertebrates and offered a convenient method to study SEC differentiation in the developing zebrafish embryo (Figure S8). Importantly, we found SECs were present at the earliest time point at which intravenous injection is possible (28 hpf). During embryonic and larval stages, SECs were maintained within the CV, but starting at 52 hpf became gradually restricted to the dPCV. No fluoHA uptake was observed in embryonic veins that develop during later stages, such as in the brain and subintestinal vasculature. These results show that SECs are one of the first EC subtypes to emerge during embryonic development and provide the first analysis of early embryonic SEC differentiation in any vertebrate.

Stabilin-2 Is Required for Uptake of Liposomes and Other Nanoparticles by SECs. The precise intracellular co-localization of fluoHA with DOPG and DSPC liposomes in SECs indicated the use of a shared receptor for endocytosis. Importantly, one of the markers for SECs in zebrafish embryos and adult mammals, Stabilin-2, has been identified as the main HA clearance receptor in the mouse liver.[40] *In vitro,* Stabilin-2 and its paralog Stabilin-1 have been shown to bind to a large variety of endogenous (mostly anionic) macromolecules[41] as well as phosphothiorate-modified antisense oligonucleotides (PS-ASO),[42] apoptotic cell bodies,[43] biotinylated albumin,[44] and carbon nanotubes.[45] *In vivo,* Stabilin-1 and Stabilin-2 were shown to mediate sequestration (but not uptake) by LSECs of aged erythrocytes in a phosphatidylserine-dependent manner.[46] Stabilin-1 and Stabilin-2 are both nonessential genes for development and normal physiology in mice, with mice lacking both Stabilin-1 and Stabilin-2 displaying deficient removal of nephrotoxic macromolecules from circulation.[37] To test if stabilins were involved in liposome uptake by SECs, embryos were first pretreated with dextran sulfate - a competitive inhibitor of scavenger receptors, including *stab1* and *stab2*.[47,48] Subsequent liposome injection (or co-injection) resulted in a striking loss of liposome uptake by SECs, offset by an increase in circulating liposomes, and particularly in the case of DOPG liposomes, an increase in macrophage uptake (Figure 3a,b). In contrast, injection of mannan, a competitive inhibitor of *mrc1a*,[49] did not inhibit liposome uptake by SECs (data not shown).

To identify the specific role of *stab1* and *stab2* in liposome uptake, mutants for both genes were generated through CRISPR/Cas9-mediated mutagenesis. Here, we report the analysis of a *stab2* mutant line, in which we identified a 4nt deletion ($stab2^{ibl2}$), leading to a frameshift in the *stab2* coding sequence and a premature stop codon (C233X) (Figure 3c, Figure S9). This mutation is predicted to remove most conserved *stab2* domains including all fasiclin domains, the HA binding Link domain, and the transmembrane and cytoplasmic segments. Homozygous $stab2^{ibl2}$ mutants displayed a strong reduction of *stab2*, but not of *stab1* or *mrc1a,* mRNA expression indicating normal SEC differentiation and nonsense-mediated decay of $stab2^{ibl2}$ mRNA (Figure S10). $Stab2^{ibl2}$ mutants survived throughout embryonic development without defects in either blood or lymphatic vascular systems, which were described previously for *stab2* morphants,[50,51] and fertile adults were identified in normal Mendelian ratios (Figure 3d,e). Consistent with the increase in circulating HA levels observed in mouse Stab2 knockouts,[52] a complete loss of fluoHA uptake by SECs was observed in zebrafish $stab2^{ibl2}$ mutants, showing a conserved role for *stab2* in HA clearance in vertebrates (Figure 3f). Importantly, when either DOPG or DSPC liposomes were injected in $stab2^{ibl2}$ mutants, a strong reduction of liposome endocytosis by SECs was observed, offset by an increase in circulating liposome levels and an increase in macrophage uptake (Figure 3g,h). Differential liposome uptake in neighboring venous ECs of embryos with a mosaic loss of *stab2* function indicated a cell-autonomous role of *stab2*

DOI: 10.1021/acsnano.7b06995
ACS Nano XXXX, XXX, XXX–XXX

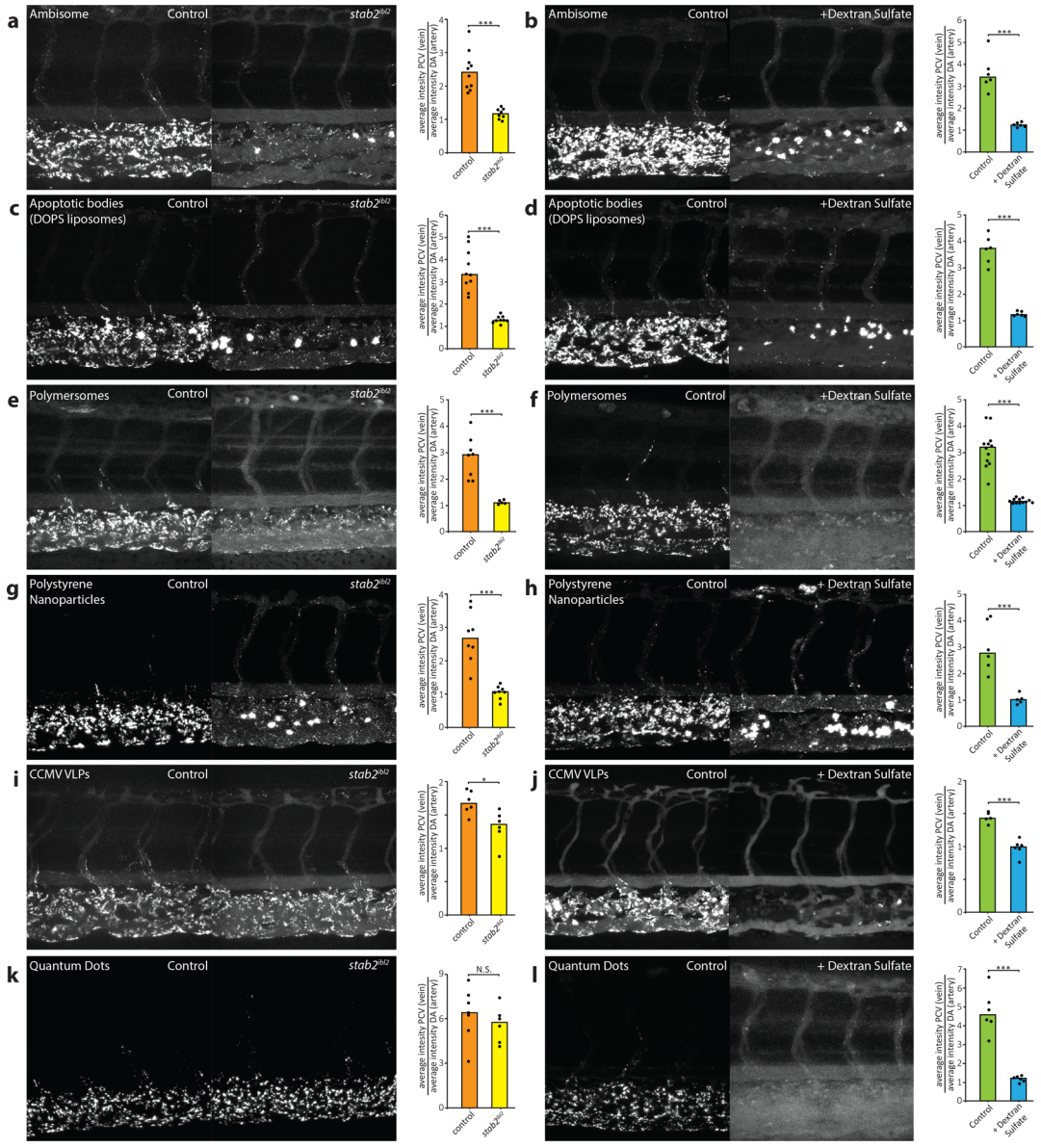

Figure 4. *stab2*-mediated scavenging of anionic nanoparticles *in vivo*. (a–i) Tissue level view of DOPS liposome (a, b), PIB-PEG polymersome (c, d), carboxylated polystyrene nanoparticle (e, f), CCMV virus-like particle (g, h), and carboxylated quantum dot (i, j) distribution at 1 hpi in *stab2*^{ibl2} and sibling control embryos (a, c, e, g, i) or control and dextran sulfate injected embryos (b, d, f, h, j). Quantification of nanoparticle levels associated with venous *vs* arterial endothelial cells based on rhodamine fluorescence intensity associated with caudal vein *vs* DA. (a–j) Bar height represents median values, dots represent individual data points, and brackets indicate significantly different values (*: $p < 0.05$, **: $p < 0.01$, ***: $p < 0.001$, N.S.: not significant) based on Mann–Whitney test. $n = 5–12$ per group (in two experiments).

function in liposome uptake by SECs (Figure S11). For the original three liposome formulations screened, loss of *stab2* function affected AmBisome, but not Myocet or EndoTAG-1 biodistribution (Figure 3i–k). Since both AmBisome and EndoTAG-1 accumulated within SECs of wild-type embryos, *stab2*-mediated uptake by SECs appears dependent on specific physicochemical properties of liposomes and *stab2* does not function in the clearance of cationic liposomes.

In vivo, several other scavenger receptors with similar binding profiles to *stab2* are expressed,[11] not only on SECs but also on other endothelial cells and macrophages. Given the significant increase in circulating DOPG, DSPC, and AmBisome liposomes in *stab2*^{ibl2} mutants, *stab2* clearly plays a dominant role in removal of these liposomes from circulation compared to other scavenger receptors (including the structurally related *stab1*). Similarly, clearance of PS-ASOs was recently shown to be dominated by Stab2 in the mouse liver.[42] To test the generality of *stab2* function, several other polyanionic nanoparticles were injected in wild-type and *stab2*^{ibl2} mutant embryos as well as following dextran sulfate injection (Figure 4a–l). These included endogenous (DOPS liposomes, a model for apoptotic cell fragments), viral (Cowpea Chlorotic Mottle Virus-like particles, CCMV VLPs),[53] polymeric (polymersomes[54] and polystyrene beads), and inorganic (quantum dots, QDs) nanoparticles. All of these particles were endocytosed selectively by SECs in zebrafish embryos, and in all cases SEC endocytosis could be inhibited by dextran sulfate. However, not all nanoparticles were dependent on *stab2* for SEC endocytosis. Although uptake by SECs of DOPS liposomes, polymersomes, and polystyrene nanoparticles was

DOI: 10.1021/acsnano.7b06995
ACS Nano XXXX, XXX, XXX–XXX

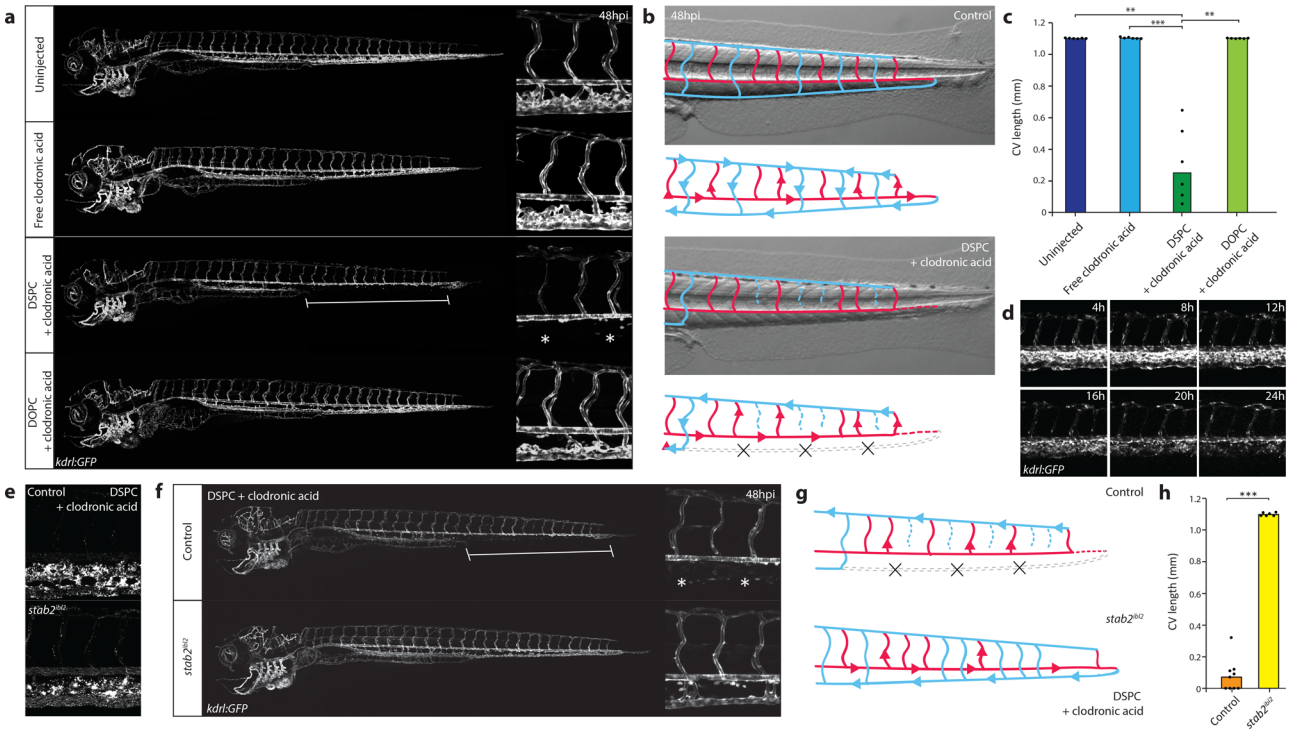

Figure 5. Nanoparticle-mediated SEC deletion. (a) Whole-embryo and tissue level views at 48 hpi of the blood vasculature in *kdrl:GFP* transgenic control embryos, embryos injected with 1 mg/mL clodronic acid, or embryos injected with liposomes containing 1 mg/mL clodronic acid (DSPC or DOPC liposomes). Complete deletion of the caudal vein is observed in embryos injected with DSPC liposomes containing clodronic acid (brackets and asterisks). (b) Schematic representation of blood flow in control embryos or embryos injected with DSPC liposomes containing 1 mg/mL clodronic acid. Blue indicates venous or capillary blood vessels, and red indicates arterial blood vessels. Arrowheads indicate direction of blood flow (based on observations from Movie S1). The removal of the CV (dashed lines) leads to a rerouting of blood flow through the DLAV. (c) Quantification of PCV length in injected embryos. Bar height represents median values, dots represent individual data points, and brackets indicate significant values (: $p < 0.01$, ***: $p < 0.001$) based on Kruskal–Wallis and Dunn's tests with Bonferroni correction for multiple testing. $n = 6$ individually injected embryos per group (in two experiments). (d) Progression of SEC deletion. Individual frames from Movie S2 at indicated time points after injection of DSPC liposomes containing 1 mg/mL clodronic acid, injected into *kdrl:GFP* transgenic embryos. SEC fragmentation in this case is observed mostly between 12 hpi and 16 hpi, followed by a gradual loss of fluorescence or removal of cellular debris. (e) Tissue level view of distribution of DSPC liposomes containing 1 mg/mL clodronic acid at 1 hpi in *stab2*^{ibl2} and sibling control embryos. (f) Whole-embryo and tissue level views at 48 hpi of the blood vasculature in *kdrl:GFP* transgenic *stab2*^{ibl2} and sibling embryos. Embryos were injected with DSPC liposomes containing 1 mg/mL clodronic acid. Complete deletion of the caudal vein is observed in sibling control (brackets and asterisks), but not *stab2*^{ibl2} mutant embryos. (g) Schematic representation of blood flow in sibling control embryos or *stab2*^{ibl2} homozygous mutants, both injected with DSPC liposomes containing approximately 1 mg/mL clodronic acid. Blue indicates venous or capillary blood vessels, and red indicates arterial blood vessels. Arrowheads indicate direction of blood flow (based on observations from Movie S3). The removal of the CV (dashed lines) leads to a rerouting of blood flow through the DLAV in control embryos but not in *stab2*^{ibl2} homozygous mutants. (h) Quantification of PCV length in injected embryos. Bar height represents median values, dots represent individual data points, and brackets indicate significant values (***: $p < 0.001$) based on Mann–Whitney test.**

strongly decreased in *stab2*^{ibl2} mutants, uptake of CCMV VLPs was only partly dependent on *stab2* and QD uptake appeared *stab2*-independent. Alternatively, QD uptake by SECs is also mediated in part by *stab2*, but its function is masked in *stab2*^{ibl2} mutants through redundancy with other scavenger receptors (such as *stab1*) that can be inhibited by dextran sulfate. CCMV VLPs (28 nm) and QDs (<10 nm) were the smallest nanoparticles screened in this study, suggesting size may be an important determinant of scavenger receptor–nanoparticle interactions.

Targeted Liposomal Drug Delivery to SECs. Finally, to demonstrate we could extend the observed interaction of nanoparticles with SECs to cell-selective drug delivery, we encapsulated a model drug, clodronic acid, within DSPC liposomes (Table S2). Clodronic acid requires active transport (endocytosis or phagocytosis) across the target cell membrane to illicit a cytotoxic effect.[55] Liposome-mediated intracellular delivery of clodronic acid into monocytes/macrophages is used extensively as a research tool to selectively remove these cell populations *in vivo*.[56] After 12–24 hpi, synchronous changes in the morphology of the CHT and caudal vein ECs were observed, followed by a gradual loss of *kdrl:GFP*$^{+}$ endothelial cells or cell fragments and ultimately leading to the complete disappearance of the caudal vein between 24 and 48 hpi (Figure 5a–d, Movie S1 and S2). The PCV and other cell types within the CHT, including *mpeg:GFP*+ macrophages (most of which are not exposed to circulating nanoparticles) as well as *mpx:GFP*+ neutrophils, were largely unaffected (Figure S12). Injection of free clodronic acid (a control demonstrating the requirement of liposomal encapsulation) did not result in any observable changes to the venous endothelium. Similarly, injection of freely circulating DOPC-clodronic acid liposomes (a control demonstrating the requirement of selective nanoparticle uptake by SECs) did not affect the venous

DOI: 10.1021/acsnano.7b06995
ACS Nano XXXX, XXX, XXX–XXX

endothelium. The development of the dorsal aorta was unaffected by deletion of the CV and CHT, and blood supply to the caudal parts of the embryo was maintained through a rerouting of blood cells into the intersegmental vessels and dorsal longitudinal anastomotic vessel (DLAV). Embryos with a complete loss of the CV and CHT endothelial cells were agile and could survive at least until 6 dpf. Imaging of fluorescent DSPC-clodronic acid liposomes revealed selective *stab2*-dependent uptake by SECs analogous to empty DSPC liposomes (Figure 5e). Importantly, loss of *stab2* function as observed in *stab2*^{ibl2} mutant embryos rescued the CV phenotype induced by injection of DSPC-clodronic acid liposomes (Figure 5 f-h, Movie S3). These results identify *stab2*-mediated uptake of liposomes by SECs as a simple strategy for intracellular compound delivery to this cell type in zebrafish embryos.

CONCLUSION

In summary, we show *stab2* is an important (scavenger) receptor mediating the uptake of circulating nanoparticles by SECs. In particular, anionic nanoparticles, between 50 and 250 nm in size, are avidly taken up by SECs in a *stab2*-dependent fashion. Here, binding and uptake appear independent of material and functional properties of nanoparticles and are solely dependent on surface charge. Given the comparable sizes and surface charge of many blood-borne viruses,[16−18,57] clearance of these circulating pathogens by LSECs is also potentially mediated by *stab2*. These findings, combined with the high expression of *stab2* by LSECs within the mammalian liver,[11] implicate SECs as an important cell-type in the binding, uptake, and clearance of administered nanoparticles. As such, we support the re-adoption of the RES, over the MPS, as the most accurate term to describe the specialized cellular components involved in nanoparticle clearance from circulation.[58]

The ultimate goal of many nanoparticle-based technologies is cell-type-specific targeting. Yet reported targeting efficiencies rarely surpass 1% of the total injected nanoparticle dose.[1] A major contributing factor has been off-target nanoparticle interactions within the mammalian liver.[5] By revealing the molecular basis of nanoparticle interactions with specific cells of the embryonic zebrafish, we have been able to demonstrate nanoparticle targeting of, and drug delivery to, specific cell types with homologues in the mammalian liver. In addition, we show these interactions can be effectively inhibited by dextran sulfate. As *stab2* is not essential for normal adult physiology,[37] this offers a simple method to extend circulation lifetimes of nanoparticles by minimizing potential off-target liver interactions.[59] This will likely be particularly beneficial in instances where active targeting of nanoparticles to cell types beyond the liver (for example, cancer cells) is desired.

Importantly, the SEC/selective drug delivery we describe has not resulted from adding further complexity to nanoparticle designs. Instead, through systematic screening of "simple" nanoparticles (*i.e.*, liposomes composed of a single phospholipid), we have established what general properties and molecular mechanisms direct nanoparticles to specific cell types. The use of the embryonic zebrafish as a model organism, and the ability to visualize nanoparticle−cell interactions at high resolution in living organisms, has been essential in this process. We therefore propose that the embryonic zebrafish, with its established extensive genetic toolkit, is a valuable preclinical *in vivo* model allowing screening, optimization, and mechanistic understanding of nanoparticle biodistribution, predictive of their behavior in mammals.[26]

MATERIALS AND METHODS

Reagents. Fluorescein-labeled hyaluronic acid (fluoHA) was prepared through conjugation of hyaluronic acid (100 kDa) with fluorescein isothiocyanate (Isomer I, Sigma-Aldrich) as previously described.[60] Additional fluoHA was provided as a kind gift from W. Jiskoot (Leiden University, The Netherlands). Colloidal Li-Car was prepared as previously described.[61] Rhodamine-loaded polymersomes on polyisobutadiene/polyethylene glycol (PIB/PEG) block copolymers[54] were a kind gift from S. Askes and S. Bonnet (Leiden University, The Netherlands). Atto-647 labeled CCMV-virus-like particles (t = 3, 28 nm)[53] were a kind gift from M. de Ruiter and J. Cornelissen (Twente University, The Netherlands). Purchased reagents are described in the Supporting Information.

Liposome Preparation and Characterization. All liposomes (without encapsulated drugs) were formulated in ddH_2O at a total lipid concentration of 1 mM. Individual lipids, as stock solutions (1−10 mM) in chloroform, were combined at the desired molar ratios and dried to a film, first under a stream of N_2 and then >1h under vacuum. With the exception of Myocet 325 and 464 nm, lipid films were hydrated in 1 mL ddH_2O at >65 °C (with gentle vortexing if necessary) to form large/giant multilamellar vesicles. Large unilamellar vesicles were formed through extrusion above the T_m of all lipids (>65 °C, Mini-extruder with heating block, Avanti Polar Lipids, Alabaster, US). Hydrated lipids were passed 11 times through 2 × 400 nm polycarbonate (PC) membranes (Nucleopore Track-Etch membranes, Whatman), followed by 11 times through 2 × 100 nm PC pores. All liposomes were stored at 4 °C. With the exception of DSPC liposomes (significant aggregation after 1 week storage), all liposomes were stable for at least 1 month. Myocet 325 and 464 nm liposomes were formulated by gentle hydration of lipid films at 35 °C (without vortexing). In the case of 464 nm Myocet liposomes, hydrated lipids were passed through a 800 nm PC membrane 7 times at 35 °C. In the case of 325 nm Myocet liposomes, hydrated lipids were passed through a 400 nm PC membrane 7 times at 35 °C. See Supporting Information for nanoparticle characterization methods and Table S1 for all lipid compositions, size, and zeta potentials of nanoparticles used in this study.

Clodronic Acid Encapsulation and Quantification. Lipid films (10 mM total lipids) were hydrated with ddH_2O containing 200 mgmL^{-1} clodronic acid (1 mL) and formulated through extrusion as described for the corresponding "empty" liposomes. Unencapsulated clodronic acid was removed by size exclusion chromatography (illustra NAP Sephadex G-25 DNA grade premade columns (GE Healthcare) used according to the supplier's instructions). Eluted clodronic acid-encapsulated liposomes were diluted 2.5× during SEC and injected without further dilution. Quantification of encapsulated clodronic acid was determined by UV absorbance as previously reported.[62] Briefly, liposomes were first destroyed through a 1:1 dilution with 1% v/v Triton X-100 solution before further dilution into an acidic $CuSO_4$ solution (1:2.25:2.25; Liposome-Triton X-100 mix: 3 mM HNO_3: 4 mM $CuSO_4$). The concentration of clodronic acid was determined by UV absorbance (Cary 3 Bio UV−vis spectrometer) at 240 nm and quantified against a predetermined calibration curve (50 μM to 2.5 mM clodronic acid). All UV−vis absorbance measurements were taken at room temperature. Blanks were made using liposome solutions without encapsulated clodronic acid but prepared otherwise identically (including SEC procedure). The final encapsulated clodronic acid concentration varied between 0.9 and 1.7 mg mL^{-1} (see Supporting Information Table S2).

Zebrafish Strains, *in Situ* Hybridization, and CRISPR/Cas9 Mutagenesis. Zebrafish (*Danio rerio*, strain AB/TL) were maintained and handled according to the guidelines from the Zebrafish Model Organism Database (http://zfin.org) and in compliance with the directives of the local animal welfare committee of Leiden University. Fertilization was performed by natural spawning at the beginning of the light period, and eggs were raised at 28.5 °C in egg water (60 ug/

DOI: 10.1021/acsnano.7b06995
ACS Nano XXXX, XXX, XXX−XXX

mL Instant Ocean sea salts). The following previously established zebrafish lines were used *Tg(kdrl:GFP)*^{s843},[63] *Tg(kdrl:RFP-CAAX)*^{s916},[38] *Tg(mpeg:GFP)*^{gl22},[64] *Tg(mpeg:RFP-CAAX)*^{ump2},[65] *Tg-(flt1*^{enh}*:RFP)*^{hu5333},[66] *Tg(flt4*^{BAC}*:YFP)*^{hu7135},[67] and *Tg(mpx:GFP)*^{uwm1}.[68] Whole-mount *in situ* hybridization was performed as described.[69] Supporting Information Table S3 lists primers for probe generation. Cloning-free sgRNAs for CRISPR/Cas9 mutagenesis were designed and synthesized as described.[70] sgRNAs (125 pg) and cas9 mRNA (300 pg) were co-injected into single-cell wild-type, albino or *flt4:YFP; flt1:RFP* transgenic embryos. Mutagenesis efficacy, founder identification, and genotyping were performed using CRISPR-STAT.[71] The nucleotide sequences and predicted *stab2* amino acid sequences in the *stab2*^{ibl2} line are shown in Figure S11. Table S3 lists guide RNA sequences and genotyping primers. For mosaic analysis, heterozygous embryos (*stab2*$^{ibl/+}$) obtained from a cross between a *stab2*^{ibl2} homozygous parent and a *kdrl:GFP* (*stab2*$^{+/+}$) parent were co-injected with sgRNAs (125 pg) and cas9 mRNA (300 pg) to create second-hit mutations in the wild-type allele.

Zebrafish Intravenous Injections. Liposomal formulations were injected into 2 day old zebrafish embryos (52−56 hpf) using a modified microangraphy protocol.[72] Embryos were anesthetized in 0.01% tricaine and embedded in 0.4% agarose containing tricaine before injection. To improve reproducibility of microangiography experiments, 1 nL volumes were calibrated and injected into the sinus venosus/duct of Cuvier. We created a small injection space by penetrating the skin with the injection needle and gently pulling the needle back, thereby creating a small pyramidal space in which the liposomes and polymers were injected. Successfully injected embryos were identified through the backward translocation of venous erythrocytes and the absence of damage to the yolk ball, which would reduce the amount of liposomes in circulation. For injections at later stages (>80 hpf), 0.5 nL volumes were injected into the CCV. The following concentrations were injected: dextran sulfate (20 mg/mL), FluoHA (0.2 mg/mL), oxLDL (1 mg/mL), CCMV-VLP (1 mg/mL), QDs (1:25 dilution), lithium carmine (1:50 dilution), polymersomes (1 mg/mL), latex beads (1:10 dilution). Dextran sulfate was injected 20 min prior to nanoparticle injection.

Zebrafish Imaging and Quantification. For each treatment or time point, at least six individual embryos (biological replicates) using at minimum two independently formulated liposome preparations were imaged using confocal microscopy. Embryos were randomly picked from a dish of 20−60 successfully injected embryos (exclusion criteria were: no backward translocation of erythrocytes after injection and/or damage to the yolk ball). Confocal z-stacks were captured on a Leica TCS SPE confocal microscope, using a 10× air objective (HCX PL FLUOTAR) or a 40× water-immersion objective (HCX APO L). For whole-embryo views, 3−5 overlapping z-stacks were captured to cover the complete embryo. Laser intensity, gain, and offset settings were identical between stacks and sessions. Images were processed and quantified using the Fiji distribution of ImageJ.[73,74] Quantification (not blinded) of liposome biodistribution was performed on 40× confocal z-stacks (with an optical thickness of 2 μm/slice) as described in the Supporting Information.

Mouse Injections and Imaging. All experiments were performed in accordance with the guidelines of the Animal Welfare Committee of the Royal Netherlands Academy of Arts and Sciences, The Netherlands. Tg(TIE2GFP)287Sato/J mice were sedated using isoflurane inhalation anesthesia (1.5−2% isoflurane/O_2 mixture). 100 μL of DOPG liposomes (10 mM DOPG + 1% Rhod-PE) diluted 1:5 in PBS were injected retro-orbitally with an insulin syringe (BD). After 1 h, mice were sacrificed, and organs were harvested and imaged *ex vivo* on glass bottom dishes. Images were taken with a Leica SP8 multiphoton microscope with a chameleon Vision-S (Coherent Inc.), equipped with four HyD detectors: HyD1 (<455 nm), HyD2 (455−490 nm), HyD3 (500−550 nm), and HyD4 (560−650 nm). Different wavelengths between 700 nm and 1150 nm were used for excitation; HA and Rhod-PE were excited with a wavelength of 960/1050 nm and detected in HyD3 and HyD4. All images were in 12 bit and acquired with a 25× (HCX IRAPO N.A. 0.95 WD 2.5 mm) water objective.

Statistical Analysis and Data Availability. Because of small sample sizes, nonparametric tests were used exclusively. For comparisons between two groups, two-tailed Mann−Whitney tests were performed. For comparisons between multiple groups, we used Kruskal−Wallis tests followed by two-tailed Dunn's tests with Bonferroni correction using the PMCMR package in R.[75] No statistical methods were used to predetermine sample size, but group sizes were >5 in order for the null distribution of the Kruskal−Wallis statistic to approximate the X^2 distribution (with $k-1$ degrees of freedom). With the exception of Figure 1e, graphs show all individual data points and the median. Confocal image stacks (raw data) are available from the corresponding authors upon reasonable request.

ASSOCIATED CONTENT

Supporting Information

The Supporting Information is available free of charge on the ACS Publications website at DOI: 10.1021/acsnano.7b06995.

Supporting information, methods, tables and figures (PDF)

Movie S1: An uninjected control embryo and three DSPC-clodronic acid (10mM total lipids) liposome injected embryos showing blood flow dynamics in the tail region and normal embryonic development 48 h after injection. Black arrows indicate the most caudal end of the PCV that contains bloodflow, and white arrows indicate the most caudal perfused ISV (AVI)

Movie S2: Time lapse confocal imaging of a *kdrl:GFP* transgenic embryo injected with DSPC-clodronic acid (10 mM total lipids) liposome. Imaging started 6 hpi. Confocal z-stacks were captured every 20 minutes for 24 h (AVI)

Movie S3: Three sibling control embryo and three *stab2*^{ibl2} homozygous mutants DSPC-clodronic acid (10 mM total lipids) liposome injected embryos showing blood flow dynamics in the tail region and normal embryonic development 48 h after injection (AVI)

AUTHOR INFORMATION

Corresponding Authors

*E-mail: j.bussmann@chem.leidenuniv.nl.
*E-mail: a.kros@chem.leidenuniv.nl.
*E-mail: f.campbell@chem.leidenuniv.nl.

ORCID

Alexander Kros: 0000-0002-3983-3048
Jeroen Bussmann: 0000-0003-2814-3305

Present Address

#Princess Máxima Center for Pediatric Oncology, Utrecht 3584CT, The Netherlands

Author Contributions

⊥These authors contributed equally.

Notes

The authors declare no competing financial interest.

ACKNOWLEDGMENTS

This work was supported by The Netherlands Organization for Scientific Research (NWO, Dutch Technology Foundation STW, project no. 12520 (J.B.), and NWO-VICI, project no. 724.014.001, F.C., G.A.-A., J.B., A.K.), "Stiftung zur Förderung des pharmazeutischen Nachwuchses in Basel" and "Freiwilligen Akademischen Gesellschaft Basel" (S.S.) and the Dutch Cancer Society (KWF, project no. 6660, F.L.B.)

DOI: 10.1021/acsnano.7b06995
ACS Nano XXXX, XXX, XXX−XXX

REFERENCES

(1) Wilhelm, S.; Tavares, A. J.; Dai, Q.; Ohta, S.; Audet, J.; Dvorak, H. F.; Chan, W. C. W. Analysis of Nanoparticle Delivery to Tumours. *Nat. Rev. Mater.* **2016**, *1*, 16014.

(2) Blanco, E.; Shen, H.; Ferrari, M. Principles of Nanoparticle Design for Overcoming Biological Barriers to Drug Delivery. *Nat. Biotechnol.* **2015**, *33*, 941−951.

(3) Dawidczyk, C. M.; Kim, C.; Park, J. H.; Russell, L. M.; Lee, K. H.; Pomper, M. G.; Searson, P. C. State-of-the-Art in Design Rules for Drug Delivery Platforms: Lessons Learned from FDA-Approved Nanomedicines. *J. Controlled Release* **2014**, *187*, 133−144.

(4) Wang, A. Z.; Langer, R.; Farokhzad, O. C. Nanoparticle Delivery of Cancer Drugs. *Annu. Rev. Med.* **2012**, *63*, 185−198.

(5) Zhang, Y. N.; Poon, W.; Tavares, A. J.; McGilvray, I. D.; Chan, W. C. Nanoparticle-Liver Interactions: Cellular Uptake and Hepatobiliary Elimination. *J. Controlled Release* **2016**, *240*, 332−348.

(6) Bertrand, N.; Leroux, J. C. The Journey of a Drug-Carrier in the Body: An Anatomo-Physiological Perspective. *J. Controlled Release* **2012**, *161*, 152−163.

(7) Tsoi, K. M.; MacParland, S. A.; Ma, X. Z.; Spetzler, V. N.; Echeverri, J.; Ouyang, B.; Fadel, S. M.; Sykes, E. A.; Goldaracena, N.; Kaths, J. M.; Conneely, J. B.; Alman, B. A.; Selzner, M.; Ostrowski, M. A.; Adeyi, O. A.; Zilman, A.; McGilvray, I. D.; Chan, W. C. Mechanism of Hard-Nanomaterial Clearance by the Liver. *Nat. Mater.* **2016**, *15*, 1212−1221.

(8) Rothkopf, C.; Fahr, A.; Fricker, G.; Scherphof, G. L.; Kamps, J. A. Uptake of Phosphatidylserine-Containing Liposomes by Liver Sinusoidal Endothelial Cells in the Serum-Free Perfused Rat Liver. *Biochim. Biophys. Acta, Biomembr.* **2005**, *1668*, 10−16.

(9) Kamps, J. A. A. M.; Morselt, H. W. M.; Swart, P. J.; Meijer, D. K. F.; Scherphof, G. L. Massive Targeting of Liposomes, Surface-Modified with Anionized Albumins, to Hepatic Endothelial Cells. *Proc. Natl. Acad. Sci. U. S. A.* **1997**, *94*, 11681−11685.

(10) Park, J. K.; Utsumi, T.; Seo, Y. E.; Deng, Y.; Satoh, A.; Saltzman, W. M.; Iwakiri, Y. Cellular Distribution of Injected PLGA-Nanoparticles in the Liver. *Nanomedicine* **2016**, *12*, 1365−1374.

(11) Sorensen, K. K.; Simon-Santamaria, J.; McCuskey, R. S.; Smedsrod, B. Liver Sinusoidal Endothelial Cells. *Compr. Physiol.* **2015**, *5*, 1751−1774.

(12) MacPhee, P. J.; Schmidt, E. E.; Groom, A. C. Intermittence of Blood Flow in Liver Sinusoids, Studied by High-Resolution *in Vivo* Microscopy. *Am. J. Physiol.* **1995**, *269*, G692−8.

(13) Wisse, E. An Electron Microscopic Study of the Fenestrated Endothelial Lining of Rat Liver Sinusoids. *J. Ultrastruct. Res.* **1970**, *31*, 125−150.

(14) Aschoff, L. Das Reticulo-Endotheliale System. *Ergebnisse der Inneren Medizin und Kinderheilkunde* **1924**, 1−118.

(15) Seternes, T.; Sorensen, K.; Smedsrod, B. Scavenger Endothelial Cells of Vertebrates: A Nonperipheral Leukocyte System for High-Capacity Elimination of Waste Macromolecules. *Proc. Natl. Acad. Sci. U. S. A.* **2002**, *99*, 7594−7597.

(16) Ganesan, L. P.; Mohanty, S.; Kim, J.; Clark, K. R.; Robinson, J. M.; Anderson, C. L. Rapid and Efficient Clearance of Blood-Borne Virus by Liver Sinusoidal Endothelium. *PLoS Pathog.* **2011**, *7*, e1002281.

(17) Mates, J. M.; Yao, Z. L.; Cheplowitz, A. M.; Suer, O.; Phillips, G. S.; Kwiek, J. J.; Rajaram, M. V. S.; Kim, J.; Robinson, J. M.; Ganesan, L. P.; Anderson, C. L. Mouse Liver Sinusoidal Endothelium Eliminates HIV-Like Particles from Blood at a Rate of 100 Million per Minute by a Second-Order Kinetic Process. *Front. Immunol.* **2017**, *8*, 35.

(18) Breiner, K. M.; Schaller, H.; Knolle, P. A. Endothelial Cell-Mediated Uptake of a Hepatitis B Virus: A New Concept of Liver Targeting of Hepatotropic Microorganisms. *Hepatology* **2001**, *34*, 803−808.

(19) Knolle, P. A.; Wohlleber, D. Immunological Functions of Liver Sinusoidal Endothelial Cells. *Cell. Mol. Immunol.* **2016**, *13*, 347−353.

(20) Sorensen, K. K.; McCourt, P.; Berg, T.; Crossley, C.; Le Couteur, D.; Wake, K.; Smedsrod, B. The Scavenger Endothelial Cell: A New Player in Homeostasis and Immunity. *Am. J. Physiol Regul Integr Comp Physiol* **2012**, *303*, R1217−R1230.

(21) Allen, T. M.; Cullis, P. R. Liposomal Drug Delivery Systems: From Concept to Clinical Applications. *Adv. Drug Delivery Rev.* **2013**, *65*, 36−48.

(22) Sercombe, L.; Veerati, T.; Moheimani, F.; Wu, S. Y.; Sood, A. K.; Hua, S. Advances and Challenges of Liposome Assisted Drug Delivery. *Front. Pharmacol.* **2015**, *6*, 286.

(23) Evensen, L.; Johansen, P. L.; Koster, G.; Zhu, K.; Herfindal, L.; Speth, M.; Fenaroli, F.; Hildahl, J.; Bagherifam, S.; Tulotta, C.; Prasmickaite, L.; Mælandsmo, G. M.; Snaar-Jagalska, E.; Griffiths, G. Zebrafish as a Model System for Characterization of Nanoparticles against Cancer. *Nanoscale* **2016**, *8*, 862−877.

(24) Fenaroli, F.; Westmoreland, D.; Benjaminsen, J.; Kolstad, T.; Skjeldal, F. M.; Meijer, A. H.; Van Der Vaart, M.; Ulanova, L.; Roos, N.; Nyström, B.; Hildahl, J.; Griffiths, G. Nanoparticles as Drug Delivery System against Tuberculosis in Zebrafish Embryos: Direct Visualization and Treatment. *ACS Nano* **2014**, *8*, 7014−7026.

(25) Jiang, X. Y.; Sarsons, C. D.; Gomez-Garcia, M. J.; Cramb, D. T.; Rinker, K. D.; Childs, S. J. Quantum Dot Interactions and Flow Effects in Angiogenic Zebrafish (Danio Rerio) Vessels and Human Endothelial Cells. *Nanomedicine* **2017**, *13*, 999−1010.

(26) Sieber, S.; Grossen, P.; Detampel, P.; Siegfried, S.; Witzigmann, D.; Huwyler, J. Zebrafish as an Early Stage Screening Tool to Study the Systemic Circulation of Nanoparticulate Drug Delivery Systems *in Vivo*. *J. Controlled Release* **2017**, *264*, 180−191.

(27) Batist, G.; Barton, J.; Chaikin, P.; Swenson, C.; Welles, L. Myocet (Liposome-Encapsulated Doxorubicin Citrate): A New Approach in Breast Cancer Therapy. *Expert Opin. Pharmacother.* **2002**, *3*, 1739−1751.

(28) Schmitt-Sody, M.; Strieth, S.; Krasnici, S.; Sauer, B.; Schulze, B.; Teifel, M.; Michaelis, U.; Naujoks, K.; Dellian, M. Neovascular Targeting Therapy: Paclitaxel Encapsulated in Cationic Liposomes Improves Antitumoral Efficacy. *Clin. Cancer Res.* **2003**, *9*, 2335−2341.

(29) Cornely, O. A.; Maertens, J.; Bresnik, M.; Ebrahimi, R.; Ullmann, A. J.; Bouza, E.; Heussel, C. P.; Lortholary, O.; Rieger, C.; Boehme, A.; Aoun, M.; Horst, H. A.; Thiebaut, A.; Ruhnke, M.; Reichert, D.; Vianelli, N.; Krause, S. W.; Olavarria, E.; Herbrecht, R. Liposomal Amphotericin B as Initial Therapy for Invasive Mold Infection: A Randomized Trial Comparing a High-Loading Dose Regimen with Standard Dosing (AmBiLoad Trial). *Clin. Infect. Dis.* **2007**, *44*, 1289−1297.

(30) Immordino, M. L.; Dosio, F.; Cattel, L. Stealth Liposomes: Review of the Basic Science, Rationale, and Clinical Applications, Existing and Potential. *Int. J. Nanomedicine* **2006**, *1*, 297−315.

(31) Murayama, E.; Kissa, K.; Zapata, A.; Mordelet, E.; Briolat, V.; Lin, H. F.; Handin, R. I.; Herbomel, P. Tracing Hematopoietic Precursor Migration to Successive Hematopoietic Organs during Zebrafish Development. *Immunity* **2006**, *25*, 963−975.

(32) Isogai, S.; Horiguchi, M.; Weinstein, B. M. The Vascular Anatomy of the Developing Zebrafish: An Atlas of Embryonic and Early Larval Development. *Dev. Biol.* **2001**, *230*, 278−301.

(33) Cho, E. C.; Xie, J. W.; Wurm, P. A.; Xia, Y. N. Understanding the Role of Surface Charges in Cellular Adsorption versus Internalization by Selectively Removing Gold Nanoparticles on the Cell Surface with a I-2/KI Etchant. *Nano Lett.* **2009**, *9*, 1080−1084.

(34) Hen, G.; Nicenboim, J.; Mayseless, O.; Asaf, L.; Shin, M.; Busolin, G.; Hofi, R.; Almog, G.; Tiso, N.; Lawson, N. D.; Yaniv, K. Venous-Derived Angioblasts Generate Organ-Specific Vessels during Zebrafish Embryonic Development. *Development* **2015**, *142*, 4266−4278.

(35) Koltowska, K.; Paterson, S.; Bower, N. I.; Baillie, G. J.; Lagendijk, A. K.; Astin, J. W.; Chen, H. J.; Francois, M.; Crosier, P. S.; Taft, R. J.; Simons, C.; Smith, K. A.; Hogan, B. M. Mafba Is a Downstream Transcriptional Effector of Vegfc Signaling Essential for Embryonic Lymphangiogenesis in Zebrafish. *Genes Dev.* **2015**, *29*, 1618−1630.

(36) Stapelfeldt, H.; Jun, H.; Skibsted, L. H. Fluorescence Properties of Carminic Acid in Relation to Aggregation, Complex Formation and

DOI: 10.1021/acsnano.7b06995
ACS Nano XXXX, XXX, XXX−XXX

Oxygen Activation in Aqueous Food Models. *Food Chem.* **1993**, *48*, 1−11.
(37) Schledzewski, K.; Géraud, C.; Arnold, B.; Wang, S.; Gröne, H. J.; Kempf, T.; Wollert, K. C.; Straub, B. K.; Schirmacher, P.; Demory, A.; Schönhaber, H.; Gratchev, A.; Dietz, L.; Thierse, H. J.; Kzhyshkowska, J.; Goerdt, S. Deficiency of Liver Sinusoidal Scavenger Receptors Stabilin-1 and −2 in Mice Causes Glomerulofibrotic Nephropathy via Impaired Hepatic Clearance of Noxious Blood Factors. *J. Clin. Invest.* **2011**, *121*, 703−714.
(38) Hogan, B. M.; Bos, F. L.; Bussmann, J.; Witte, M.; Chi, N. C.; Duckers, H. J.; Schulte-Merker, S. ccbe1 Is Required for Embryonic Lymphangiogenesis and Venous Sprouting. *Nat. Genet.* **2009**, *41*, 396−398.
(39) Wong, K. S.; Proulx, K.; Rost, M. S.; Sumanas, S. Identification of Vasculature-Specific Genes by Microarray Analysis of Etsrp/Etv2 Overexpressing Zebrafish Embryos. *Dev. Dyn.* **2009**, *238*, 1836−1850.
(40) Zhou, B.; Weigel, J. A.; Fauss, L.; Weigel, P. H. Identification of the Hyaluronan Receptor for Endocytosis (HARE). *J. Biol. Chem.* **2000**, *275*, 37733−37741.
(41) Simon-Santamaria, J.; Malovic, I.; Warren, A.; Oteiza, A.; Le Couteur, D.; Smedsrod, B.; McCourt, P.; Sorensen, K. K. Age-Related Changes in Scavenger Receptor-Mediated Endocytosis in Rat Liver Sinusoidal Endothelial Cells. *J. Gerontol., Ser. A* **2010**, *65*, 951−960.
(42) Miller, C. M.; Donner, A. J.; Blank, E. E.; Egger, A. W.; Kellar, B. M.; Ostergaard, M. E.; Seth, P. P.; Harris, E. N. Stabilin-1 and Stabilin-2 Are Specific Receptors for the Cellular Internalization of Phosphorothioate-Modified Antisense Oligonucleotides (ASOs) in the Liver. *Nucleic Acids Res.* **2016**, *44*, 2782−2794.
(43) Park, S. Y.; Jung, M. Y.; Kim, H. J.; Lee, S. J.; Kim, S. Y.; Lee, B. H.; Kwon, T. H.; Park, R. W.; Kim, I. S. Rapid Cell Corpse Clearance by Stabilin-2, a Membrane Phosphatidylserine Receptor. *Cell Death Differ.* **2008**, *15*, 192−201.
(44) Balogh, P.; Petz, A. Selective Binding of Biotinylated Albumin to the Lymphoid Microvasculature. *Histochem. Cell Biol.* **2005**, *123*, 357−363.
(45) Alidori, S.; Bowman, R. L.; Yarilin, D.; Romin, Y.; Barlas, A.; Mulvey, J. J.; Fujisawa, S.; Xu, K.; Ruggiero, A.; Riabov, V.; Thorek, D. L.; Ulmert, H. D.; Brea, E. J.; Behling, K.; Kzhyshkowska, J.; Manova-Todorova, K.; Scheinberg, D. A.; McDevitt, M. R. Deconvoluting Hepatic Processing of Carbon Nanotubes. *Nat. Commun.* **2016**, *7*, 12343.
(46) Lee, S. J.; Park, S. Y.; Jung, M. Y.; Bae, S. M.; Kim, I. S. Mechanism for Phosphatidylserine-Dependent Erythrophagocytosis in Mouse Liver. *Blood* **2011**, *117*, 5215−5223.
(47) Harris, E. N.; Weigel, P. H. The Ligand-Binding Profile of HARE: Hyaluronan and Chondroitin Sulfates A, C, and D Bind to Overlapping Sites Distinct from the Sites for Heparin, Acetylated Low-Density Lipoprotein, Dermatan Sulfate, and CS-E. *Glycobiology* **2008**, *18*, 638−648.
(48) Tamura, Y.; Adachi, H.; Osuga, J.; Ohashi, K.; Yahagi, N.; Sekiya, M.; Okazaki, H.; Tomita, S.; Iizuka, Y.; Shimano, H.; Nagai, R.; Kimura, S.; Tsujimoto, M.; Ishibashi, S. FEEL-1 and FEEL-2 Are Endocytic Receptors for Advanced Glycation End Products. *J. Biol. Chem.* **2003**, *278*, 12613−12617.
(49) Kawasaki, T.; Etoh, R.; Yamashina, I. Isolation and Characterization of a Mannan-Binding Protein from Rabbit Liver. *Biochem. Biophys. Res. Commun.* **1978**, *81*, 1018−1024.
(50) Rost, M. S.; Sumanas, S. Hyaluronic Acid Receptor Stabilin-2 Regulates Erk Phosphorylation and Arterial–Venous Differentiation in Zebrafish. *PLoS One* **2014**, *9*, e88614.
(51) Stoll, S. J.; Bartsch, S.; Kroll, J. HOXC9 Regulates Formation of Parachordal Lymphangioplasts and the Thoracic Duct in Zebrafish via Stabilin 2. *PLoS One* **2013**, *8*, e58311.
(52) Hirose, Y.; Saijou, E.; Sugano, Y.; Takeshita, F.; Nishimura, S.; Nonaka, H.; Chen, Y.-R.; Sekine, K.; Kido, T.; Nakamura, T.; Kato, S.; Kanke, T.; Nakamura, K.; Nagai, R.; Ochiya, T.; Miyajima, A. Inhibition of Stabilin-2 Elevates Circulating Hyaluronic Acid Levels and Prevents Tumor Metastasis. *Proc. Natl. Acad. Sci. U. S. A.* **2012**, *109*, 4263−4268.
(53) Verwegen, M.; Cornelissen, J. J. L. M. Clustered Nanocarriers: The Effect of Size on the Clustering of CCMV Virus-like Particles with Soft Macromolecules. *Macromol. Biosci.* **2015**, *15*, 98−110.
(54) Askes, S. H. C.; Pomp, W.; Hopkins, S. L.; Kros, A.; Wu, S.; Schmidt, T.; Bonnet, S. Imaging Upconverting Polymersomes in Cancer Cells: Biocompatible Antioxidants Brighten Triplet−Triplet Annihilation Upconversion. *Small* **2016**, *12*, 5579−5590.
(55) Plosker, G. L.; Goa, K. L. Clodronate. A Review of Its Pharmacological Properties and Therapeutic Efficacy in Resorptive Bone Disease. *Drugs* **1994**, *47*, 945−982.
(56) van Rooijen, N.; Hendrikx, E. Liposomes for Specific Depletion of Macrophages from Organs and Tissues. *Methods Mol. Biol.* **2010**, *605*, 189−203.
(57) Michen, B.; Graule, T. Isoelectric Points of Viruses. *J. Appl. Microbiol.* **2010**, *109*, 388−397.
(58) Elvevold, K.; Smedsrod, B.; Martinez, I. The Liver Sinusoidal Endothelial Cell: A Cell Type of Controversial and Confusing Identity. *Am. J. Physiol Gastrointest Liver Physiol* **2008**, *294*, G391−400.
(59) Patel, K. R.; Li, M. P.; Baldeschwieler, J. D. Suppression of Liver Uptake of Liposomes by Dextran Sulfate 500. *Proc. Natl. Acad. Sci. U. S. A.* **1983**, *80*, 6518−6522.
(60) de Belder, A. N.; Wik, K. O. Preparation and Properties of Fluorescein-Labelled Hyaluronate. *Carbohydr. Res.* **1975**, *44*, 251−257.
(61) Kawai, Y.; Smedsrod, B.; Elvevold, K.; Wake, K. Uptake of Lithium Carmine by Sinusoidal Endothelial and Kupffer Cells of the Rat Liver: New Insights into the Classical Vital Staining and the Reticulo-Endothelial System. *Cell Tissue Res.* **1998**, *292*, 395−410.
(62) Voloshin, T.; Alishekevitz, D.; Kaneti, L.; Miller, V.; Isakov, E.; Kaplanov, I.; Voronov, E.; Fremder, E.; Benhar, M.; Machluf, M.; Apte, R. N.; Shaked, Y. Blocking IL1 Pathway Following Paclitaxel Chemotherapy Slightly Inhibits Primary Tumor Growth but Promotes Spontaneous Metastasis. *Mol. Cancer Ther.* **2015**, *14*, 1385−1394.
(63) Jin, S.-W. Cellular and Molecular Analyses of Vascular Tube and Lumen Formation in Zebrafish. *Development* **2005**, *132*, 5199−5209.
(64) Ellett, F.; Pase, L.; Hayman, J. W.; Andrianopoulos, A.; Lieschke, G. J. mpeg1 Promoter Transgenes Direct Macrophage-Lineage Expression in Zebrafish. *Blood* **2011**, *117*, e49.
(65) Nguyen-Chi, M.; Phan, Q. T.; Gonzalez, C.; Dubremetz, J.-F.; Levraud, J.-P.; Lutfalla, G. Transient Infection of the Zebrafish Notochord with E. Coli Induces Chronic Inflammation. *Dis. Models & Mech.* **2014**, *7*, 871−882.
(66) Bussmann, J.; Bos, F. L.; Urasaki, A.; Kawakami, K.; Duckers, H. J.; Schulte-Merker, S. Arteries Provide Essential Guidance Cues for Lymphatic Endothelial Cells in the Zebrafish Trunk. *Development* **2010**, *137*, 2653−2657.
(67) Hogan, B. M.; Herpers, R.; Witte, M.; Helotera, H.; Alitalo, K.; Duckers, H. J.; Schulte-Merker, S. Vegfc/Flt4 Signalling Is Suppressed by Dll4 in Developing Zebrafish Intersegmental Arteries. *Development* **2009**, *136*, 4001−4009.
(68) Mathias, J. R.; Perrin, B. J.; Liu, T.-X.; Kanki, J.; Look, A. T.; Huttenlocher, A. Resolution of Inflammation by Retrograde Chemotaxis of Neutrophils in Transgenic Zebrafish. *J. Leukocyte Biol.* **2006**, *80*, 1281−1288.
(69) Thisse, C.; Thisse, B. High-Resolution *in Situ* Hybridization to Whole-Mount Zebrafish Embryos. *Nat. Protoc.* **2008**, *3*, 59−69.
(70) Varshney, G. K.; Pei, W.; Lafave, M. C.; Idol, J.; Xu, L.; Gallardo, V.; Carrington, B.; Bishop, K.; Jones, M.; Li, M.; Harper, U.; Huang, S. C.; Prakash, A.; Chen, W.; Sood, R.; Ledin, J.; Burgess, S. M. High-Throughput Gene Targeting and Phenotyping in Zebrafish Using CRISPR/Cas9. *Genome Res.* **2015**, *25*, 1030−1042.
(71) Carrington, B.; Varshney, G. K.; Burgess, S. M.; Sood, R. CRISPR-STAT: An Easy and Reliable PCR-Based Method to Evaluate Target-Specific sgRNA Activity. *Nucleic Acids Res.* **2015**, *43*, e157.
(72) Weinstein, B. M.; Stemple, D. L.; Driever, W.; Fishman, M. C. Gridlock, a Localized Heritable Vascular Patterning Defect in the Zebrafish. *Nat. Med.* **1995**, *1*, 1143−1147.
(73) Schindelin, J.; Arganda-Carreras, I.; Frise, E.; Kaynig, V.; Longair, M.; Pietzsch, T.; Preibisch, S.; Rueden, C.; Saalfeld, S.; Schmid, B.; Tinevez, J.-Y.; White, D. J.; Hartenstein, V.; Eliceiri, K.;

DOI: 10.1021/acsnano.7b06995
ACS Nano XXXX, XXX, XXX−XXX

Tomancak, P.; Cardona, A. Fiji: An Open-Source Platform for Biological-Image Analysis. *Nat. Methods* **2012**, *9*, 676−682.
(74) Schneider, C. A.; Rasband, W. S.; Eliceiri, K. W. NIH Image to ImageJ: 25 Years of Image Analysis. *Nat. Methods* **2012**, *9*, 671−675.
(75) Pohlert, T. The Pairwise Multiple Comparison of Mean Ranks Package (PMCMR). *R Package*; R Foundation: Vienna, Austria, 2014. https://cran.r-project.org/web/packages/PMCMR/index.html

DOI: 10.1021/acsnano.7b06995
ACS Nano XXXX, XXX, XXX−XXX

Chapter IV-I

Optimization-by-Design of Hepatotropic Lipid Nanoparticles Targeting the Sodium-Taurocholate Cotransporting Polypeptide

Dominik Witzigmann, Philipp Uhl, **Sandro Sieber**, Christina Kaufman, Tomaz Einfalt, Katrin Schöneweis, Philip Grossen, Jonas Buck, Yi Ni, Susanne H. Schenk, Janine Hussner, Henriette E. Meyer zu Schwabedissen, Gabriela Québatte, Walter Mier, Stephan Urban, Jörg Huwyler.

Manuscript: in revision, eLife

Highlights: Nanomedicines can be actively targeted to selected cell types expressing specific receptors. To this end, complementary targeting ligands are coupled to the nanoparticle surface. In case of actively targeted nanomedicines, the identification of the correct type and optimal amount of targeting ligand on the surface are key questions which have to be investigated. In this study, a Hepatitis B Virus (HBV) derived peptide was identified as a suitable targeting ligand for the sodium-taurocholate cotransporting polypeptide (NTCP) expressed on the sinusoidal membrane of hepatocytes. *In vitro* uptake studies were performed and circulation properties of different nanoparticle formulations were tested in the zebrafish model. Next, NTCP expressing cells were xenotransplanted in zebrafish and the optimal targeting ligand density on the nanoparticle surface was assessed. Optimized lead formulations were selected and their targeting properties were analyzed in a mouse *in vivo* study. Interestingly, results obtained in the zebrafish model were highly predictive for the effects in mice.

Optimization-by-Design of Hepatotropic Lipid Nanoparticles Targeting the Sodium-Taurocholate Cotransporting Polypeptide

Dominik Witzigmann,[*,†,‡] *Philipp Uhl,*[¶] *Sandro Sieber,*[†] *Christina Kaufman,*[¶,§] *Tomaz Einfalt,*[†] *Katrin Schöneweis,*[§] *Philip Grossen,*[†] *Jonas Buck,*[†] *Yi Ni,*[§] *Susanne H. Schenk,*[†] *Janine Hussner,*[⊥] *Henriette E. Meyer zu Schwabedissen,*[⊥] *Gabriela Québatte,*[†] *Walter Mier,*[¶] *Stephan Urban,*[§] *Jörg Huwyler**[*,†]

[†] Division of Pharmaceutical Technology, Department of Pharmaceutical Sciences, University of Basel, Basel, Switzerland

[‡] Department of Biochemistry and Molecular Biology, University of British Columbia, Vancouver, British Columbia, Canada.

[¶] Department of Nuclear Medicine, University Hospital Heidelberg, INF 400, Heidelberg, Germany

[§] Department of Infectious Diseases, Molecular Virology, University Hospital Heidelberg, INF 344, Heidelberg, Germany

[⊥]Division of Biopharmacy, Department of Pharmaceutical Sciences, University of Basel, Basel, Switzerland

ABSTRACT

Active targeting and specific drug delivery to parenchymal liver cells is a promising strategy to treat various liver disorders. Here, we modified synthetic lipid-based nanoparticles with targeting peptides derived from the hepatitis B virus large envelope protein (HBVpreS) to specifically target the sodium-taurocholate cotransporting polypeptide (NTCP; SLC10A1) on the sinusoidal membrane of hepatocytes. Physicochemical properties of targeted nanoparticles were optimized and NTCP-specific, ligand-dependent binding and internalization was confirmed *in vitro*. The pharmacokinetics and targeting capacity of selected lead formulations was investigated *in vivo* using the emerging zebrafish screening model. Liposomal nanoparticles modified with 0.25 mol% of a short myristoylated HBV derived peptide, *i.e.* Myr-HBVpreS2-31, showed an optimal balance between systemic circulation, avoidance of blood clearance, and targeting capacity. Pronounced liver enrichment, active NTCP-mediated targeting of hepatocytes and efficient cellular internalization was confirmed in mice by ^{111}In gamma scintigraphy and fluorescence microscopy demonstrating the potential of our hepatotropic, ligand-modified nanoparticles.

KEYWORDS: nanoparticles, liposomes, hepatitis B virus (HBV), hepatocyte targeting, NTCP, zebrafish, Myrcludex B

TABLE OF CONTENTS GRAPHIC

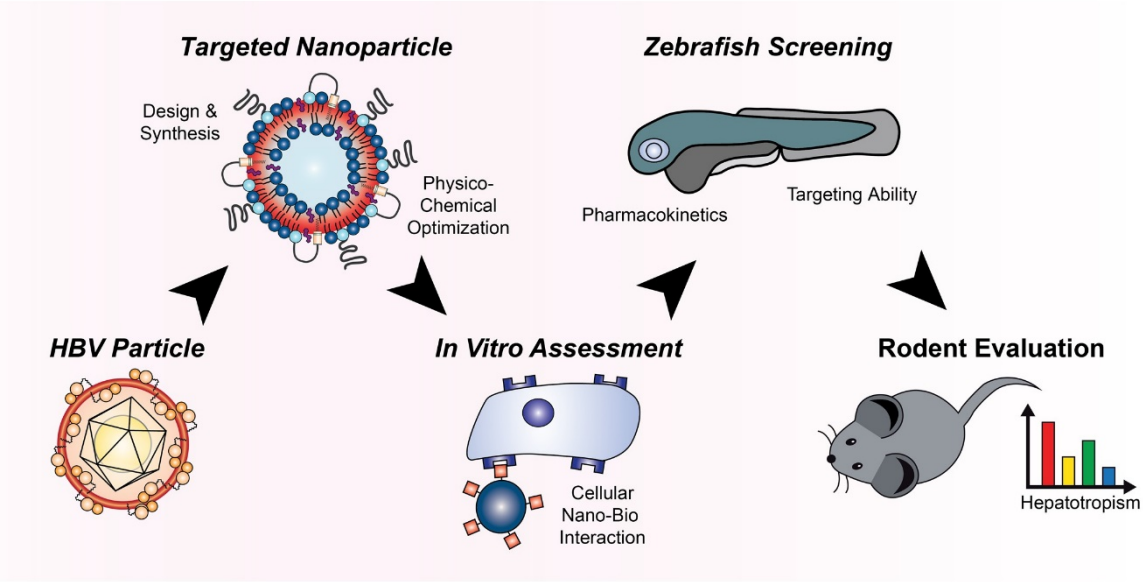

INTRODUCTION

The design of hepatotropic drug carriers is of great interest for the treatment of various liver disorders.(Williams et al., 2014; Poelstra et al., 2012; Reddy and Couvreur, 2011) In particular for the cell-type specific delivery of macromolecular therapeutic agents, selective targeting of parenchymal liver cells and internalization is needed. Previously, hepatocyte targeted nanoparticles have been developed exploiting endogenous and exogenous targeting ligand-based mechanisms using glycan, protein or antibody modifications of the nanoparticle surface.(Akinc et al., 2010, 2009; Barrett et al., 2014; Detampel et al., 2014; Witzigmann et al., 2016) Most established systems for liver-specific drug delivery rely on targeting the hepatic asialoglycoprotein (ASGPR) or low density lipoprotein (LDLR) receptors. However, studies investigating alternative targeting strategies based on other hepatocyte-specific receptors are limited. In this respect, a promising alternative might be offered by the hepatitis B virus (HBV), which shows a pronounced efficacy to infect the human liver due to its strong affinity to hepatocytes. Less than 10 virus particles have been shown to be sufficient to efficiently target hepatocytes of chimpanzees resulting in a pathogenic HBV infection.(Asabe et al., 2009) The reason for its extraordinary liver tropism is a highly specific amino acid sequence in the large HBV envelope protein (*i.e.* HBVpreS1 domain), which is essential for target receptor recognition.(Meier et al., 2013; Schieck et al., 2013) For decades, the specific target of HBV on the sinusoidal membrane of hepatocytes was unknown until in 2012 the interaction with the human sodium-taurocholate cotransporting polypeptide (NTCP/SLC10A1) was identified.(Yan et al., 2012) Subsequently, Urban and colleagues performed a fine mapping of the HBVpreS sequence to identify the amino acids responsible for efficient binding.(Schulze et al., 2010; Ni et al., 2014; Schieck et al., 2013) As a result, the first HBV/HDV entry inhibitor, a myristoylated peptide named Myrcludex B, was developed and successfully introduced in clinics (currently phase II clinical trials).(Blank et al., 2016; Urban et al., 2014) Myrcludex B binds with

high affinity and specificity to human NTCP on the sinusoidal membrane of hepatocytes thereby blocking binding of virus particles to their target cells.

Based on these findings, the question arises whether Myrcludex B might serve as a targeting ligand to design a hepatotropic, NTCP-specific nanoparticle. In recent years, several groups have therefore attempted to develop targeting strategies based on HBV envelope proteins, e.g. recombinant HBV envelope protein particles (bio-nanocapsules) or HBV preS1-derived functionalized liposomes.(Liu et al., 2016; Somiya et al., 2016, 2015; Zhang et al., 2015, 2014) However, the nanoparticulate drug delivery systems developed had physicochemical properties (e.g. size, colloidal stability, and immunogenic potential), which were sub-optimal for efficient *in vivo* targeting of hepatocytes. Especially the size of the nano-formulations presented a limitation. Most developed formulations had sizes above the average diameter of hepatic fenestrations in healthy humans (i.e. 100 nm)(Wisse et al., 2008) thereby limiting the passage through liver fenestrations and consequently the access to the space of Disse and the sinusoidal membrane of hepatocytes. Notably, the liver fenestrae diameter of rodents show high species and strain differences ranging from around 100 nm to 160 nm, possibly explaining positive liver targeting of published formulations.(Braet and Wisse, 2002; Steffan et al., 1987; Wisse et al., 2008) In addition, a nanoparticle size above 100 nm triggers phagocytosis by cells of the reticuloendothelial system (*i.e.* hepatic Kupffer cells and spleen macrophages) resulting in rapid blood clearance.(Kettiger et al., 2013) Both factors significantly decrease the likelihood of reaching the parenchymal liver tissue and increase the risk for potential off-target effects in untargeted tissues.

Surface properties are another important characteristic of nanoparticles. The surface charge (i.e. ζ potential) should be slightly negative(Xiao et al., 2011) to prevent sequestration of particles in the lung (*i.e.* due to a positive charge)(Ishiwata et al., 2000) or rapid clearance by cells expressing scavenger receptors (*i.e.* due to an excessive negative charge)(Rothkopf et al., 2005). According to the classical

Derjaguin-Landau-Verwey-Overbeek (DLVO) theory of colloids, a neutral charge has to be avoided to prevent particle agglomeration. In addition to surface charge, steric stabilization by PEGylation mediates long circulating properties and prevents opsonization.(Karmali and Simberg, 2011; Milla et al., 2012)

It was the aim of the present study to design a nanoparticle based on liposomes combined with derivatives of Myrcludex B to efficiently target hepatocytes while minimizing interactions with off-target cell types. Optimization of physicochemical properties of the nanoparticles included size and charge optimization and steric shielding by PEGylation. Derivatives of Myrcludex B were selected based on target binding, cellular uptake and their impact on the colloidal stability of nanoparticles. For the lipid membrane composition, we used a FDA and EMA approved multi-component lipid formulation based on Doxil® (*i.e.* liposomal formulation of doxorubicin).(Barenholz, 2012) To design an optimal targeted system, several Myrcludex B derivatives with variations in the peptide sequence or fatty acid modification were covalently linked to the distal end of PEG-lipids. NTCP-specific and ligand-dependent uptake was confirmed *in vitro* using human liver-derived cell lines. Recently, Shan et al. reported huge discrepancies between *in vitro* systems and rodent experiments during the development of targeted nanomedicines.(Shan et al., 2015) Therefore, we used the zebrafish as a complementary *in vivo* screening model based on our previous work. (Sieber et al., 2018; Campbell et al., 2018; Einfalt et al., 2018; Sieber et al., 2017) We assessed the effect of nanoparticles` ligand type and ligand density on their pharmacokinetics. To this end, human derived cell lines lacking or expressing the human NTCP (hNTCP) were xenotransplanted into zebrafish embryos prior to systemic administration of nanoparticles. Finally, tissue distribution of dual-labeled nanoparticles was quali- (fluorescence-based) and quantitatively (radionuclide-based) investigated *in vivo* in mice to demonstrate the targeting potential of our hepatotropic nanoparticle platform in higher vertebrates.

RESULTS AND DISCUSSION

Design and characterization of a hepatotropic nanoparticle for NTCP-specific targeting

The aim of our study was the design of a hepatotropic, targeting ligand-modified nanoparticle. To this end, the surface of liposomal nanoparticles was modified using targeting peptides or lipopeptides derived from the preS1 domain of the HBV large envelope protein (Figure 1A). Based on a previous screening of 26 HBVpreS peptide variants, we selected Myrcludex B, the first HBV entry inhibitor (Blank et al., 2016; Bogomolov et al., 2016), and five additional Myrcludex B derived peptides to evaluate the influence of amino acid sequence variations or acyl chain modifications on targeting efficiency and thereby optimize our hepatotropic nanoparticle. All Myrcludex B derived (lipo)peptides were synthesized in high yields and purity by standard solid phase peptide synthesis using Fmoc-chemistry.(Schieck et al., 2013, 2010; Müller et al., 2013) Lipopeptides were N-terminally modified using the fatty acids myristic acid (saturated C14) or capric acid (saturated C10), since our previous studies have shown that fatty acid modification is key for mediating interactions with target cells. C-termini of synthesized targeting (lipo)peptides were modified with cysteine residues to allow conjugation to the distal end of PEGylated phospholipids (DSPE-PEG2000-Maleimide) integrated into sterically stabilized liposomes. Coupling was achieved by a chemically reactive maleimide, giving rise to a metabolically stable thioether bond suitable for applications in living organisms (Figure 1A). Successful conjugation of Myrcludex B to lipid-based nanoparticles was demonstrated by fluorescence correlation spectroscopy using Myrcludex B-Atto488. The autocorrelation curve of nanoparticle conjugated peptides showed a significant shift to longer diffusion times as compared to the free peptide, with average diffusion times of τ_d = 1639 µs and τ_d = 192 µs, respectively (Figure 1–figure supplement 1).

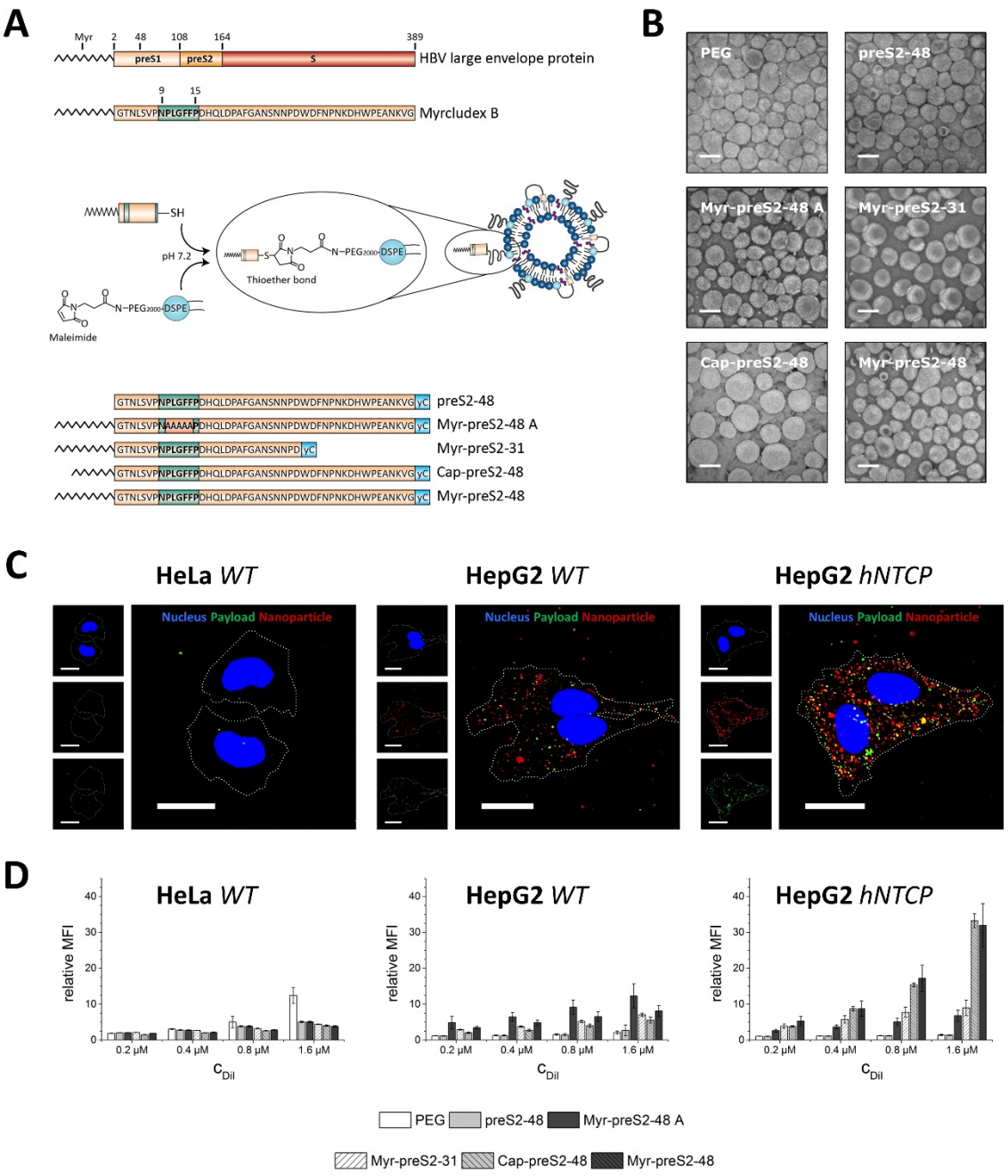

Figure 1. Hepatotropic nanoparticles based on liposomes modified with Myrcludex B-derived peptides for NTCP-specific targeting. (A) Schematic representation of peptides derived from Hepatitis B virus (HBV) large envelope protein including the first entry inhibitor, Myrcludex B. Different peptides were conjugated via thiol function to the distal end of PEG chains integrated in the nanoparticle structure using maleimide chemistry. The most important amino acid sequence (9-15) for NTCP-specific binding is highlighted in green color in each lipopeptide. (B) Representative transmission electron microscopy images

of different Myrcludex B-derived lipopeptide conjugated nanoparticles. Scale bar = 100 nm. (C) Uptake of Myrcludex B-modified nanoparticles into human cells with variable NTCP expression levels. Nanoparticles have a dual fluorescent label, *i.e.* lipophilic membrane label (DiI, red) and hydrophilic payload incorporation (carboxyfluorescein, green). Representative confocal laser scanning microscopy maximum intensity projections for Myr-preS2-48 modified nanoparticles after 30 min are shown. Dotted lines indicate cell membranes. Blue signal: Hoechst stain of cell nuclei. Scale bar = 10 µm. (D) Flow cytometry analysis of uptake rate into non-hepatic HeLa cells, liver-derived HepG2 cells and hNTCP overexpressing HepG2 cells. Increasing concentrations of nanoparticles (C_{DiI}) modified with different Myrcludex B-derived peptides were evaluated. Relative mean fluorescence intensities (MFI) of DiI signals normalized to untreated cells are given. All values are shown as mean ± SD of biological replicates ($n \geq 3$ independent experiments). Numerical data for all graphs are shown in the Figure 1-source data.

Liposome membrane partition coefficients of mono fatty acid modifications are orders of magnitudes lower as compared to di-lipid anchors.(Sauer et al., 2006) Therefore, the distearoyl anchor of DSPE results in a stable incorporation of the PEGylated phospholipid-targeting ligand conjugate in the lipid bilayer of liposomes (membrane partition coefficient > 10^3 mM^{-1}), whereas the PEG linker offers a flexibility to the distally tethered lipopeptides to extend away from the liposome surface. In addition, a thermodynamically favorable backward bending insertion of the acyl chain into the liposomal membrane is possible. A slight change in transition temperature evaluated by pressure perturbation calorimetry and differential scanning calorimetry confirmed this hypothesis (data not shown). The formulation yield of modified nanoparticles after purification was dependent on the conjugated Myrcludex B derived (lipo)peptide with preS2-48 >Myr-preS2-31 >Myr-preS2-48A ≥Myr-preS2-48 >Cap-preS2-48.

Light scattering and electron microscopy verified that all nanoparticles, *i.e.* Myrcludex B-derived peptide conjugated liposomes (modified without or with C14 acyl moiety) had a spherical morphology with a small size around 90 nm, narrow size distribution, *i.e.* PDI<0.2 and a slightly negative zeta potential

(Figure 1B, Table 1). Only a small increase in the hydrodynamic size of about 2 nm was observed after conjugation of Myrcludex B-derived peptides (Table 1). The zeta potential of nanoparticles remained negative due to a negative net charge of Myrcludex B-derived lipopeptides at physiological pH. Thus, the physicochemical properties of nanoparticles were not significantly influenced by the surface modification with HBVpreS derived lipopeptides containing C14 acyl chains. An exception were nanoparticles modified with Cap-preS2-48, which had an average diameter of 134.28 nm and a PDI of 0.24 (Figure 1B, Table 1).

Table 1. Physicochemical characteristics of nanoparticles with different surface modifications. Hydrodynamic size [nm], polydispersity index (PDI), and zeta potential [mV] were analyzed using dynamic and electrophoretic light scattering. All values are shown as mean ± SD of $n \geq 3$ independent experiments. Numerical data for all nanoparticles are shown in the Table 1-source data.

Surface Modification	Size [nm] ± SD	PDI ± SD	Zeta Potential [mV] ± SD
PEG	88.53 ± 5.89	0.05 ± 0.01	-5.93 ± 0.63
preS2-48	90.74 ± 5.83	0.06 ± 0.02	-3.34 ± 1.38
Myr-preS2-48 A	90.77 ± 4.98	0.06 ± 0.04	-13.35 ± 3.08
Myr-preS2-31	89.10 ± 4.38	0.10 ± 0.02	-9.82 ± 0.87
Cap-preS2-48	134.28 ± 36.23	0.24 ± 0.04	-8.39 ± 1.13
Myr-preS2-48	92.21 ± 6.78	0.12 ± 0.08	-10.70 ± 4.25

It is tempting to speculate, that the C10 acyl chain of Cap-preS2-48 interfered with liposome membrane stability. As compared to longer acyl chains the backward bending insertion of C10 acyl chains into intra-liposomal membranes is less stable, thus promoting faster dissociation and possible interactions with neighboring liposomes due to re-association with inter-liposomal membranes. This was also indicated

by formation of aggregates resulting in shorter storage stability (data not shown). Previously published studies reporting a rapid partitioning of shorter lipid anchors from liposomal vesicles support our observation of unfavorable liposome interactions for Cap-preS2-48.(Sauer et al., 2006; Webb et al., 1998)

Cellular uptake and viability

Next, we investigated the biocompatibility and targeting capacity of our ligand-modified nanoparticles in a panel of three different cell lines *in vitro, i.e.* non-hepatic HeLa cells devoid of hNTCP (negative control), liver-derived wild type HepG2 cells (HepG2 *WT*, hepatocyte control cell line with no detectable hNTCP expression based on PCR) and HepG2 cells overexpressing the human NTCP (HepG2 *hNTCP*). We used lentiviral transduced cells overexpressing hNTCP as a positive control to confirm the specificity of our system since human liver derived cell lines such as HepG2 and HuH7 down-regulated NTCP during oncogenic transformation (i.e. NTCP expression levels are significantly decreased in hepatocellular carcinoma).(Lempp et al., 2016) In all cell lines, nanoparticles showed a high cytocompatibility up to the highest tested lipid concentration of 8 mM, which is far beyond liposome blood concentrations achievable in a clinical setting (Figure 1–figure supplement 2 demonstrating no decrease of cell viability using the MTT assay).(Barpe et al., 2010)

In vitro uptake studies revealed that Myrcludex B-modified nanoparticles were rapidly internalized within 30 min into liver-derived HepG2 cell lines whereas no binding or cellular uptake was observed in non-hepatic HeLa cells (Figure 1C, representative confocal laser scanning microscopy images for Myr-preS2-48 modified nanoparticles). Both the liposomal nanoparticle (DiI signal) and the encapsulated payload (carboxyfluorescein (CF) signal), were detected intracellularly. Notably, CF was encapsulated into our nanoparticles at a fluorescence self-quenching concentration (i.e. 60 mM, Figure 1–figure

supplement 3). Thus, CF fluorescence increases significantly after overcoming the Förster critical transfer distances, i.e. release of CF from nanoparticles into surrounding environment.(Chen and Knutson, 1988) Specific uptake of nanoparticles with NTCP-binding component preS-peptide was enhanced with increasing hNTCP expression levels (Figures 1C, D and Figure 1–figure supplement 4) demonstrating a high target specificity (*i.e.* HeLa *WT* < HepG2 *hNTCP*). Surprisingly, the highest DiI signal (and not CF signal) in HeLa cells was observed with PEGylated nanoparticles. It is tempting to speculate that nanoparticle modification with Myrcludex B-derived lipopeptides decreases the interaction with negatively charged cell membranes of hNTCP deficient cells (*e.g.* HeLa) due to a negative net charge of lipopeptides at physiological pH and thus increased electrostatic repulsion. Uptake studies with a different liver-derived cell line (HuH7) comparing wild type and hNTCP overexpressing cells confirmed the hNTCP specific interaction. Overexpression of hNTCP again resulted in a strong enrichment of cellular uptake ruling out an involvement of cell-line specific artefacts (Figure 1–figure supplement 5).

Time-dependent uptake studies of nanoparticles with different payloads (i.e. FITC-labeled peptide, propidium iodide, and doxorubicin) confirmed the rapid binding and internalization process of Myr-preS2-31 modified nanoparticles (Figure 1–figure supplement 6, 7, and 8). Conclusively, small molecular payloads as well as larger compounds could be successfully incorporated into nanoparticles to enhance their internalization into *NTCP* expressing cells. Interestingly, Myr-preS2-31 modification enhanced the cytotoxic effects of propidium iodide and doxorubicin as compared to PEGylated nanoparticles (Figure 1–figure supplement 7 and 8) demonstrating that the payload is active and reaches the cytosol. Of note, propidium iodide is a cell membrane impermeable drug. Thus, NTCP-targeted nanoparticles enabled internalization into cells and successful release into cytosol indicated by enhanced cytotoxic effects and nuclear counterstain.

Competition of NTCP-specific cellular binding and uptake of targeting ligand-modified nanoparticles

To confirm specificity of NTCP interactions with Myrcludex B derived ligands, we used pre-incubations with free Myrcludex B-Atto565 to competitively inhibit nanoparticle binding and cellular uptake (Figure 2A). Fluorescently labeled Myrcludex B can be considered to be a suitable blocking agent since its binding to NTCP expressing HepG2 *hNTCP* cells results in a significant shift in fluorescence signal as compared to control cells (data not shown). Uptake inhibition of nanoparticles modified with Myr-preS2-31, Cap-preS2-48, and Myr-preS2-48 by free Myrcludex B-fluorescein was confirmed by flow cytometry (Figure 2B). In contrast, the uptake of Myr-preS2-48A modified nanoparticles was not significantly inhibited by free Myrcludex B, most probably due to differences in the amino acid sequence (see difference in essential amino acid sequence highlighted in Figure 1A). By incubation of cells in presence of NaN_3 or at low temperature (i.e. 4°C), we confirmed that the uptake of NTCP targeted nanoparticles is an energy-dependent process (Figure 2A). These results demonstrate that hepatotropism of nanoparticles is mediated by NTCP and that the cellular uptake of the carrier is an active and energy-dependent process.

Selection of the optimal hepatotropic Myrcludex B-derived lipopeptide

After evaluating the formulation yield, physicochemical characteristics (i.e. storage/colloidal stability, hydrodynamic diameter, size distribution, zeta potential) and the targeting capacity of our NTCP-specific nanoparticles *in vitro*, we identified Myr-preS2-48 and Myr-preS2-31 as lead structures and used these for further investigations. This choice was based on the following observations:

First, only nanoparticles modified with lipopeptides but not peptides without conjugated fatty acid (e.g. preS2-48) can bind to NTCP. This set of experiments confirmed that the acyl modification of peptides

on nanoparticles` surface is a crucial prerequisite for hepatocyte binding as reported recently for free peptides.(Meier et al., 2013; Schieck et al., 2013) Only acyl modified peptides increased nanoparticle binding and internalization. Second, liposomes decorated with peptides conjugated to capric acid had a reduced colloidal stability. Their storage stability was limited due to particle aggregation. Furthermore, their size of around 134 nm exceeds the diameter of liver sinusoid fenestrations presumably limiting their access to the space of Disse. Third, Myr-preS2-48A modified nanoparticles were excluded due to poor NTCP specificity as demonstrated by the lack of binding competition by free Myrcludex B. In addition, the uptake of these nanoparticles was independent of NTCP expression levels and even higher in HepG2 wild type cells (Figure 1D).

Mechanistic studies on NTCP mediated cellular binding and internalization

In order to demonstrate the importance of covalent peptide attachment, we used a triple fluorescence labeling strategy (Figure 2C). The targeting ligand Myrcludex B was labeled with Atto633, the liposomal phospholipid bilayer was labeled with DiI, and the aqueous cargo payload of nanoparticles consisted of CF. Myr-preS2-31-K-Atto633 was labeled at an additionally introduced lysine at position 2, in order to still allow conjugation to the nanoparticle surface by the terminal cysteine. Recently, we have shown that additional N-terminal amino acids do not interfere with specific liver enrichment (for comparison Myr-preS -11-48).(Schieck et al., 2013)

First, CF-loaded, DiI-labeled nanoparticles were incubated with Myr-preS2-31-K-Atto633 and purified using size exclusion chromatography to remove free targeting ligand. Cell experiments confirmed successful removal of free Myr-preS2-31-K-Atto633 (no signal on cell membrane) and as expected no uptake of PEGylated nanoparticles. As a control, we added a mixture of free Myr-preS2-31-K-Atto633 and PEGylated nanoparticles to HepG2 *hNTCP* cells without prior purification. Notably, a

strong fluorescence signal on the cell membrane was observed due to specific binding of free Myr-preS2-31-K-Atto633 to hNTCP indicating specific targeting despite an additional N-terminal amino acid. Free Myr-preS2-31-K-Atto633 did not interact with PEGylated nanoparticles and thus did not trigger nanoparticle entry into HepG2 *hNTCP* cells. Finally, we covalently linked the Myr-preS2-31-K-Atto633 to the nanoparticle surface by Michael addition of the distal cysteine residue to maleimide-functionalized pegylated phospholipids integrated in the nanoparticle structure. A strong cellular binding and uptake of Myr-preS2-31-K-Atto633 modified nanoparticles was observed already within one hour.

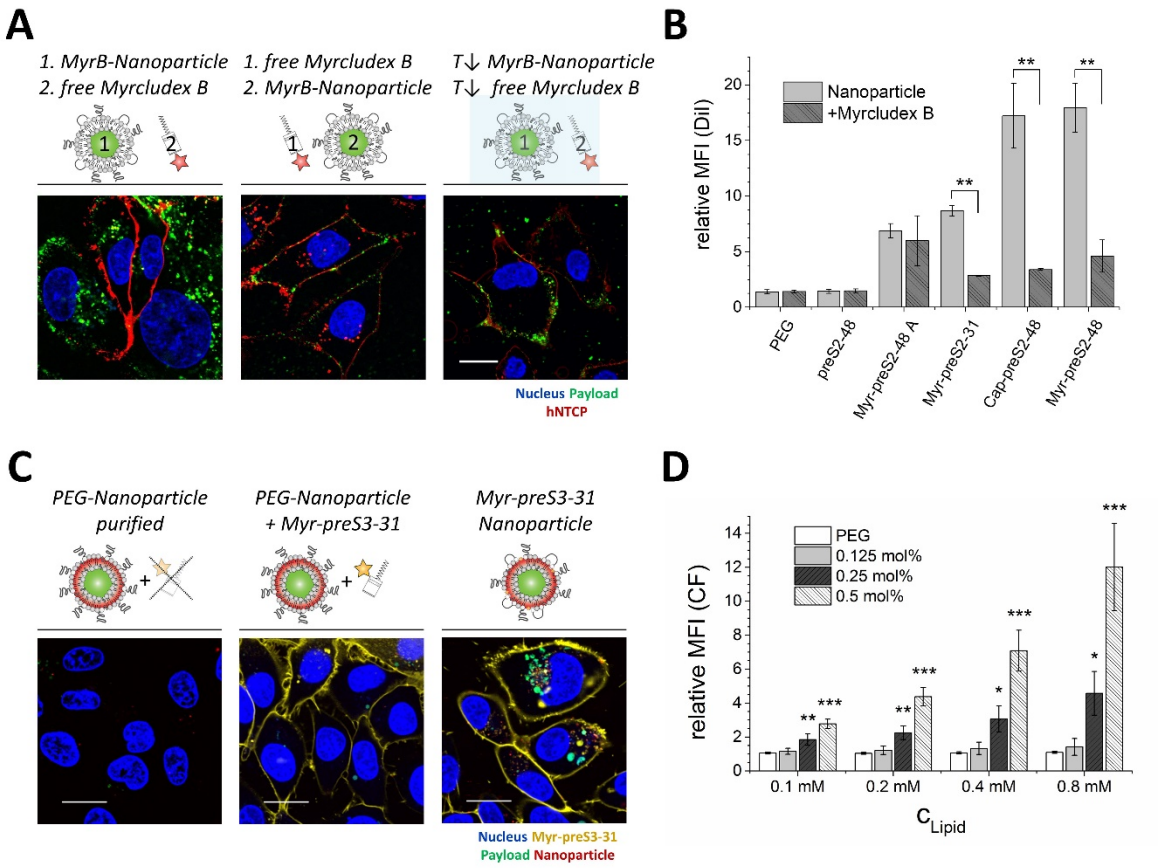

Figure 2. NTCP-specific and ligand-dependent uptake of Myrcludex B-derived lipopeptide conjugated nanoparticles into liver-derived cells *in vitro*. (A) Competitive inhibition study of Myrcludex B (MyrB)-conjugated nanoparticle uptake (carboxyfluorescein payload, green signal) into HepG2-*hNTCP* already after 30 min. Free Atto-565 labeled Myrcludex B (red signal) was added after (left panel) or before (middle panel) nanoparticle. Uptake studies at lower temperature (T↓, 4°C, right

panel) were performed to demonstrate energy-dependent process of nanoparticle internalization. Representative confocal laser scanning microscopy images are shown. Blue signal: Hoechst stain of cell nuclei. Scale bar = 10 µm. (B) Quantification of nanoparticle uptake in absence or presence of free Myrcludex B dependent on different Myrcludex B derived peptide modification. All values are shown as mean ± SD of biological replicates (n = 3 independent experiments). **p < 0.01. (C) Uptake study of nanoparticles (membrane dye, DiI, red signal) loaded with carboxyfluorescein (green signal) into HepG2-*hNTCP* without, mixed or covalently modified with Atto-633 conjugated Myr-preS2-31 (yellow signal). Myr-preS2-31-K-Atto633 is covalently linked to surface via stable thioether bond (right panel). Representative confocal laser scanning microscopy images are shown. Blue signal: Hoechst stain of cell nuclei. Scale bar = 10 µm. (D) Concentration (C_{Lipid}) dependent uptake of nanoparticles modified with different amounts of Myr-preS2-31 analyzed by flow cytometry and based on CF signal. All values are shown as mean ± SD of biological replicates (n = 4 independent experiments). *p < 0.05, **p < 0.01, ***p < 0.001. Numerical data for all graphs are shown in the Figure 2-source data.

Interestingly, nanoparticles including their payload entered the target cell whereas the targeting ligand remained on the cell surface. Since Myrcludex B has a remarkably high affinity to the NTCP (K_D of 67 nM),(Meier et al., 2013) it is tempting to speculate that the targeting ligand is retained by NTCP on the cell surface while the dissociated liposome payload is internalized and further processed by a yet unknown mechanism. Of note, intracellular CF signals were considerably higher as compared to DiI signals. This might also indicate liposome dissociation and perhaps loss of DiI during the internalization process. Uptake experiments using pharmacological pathway inhibitors suggested a partially clathrin-dependent and caveolin-independent mechanism which differs from the process of phagocytosis and micropinocytosis (Figure 2–figure supplement 1). Intriguingly, additional factors besides NTCP binding seem to contribute to this process. Non-hepatic HeLa cells transduced with mouse NTCP (mNtcp) or hNTCP can bind Myrcludex B-modified nanoparticles. However, binding is reduced as compared to binding in hepatic cell lines and no uptake is observed (Figure 2–figure supplement 2). Thus, additional hepatic cell dependent factors seem to play a role for efficient binding and internalization. Indeed, Verrier *et al.* reported recently that glypican 5 expression is an important co-factor for HBV entry.(Verrier et al.,

2016) Notably, uptake experiments using psgA745 cells (CHO xylosyltransferase mutants) overexpressing NTCP showed that binding of Myrcludex B alone is not influenced by glycosaminoglycans (Figure 2–figure supplement 3). In sharp contrast, binding of nanoparticles could be partially inhibited in HepG2 *WT* cells using heparan sulfate suggesting an involvement of glycosaminoglycans in the binding and subsequent internalization process of nanoparticles for hepatic cells (Figure 2–figure supplement 4). Therefore, it will be an important step for the design of next-generation carrier systems to elucidate such co-factors in detail and adapt the nano-sized delivery system accordingly.

To demonstrate concentration-dependent nanoparticle uptake of Myr-preS2-31 and investigate the effect of ligand density, qualitative and quantitative fluorescence techniques were used (Figure 2D). Therefore, we performed *in vitro* experiments using nanoparticles with variable amounts of coupled Myr-preS2-31 (0 mol% - 0.5 mol% initial maleimide functionalities on nanoparticle surface). With increasing targeting ligand concentration, a significant increase in cellular uptake was observed (Figure 2D, Figure 2–figure supplement 5). Notably, we identified a threshold value of at least 0.25 mol% for efficient cell binding by qualitative confocal imaging as well as quantitative flow cytometry experiments (Figure 2D, Figure 2–figure supplement 5). Below this value, no uptake was observed, whereas above 0.25 mol% cellular binding was improved. Stoichiometric estimations assuming a bilayer thickness of 5 nm, a phosphatidylcholine headgroup area of 0.71 nm^2 and an equal distribution of DSPE-PEG in the outer and inner nanoparticle membrane result in 157±16, 79±8, or 39±4 maleimide moieties per liposome capable for lipopeptide conjugation corresponding to 0.5 mol%, 0.25 mol%, or 0.125 mol%, respectively.(Maurer et al., 2001) Thus, a minimum of 80 functional maleimide moieties per nanoparticle is necessary for efficient cellular targeting after Myr-preS2-31 conjugation.

In vivo systemic circulation in the zebrafish vertebrate model

Since *in vitro* experimental models are not able to mimic the physiological complexity of nano-bio interactions at an organ level, we screened in the next step the effect of ligand density on pharmacokinetics of nanoparticles *in vivo* for Myr-preS2-48 and Myr-preS2-31 (Figure 3). Recently, we have reported that the zebrafish is a valuable pre-clinical tool to assess the systemic circulation and blood clearance of nanoparticulate drug delivery systems *in vivo*.(Sieber et al., 2017; Campbell et al., 2018; Sieber et al., 2018; Park, 2017; Yin et al., 2018)

Thus, we injected DiI labeled nanoparticles modified with different amounts of targeting ligand (0.125 mol% - 1.0 mol%) into the duct of Cuvier of transgenic kdrl:EGFPs843 zebrafish embryos which express GFP in the vasculature endothelial cells. Already one hour post injection, a clear qualitative difference in circulation characteristics of tested nanoparticles was detected. With increasing ligand density on the nanoparticle surface, the systemic circulation of nanoparticles decreased for both peptides (Figure 3) indicating that ligand modification of nanoparticles interferes with the shielding properties of PEG. Increased blood clearance was thereby paralleled by accumulation in the posterior caudal vein region. The observed binding pattern did not match a *stabilin-2* scavenger receptor dependent nanoparticle clearance which would be indicative for interactions with mammalian liver sinusoidal endothelial cells (LSECs).(Campbell et al., 2018) More likely a sequestration by macrophages is responsible for this clearance mechanism corresponding to an accumulation in the spleen of rodents.(Sieber et al., 2018)

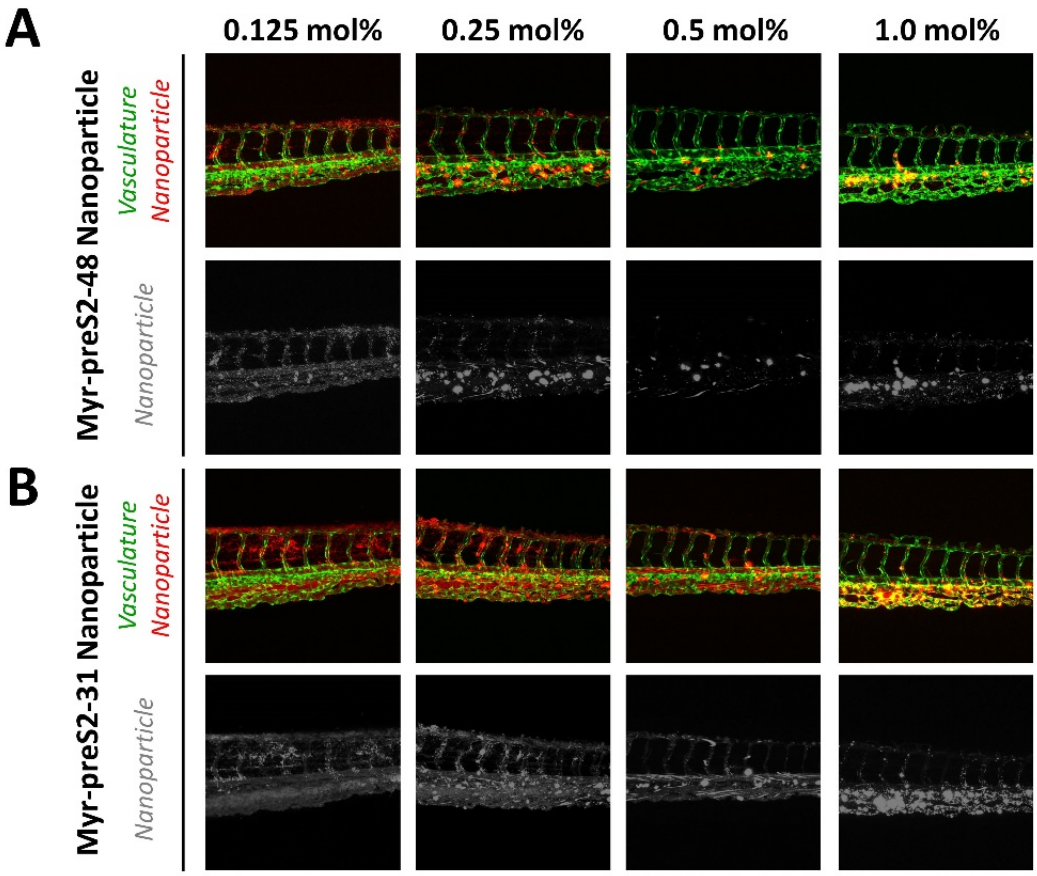

Figure 3. Systemic circulation of Myrcludex B-derived lipopeptide conjugated nanoparticles *in vivo* in the zebrafish model. Nanoparticles were modified with different amounts of (A) Myr-preS2-48 or (B) short Myr-preS2-31 and injected into transgenic zebrafish embryos expressing green fluorescent protein in their vasculature endothelial cells (green signal). Membrane of nanoparticles was fluorescently labeled using DiI (red signal). Representative confocal laser scanning microscopy images of tail region one hour post injection.

Interestingly, nanoparticles modified with the shorter targeting peptide, *i.e.* Myr-preS2-31, showed increased systemic circulation (Figure 3B) as compared to Myr-preS2-48 modified nanoparticles (Figure 3A) at similar ligand densities. Thus, Myr-preS2-31 modified nanoparticles were selected for further investigations. However, nanoparticles modified with more than 0.5 mol% Myr-preS2-31 were as well excluded from further evaluation due to their poor systemic circulation and high clearance rate.

In vivo targeting ability in the zebrafish vertebrate model

In a next step, we investigated the targeting capacity of Myr-preS2-31 modified nanoparticles to human cells *in vivo* in the zebrafish model (Figure 4). For this approach, we used HEK293 cells stably expressing GFP for further genetic modification and establishment of xenotransplants.(Witzigmann et al., 2015b) HEK293-GFP cells were transiently transfected with hNTCP to express the targeting factor for our hepatotropic nanoparticles. Wild type HEK293-GFP without hNTCP served as control. Both cell lines were injected into ABC/TU wild type zebrafish embryos to create human xenotranplants. The different nanoparticles were injected as soon as transgenic human cells stopped circulating and remained in the caudal vasculature tail region (*i.e.* after approximately one hour). Interestingly, a clear difference in targeting capacity dependent on hNTCP expression and ligand density was revealed. Whereas there was no significant difference in targeting capacity at different ligand densities for hNTCP deficient HEK293-GFP cells (Figure 4A), a significant increase in binding to HEK293-GFP cells was observed if hNTCP was overexpressed as the nanoparticles could bind specifically and be readily internalized (Figure 4B). Most importantly, this was only valid for nanoparticles modified with 0.25mol% Myr-preS2-31 (Figure 4, quantitative analysis). This illustrates that ligand density highly influences the balance between systemic circulation, systemic clearance rate and targeting efficiency of our liposome-based nanoparticles:

Nanoparticles modified with ligand densities below 0.25 mol% show a favorable systemic circulation but have an insufficient targeting ability. This also confirms our observations *in vitro*, where nanoparticles with a ligand density below 0.25mol% did not significantly bind to HepG2 *hNTCP* cells. In sharp contrast, nanoparticles modified with higher Myr-preS2-31 targeting ligand densities (*i.e.* 0.5 mol%) have increased targeting ability *in vitro*. However, decreased systemic circulation and a high clearance rate under *in vivo* conditions counteract the advantage of higher ligand densities. Nanoparticles

modified with 0.25 mol% Myr-preS2-31 have the highest targeting efficiency due to an ideal balance between target affinity and long circulation time *in vivo*. It should be noted that nanoparticles are internalized by target cells (Figure 4B) whereas free Myrcludex B apparently binds with high affinity to target cells but is not internalized (Figure 4–figure supplement 1). This phenomenon was recently observed by our team in rodents (data not shown) and was also reported from clinical trials in humans.

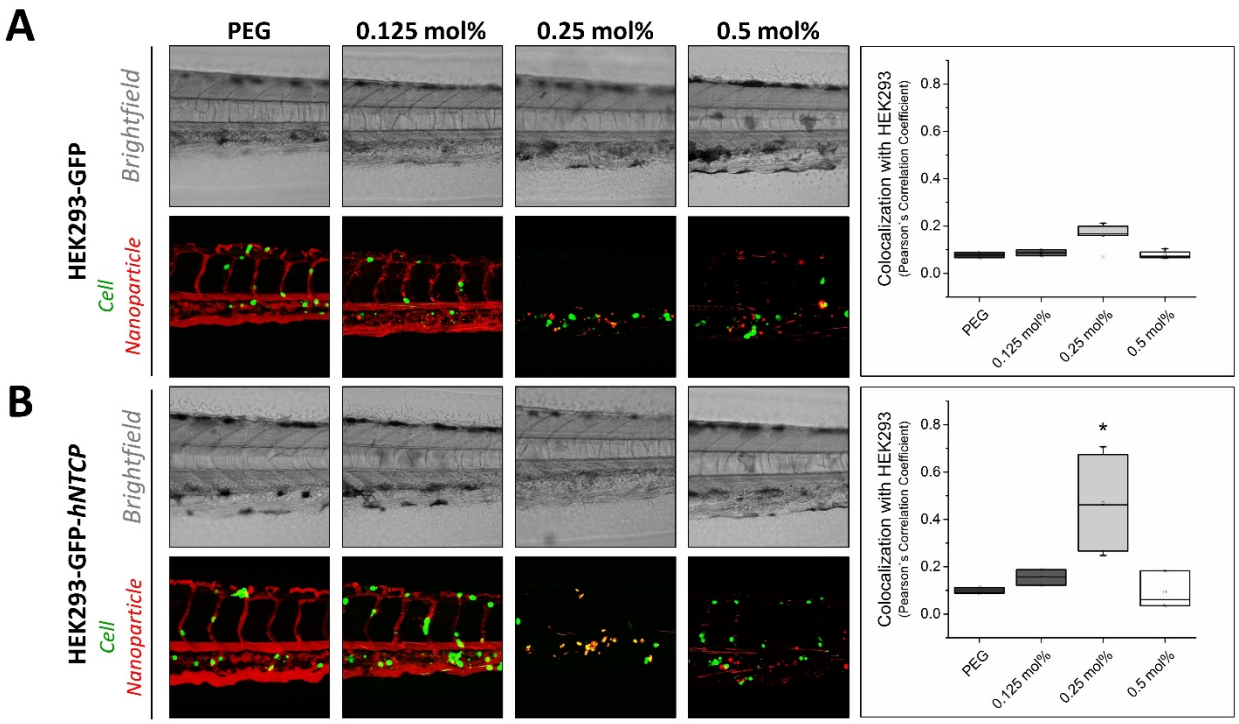

Figure 4. Targeting ability of Myr-preS2-31 conjugated nanoparticles *in vivo* in xenotransplanted zebrafish embryos. Nanoparticles were modified with different amounts of Myr-preS2-31 and injected into wild type zebrafish embryos xenotransplanted with human, GFP expressing HEK293 cells (green signal), (A) deficient or (B) expressing hNTCP. Membrane of nanoparticles was fluorescently labeled using DiI (red signal). Yellow signals demonstrate colocalization (*i.e.* binding and internalization) of nanoparticles with HEK293-GFP cells. Representative brightfield and fluorescence images of tail region one hour post injection are shown. Quantitative analysis of nanoparticle binding to HEK293-GFP cells is represented by Pearson´s Correlation Coefficient (PCC). All values are shown as box plots of biological replicates ($n \geq 2$ independent experiments). *$p < 0.05$. Numerical data for all graphs are shown in the Figure 4-source data.

In vivo liver targeting of Myr-preS2-31 conjugated nanoparticles in mice

To elucidate the influence of ligand density on hepatotropism of our nanoparticles *in vivo* in mammals, we evaluated the pharmacokinetic properties of Myr-preS2-31 conjugated nanoparticles in mice. For this set of experiments, we used a dual labeling approach. The radioactive nuclide indium-111 (^{111}In) was used for whole-body imaging and biodistribution studies whereas fluorescence labeling with DiI was used to evaluate intra-organ nanoparticle distribution. Importantly, we incorporated DTPA-conjugated DSPE into the lipid bilayer to chelate ^{111}In on the surface of nanoparticles. This radiolabeling strategy has distinct advantages as compared to other labeling techniques or loading of ^{111}In-oxine into nanoparticles.(van der Geest et al., 2015) First, this radiolabeling method is robust, fast (within 45 min) and efficient with labeling efficiencies above 90%. Notably, free ^{111}In was easily removed from nanoparticle formulations prior to injection using size exclusion chromatography (NAP-5 columns). Second, DTPA-DSPE enables retention of ^{111}In in serum for at least 48 h at 37 °C (>98% label retention) demonstrating the high stability necessary for *in vivo* studies of nanoparticulate drug delivery systems.(van der Geest et al., 2015) Third, free ^{111}In is rapidly eliminated via kidneys and excreted in the urine as shown previously.(Harrington et al., 2000; Shih et al., 2017) This offers an easy assessment to differentiate between non-bound and nanoparticle bound ^{111}In.

Four different lipid-based nanoparticles were prepared and injected intravenously into the tail vein of mice, *i.e.* PEGylated liposomes (negative control) and nanoparticles modified with 0.125 mol%, 0.25 mol% and 0.5 mol% Myr-preS2-31. One-hour post injection, plasma and organs were harvested to perform a quantitative biodistribution analysis *ex vivo* (Figure 5A). PEGylated nanoparticles showed the typical biodistribution of sterically stabilized nanoparticles with a strong signal in the blood (Figure 5A). Myr-preS2-31 conjugated liposomes demonstrated different biodistribution patterns depending on ligand density (Figure 5A). Modification of nanoparticles with 0.125 mol% Myr-preS2-31 did not alter the

systemic circulation significantly (*i.e.* high blood pool signal). Only a minor increase in liver accumulation was observed as compared to ligand-lacking PEGylated nanoparticles (Figure 5A).

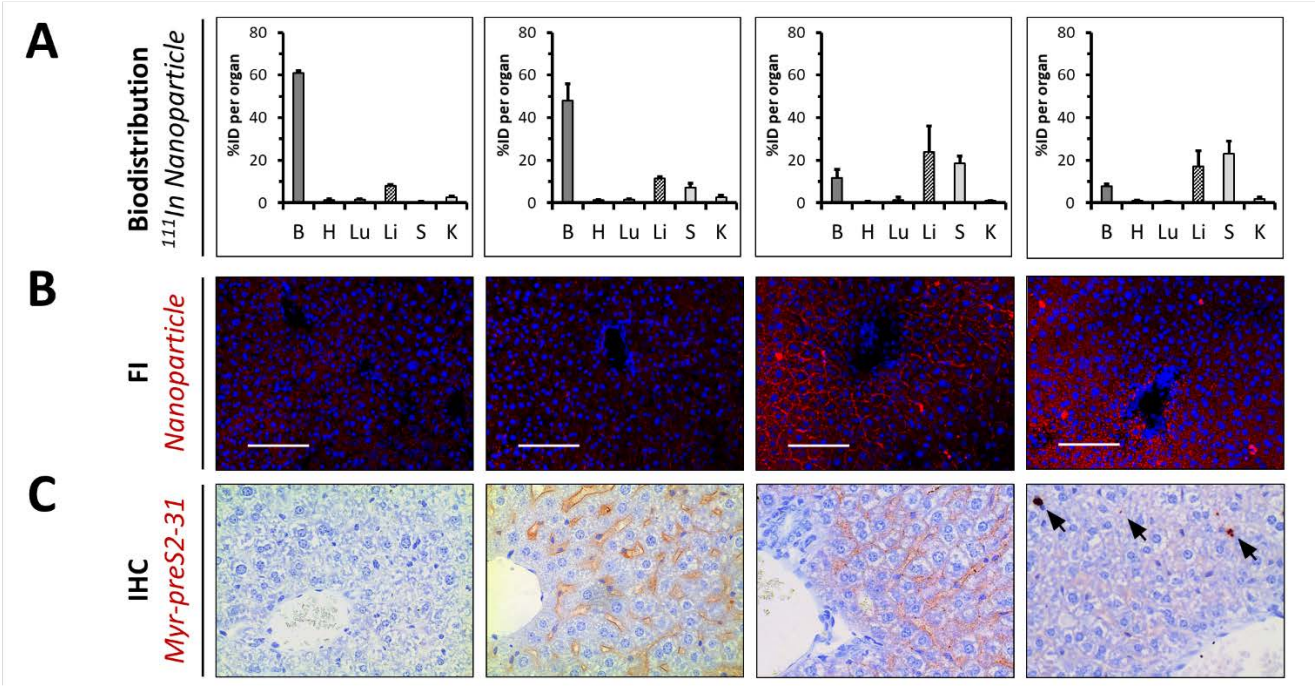

Figure 5. *In vivo* biodistribution and liver targeting of Myr-preS2-31 conjugated nanoparticles in mice. Nanoparticles were modified with different amounts of Myr-preS2-31 and labeled with radioactive ^{111}In and fluorescent membrane dye (DiI, red signal). (A) Quantitative biodistribution studies were performed 1 hour post injection. Radioactivity of each organ was determined with a γ-counter and the percentage of injected dose (%ID) per organ was calculated. B=blood, H=heart, Lu=lung, Li=liver, S=spleen, K=kidney. All values are shown as mean ± SD of biological replicates (n = 3 independent experiments). Numerical data for all graphs are shown in the Figure 5-source data. (B) Fluorescence imaging (FI) of nanoparticles (DiI, red signal) in liver cryo-sections. Blue signal: Hoechst stain of cell nuclei. Scale bar = 100 µm. (C) Immunohistochemistry (IHC) of Myr-preS2-31 (red signal) in the liver sections 1 hour after intravenous injection. Mice liver sections were stained with anti-Myr-preS2-31 antibody (MA18/7). Blue signals represent cell nuclei. Arrows indicate distinct localized accumulations.

Interestingly, nanoparticles modified with 0.25 mol% Myr-preS2-31 significantly enriched binding to the liver (Figure 5A). Further increase in ligand density (0.5 mol%) resulted in an increase in spleen accumulation, *i.e.* enhanced clearance by cells of the reticuloendothelial system (Figure 5A). Of note,

none of the nanoparticle formulation resulted in an elimination via kidneys demonstrating the high stability and retention of the DTPA-DSPE chelated ^{111}In. In order to highlight the ligand-density dependent hepatotropism, we calculated ratios between the blood pool and important organs, *i.e.* liver (*i.e.* target organ), spleen (*i.e.* clearance organ), and kidney (*i.e.* control organ since nanoparticle bound ^{111}In should not show renal excretion) (Figure 5–figure supplement 1). Indeed, Myr-preS2-31 modification ≥ 0.25 mol% resulted in increased liver/spleen-to-blood ratios. Strikingly, nanoparticles modified with 0.25 mol% Myr-preS2-31 demonstrated a significant increase in the liver-to-kidney ratio confirming our conclusions from the zebrafish model, *i.e.* 0.25 mol% Myr-preS2-31 as an optimal ligand density (Figure 4B). Planar gamma scintigraphy imaging of injected mice confirmed these observations (Figure 5–figure supplement 2).

The biodistribution studies were combined with fluorescence imaging of nanoparticle distribution (Figure 5B, Figure 5–figure supplement 3) and immunohistochemistry of Myr-preS2-31 distribution (Figure 5C, Figure 5–figure supplement 3-6) in liver, spleen, and kidney (*i.e.* nanoparticles and Myr-preS2-31 should not show renal excretion). PEGylated nanoparticles showed a weak fluorescent signal in the liver (Figure 5B). Importantly, these signals were not associated with the sinusoidal membrane of hepatocytes but arose from the high hepatic blood supply (Figure 5–figure supplement 5). No signals were observed in spleen and kidney (Figure 5–figure supplement 3). Modification of nanoparticles with 0.125 mol% Myr-preS2-31 did not result in significantly increased liver levels. A marginal binding of nanoparticles to hepatocyte membrane was visually observed (Figure 5B, C). This supports our hypothesis that a threshold level of targeting ligand density present on the nanoparticle surface is necessary for successful targeting. Importantly, strong signals for nanoparticles modified with 0.25 mol% Myr-preS2-31 were observed on the basolateral membrane of parenchymal liver cells (Figure 5B, C) demonstrating the strong hepatotropism of our nanoparticles. Further increasing the

ligand density (*i.e.* 0.5 mol%) was detrimental and resulted in a diffuse hepatic staining pattern. Nanoparticles and their payload were detected as punctuated signals in the whole liver and did not show a specific membrane staining (Figure 5B, Figure 5–figure supplement 6). Myr-preS2-31 was detected in distinct localized areas only (Figure 5C). We conclude that nanoparticles modified with excessive Myr-preS2-31 densities (0.5mol%) are rapidly cleared by and liver resident macrophages, *i.e.* Kupffer cells. Subsequent re-distribution phenomena result in an unspecific nanoparticle signal in the whole liver.

Competition of NTCP-specific uptake into mouse hepatocytes *in vivo*

Since nanoparticles modified with 0.25 mol% Myr-preS2-31 allowed highly efficient liver targeting, we next investigated the NTCP specificity and the internalization process (Figure 6A). Therefore, we injected either labeled nanoparticles alone or together with free unlabeled Myrcludex B into mice (Figure 6B). Co-injection of Myrcludex B resulted in a clear decrease in liver enrichment by competitive inhibition of NTCP-binding as demonstrated by a change of signal.

To reveal the localization of nanoparticles, we performed a confocal microscopy analysis of liver cryo-sections (Figure 6C). We stained liver cryo-sections using antibodies against mNtcp and Myr-preS2-31 (MA 18/7). Interestingly, nanoparticles that were internalized into parenchymal liver cells did not co-localize with mNtcp fluorescent signals. Myr-preS2-31 still colocalized with mNtcp suggesting that the targeting ligand was separated from the nanoparticle during cellular internalization as already observed in *in vitro* experiments. This phenomenon was confirmed by a colocalization analysis (Figure 6C). The observed cellular uptake is a surprising finding since HBV possesses pronounced host species specificity with regard to binding and infectivity. HBV binds to murine hepatocytes but cannot infect mice due to the lack of host cell dependency factors.(Lempp et al., 2016) Therefore, chimeric mice transplanted with primary human hepatocytes have been developed to study anti-HBV drugs.(Petersen et al., 2008;

Lütgehetmann et al., 2012) In humans or chimpanzees only, HBV specifically binds to hepatocytes and subsequently infects the host.

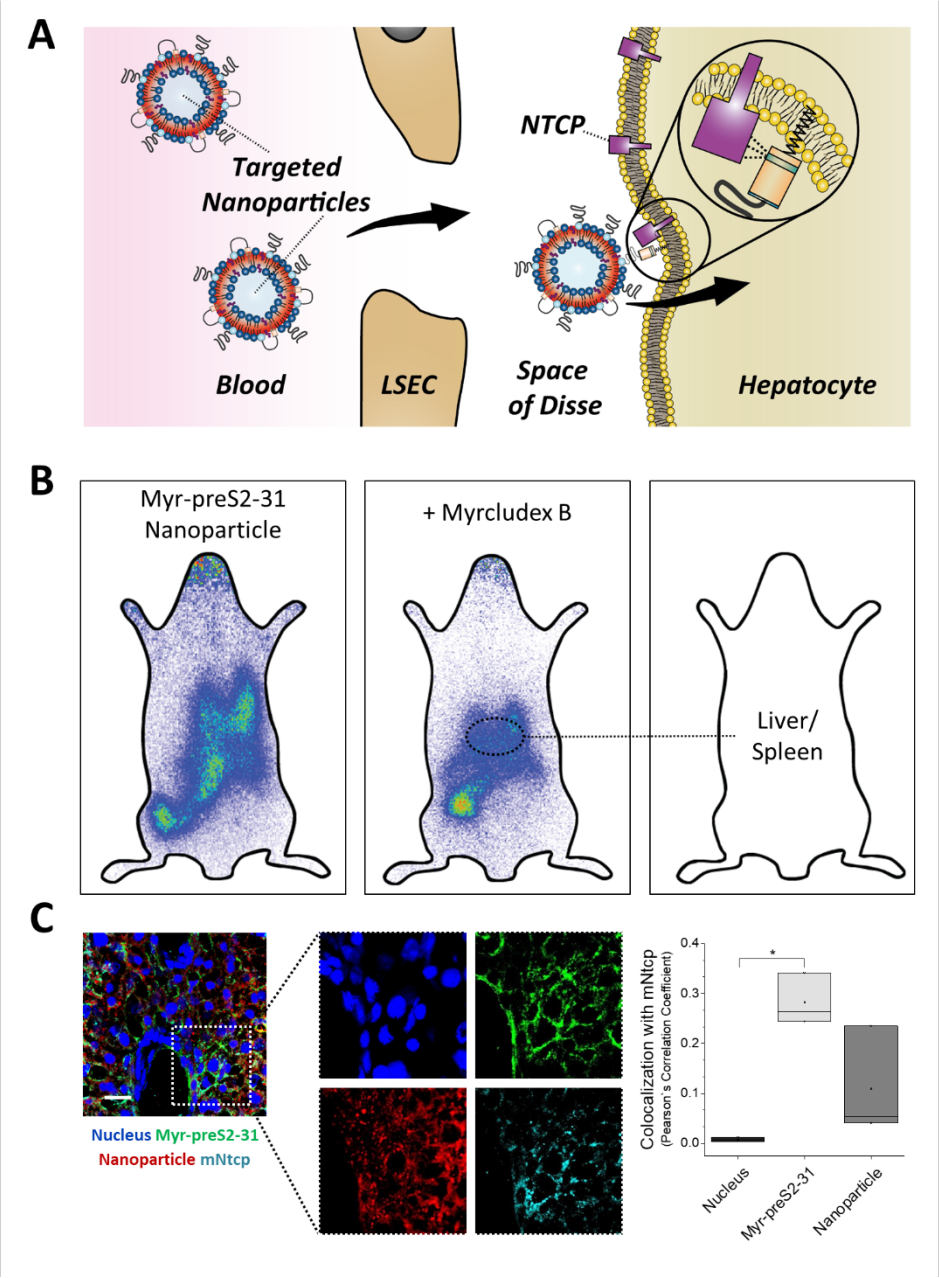

Figure 6. NTCP-specific uptake of Myr-preS2-31 conjugated nanoparticles into hepatocytes *in vivo* in mice. (A) Schematic representation of NTCP-targeted nanoparticle binding to hepatocytes. Circulating nanoparticles pass the fenestrae of liver sinusoidal endothelial cells (LSEC) and subsequently bind to the NTCP in the basolateral membrane of hepatocytes facing the space of Disse. Prior to Myr-preS2-31 mediated NTCP binding, the myristoyl chain is inserted into the lipid bilayer. In

close proximity to hepatocytes, acyl chain switches into cellular membrane due to high affinity of essential peptide sequence to NTCP binding site, thereby consolidating target transporter binding. (B) Nanoparticles were modified with 0.25mol% of Myr-preS2-31 and labeled with radioactive ^{111}In and fluorescent membrane dye (DiI, red signal). Planar imaging of mice one hour post-injection. Competitive inhibition of liver binding by co-injection of free Myrcludex B clearly demonstrates NTCP-specific binding. Positions of liver and spleen are indicated by small circles. (C) Immunfluorescence staining of nanoparticles (red signal), targeting ligand (Myr-preS2-31, green signal, antibody staining), and mNtcp (cyan signal, antibody staining) in liver cryosections. Nuclei staining (blue signal) served as control for complete internalization; no overlap with mNtcp. Scale bar = 20 µm. Colocalization analysis with mNtcp is represented by Pearson´s Correlation Coefficient (PCC). All values are shown as box plots of biological replicates (n = 3 independent experiments). *p < 0.05. Numerical data for all graphs are shown in the Figure 6-source data.

Importantly, our NTCP-targeted nanoparticles apparently lack this species specificity. In contrast to HBV, our hepatotropic nanoparticles specifically bind to mouse hepatocytes in a mNtcp-dependent manner and are subsequently internalized. The exact molecular interactions behind this internalization process will require additional studies to elucidate structural determinants important for cellular uptake and to better understand viral entry mechanisms, which are still unknown.(Glebe and Urban, 2007)

CONCLUSIONS

In conclusion, the combination of *in vitro* investigations, the zebrafish model and *in vivo* experiments in rodents offered a unique approach to optimize our targeting ligand modified nanoparticles. The zebrafish model demonstrated to be an excellent tool to pre-screen various nanoparticle formulations, to assess the effect of Myrcludex B modifications on their pharmacokinetics and biodistribution, and thus increase the accuracy of predictions for experiments in rodents. The proposed NTCP targeted delivery platform is an alternative and promising approach to current liver targeting strategies. These delivery systems can

increase liver uptake levels, decrease accumulation in off-target tissues and at the same time avoid clearance by the reticuloendothelial system by mimicking HBV targeting properties. For future clinical applications, small molecule drugs, nucleic acids or proteins need to be encapsulated and studied in appropriate disease models. In particular, we see a great potential for our nanoparticle targeting strategy in the field of metabolic diseases of the liver.

MATERIALS AND METHODS

Synthesis of Myrcludex B-derived peptides. Different peptides were produced by fluorenylmethoxycarbonyl/t-butyl (Fmoc/tBu) solid-phase synthesis using an Applied Biosystems 433A peptide synthesizer and modified with acyl chains as described previously.(Schieck et al., 2013) Atto fluorescence dyes were either linked to the distal cysteine residue by maleimide chemistry or to the ε-amino group of an additionally introduced D-lysine at position 2 by NHS chemistry for mechanistic studies based on a triple fluorescence labeling strategy. In contrast to all other amino acids of Mycludex B-derived lipopeptides, a D-amino acid was introduced in the latter case due to the chemical synthesis strategy used. Peptides were purified using preparative reverse-phase high performance liquid chromatography (HPLC, LaPrep P110, VWR International GmbH) with a Reprosil-Gold 120 C18 4 µm column (Dr. Maisch GmbH) and a variable gradient adapted to the peptides properties in a range of 100% H_2O to 100% acetonitrile, both containing 0.1% TFA. Peptide identity was verified using an analytical Agilent 1100 HPLC system equipped with a Chromolith Performance RP-C18e column (Merck KGaA) coupled to a mass spectrometer (Exactive, Thermo Fisher Scientific).

Preparation of hepatotropic nanoparticles. Hepatotropic nanoparticles based on liposomes were prepared using the film rehydration extrusion method as described previously.(Detampel et al., 2014) The lipid membrane composition of nanoparticles consisted of DSPC (Lipoid AG), cholesterol (Sigma-Aldrich), DSPE-PEG2000 (Lipoid AG) at a molar ratio of 52.7:42.3:5. For the conjugation of HBV-derived peptides, DSPE-PEG2000 was replaced by DSPE-PEG2000-maleimide (Avanti Polar Lipids) at indicated molar ratios. For fluorescence labeling of lipid membrane, 1mol% DiI (Thermo Fisher Scientific) was added to the lipid composition replacing DSPC. For radioactive labeling with ^{111}In, DSPC was replaced by 3 mol% DSPE-DTPA (Avanti Polar Lipids). Desired ratios of lipids were mixed; a homogenous thin film was prepared and dried using a Rotavapor A-134 (Büchi). Lipid films were

rehydrated using 0.01 M PBS pH 7.2 containing 1 mM EDTA (Sigma-Aldrich) to prevent metal ion catalyzed maleimide oxidation. For passive loading and fluorescence labeling of inner core, a 60 mM 5(6)-carboxyfluorescein (Sigma-Aldrich) solution (pH 7.4) was used for the rehydration step. At this concentration >98% of the fluorescence is self-quenched (Figure 1–figure supplement 3). Resulting multilamellar vesicles were subjected to five freeze-thaw cycles and extruded 11 times through a polycarbonate membrane (Avanti Polar Lipids) with a pore size of 100 nm followed by 11 times through a polycarbonate membrane with a 50 nm pore size 10°C above transition temperature (i.e. 65°C for DSPC-based formulations). For functionalization with HBV-derived peptides, nanoparticles were mixed with peptides at molar maleimide-to-cysteine ratio of 1:1 and incubated at RT overnight. To remove non-conjugated peptides and/or free hydrophilic dye, size exclusion chromatography using a Sephadex G50 column (GE Healthcare) eluted with 0.01 M PBS pH 7.4 was performed. The size exclusion chromatography column was coupled to an UV detector to analyze recovery of nanoparticles based on peak areas. Hepatotropic nanoparticles were concentrated to a final lipid concentration of 10 mM using Amicon Ultra-4 centrifugal filter units with a 100 kDa molecular weight cut-off (Millipore). DiI and cholesterol were used as marker lipids to quantify total lipid content. DiI content was quantified based on relative fluorescence signals as compared to liposome standards and in combination with Triton X-100 treatment to account for potential DiI self-quenching. Samples were excited at 561 nm and fluorescence signals were recorded using a Spectramax M2 microplate reader (Molecular Devices). The cholesterol content was determined using the Cholesterol E cholesterol assay kit from Wako following the manufacturer's protocol.

Loading of compounds into hepatotropic nanoparticles.

FITC-peptide loading. For passive loading of FITC-Ahx-yKKEEEK into nanoparticles, a 2 mg/mL FITC-peptide solution in a mixture of PBS/DMSO/EtOH at pH 7.0 was used for the rehydration step of

the homogenous lipid film. Resulting multilamellar vesicles were processed as described in the methods section.

Propidium iodide loading. For passive loading of propidium iodide into nanoparticles, a 10 mg/mL propidium iodide solution in PBS was used for the rehydration step of the homogenous lipid film. Resulting multilamellar vesicles were processed as described in the methods section including a final purification step.

Doxorubicin loading. For loading of doxorubicin, an active drug loading strategy based on a citrate gradient was used as previously described.(Mayer et al., 1990) The homogenous lipid film was rehydrated using a 300 mM citrate buffer at pH 4.0 and multilamellar vesicles were processed as described in the methods section. The pH of the external buffer solution was adjusted to pH 7.0 and nanoparticles were incubated with 2 mg/mL doxorubicin at 65°C for 15 min. Free doxorubicin was removed by size exclusion chromatography.

Physicochemical characterization of hepatotropic nanoparticles.

Dynamic light scattering. Size and size distribution (polydispersity index, PDI) of nanoparticles were analyzed using a Delsa Nano C Particle Analyzer (Beckman Coulter) equipped with a 658 nm laser. Samples were measured in D-PBS at RT and a measurement angle of 165°. Data were converted using the CONTIN particle size distribution analysis (Delsa Nano V3.73/2.30, Beckman Coulter Inc.).

Electrophoretic light scattering. Zeta potential of nanoparticles was analyzed using a Delsa Nano C Particle Analyzer. Samples were measured in D-PBS at RT and a measurement angle of 15°. Data were converted using the Smoluchowski equation (Delsa Nano V3.73/2.30).

Transmission electron microscopy. Size and morphology of nanoparticles were analyzed using transmission electron microscopy (TEM) as described previously.(Witzigmann et al., 2015a) In brief, samples were deposited on a 400-mesh carbon-coated copper grid, negatively stained with 2% uranylacetate, and analyzed using a CM-100 electron microscope operating at 80 kV (Philips).

Fluorescence correlation spectroscopy. Fluorescence correlation spectroscopy (FCS) analysis of nanoparticles was performed as described previously.(Uhl et al., 2017) In brief, Atto488, Myr-preS2-48-Atto488 and Myr-preS2-48-Atto488 conjugated nanoparticles were analyzed using an inverted confocal fluorescence laser scanning microscope (Zeiss LSM 510-META/Confocor 2) equipped with a 40× water immersion objective lens (Zeiss C-Apochromat 40×, numerical aperture 1.2). Fluorescence intensity fluctuations were measured for three independent samples and each measurement was repeated 20-30 times. Autocorrelation functions were fitted using a two-component model and diffusion times were calculated.

Cell Culture. All human cell lines were cultured at 37 °C under 5% CO_2 and saturated humidity in Dulbecco's modified Eagle's culture medium high glucose (DMEM, Sigma-Aldrich) supplemented with 10% fetal calf serum (Amimed), penicillin (100 units/mL, Sigma-Aldrich), and streptomycin (100 µg/mL, Sigma-Aldrich). Stable NTCP expressing liver derived cell lines, i.e. HepG2 *hNTCP* and HuH7 *hNTCP*, were created by lentiviral transduction as published previously.(Ni et al., 2014) For uptake experiments, different cell lines were seeded at a density of 2.5×10^4 cells/cm^2 and allowed to adhere for 24 h. For confocal laser scanning microscopy experiments, cells were grown on poly-D-lysine (Sigma-Aldrich) coated glass cover slips (#1.5, Menzel) or well plates (TPP).

Transfection of cell lines. For transient expression of the transporter, plasmids encoding for mNtcp (Slc10a1) or hNTCP (SLC10A1) were generated, amplifying the coding sequence from commercially obtained mRNA (Amsbio) by PCR. The following primers were used:

hNTCP_for: 5′-ATGGAGGCCCACAACGCGTCT-3′,

hNTCP_rev 5′-CTAGGCTGTGCAAGGGGA-3′;

mNtcp_for 5`-GTGTTCACTGGGTCGGAGGATG-‘3,

mNtcp_rev1 5`-CAGGTCCAGAGCAAATACTCATAGGAG-‘3.

Subsequently the amplicons were ligated into pEF6-V5/HIS (Invitrogen), followed by sequence verification (Microsynth). The resulting plasmids mNtcp-pEF6 and hNTCP-pEF6 and Lipofectamine 3000 (Sigma-Aldrich) were used for transfection of human cell lines. A standard transfection protocol was developed as follows: Plasmid DNA and P3000 reagent were diluted in Opti-MEM (Sigma-Aldrich) and rapidly mixed with Lipofectamine 3000 diluted Opti-MEM using a DNA-to-Lipofectamine 3000 w/V ratio of 3. After 5 min incubation, the transfection mix was added to adhered cells at a plasmid DNA concentration of 1 μg/mL. Control cells were either transfected with empty pEF6 vector or treated with Opti-MEM alone.

Assessment of cytocompatibility of nanoparticles. To assess the cytocompatibility of nanoparticles modified with different Myrcludex B derived peptides a MTT cell viability assay was performed. Wild type HeLa cells, liver-derived wild type HepG2 cells and HepG2 *hNTCP* were seeded and cultured as described above. Nanoparticles were added to cells at final concentrations of 0.25 mM – 8 mM. After 24 h, MTT reagent (Sigma-Aldrich) was added to cells for 4 h. Formazan dye crystals were solubilized for 2 h using a mixture containing 3% (v/v) sodium dodecyl sulfate (Sigma-Aldrich) and 40 mM hydrochloric acid in isopropanol (Sigma-Aldrich). Absorption of reduced MTT and background signals

were measured using a Spectramax M2 microplate reader at 570 nm and 670 nm, respectively. Control cells treated with buffer were used to calculate relative cell viability.

Uptake of nanoparticles *in vitro*. To assess the uptake rate and intracellular localization of nanoparticles, cell lines were incubated with different concentrations of nanoparticles at 37°C or 4°C. Nanoparticles were loaded with 5(6)-carboxyfluorescein (payload) and/or incorporated DiI in their phospholipid-membrane. Myrcludex B derived peptides were fluorescently labeled if necessary as indicated above. At the indicated time points, confocal laser scanning microscopy or flow cytometry were used for qualitative and quantitative analysis, respectively.

Competitive inhibition experiments in vitro. NTCP-specific uptake of nanoparticles was investigated by pre-incubation with 400 nM free Myrcludex B fluorescently labeled with Atto-565 or Atto-488 as indicated.

Binding mechanism studies in vitro. The hepatic cell dependent binding mechanism of nanoparticles was investigated by pre-incubation with 300 µg/mL heparin sulfate.

Uptake mechanism studies on NTCP mediated internalization in vitro. The uptake mechanism of nanoparticles into HepG2 *hNTCP* cells was investigated using different pharmacological pathway inhibitors as described previously.(Lunov et al., 2011) Cells were pre-incubated using 100 µg/mL colchicine (micropinocytosis inhibitor), 10 µg/mL chlorpromazine (inhibitor of clathrin-mediated endocytosis), or 25 µg/mL nystatine (inhibitor of caveolin-mediated endocytosis) for 30 min before addition of nanoparticles.

Confocal laser scanning microscopy. At indicated time points, cell nuclei were counterstained for 5 min using 1.0 µg/mL Hoechst 33342 (Sigma-Aldrich), washed with PBS and embedded using ProLong

Gold antifading reagent (Invitrogen Life Technologies). For live cell imaging, cell nuclei were counterstained with Hoechst 33342, and if indicated cell membranes were stained with Cell Mask Deep Red Plasma Membrane Stain (1.0 μg/mL, Thermo Fisher Scientific) and NTCP was stained using fluorescently labeled Myrcludex B. Confocal laser scanning microscopy analysis was performed using an Olympus FV-1000 inverted microscope (Olympus Ltd.), equipped with a 60× PlanApo N oil-immersion objective (numerical aperture 1.40).

Flow cytometry analysis. To quantify the uptake rate of nanoparticles into non-hepatic and hepatic cell lines with different NTCP expression levels, flow cytometry analysis was performed. Cells were detached using 0.25% trypsin/EDTA (Sigma-Aldrich), washed twice with PBS and re-suspended in PBS containing 1% fetal calf serum, 0.05% NaN3, and 2.5 mM EDTA. At least 10,000 cells per setting were analyzed using a FACS Canto II flow cytometer (Becton Dickinson). Doublets were excluded and DiI or CF signals were measured. Relative mean fluorescence intensities (MFI) of DiI or CF signals normalized to untreated cells were calculated using Flow Jo VX software (TreeStar).

Zebrafish embryo culture. Zebrafish embryos (*Danio rerio*) are a well-established vertebrate screening model for engineered nanomaterials.(Campbell et al., 2018; Einfalt et al., 2018; Sieber et al., 2017) They were maintained in accordance with Swiss animal welfare regulations as described previously.(Sieber et al., 2017) In brief, eggs from wild type ABC/TU and transgenic kdrl:EGFPs843 adult zebrafish were maintained in media at 28°C. Formation of pigment cells was prevented by 1-phenyl 2-thiourea (PTU, Sigma-Aldrich).

Injection of nanoparticles into zebrafish embryos. To assess the systemic circulation of nanoparticles, samples were injected into transgenic kdrl:EGFPs843 zebrafish embryos (2 dpf) as described previously.(Sieber et al., 2017) In brief, calibrated volumes of 1 nL were injected into the duct

of Cuvier of anesthetized and agarose-embedded zebrafish embryos using a micromanipulator (Wagner Instrumentenbau KG), a pneumatic Pico Pump PV830 (WPI), and a Leica S8APO microscope (Leica). The tail region of zebrafish embryos was imaged 1 hour post injection (hpi) using an Olympus FV-1000 inverted confocal laser scanning microscope equipped with a 20× UPlanSApo (numerical aperture 0.75) objective.

Targeting of xenotransplanted human cells in the zebrafish model. Human HEK293 cells deficient or overexpressing hNTCP were detached from 6-well cell culture dishes using 1 mL pre-warmed DMEM, washed (5 min at 200 g) and resuspended in 10 µL DMEM. Human cells (3 nL) were injected into the duct of Cuvier of ABC/TU zebrafish embryos. As soon as transgenic human cells stopped circulating and remained in the caudal vasculature tail region (after approximately 2 hpi), nanoparticles (1 nL) were injected as described above. Brightfield and fluorescence images of the tail region were taken 1 hpi of nanoparticles.

Colocalization analysis. Binding of nanoparticles to HEK293 cells was analyzed using the JaCoP plug-in in Fiji. Therefore, Pearson´s Correlation Coefficient (PCC) was determined to assess the extent of colocalization.(Bolte and Cordelières, 2006)

Radioactive labeling of nanoparticles with ^{111}In. Labeling of nanoparticles with ^{111}In was performed with modifications as described previously.(van der Geest et al., 2015) Nanoparticles were prepared as described above in PBS at a total lipid concentration of 60 mM (including 3 mol% DSPE-DTPA). Size exclusion chromatography was used to exchange the buffer system to citrate buffered saline pH 5.4, fractions were pooled and finally concentrated using Amicon Ultra-4 centrifugal filter units (100 kDa size exclusion). Nanoparticles (30 µmol) were incubated with 40 µl of $^{111}InCl_3$ (Mallinckrodt Pharmaceuticals) at 37°C for 45 min using a thermocycler. After incubation, ^{111}In labeled nanoparticles

were purified using NAP-5 columns (GE Healthcare) by elution with sterile saline (B. Braun Medical Inc.). Fractions of 250 µL were collected and activity of each fraction was determined.

Planar imaging of mice *in vivo*. All mice experiments were carried out in accordance with German legislation on animal welfare. Female NMRI mice (6-8 weeks) were obtained from Janvier Laboratories. For planar imaging, mice were anesthetized with Isoflurane (Baxter) and ^{111}In labeled nanoparticles with a total activity of 8-10 MBq (corresponding to 100 µL) were intravenously injected into the tail vein. Afterwards, the animals were placed in prone position on a planar gamma-imager (Biospace) equipped with a high energy collimator as described previously.(Müller et al., 2013; Wischnjow et al., 2016) Images were recorded at the indicated time points with 10 min acquisition time.

Organ biodistribution of nanoparticles in mice *in vivo*. For biodistribution studies, ^{111}In labeled nanoparticles with a total activity of 1-2 MBq (corresponding to 100 µL) were intravenously injected into the tail vein of wild type mice. Animals were sacrificed (n = 3 per nanoparticle administration) 1 hour post injection, organs were harvested and the radioactivity in each organ was measured with a Berthold LB 951G gamma counter. Each organ-associated activity was related to the injected dose. The percentage of injected dose (%ID) per organ was calculated using standard values for organ weights.(Mühlfeld et al., 2003)

Fluorescence imaging of nanoparticles in tissue cryo-sections. Nanoparticles incorporating 1mol% DiI were intravenously injected into the tail vein of wildtype mice. Animals were sacrificed 1 hour post injection and organs were snap-frozen in liquid nitrogen. Cryo-sections of 16 µm were mounted on Superfrost Plus Ultra microscope slides (Thermo Fisher Scientific) and counterstained with Hoechst 33342 (2 µg/mL). Slides were embedded in Prolong Gold Antifade Mountant (Thermo Fisher Scientific),

sealed with nail polisher and analyzed using an Olympus FV-1000 inverted confocal laser scanning microscope equipped with a 40x UPlanFL N oil-immersion objective (numerical aperture 1.30).

Immunohistochemistry of targeting ligand in tissue sections. After intravenous tail vein injection of nanoparticles, the mice were euthanized, organs were harvested, rinsed with PBS and immediately placed in a 4% formaldehyde solution in PBS. After fixation for 24 h, organs were dehydrated and embedded in paraffin. Sections of 5 µm thicknesses were cut using a microtome MICROM HM 355, placed onto a microscope slide and dried at 37°C. After dewaxing and rehydration, epitope retrieval was performed. The primary antibody against Myr-preS2-31 (MA18/7, kind gift from Wolfram Gerlich) was added overnight at 4°C, before incubation with the secondary antibody. Finally, slides were counterstained with hemalum (Merck KGaA) for 10 min, blued with tap water and mounted using Aquatex (Merck Millipore).

Immunofluorescence imaging of liver cryo-sections. Animals were sacrificed 3 hour post injection of nanoparticles and liver cryo-sections (16 µm) were prepared as described above. Slides were stained using primary antibodies against Myr-preS2-31 (MA18/7, 1:100 dilution) and mNtcp (provided by Prof. Bruno Stieger, University Zürich, 1:100 dilution). Finally, cell nuclei were counterstained with Hoechst 33342 (2 µg/mL) and analyzed by confocal microscopy as described above.

Statistical analysis. Statistical analysis for all experiments was performed by one-way analysis of variance (ANOVA) followed by Bonferroni post-hoc test using OriginPro 9.1 software (OriginLab Corporation). Differences between groups were considered to be statistically significant at the indicated p-values.

REFERENCES

Akinc A, Goldberg M, Qin J, Dorkin JR, Gamba-Vitalo C, Maier M, Jayaprakash KN, Jayaraman M, Rajeev KG, Manoharan M, Koteliansky V, Röhl I, Leshchiner ES, Langer R, Anderson DG. 2009. Development of Lipidoid–siRNA Formulations for Systemic Delivery to the Liver. *Mol Ther* **17**:872–879. doi:10.1038/mt.2009.36

Akinc A, Querbes W, De S, Qin J, Frank-Kamenetsky M, Jayaprakash KN, Jayaraman M, Rajeev KG, Cantley WL, Dorkin JR, Butler JS, Qin L, Racie T, Sprague A, Fava E, Zeigerer A, Hope MJ, Zerial M, Sah DW, Fitzgerald K, Tracy MA, Manoharan M, Koteliansky V, Fougerolles A de, Maier MA. 2010. Targeted Delivery of RNAi Therapeutics With Endogenous and Exogenous Ligand-Based Mechanisms. *Mol Ther* **18**:1357–1364. doi:10.1038/mt.2010.85

Asabe S, Wieland SF, Chattopadhyay PK, Roederer M, Engle RE, Purcell RH, Chisari FV. 2009. The Size of the Viral Inoculum Contributes to the Outcome of Hepatitis B Virus Infection. *J Virol* **83**:9652–9662. doi:10.1128/JVI.00867-09

Barenholz Y. 2012. Doxil®--the first FDA-approved nano-drug: lessons learned. *J Control Release Off J Control Release Soc* **160**:117–134. doi:10.1016/j.jconrel.2012.03.020

Barpe DR, Rosa DD, Froehlich PE. 2010. Pharmacokinetic evaluation of doxorubicin plasma levels in normal and overweight patients with breast cancer and simulation of dose adjustment by different indexes of body mass. *Eur J Pharm Sci Off J Eur Fed Pharm Sci* **41**:458–463. doi:10.1016/j.ejps.2010.07.015

Barrett SE, Burke RS, Abrams MT, Bason C, Busuek M, Carlini E, Carr BA, Crocker LS, Fan H, Garbaccio RM, Guidry EN, Heo JH, Howell BJ, Kemp EA, Kowtoniuk RA, Latham AH, Leone AM, Lyman M, Parmar RG, Patel M, Pechenov SY, Pei T, Pudvah NT, Raab C, Riley S, Sepp-Lorenzino L, Smith S, Soli ED, Staskiewicz S, Stern M, Truong Q, Vavrek M, Waldman JH, Walsh ES, Williams JM, Young S, Colletti SL. 2014. Development of a liver-targeted siRNA delivery platform with a broad therapeutic window utilizing biodegradable polypeptide-based polymer conjugates. *J Controlled Release* **183**:124–137. doi:10.1016/j.jconrel.2014.03.028

Blank A, Markert C, Hohmann N, Carls A, Mikus G, Lehr T, Alexandrov A, Haag M, Schwab M, Urban S, Haefeli WE. 2016. First-in-human application of the novel hepatitis B and hepatitis D virus entry inhibitor myrcludex B. *J Hepatol* **65**:483–489. doi:10.1016/j.jhep.2016.04.013

Bogomolov P, Alexandrov A, Voronkova N, Macievich M, Kokina K, Petrachenkova M, Lehr T, Lempp FA, Wedemeyer H, Haag M, Schwab M, Haefeli WE, Blank A, Urban S. 2016. Treatment of chronic hepatitis D with the entry inhibitor myrcludex B: First results of a phase Ib/IIa study. *J Hepatol* **65**:490–498. doi:10.1016/j.jhep.2016.04.016

Bolte S, Cordelières FP. 2006. A guided tour into subcellular colocalization analysis in light microscopy. *J Microsc* **224**:213–232. doi:10.1111/j.1365-2818.2006.01706.x

Braet F, Wisse E. 2002. Structural and functional aspects of liver sinusoidal endothelial cell fenestrae: a review. *Comp Hepatol* **1**:1.

Campbell F, Bos FL, Sieber S, Arias-Alpizar G, Koch BE, Huwyler J, Kros A, Bussmann J. 2018. Directing Nanoparticle Biodistribution through Evasion and Exploitation of Stab2-Dependent Nanoparticle Uptake. *ACS Nano* **12**:2138–2150. doi:10.1021/acsnano.7b06995

Chen RF, Knutson JR. 1988. Mechanism of fluorescence concentration quenching of carboxyfluorescein in liposomes: Energy transfer to nonfluorescent dimers. *Anal Biochem* **172**:61–77. doi:10.1016/0003-2697(88)90412-5

Detampel P, Witzigmann D, Krähenbühl S, Huwyler J. 2014. Hepatocyte targeting using pegylated asialofetuin-conjugated liposomes. *J Drug Target* **22**:232–241. doi:10.3109/1061186X.2013.860982

Einfalt T, Witzigmann D, Edlinger C, Sieber S, Goers R, Najer A, Spulber M, Onaca-Fischer O, Huwyler J, Palivan CG. 2018. Biomimetic artificial organelles with in vitro and in vivo activity triggered by reduction in microenvironment. *Nat Commun* **9**:1127. doi:10.1038/s41467-018-03560-x

Glebe D, Urban S. 2007. Viral and cellular determinants involved in hepadnaviral entry. *World J Gastroenterol* **13**:22–38.

Harrington KJ, Rowlinson-Busza G, Syrigos KN, Uster PS, Abra RM, Stewart JSW. 2000. Biodistribution and pharmacokinetics of ^{111}In-DTPA-labelled pegylated liposomes in a human tumour xenograft model: implications for novel targeting strategies. *Br J Cancer* **83**:232–238. doi:10.1054/bjoc.1999.1232

Ishiwata H, Suzuki N, Ando S, Kikuchi H, Kitagawa T. 2000. Characteristics and biodistribution of cationic liposomes and their DNA complexes. *J Control Release Off J Control Release Soc* **69**:139–148.

Karmali PP, Simberg D. 2011. Interactions of nanoparticles with plasma proteins: implication on clearance and toxicity of drug delivery systems. *Expert Opin Drug Deliv* **8**:343–357. doi:10.1517/17425247.2011.554818

Kettiger H, Schipanski A, Wick P, Huwyler J. 2013. Engineered nanomaterial uptake and tissue distribution: from cell to organism. *Int J Nanomedicine* **8**:3255–3269. doi:10.2147/IJN.S49770

Lempp FA, Mutz P, Lipps C, Wirth D, Bartenschlager R, Urban S. 2016. Evidence that hepatitis B virus replication in mouse cells is limited by the lack of a host cell dependency factor. *J Hepatol* **64**:556–564. doi:10.1016/j.jhep.2015.10.030

Liu Q, Somiya M, Kuroda S. 2016. Elucidation of the early infection machinery of hepatitis B virus by using bio-nanocapsule. *World J Gastroenterol* **22**:8489–8496. doi:10.3748/wjg.v22.i38.8489

Lunov O, Syrovets T, Loos C, Beil J, Delacher M, Tron K, Nienhaus GU, Musyanovych A, Mailänder V, Landfester K, Simmet T. 2011. Differential Uptake of Functionalized Polystyrene Nanoparticles by Human Macrophages and a Monocytic Cell Line. *ACS Nano* **5**:1657–1669. doi:10.1021/nn2000756

Lütgehetmann M, Mancke LV, Volz T, Helbig M, Allweiss L, Bornscheuer T, Pollok JM, Lohse AW, Petersen J, Urban S, Dandri M. 2012. Humanized chimeric uPA mouse model for the study of hepatitis B and D virus interactions and preclinical drug evaluation. *Hepatology* **55**:685–694. doi:10.1002/hep.24758

Maurer N, Fenske DB, Cullis PR. 2001. Developments in liposomal drug delivery systems. *Expert Opin Biol Ther* **1**:923–947. doi:10.1517/14712598.1.6.923

Mayer LD, Tai LC, Bally MB, Mitilenes GN, Ginsberg RS, Cullis PR. 1990. Characterization of liposomal systems containing doxorubicin entrapped in response to pH gradients. *Biochim Biophys Acta* **1025**:143–151.

Meier A, Mehrle S, Weiss TS, Mier W, Urban S. 2013. Myristoylated PreS1-domain of the hepatitis B virus L-protein mediates specific binding to differentiated hepatocytes. *Hepatol Baltim Md* **58**:31–42. doi:10.1002/hep.26181

Milla P, Dosio F, Cattel L. 2012. PEGylation of proteins and liposomes: a powerful and flexible strategy to improve the drug delivery. *Curr Drug Metab* **13**:105–119.

Mühlfeld AS, Segerer S, Hudkins K, Carling MD, Wen M, Farr AG, Ravetch JV, Alpers CE. 2003. Deletion of the Fcγ Receptor IIb in Thymic Stromal Lymphopoietin Transgenic Mice Aggravates

Membranoproliferative Glomerulonephritis. *Am J Pathol* **163**:1127–1136. doi:10.1016/S0002-9440(10)63472-4

Müller T, Mehrle S, Schieck A, Haberkorn U, Urban S, Mier W. 2013. Liver Imaging with a Novel Hepatitis B Surface Protein Derived SPECT-Tracer. *Mol Pharm* **10**:2230–2236. doi:10.1021/mp400038r

Ni Y, Lempp FA, Mehrle S, Nkongolo S, Kaufman C, Fälth M, Stindt J, Königer C, Nassal M, Kubitz R, Sültmann H, Urban S. 2014. Hepatitis B and D Viruses Exploit Sodium Taurocholate Co-transporting Polypeptide for Species-Specific Entry into Hepatocytes. *Gastroenterology* **146**:1070-1083.e6. doi:10.1053/j.gastro.2013.12.024

Park K. 2017. Cover Story: Zebrafish as a screening tool for the systemic circulation of nanoparticles. *J Controlled Release* **264**:342. doi:10.1016/j.jconrel.2017.09.037

Petersen J, Dandri M, Mier W, Lütgehetmann M, Volz T, Weizsäcker F von, Haberkorn U, Fischer L, Pollok J-M, Erbes B, Seitz S, Urban S. 2008. Prevention of hepatitis B virus infection *in vivo* by entry inhibitors derived from the large envelope protein. *Nat Biotechnol* **26**:335–341. doi:10.1038/nbt1389

Poelstra K, Prakash J, Beljaars L. 2012. Drug targeting to the diseased liver. *J Controlled Release*, Drug Delivery Research in Europe **161**:188–197. doi:10.1016/j.jconrel.2012.02.011

Reddy LH, Couvreur P. 2011. Nanotechnology for therapy and imaging of liver diseases. *J Hepatol* **55**:1461–1466. doi:10.1016/j.jhep.2011.05.039

Rothkopf C, Fahr A, Fricker G, Scherphof GL, Kamps J a. a. M. 2005. Uptake of phosphatidylserine-containing liposomes by liver sinusoidal endothelial cells in the serum-free perfused rat liver. *Biochim Biophys Acta* **1668**:10–16. doi:10.1016/j.bbamem.2004.10.013

Sauer I, Nikolenko H, Keller S, Abu Ajaj K, Bienert M, Dathe M. 2006. Dipalmitoylation of a cellular uptake-mediating apolipoprotein E-derived peptide as a promising modification for stable anchorage in liposomal drug carriers. *Biochim Biophys Acta BBA - Biomembr* **1758**:552–561. doi:10.1016/j.bbamem.2006.03.017

Schieck A, Müller T, Schulze A, Haberkorn U, Urban S, Mier W. 2010. Solid-phase synthesis of the lipopeptide Myr-HBVpreS/2-78, a hepatitis B virus entry inhibitor. *Mol Basel Switz* **15**:4773–4783. doi:10.3390/molecules15074773

Schieck A, Schulze A, Gähler C, Müller T, Haberkorn U, Alexandrov A, Urban S, Mier W. 2013. Hepatitis B virus hepatotropism is mediated by specific receptor recognition in the liver and not restricted to susceptible hosts. *Hepatol Baltim Md* **58**:43–53. doi:10.1002/hep.26211

Schulze A, Schieck A, Ni Y, Mier W, Urban S. 2010. Fine mapping of pre-S sequence requirements for hepatitis B virus large envelope protein-mediated receptor interaction. *J Virol* **84**:1989–2000. doi:10.1128/JVI.01902-09

Shan D, Li J, Cai P, Prasad P, Liu F, Rauth AM, Wu XY. 2015. RGD-conjugated solid lipid nanoparticles inhibit adhesion and invasion of α<Subscript>v</Subscript>β<Subscript>3</Subscript> integrin-overexpressing breast cancer cells. *Drug Deliv Transl Res* **5**:15–26. doi:10.1007/s13346-014-0210-2

Shih B-B, Chang Y-F, Cheng C-C, Yang H-J, Chang K-W, Ho A-S, Lin H-C, Yeh C, Chang C-C. 2017. SPECT imaging evaluation of 111indium-chelated cetuximab for diagnosing EGFR-positive tumor in an HCT-15-induced colorectal xenograft. *J Chin Med Assoc JCMA* **80**:766–773. doi:10.1016/j.jcma.2017.02.010

Sieber S, Grossen P, Detampel P, Siegfried S, Witzigmann D, Huwyler J. 2017. Zebrafish as an early stage screening tool to study the systemic circulation of nanoparticulate drug delivery systems in vivo. *J Controlled Release* **264**:180–191. doi:10.1016/j.jconrel.2017.08.023

Sieber S, Grossen P, Uhl P, Detampel P, Mier W, Witzigmann D, Huwyler J. 2018. Zebrafish as a predictive screening model to assess macrophage clearance of liposomes in vivo. *Nanomedicine Nanotechnol Biol Med*. doi:accepted November 2018

Somiya M, Liu Q, Yoshimoto N, Iijima M, Tatematsu K, Nakai T, Okajima T, Kuroki K, Ueda K, Kuroda S. 2016. Cellular uptake of hepatitis B virus envelope L particles is independent of sodium taurocholate cotransporting polypeptide, but dependent on heparan sulfate proteoglycan. *Virology* **497**:23–32. doi:10.1016/j.virol.2016.06.024

Somiya M, Sasaki Y, Matsuzaki T, Liu Q, Iijima M, Yoshimoto N, Niimi T, Maturana AD, Kuroda S. 2015. Intracellular trafficking of bio-nanocapsule-liposome complex: Identification of fusogenic activity in the pre-S1 region of hepatitis B virus surface antigen L protein. *J Control Release Off J Control Release Soc* **212**:10–18. doi:10.1016/j.jconrel.2015.06.012

Steffan AM, Gendrault JL, Kirn A. 1987. Increase in the number of fenestrae in mouse endothelial liver cells by altering the cytoskeleton with cytochalasin B. *Hepatol Baltim Md* **7**:1230–1238.

Uhl P, Pantze S, Storck P, Parmentier J, Witzigmann D, Hofhaus G, Huwyler J, Mier W, Fricker G. 2017. Oral delivery of vancomycin by tetraether lipid liposomes. *Eur J Pharm Sci Off J Eur Fed Pharm Sci* **108**:111–118. doi:10.1016/j.ejps.2017.07.013

Urban S, Bartenschlager R, Kubitz R, Zoulim F. 2014. Strategies to inhibit entry of HBV and HDV into hepatocytes. *Gastroenterology* **147**:48–64. doi:10.1053/j.gastro.2014.04.030

van der Geest T, Laverman P, Gerrits D, Franssen GM, Metselaar JM, Storm G, Boerman OC. 2015. Comparison of three remote radiolabelling methods for long-circulating liposomes. *J Control Release Off J Control Release Soc* **220**:239–244. doi:10.1016/j.jconrel.2015.10.043

Verrier ER, Colpitts CC, Bach C, Heydmann L, Weiss A, Renaud M, Durand SC, Habersetzer F, Durantel D, Abou-Jaoudé G, López Ledesma MM, Felmlee DJ, Soumillon M, Croonenborghs T, Pochet N, Nassal M, Schuster C, Brino L, Sureau C, Zeisel MB, Baumert TF. 2016. A targeted functional RNA interference screen uncovers glypican 5 as an entry factor for hepatitis B and D viruses. *Hepatol Baltim Md* **63**:35–48. doi:10.1002/hep.28013

Webb MS, Saxon D, Wong FMP, Lim HJ, Wang Z, Bally MB, Choi LSL, Cullis PR, Mayer LD. 1998. Comparison of different hydrophobic anchors conjugated to poly(ethylene glycol): effects on the pharmacokinetics of liposomal vincristine. *Biochim Biophys Acta BBA - Biomembr* **1372**:272–282. doi:10.1016/S0005-2736(98)00077-7

Williams R, Aspinall R, Bellis M, Camps-Walsh G, Cramp M, Dhawan A, Ferguson J, Forton D, Foster G, Gilmore I, Hickman M, Hudson M, Kelly D, Langford A, Lombard M, Longworth L, Martin N, Moriarty K, Newsome P, O'Grady J, Pryke R, Rutter H, Ryder S, Sheron N, Smith T. 2014. Addressing liver disease in the UK: a blueprint for attaining excellence in health care and reducing premature mortality from lifestyle issues of excess consumption of alcohol, obesity, and viral hepatitis. *Lancet Lond Engl* **384**:1953–1997. doi:10.1016/S0140-6736(14)61838-9

Wischnjow A, Sarko D, Janzer M, Kaufman C, Beijer B, Brings S, Haberkorn U, Larbig G, Kübelbeck A, Mier W. 2016. Renal Targeting: Peptide-Based Drug Delivery to Proximal Tubule Cells. *Bioconjug Chem* **27**:1050–1057. doi:10.1021/acs.bioconjchem.6b00057

Wisse E, Jacobs F, Topal B, Frederik P, Geest BD. 2008. The size of endothelial fenestrae in human liver sinusoids: implications for hepatocyte-directed gene transfer. *Gene Ther* **15**:1193–1199. doi:10.1038/gt.2008.60

Witzigmann D, Detampel P, Porta F, Huwyler J. 2016. Isolation of multiantennary N -glycans from glycoproteins for hepatocyte specific targeting via the asialoglycoprotein receptor. *RSC Adv* **6**:97636–97640. doi:10.1039/C6RA18297F

Witzigmann D, Sieber S, Porta F, Grossen P, Bieri A, Strelnikova N, Pfohl T, Prescianotto-Baschong C, Huwyler J. 2015a. Formation of lipid and polymer based gold nanohybrids using a nanoreactor approach. *RSC Adv* **5**:74320–74328. doi:10.1039/C5RA13967H

Witzigmann D, Wu D, Schenk SH, Balasubramanian V, Meier W, Huwyler J. 2015b. Biocompatible polymer-Peptide hybrid-based DNA nanoparticles for gene delivery. *ACS Appl Mater Interfaces* **7**:10446–10456. doi:10.1021/acsami.5b01684

Xiao K, Li Y, Luo J, Lee JS, Xiao W, Gonik AM, Agarwal RG, Lam KS. 2011. The effect of surface charge on in vivo biodistribution of PEG-oligocholic acid based micellar nanoparticles. *Biomaterials* **32**:3435–3446. doi:10.1016/j.biomaterials.2011.01.021

Yan H, Zhong G, Xu G, He W, Jing Z, Gao Z, Huang Y, Qi Y, Peng B, Wang H, Fu L, Song M, Chen P, Gao W, Ren B, Sun Y, Cai T, Feng X, Sui J, Li W. 2012. Sodium taurocholate cotransporting polypeptide is a functional receptor for human hepatitis B and D virus. *eLife* **1**:e00049. doi:10.7554/eLife.00049

Yin B, Li KHK, Ho LWC, Chan CKW, Choi CHJ. 2018. Toward Understanding in Vivo Sequestration of Nanoparticles at the Molecular Level. *ACS Nano*. doi:10.1021/acsnano.8b00141

Zhang Q, Zhang X, Chen T, Wang X, Fu Y, Jin Y, Sun X, Gong T, Zhang Z. 2015. A safe and efficient hepatocyte-selective carrier system based on myristoylated preS1/21-47 domain of hepatitis B virus. *Nanoscale* **7**:9298–9310. doi:10.1039/c4nr04730c

Zhang X, Zhang Q, Peng Q, Zhou J, Liao L, Sun X, Zhang L, Gong T. 2014. Hepatitis B virus preS1-derived lipopeptide functionalized liposomes for targeting of hepatic cells. *Biomaterials* **35**:6130–6141. doi:10.1016/j.biomaterials.2014.04.037

ASSOCIATED CONTENT

Figure Supplements

Supplementary data on fluorescence correlation spectroscopy, biocompatibility, carboxyfluorescein self-quenching, NTCP-specific targeting *in vitro* in genetically modified HuH7 and HeLa cells, time-dependent internalization of nanoparticles, binding/uptake mechanism studies *in vitro*, ligand density dependent uptake, targeting ability of free Myrcludex B in xenotransplanted zebrafish, imaging of spleen and kidney sections, liver targeting, nanoparticle binding to sinusoidal membrane of hepatocytes, biodistribution of nanoparticles modified with 0.5 mol% Myr-preS2-31.

ARTICLE AND AUTHOR INFORMATION

Corresponding Authors (*)

Dr. Dominik Witzigmann; phone: +1-604-827-0085; e-mail: dominik.witzigman@unibas.ch

Prof. Dr. Jörg Huwyler; phone: +41 (0)61 207 15 13; e-mail: joerg.huwyler@unibas.ch

Funding

The authors acknowledge the financial support of the “Stiftung zur Förderung des pharmazeutischen Nachwuchses in Basel” (SS), “Freiwillige Akademische Gesellschaft Basel” (DW, SS), “Novartis University Basel Excellence Scholarship for Life Sciences” (DW), the Swiss National Science Foundation (SNF grant No. 174975 and 173057, DW, JH), the Deutsche Forschungsgemeinschaft (DFG, Project 209091148, SU) and the German Center for Infection Research (DZIF, projects 5.704 and 5.807, SU).

ACKNOWLEDGMENT

We thank M. Affolter, H.G. Belting and N. Schellinx for providing zebrafish eggs, K. Leotta for support with mice experiments, S. Meßnard for sectioning of paraffin-embedded tissue, P. Scheiffele and L. Burklé for support with cryo-sectioning, and H. Heerklotz and D. Eckhardt for DSC and PPC measurements.

ETHICS

Animal experimentation: Zebrafish embryo (Danio rerio) studies were performed in strict accordance with Swiss animal welfare regulations. Mice experiments were carried out in accordance with German legislation on animal welfare. All of the animals were handled according to approved institutional animal care and use protocol of the University of Basel and University of Heidelberg.

ABBREVIATIONS

ASGPR, asialoglycoprotein receptor; CF; carboxyfluorescein; DLVO, Derjaguin-Landau-Verwey-Overbeek; EMA, European Medicines Agency; FCS, fluorescence correlation spectroscopy; FDA, US Food and Drug Administration; FI, fluorescence imaging; HDV, hepatitis D virus; HBV, hepatitis B virus; HBVpreS , hepatitis B virus large envelope protein; IHC, immunohistochemistry; LDLR, low density lipoprotein receptor; NTCP, sodium-taurocholate cotransporting polypeptide; PBS, phosphate-buffered saline; PCC, Pearson´s Correlation Coefficient; PDI, polydispersity index; PEG, polyethylene glycol; TEM, transmission electron microscopy

Figure Supplements

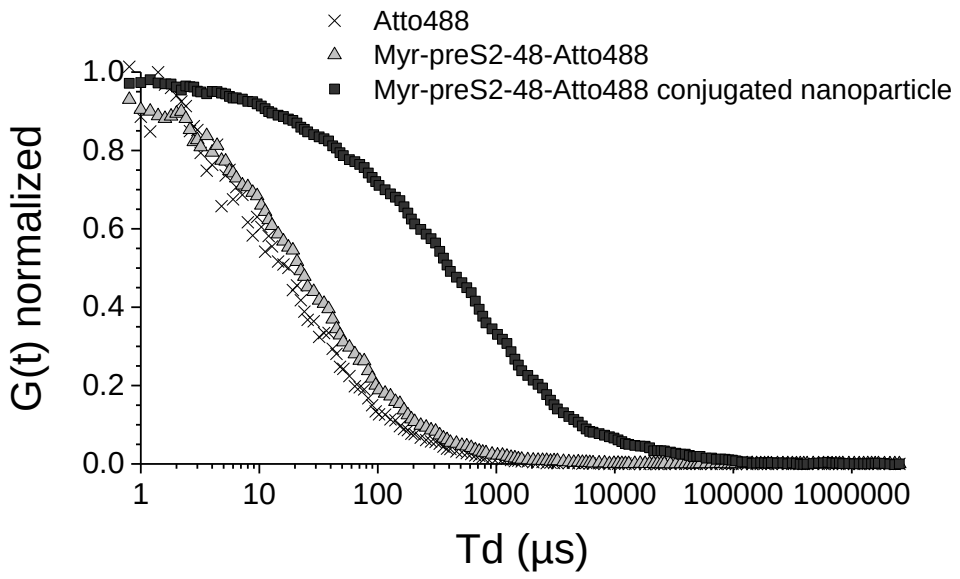

Figure 1–figure supplement 1. Characterization of hepatotropic nanoparticles based on liposomes modified with Myrcludex B (Myr-preS2-48) using fluorescence correlation spectroscopy. Autocorrelation curves of Atto488 (black cross), Myr-preS2-48 Atto488 (grey triangle), and Myr-preS2-48-Atto488 conjugated nanoparticles (black square). For comparison curves are normalized to 1 (n = 3 independent samples). Numerical data is shown in the Figure 1-source data.

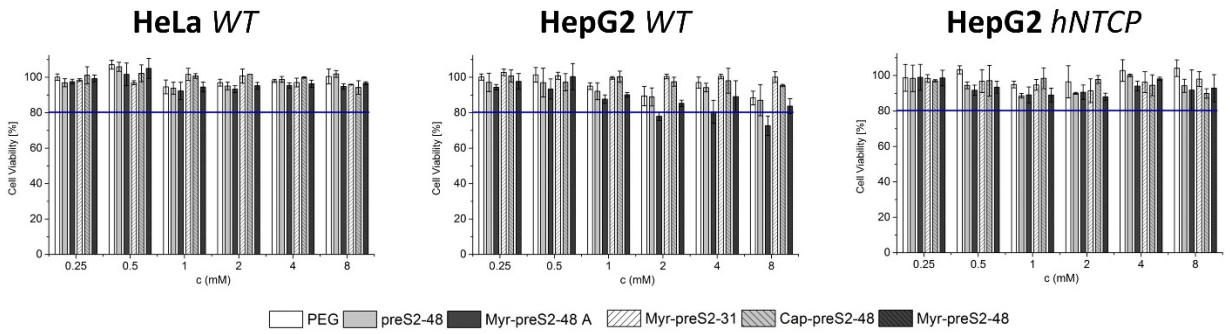

Figure 1–figure supplement 2. Assessment of cytocompatibility of nanoparticles modified with different Myrcludex B derived peptides using non-hepatic HeLa cells (HeLa *WT*), liver-derived wildtype HepG2 cells (HepG2 *WT*) and HepG2 cells overexpressing the human NTCP (HepG2 *hNTCP*) by MTT assay. All values are shown as mean ± SD of biological replicates (n = 3 independent experiments). Numerical data for all graphs are shown in the Figure 1-source data.

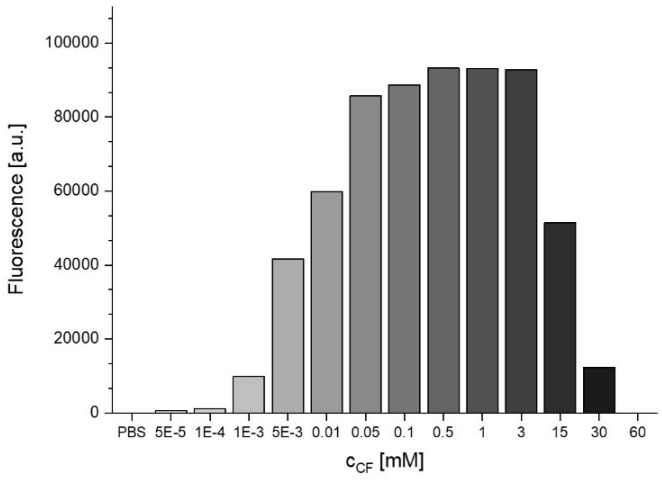

Figure 1–figure supplement 3. Concentration dependent fluorescence self-quenching of 5(6)-carboxyfluorescein. Fluorescence (arbitrary units, a.u.) of carboxyfluorescein in phosphate buffered saline (PBS, pH 7.4) at different concentrations (n = 1). Numerical data is shown in the Figure 1-source data.

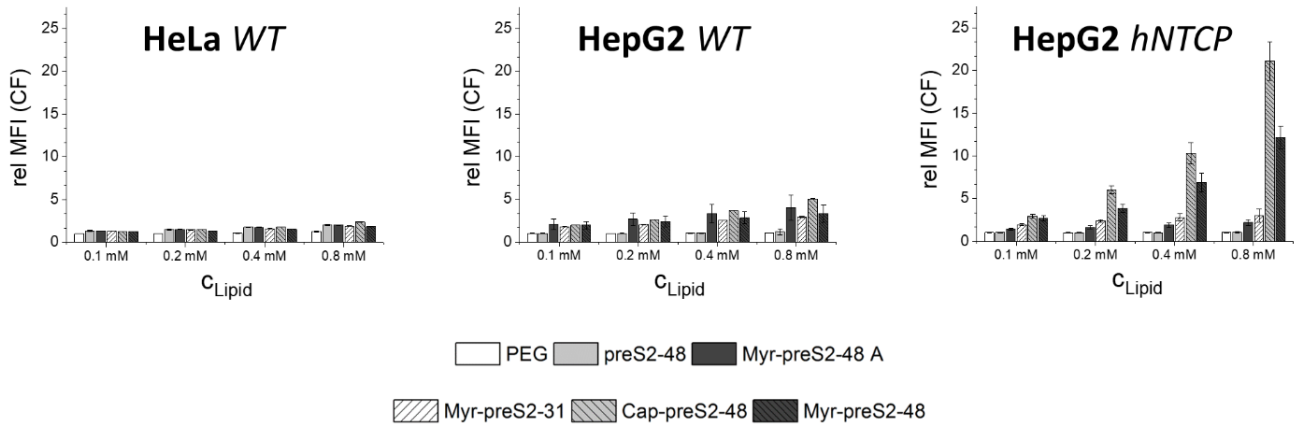

Figure 1–figure supplement 4. Flow cytometry analysis of nanoparticle uptake rate into non-hepatic HeLa cells, liver-derived HepG2 cells and hNTCP overexpressing HepG2 cells. Increasing concentrations of nanoparticles (C_{Lipid}) modified with different Myrcludex B-derived peptides were evaluated. Relative mean fluorescence intensities (MFI) of CF signals normalized to untreated cells are given. All values are shown as mean ± SD of biological replicates ($n \geq 3$ independent experiments). Numerical data for all graphs are shown in the Figure 1-source data.

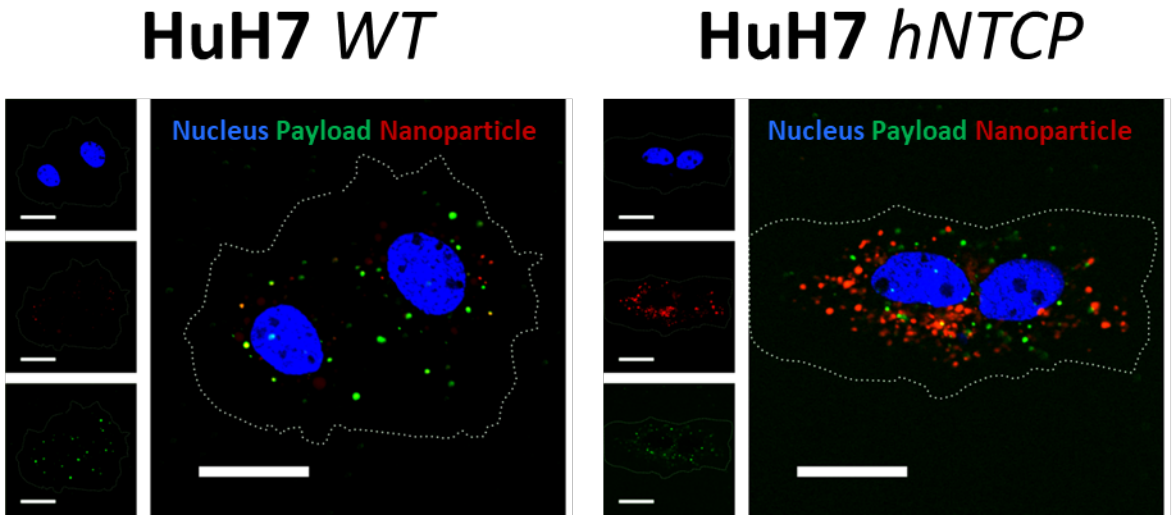

Figure 1–figure supplement 5. Uptake of Myrcludex B-modified nanoparticles into HuH7 liver-derived cells deficient (HuH7 *WT*) or overexpressing hNTCP (HuH7 *hNTCP*). Nanoparticles have a dual fluorescent label, *i.e.* lipophilic membrane label (DiI, red) and hydrophilic payload incorporation (carboxyfluorescein, green). Representative confocal laser scanning microscopy maximum intensity projections 30 min after liposome addition are shown. Blue signal: Hoechst stain of cell nuclei. Scale bar = 10 µm. Single fluorescent channels are presented as small images. Dotted lines indicate cell membranes.

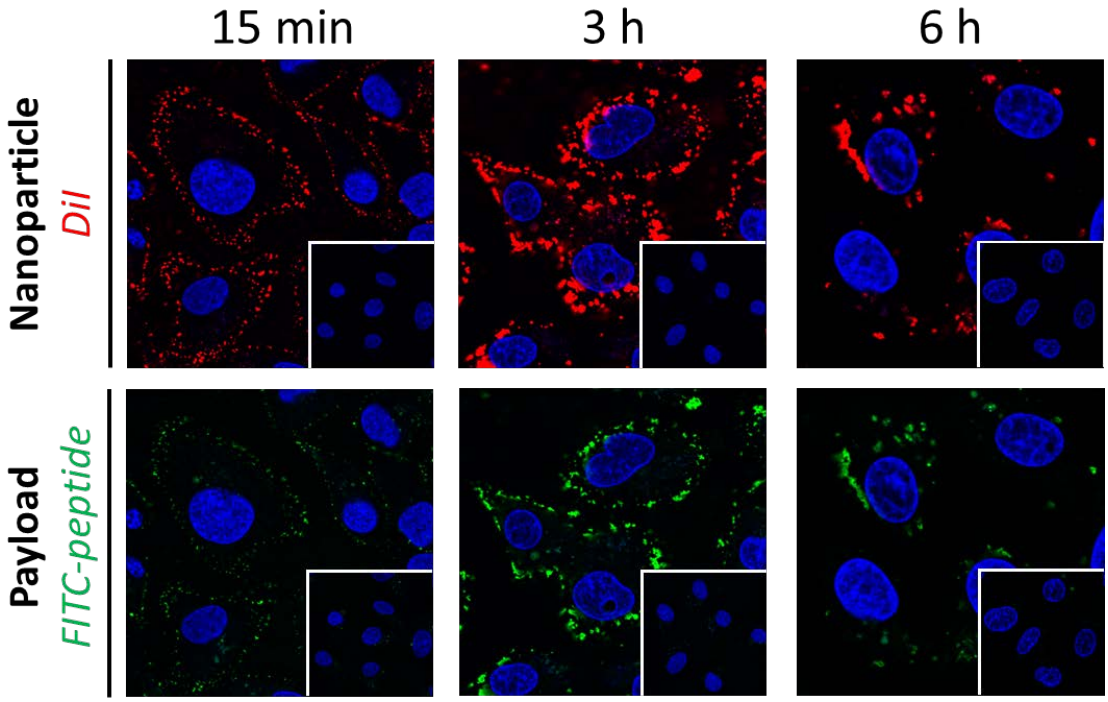

Figure 1–figure supplement 6. Time-dependent internalization of Myr-preS2-31 modified nanoparticles into hNTCP overexpressing HepG2 cells. Nanoparticles have a dual fluorescent label, i.e. lipophilic membrane label (DiI, red) and hydrophilic payload incorporation (FITC-peptide, green). Representative confocal laser images for Myr-preS2-31 modified nanoparticles after specific time points are shown. Inserts represent confocal laser images for PEG nanoparticles at the same time point. Blue signal: Hoechst stain of cell nuclei.

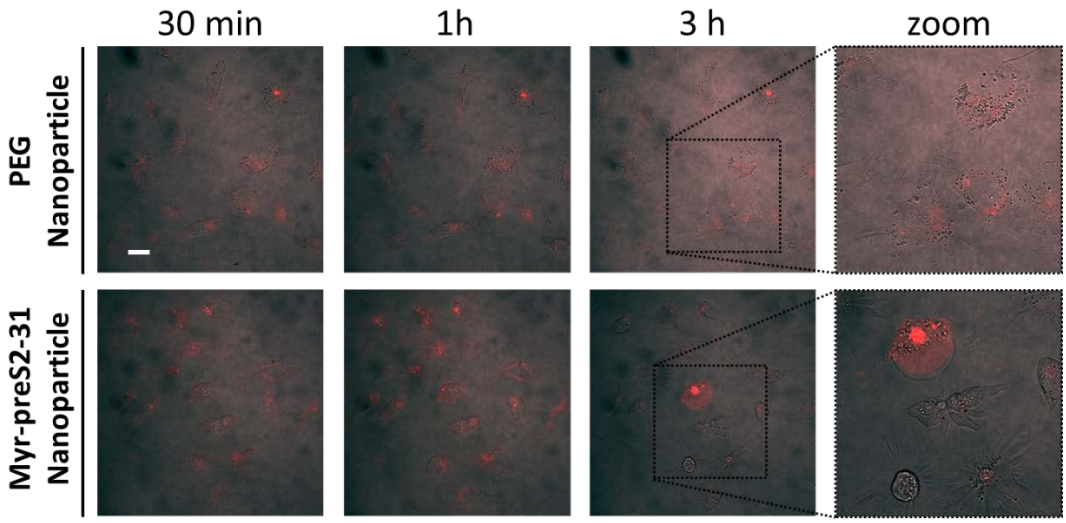

Figure 1–figure supplement 7. Time-dependent internalization and toxicity of propidium iodide loaded nanoparticles into hNTCP overexpressing HepG2 cells. Nanoparticles were passively loaded with propidium iodide (red signal). Representative confocal laser images for PEG nanoparticles and Myr-preS2-31 modified nanoparticles after specific time points are shown. Scale bar = 20 µm.

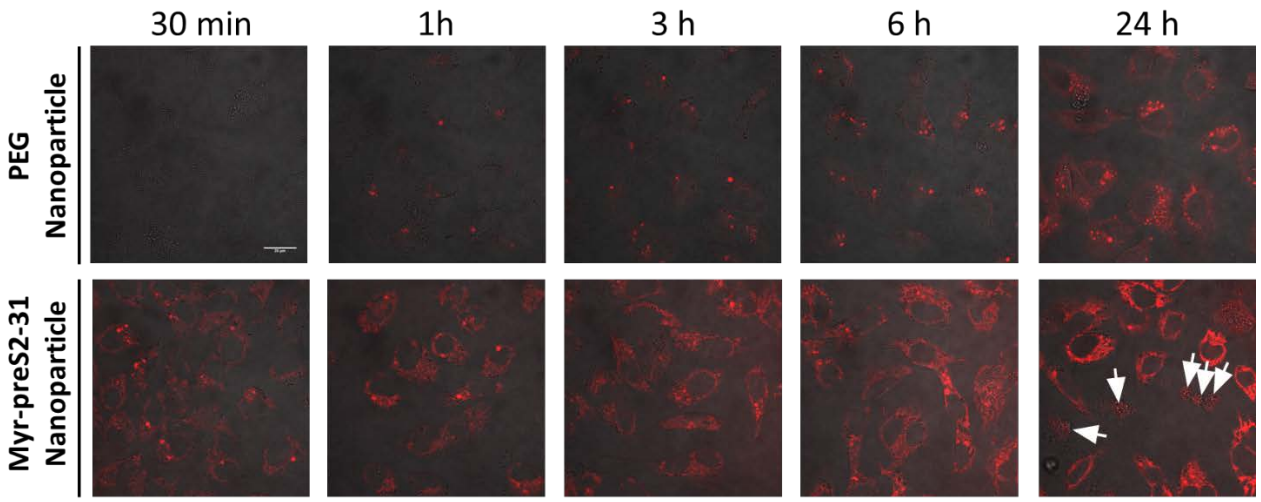

Figure 1–figure supplement 8. Time-dependent internalization and toxicity of doxorubicin loaded nanoparticles into hNTCP overexpressing HepG2 cells. Nanoparticles were actively loaded with doxorubicin (red signal) using a citrate buffer gradient. Representative confocal laser images for PEG nanoparticles and Myr-preS2-31 modified nanoparticles after specific time points are shown. Arrows indicate dead cells. Scale bar = 20 µm.

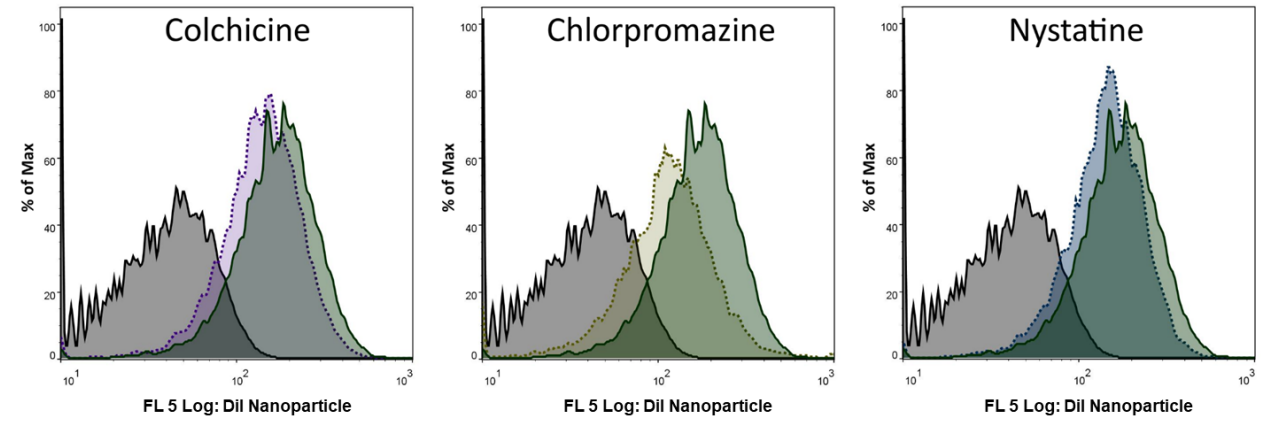

Figure 2–figure supplement 1. NTCP-dependent uptake mechanism of nanoparticles. Flow cytometry analysis of nanoparticle internalization in presence of different pharmacological pathway inhibitors. Histograms of HepG2 *hNTCP* cells incubated with PBS (gray; solid line) and nanoparticles in absence (green; solid line) or presence of colchicine (micropinocytosis inhibitor, purple; dotted line), chlorpromazine (inhibitor of clathrin-mediated endocytosis, yellow; dotted line), or nystatine (inhibitor of caveolin-mediated endocytosis, blue; dotted line).

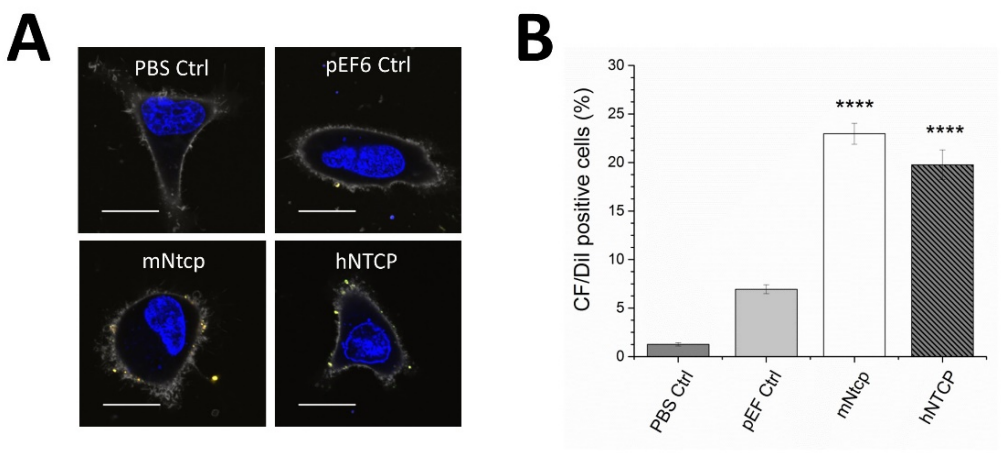

Figure 2–figure supplement 2. Uptake of Myrcludex B-modified nanoparticles into HeLa cells transfected with empty vector (pEF6 Ctrl), mNtcp or hNTCP. (A) Binding of nanoparticles was qualitatively assessed using confocal laser scanning microscopy. PBS served as mock control (PBS Ctrl). Representative images are shown 1 hour after liposome addition. Blue signal: Hoechst stain of cell nuclei. Grey signal: Cell mask stain of plasma membrane. Yellow signal: DiI labeled liposomes loaded with carboxyfluorescein. Scale bar = 10 µm. (B) Quantification of liposome binding using flow cytometry revealed significant increase of cellular binding by overexpression of mNtcp or hNTCP. All values are shown as mean ± SD of biological replicates (n = 3 independent experiments). ****$p < 0.001$. Numerical data for all graphs are shown in the Figure 2-source data.

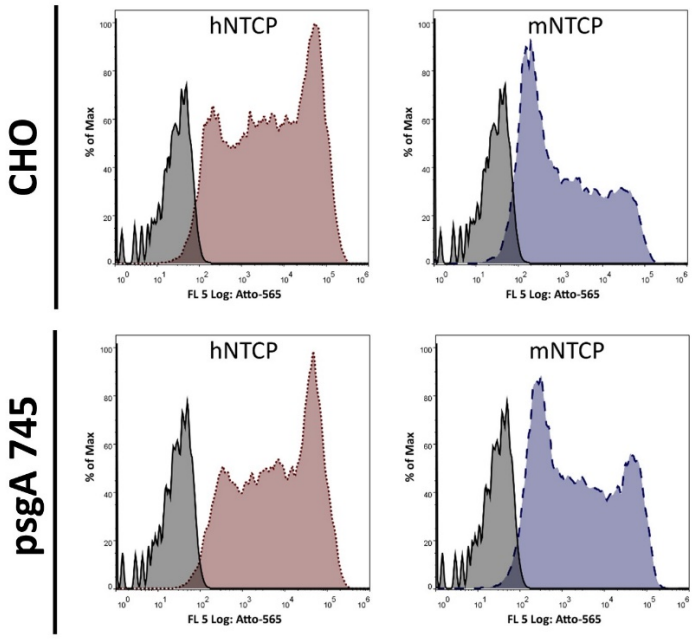

Figure 2–figure supplement 3. Influence of glycosaminoglycans (GAGs) on Myrcludex B binding. Flow cytometry analysis of Myrcludex B binding to CHO or psgA745 cells NTCP deficient (pEF6 transfected), or overexpressing hNTCP or mNtcp. psgA745 are CHO xylosyltransferase mutants deficient of GAGs. Histograms of Myrcludex B binding to cells transfected with empty vector (gray; solid line), hNTCP (red; dotted line) or mNtcp (blue; dashed line)

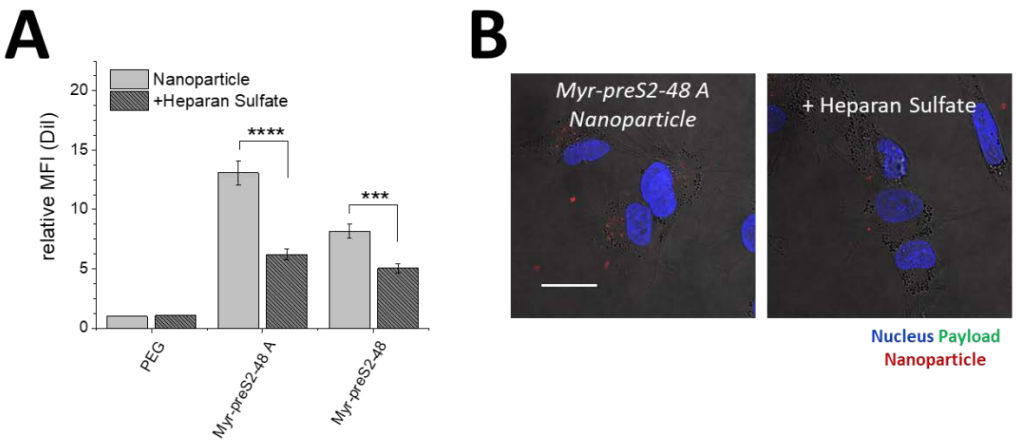

Figure 2–figure supplement 4. Uptake of nanoparticles into HepG2-*WT* cells in absence or presence of heparan sulfate. (A) Binding of PEG, Myr-preS2-48 A and Myr-preS2-48 conjugated nanoparticles was quantitatively assessed using flow cytometry. A significant decrease of cellular binding was observed in presence of heparan sulfate. All values are shown as mean ± SD of biological replicates (n = 3 independent experiments). ***p < 0.001, ****p < 0.0001. Numerical data for all graphs are shown in the Figure 2-source data. (B) Representative confocal laser scanning microscopy images of Myr-preS2-48 A nanoparticles (membrane dye, DiI, red signal) loaded with carboxyfluorescein (payload, green signal) internalized into HepG2-*hNTCP* in absence or presence of heparan sulfate. Blue signal: Hoechst stain of cell nuclei. Scale bar = 20 µm.

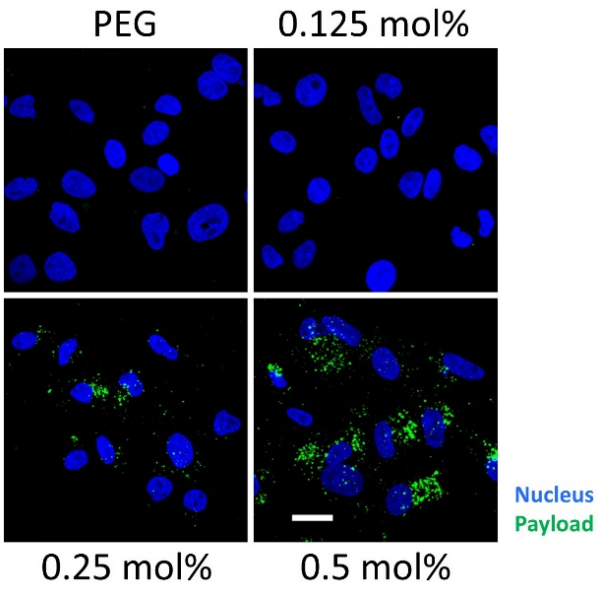

Figure 2–figure supplement 5. Ligand density dependent uptake of Myrcludex B-modified nanoparticles loaded with carboxyfluorescein (payload, green). Representative confocal laser scanning microscopy maximum intensity projections are shown. Blue signal: Hoechst stain of cell nuclei. Scale bar = 10 µm.

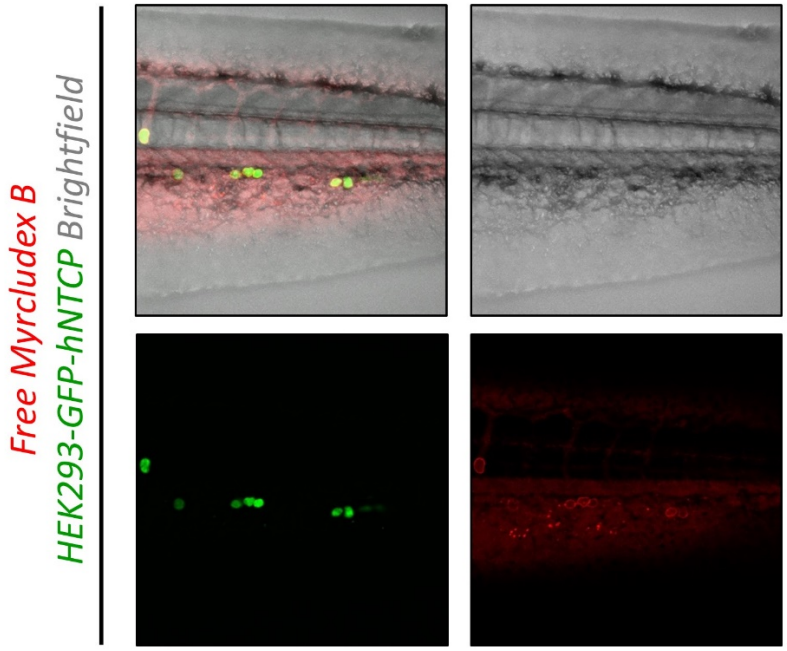

Figure 4–figure supplement 1. Targeting ability of free Myrcludex B *in vivo* in xenotransplanted zebrafish embryos. Atto-565 labeled Myrcludex B (red signal) was injected into wild type zebrafish embryos xenotransplanted with human HEK293 cells expressing hNTCP (GFP, green signal). Red signals on surface of HEK293 cells demonstrate binding of Myrcludex B. Representative brightfield and fluorescence images of tail region including a merge image one hour post injection are shown.

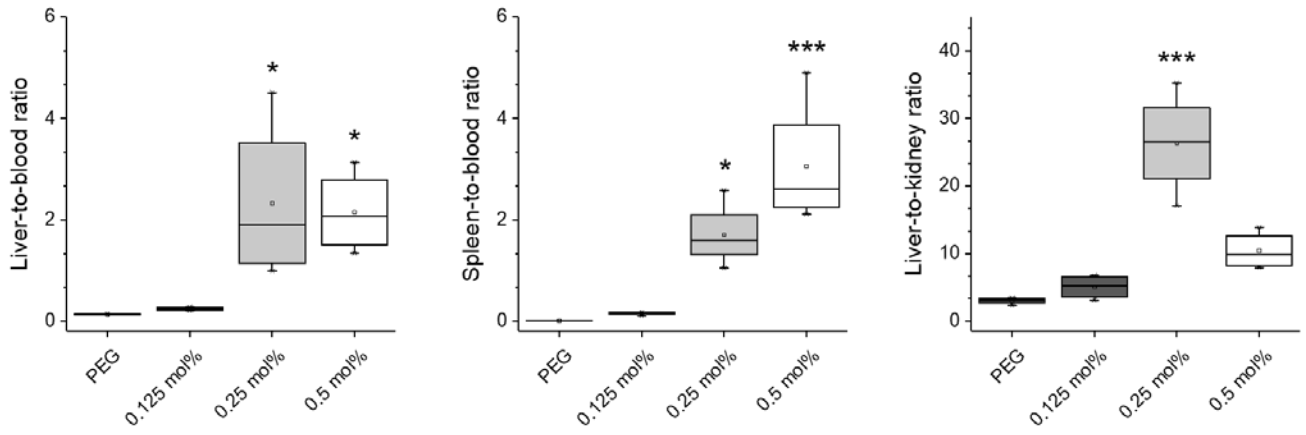

Figure 5–figure supplement 1. Organ ratios of e*x vivo* biodistribution analysis. Nanoparticles were modified with different amounts of Myr-preS2-31 and labeled with radioactive ^{111}In. Quantitative biodistribution studies were performed 1 hour post injection. Radioactivity of each organ was determined with a γ-counter. Ratios of injected dose (%ID) per organ between the blood pool level and selected organs, *i.e.* liver (*i.e.* target organ), spleen (*i.e.* clearance organ), and kidney (*i.e.* control organ since nanoparticle bound ^{111}In should not show renal excretion) were calculated. All values are shown as box plots of biological replicates (n = 3 independent experiments). *p < 0.05, **p < 0.01, ***p < 0.001.

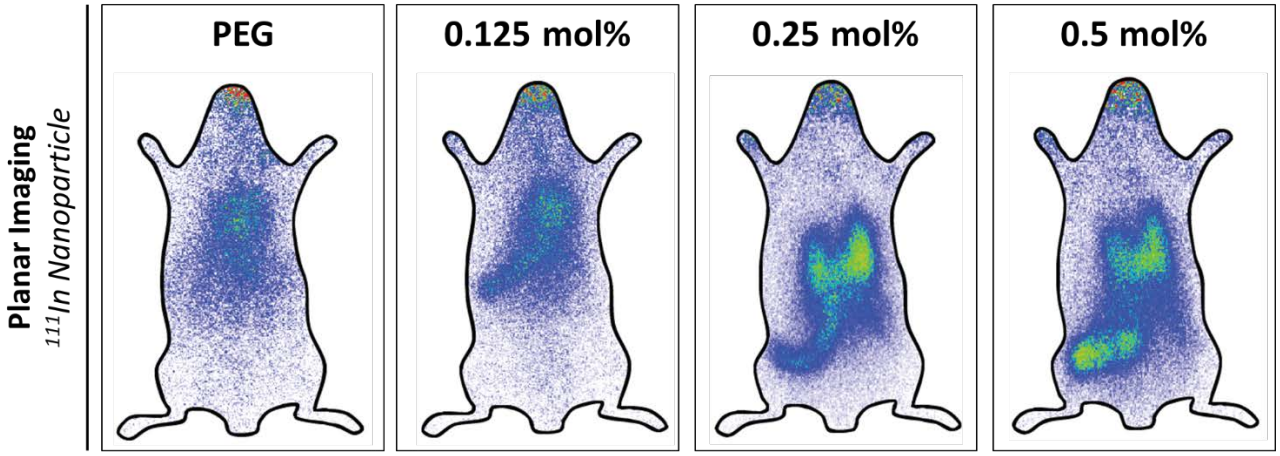

Figure 5–figure supplement 2. In vivo biodistribution and liver targeting of Myr-preS2-31 conjugated nanoparticles in mice. Nanoparticles were modified with different amounts of Myr-preS2-31. Static planar imaging of mice 15 min after intravenous injection of different ^{111}In labeled nanoparticles with approximately 8 MBq.

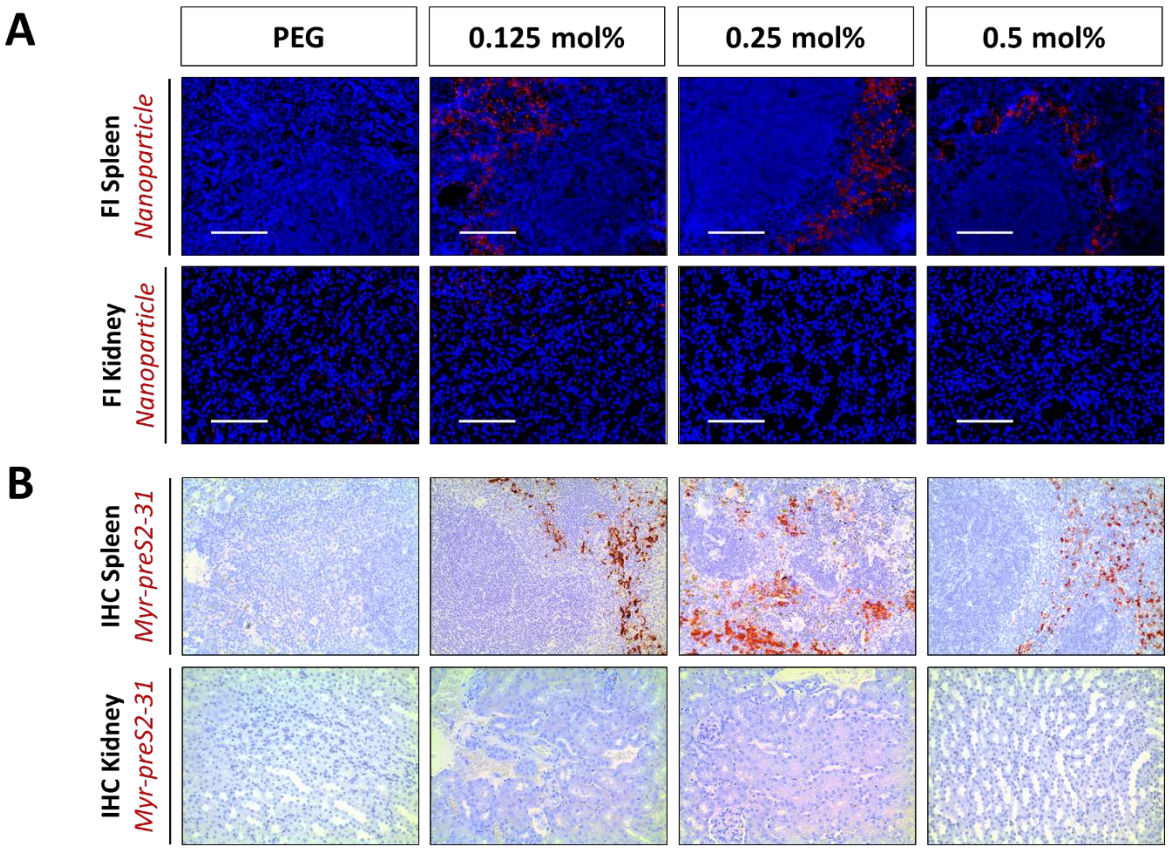

Figure 5–figure supplement 3. Intra-organ distribution of Myr-preS2-31-modified nanoparticles in spleen and kidney *in vivo* in mice dependent on ligand density. (A) Fluorescence imaging (FI) of liposomes (DiI, red signal) in spleen and kidney cryo-sections. Blue signal: Hoechst stain of cell nuclei. Scale bar = 100 µm. (B) Immunohistochemistry (IHC) of Myr-preS2-31 distribution (red signal) in spleen and kidney. Tissue sections from mice were stained with anti-Myr-preS2-31 antibody (MA18/7). Blue signals represent cell nuclei.

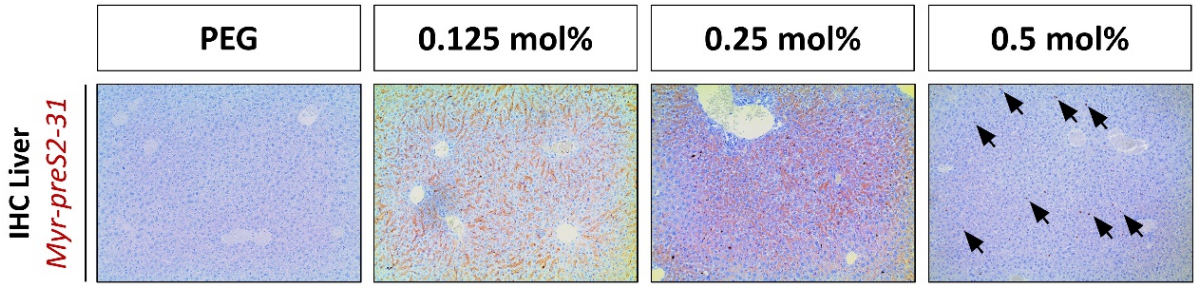

Figure 5–figure supplement 4. Liver targeting of Myr-preS2-31 conjugated nanoparticles in mice. Representative low magnification images of immunohistochemistry (IHC) of Myr-preS2-31 (red signal) in liver sections 1 hour after intravenous injection. Mice liver sections were stained with anti-Myr-preS2-31 antibody (MA18/7). Blue signals represent cell nuclei. Arrows indicate distinct localized accumulations.

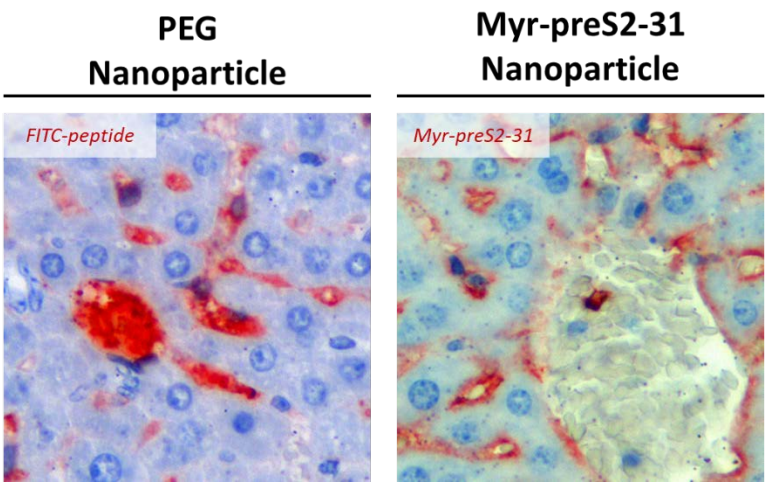

Figure 5–figure supplement 5. Specific binding of Myr-preS2-31 conjugated nanoparticles to sinusoidal membrane of hepatocytes. Immunohistochemistry of FITC-payload (PEG nanoparticles) or Myr-preS2-31 (nanoparticles modified with 0.25 mol% Myr-preS2-31) in the liver sections 1 hour after intravenous injection (red signals). Mice liver sections were stained with anti-FITC antibody or anti-Myr-preS2-31 antibody (MA18/7), respectively. Blue signals represent cell nuclei.

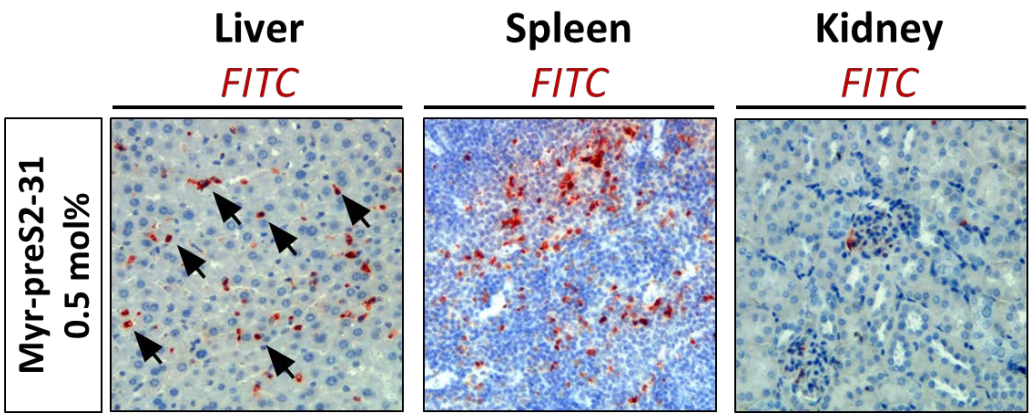

Figure 5–figure supplement 6. Biodistribution of nanoparticles modified with 0.5 mol% Myr-preS2-31 in mice. Immunohistochemistry of nanoparticles` FITC payload (red signal) in the liver, spleen, kidney sections 1 hour after intravenous injection. Tissue sections were stained with anti-FITC antibody. Blue signals represent cell nuclei. Arrows indicate distinct localized accumulations.

Chapter IV-II

Immobilization of Enzymes on PLGA Sub-Micrometer Particles by Crosslinked Layer-by-Layer Deposition

Sandro Sieber, Stefan Siegrist, Stéphanie Schwarz, Fabiola Porta, Susanne H. Schenk, Jörg Huwyler

Manuscript: Macromolecular Bioscience (2017) [43]

Highlights: Enzyme immobilization for therapeutic purposes is a promising branch of nanomedicine research. Nevertheless, current immobilization protocols have usually to be tailored and adapted to specific enzymes, due to different enzyme molecular weights, active conformations, or stabilities. In order to provide a protocol, which is applicable to different enzymes, an enzyme immobilization approach only based on enzyme and particle surface charge was developed. Two different model enzymes were immobilized on FDA approved poly(lactide-co-glycolide) (PLGA) particles via a crosslinked layer-by-layer approach. Enzyme activity and stability under enhanced temperature and decreased pH before and after immobilization were investigated. The zebrafish model was used to test the biocompatibility, stability, and activity of the designed system under biological conditions.

Immobilization of Enzymes on PLGA Sub-Micrometer Particles by Crosslinked Layer-by-Layer Deposition

Sandro Sieber, Stefan Siegrist, Stéphanie Schwarz, Fabiola Porta, Susanne H. Schenk, Jörg Huwyler*

Enzyme immobilization is of high interest for industrial applications. However, immobilization may compromise enzyme activity or stability due to the harsh conditions which have to be applied. The authors therefore present a new and improved crosslinked layer-by-layer (cLbL) approach. Two different model enzymes (acid phosphatase and β-galactosidase) are immobilized under mild conditions on biocompatible, monodisperse, sub-micrometer poly(lactide-*co*-glycolide) (PLGA) particles. The resulting PLGA enzyme systems are characterized regarding their size, surface charge, enzyme activity, storage stability, reusability, and stability under various conditions such as changing pH and temperature. The developed and characterized cLbL protocol can be easily adapted to different enzymes. Potential future uses of the technology for biomedical applications are discussed. PLGA-enzyme particles are therefore injected into the blood circulation of zebrafish embryos in order to demonstrate the in vivo stability and activity of the designed system.

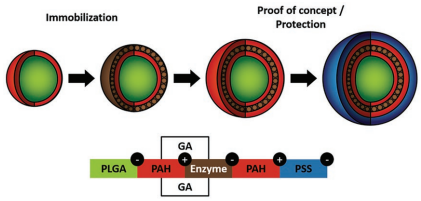

1. Introduction

Enzymes are increasingly used in industrial production due to their biocatalytic properties and potential. Examples include enantioselective production of active pharmaceutical ingredients[1] or the use of enzymes in food processing. The enzymatic treatment of milk, for example, results in lactose free milk products, which do not contain any residual lactose.[2,3] However, moderate chemical stability of many enzymes prevents their recovery from technical processes. This leads to high production costs and makes enzymes unsuitable for many applications.[4] In order to overcome these shortcomings, it was proposed to immobilize enzymes on surfaces or particles using different techniques. Through enzyme immobilization, different characteristics such as biological and chemical stability, kinetic properties, solubility and reusability can be improved. Today, a continuously growing number of immobilization techniques are available. They can mainly be divided into the immobilization on supports, entrapment, or crosslinking via the preparation of crosslinked enzyme aggregates (CLEAs) or crosslinked enzyme crystals (CLECs).[5]

Particles in the sub-micrometer range are ideal candidates for enzyme immobilization due to their high surface to volume ratio and therefore high enzyme loading capacity and the broad range of possible applications.[6] Despite the in most cases required preliminary activation of the underlying carrier and the specific reaction conditions, covalent attachment is still one of the most powerful methods for increasing enzyme stability upon immobilization.[4] However, most of these protocols require well defined and/or relatively harsh reaction conditions. As an alternative approach, physical adsorption

S. Sieber, S. Siegrist, S. Schwarz, Dr. F. Porta, Dr. S. H. Schenk, Prof. J. Huwyler
Division of Pharmaceutical Technology
Department of Pharmaceutical Sciences
University of Basel
Klingelbergstrasse 50, 4056 Basel, Switzerland
E-mail: joerg.huwyler@unibas.ch

DOI: 10.1002/mabi.201700015

based on electrostatic or hydrophobic/hydrophilic interactions can be used allowing enzymes to be adsorbed to the particle surface under mild conditions. The layer-by-layer (LbL) technique, which was already introduced in 1992 by Decher et al.,[7] offers a versatile and adaptable possibility to immobilize different enzymes on various carriers only based on their opposite electrostatic charge.[8] In this case, subsequent layers of polyelectrolytes and ionized enzymes are deposited on a solid support. The resulting "sandwich" configuration between electrolytes and enzymes allows for a high density of immobilized enzymes. A major drawback of this approach is the instability of the resulting carrier-enzyme systems resulting in enzyme desorption and the inability to wash and reuse enzyme-loaded particles.

In view of the shortcomings of both covalent and noncovalent coupling procedures, we present in this publication a novel crosslinked layer-by-layer (cLbL) immobilization technique. Combining covalent crosslinking and layer-by-layer deposition on sub-micrometer particles, the benefits of chemical and physical immobilization can both be exploited. This improved immobilization technique consists of a subsequent deposition of polyelectrolytes (PE) and enzymes on the surface of biodegradable (poly(lactide-*co*-glycolide)) (PLGA) particles using the layer-by-layer deposition technology. The coiled assembly of polyelectrolytes on the carrier facilitates multiple enzyme–PE interactions, which finally leads to an efficient and reproducible enzyme adsorption. Each PE–enzyme layer is subsequently stabilized by covalent crosslinking using glutaraldehyde (GA).[9] To this end, a PE with primary amino groups (i.e., poly(allylamine hydrochloride) (PAH)) was selected to allow for covalent crosslinking with amine groups present on enzymes. It was the goal of the present work to develop a cLBL enzyme immobilization technique and to demonstrate its applicability for industrial applications using two model enzymes (acid phosphatase and β-galactosidase). The established protocol can be adapted to different types of enzymes and allows for a fast and highly reproducible enzyme immobilization on sub-micrometer particles. Enzyme activity was monitored using colorimetric enzyme assays and Michaelis–Menten enzyme kinetics. Enzyme stability under stress conditions (i.e., storage, pH, and temperature), particle reusability, in vivo stability, and biocompatibility were investigated.

2. Experimental Section

2.1. Chemicals and Reagents

Acid phosphatase from potato (0.5–3.0 units mg^{-1}) (AP), β-galactosidase from *Aspergillus oryzae* (13.4 units mg^{-1}) (BGal), D-α-tocopherol polyethylene glycol 1000 succinate (DTPG), ethyl 3-aminobenzoate methane sulfonate (MS 222), halocarbon oil 27, 2-[4-(2-hydroxyethyl)piperazin-1-yl]ethanesulfonic acid (HEPES) buffer, paraformaldehyde, poly(allylamine hydrochloride) (M_w ≈15 000 or ≈17 500) (PAH), ester terminated poly(D,L-lactide-*co*-glycolide) (lactide:glycolide 65:35, M_w 40 000–75 000) (PLGA), poly(sodium 4-styrene sulfonate) (M_w ≈ 70 000) (PSS), *N*-phenylthiourea (PTU), NP-40, sodium deoxycholate, Tween 20 (polyoxyethylenesorbitan monolaurate), 2-mercaptoethanol, and 4-nitrophenol (4-NP) were purchased from Sigma-Aldrich (Sigma-Aldrich, Buchs, Switzerland). Dimethyl sulfoxide (DMSO), ethyl acetate, GA 50%, 5-Bromo-4-chlor-3-indoxyl-β-D-galactoside (X-β-Gal), potassium ferricyanide, potassium ferrocyanide, 2-nitrophenol-β-D-galactopyranoside (ONPG), 3-(4,5-dimethylthiazol-2-yl)-2,5-diphenyltetrazolium bromide (MTT), and 4-nitrophenylphosphate (4-NPP) were purchased from Carl Roth (Carl Roth GmbH, Karlsruhe, Germany). Agarose standard low was purchased from BioRad (BioRad, Hercules, CA). All other chemicals were of analytical grade and obtained from Merck, Darmstadt, Germany. Deionized water used for all experiments had a resistivity of 18.2 MΩ cm (Merck Millipore, Darmstadt, Germany). Activity of BGal was determined in citrate buffer (40×10^{-3} M citric acid, 60×10^{-3} M tri-sodium citrate, 1×10^{-3} M $MgCl_2$, 50×10^{-3} M 2-mercaptoethanol) at the indicated pH. If not differently noted, citrate buffers and H_2O used for particle enzyme preparation and enzyme activity assays contained 0.01% Tween 20 in order to prevent agglomeration and adsorption of processed PLGA particles on reaction container surfaces.

HEPG2 cells were cultured as described previously.[10] Primary human umbilical vein cells (HUVEC) and culture medium were from Provitro, Berlin, Germany. Primary HUVEC cells were cultured according to protocols of the supplier (Provitro, Berlin, Germany) and flasks or plates were coated with a 0.1 mg mL^{-1} rat tail collagen type 1 solution for enhanced monolayer formation. HEPG2 and HUVEC were used at passages 25–35 and passages 4–6 during MTT assays, respectively. 1% (v/v) penicillin/streptomycin was added to cell culture media.

Zebrafish embryo culture medium was prepared at final concentrations of 5×10^{-3} M sodium chloride, 0.25×10^{-3} M potassium chloride, 0.5×10^{-3} M magnesium sulfate, 0.15×10^{-3} M potassium dihydrogen phosphate, 0.05×10^{-3} M sodium phosphate dibasic, 0.5×10^{-3} M calcium chloride, 0.71×10^{-3} M sodium bicarbonate, 0.001% (w/v) methylene blue, pH 7.4.

Phosphate buffer used for all the X-β-Gal buffers was prepared at final concentrations of 23×10^{-3} M sodium phosphate monobasic, 77×10^{-3} M sodium phosphate dibasic, pH 7.3. X-β-Gal fixation buffer was prepared at a final concentration of 2% paraformaldehyde and 0.2% glutaraldehyde. X-β-Gal wash buffer was prepared at final concentrations of 2×10^{-3} M magnesium chloride, 0.02% sodium deoxycholate, and 0.02% NP-40. X-β-Gal staining buffer was prepared at final concentrations of 2×10^{-3} M magnesium chloride, 5×10^{-3} M potassium ferrocyanide, 5×10^{-3} M potassium ferricyanide, 0.02% sodium deoxycholate, 0.02% NP-40, and 1 mg mL^{-1} X-β-Gal.

2.2. PLGA Particle Preparation

PLGA particles were prepared as described previously.[11] Briefly, 100 mg of PLGA was solubilized in 1 mL of ethyl acetate overnight. The PLGA solution was added dropwise to 2 mL of a 0.3% (w/v) DTPG solution under vigorous agitation using a vortex

mixer. The emulsion was sonicated (three times for 10 s) in an ice water bath using a probe sonicator Sonifier 250 (Branson, Urdorf, Switzerland). The emulsion was diluted with 45 mL of a 0.3% (w/v) DTPG solution and stirred at 360 rpm for 3 h in order to fully evaporate the organic solvent. The resulting particles were washed three times by centrifugation using an Optima L-90K Ultracentrifuge (Beckman Coulter, Nyon, Switzerland) for 15 min at 17 000 × g and suspended in H_2O using a sonication bath. Particle concentration (mg mL^{-1}) in solution was determined by lyophilization of an aliquot (500 µL) of PLGA particles in H_2O. Particles were diluted to a final concentration of 2.85 mg mL^{-1} using H_2O.

2.3. Enzyme Immobilization

Following the new developed cLbL protocol, two different enzymes were separately immobilized on 0.5 mL of PLGA (2.85 mg mL^{-1}) particles. Subsequent layers of PAH, PSS, and GA crosslinked enzyme were deposited. In order to reach maximal enzyme adsorption, enzymes were always adsorbed onto an underlying layer of the opposite charged PE which was PAH in case of AP and PSS in case of BGal. For the particle layering with PEs, particles were incubated with 1 mL of 10 mg mL^{-1} PE (PAH in H_2O, PSS in citrate buffer pH 4.8) for 10 min on an orbital shaker using 1.5 mL plastic tubes. The excess of PEs was removed by centrifugation for 7 min at 10 000 × g followed by a washing step using 1 mL of H_2O or citrate buffer pH 4.8. Particles were resuspended by gentle sonication using a water bath sonicator (Sonorex; Bandelin, Berlin, Germany). For enzyme adsorption, PE layered PLGA particles were transferred into 4 mL glass vials and incubated with 1 mL of AP or BGal (5 or 20 mg mL^{-1}, respectively) in citrate buffer pH 4.8 for 15 min while stirred at 800 rpm. Thus, PLGA particles were loaded using an excess of enzyme under saturating conditions in order to minimize the time needed for enzyme adsorption. Covalent crosslinking of enzyme to PAH was performed by suspending a pellet of PE and enzyme layered PLGA particles in 1 mL GA (2.5%, v/v) in citrate buffer pH 4.8 followed by the same procedure as already described for the enzyme immobilization step. The excess of enzyme or GA was removed by centrifugation followed by three washing steps using 1 mL of citrate buffer pH 4.8. Particles were coated with two layers of GA crosslinked enzyme, in order to increase the amount of immobilized enzyme. As a proof of concept and to increased enzyme protection, PLGA particles coated with PEs and GA crosslinked enzyme were further coated with alternating layers of PEs. Five different types of cLbL particles were prepared. The composition of the particles is described using the following nomenclature: Using the model enzyme AP, PLGA PAH 2(AP GA) x(PAH PSS) particles were prepared and indicated as PLGA AP xPE, where x may adopt a value of 0, 1, or 2. Using BGal, corresponding particles were prepared, namely, PLGA PAH PSS 2(BGal GA) x(PAH PSS) and indicated as PLGA BGal xPE, where x may adopt a value of 0 or 1.

2.4. Characterization

Particle morphology and size were analyzed using a transmission electron microscopy (TEM) CM-100 Philips (FEI, Hillsboro, OR). Samples were stained on carbon coated copper grids using a 2% (w/v) uranyl acetate solution. Size and zeta potential of different PLGA enzyme particles were determined by dynamic light scattering (DLS) using a Delsa NanoC Particle Analyzer (Beckmann Coulter, Nyon, Switzerland). Size and zeta potential measurements of free enzymes at different pH values were carried out using a Zetasizer Nano ZSP and MPT-2 Multi-Purpose Titrator (Malvern, Herrenberg, Germany). All samples were measured in H_2O.

2.5. Michaelis–Menten Enzyme Kinetics

UV/vis spectroscopy was performed using a 96 well plate reader Spectramax M2^e (Molecular Devices, Sunnyvale, CA). All optical density measurements were carried out at a wavelength of 410 nm, using transparent 96 well plates and a sample volume of 200 µL.

Enzyme activity was determined according to Cooney.[12] One enzyme unit was defined as the amount of enzyme that hydrolyzes 1 µmol of its respective substrate per minute. All experiments were carried out at pH 4.8 since this represents the optimal working pH for both enzymes.

The Michaelis–Menten constant (K_m) and the maximum velocity (V_{max}) were determined as described in the following section. For AP, 50 µL of free or immobilized enzyme in citrate buffer pH 4.8 were incubated with 50 µL of 4-NPP in citrate buffer pH 4.8 with concentrations ranging from 0 to 8.5 × 10^{-3} M for 10 min at 37 °C and 700 rpm. The reaction was terminated by adding 100 µL of 1 M NaOH. In parallel, a blank of each sample was prepared by adding 50 µL of 4-NPP using the same concentration as mentioned above to a mixture of 50 µL free or immobilized enzyme in citrate buffer pH 4.8 and 100 µL 1 M NaOH. Samples and blanks were transferred to a 96 well plate and stored for 60 min at room temperature while slightly shaking in order to dissolve the PLGA particles. For BGal, 50 µL of free or immobilized enzyme in H_2O were incubated with 50 µL of ONPG in citrate assay 2× buffer pH 4.8 with concentrations ranging from 0 to 22 × 10^{-3} M for 10 min at 30 °C and 700 rpm. The reaction was terminated by adding 150 µL of 1 M sodium carbonate. In parallel, a blank of each sample was prepared by adding 50 µL of ONPG using the same concentration as mentioned above to a mixture of 50 µL free or immobilized enzyme in H_2O and 150 µL 1 M sodium carbonate. Samples and blanks were centrifuged for 7 min at 10 000 × g. In order to determine K_m and V_{max}, the model was fitted to the experimental data according to Equation (1). We observed an unspecific formation of background signal during the incubations due to chemical instability of the BGal substrate. This unspecific signal increased linearly over time and was subtracted from the experimental data. The Michaelis–Menten enzyme kinetics formula, adjusted for background signal, was defined as follows

$$V = \frac{V_{max} \times S}{S + K_M} - m \times S \quad (1)$$

where V_{max} = maximal velocity [µmol min^{-1} $unit^{-1}$], S = substrate concentration [µM], K_m = Michaelis–Menten constant [µM], and m = slope of unspecific background signal. Activity of enzymes was defined in terms of units, where one unit will hydrolyze 1.0 µmol of substrate per min under our assay conditions. Apparent enzyme efficiency E_{cat} was defined as V_{max}/K_M with units of [min^{-1} $unit^{-1}$].

2.6. Stress Test and Enzyme Stability

Enzyme activity was determined as described above under different stress conditions. Remaining activities were calculated as a percentage of the initial activity from untreated enzyme samples under the same activity assay conditions. pH sensitivity was measured by incubation of free and immobilized enzyme under the indicated conditions. Prior to OD measurements, particles were removed from solution by centrifugation for 7 min at 10 000 × *g*.

Temperature stress tests were performed by incubation of free and immobilized enzymes at temperatures ranging from 30 to 80 °C for 10 min. Samples were allowed to cool down to room temperature for another 10 min. The temperature treated enzyme solution was mixed with its substrate at an enzyme saturating concentration. To test storage stability, samples of free and immobilized enzymes were stored for 30 d at 4 °C in 1.5 mL plastic tubes. Remaining activities were calculated as a percentage of the initial activity of freshly prepared samples.

2.7. Repeated Use

Samples of immobilized enzymes were tested regarding their reusability. Enzyme loaded particles where separated from the incubation mix by centrifugation for 7 min at 10 000 × *g*. The collected pellet was washed with 1 mL of 0.01% Tween 20 in H_2O (w/v) followed by another activity assay. Remaining activities were indicated as percentage of the first activity assay.

2.8. Toxicity

The MTT assay was used to determine cell viability upon nanoparticle incubation. This colorimetric assay monitors NAD(P)H-dependent oxidoreductase enzyme activity of viable cells. The tetrazolium dye MTT 3-(4,5-dimethylthiazol-2-yl)-2,5-diphenyltetrazolium bromide is thereby reduced to a water-insoluble and purple colored formazan. 96 well plates were coated with a 0.1 mg mL^{-1} rat tail collagen type 1 solution prior to primary HUVEC seeding. HEPG2 and HUVEC cells were transferred to 96 well plates (20 000 and 10 000 cells per well, respectively) and allowed to attach for 24 h prior to incubation for 24 h with PLGA AP PE and PLGA BGal PE particles (10 ng mL^{-1}, 100 ng mL^{-1}, 10 μg mL^{-1}, 50 μg mL^{-1}, 100 μg mL^{-1}, and 250 μg mL^{-1}), 20 × 10^{-6} M terfenadine in 0.1% DMSO (positive control) or blank culture medium (negative control). Formazan crystals were dissolved in dimethyl sulfoxide and optical density was measured at 570 nm.

2.9. Zebrafish In Vivo Stability

A volume of 2 nL free BGal (5.2 units mL^{-1}) in H_2O 0.01% Tween 20 (w/v), PLGA BGal particles (0.5 units mL^{-1}) in H_2O 0.01% Tween 20 (w/v), and H_2O 0.01% Tween 20 (w/v) as a negative control were injected into blood circulation via the Duct of Cuvier of zebrafish embryos 2 d post fertilization in order to assess in vivo stability of the prepared formulation. Zebrafish embryos were kept in zebrafish culture media at 28 °C and bleached with PTU 1 d post fertilization. Prior to injection, zebrafish embryos were anesthetized using tricaine methanesulfonate (MS222) and immobilized in 0.3 % (w/v) agarose followed by injection using a micromanipulator (Wagner Instrumentenbau KG, Schöffengrund, Germany), a pneumatic Pico Pump PV830 (WPI, Sarasota, FL), and a Leica S8AP0 microscope (Leica, Wetzlar, Germany). 30 min post injection, zebrafish embryos were removed from the agarose. They were euthanized, washed with 2 mL X-β-Gal wash buffer, and incubated overnight at 4 °C in 2 mL of X-β-Gal fixation buffer. Fixed zebrafish embryos were washed three times for 5 min using 2 mL X-β-Gal wash buffer followed by staining in 2 mL of X-β-Gal staining buffer at 37 °C for 8 h. Active β-galactosidase cleaves the β-glycosidic bond of 5-Brom-4-chlor-3-indoxyl-β-D-galactoside (X-β-Gal), which results in blue precipitates of the insoluble dye. Samples were analyzed using a Leica DM6000B microscope using a 10× magnification. Single pictures were combined to a composite overview picture using ImageJ v1.51 picture processing software (open source software). All animal experiments were carried out in accordance with Swiss legislation on animal welfare.

2.10. Statistics

Values are means of $n \geq 3$ independent sets of experiments ± standard deviation (SD). Treatment groups were compared by one-way analysis of variance and Tukey's post hoc test. Statistically significant differences ($p \leq 0.05$) were marked by an asterisk. Used software was Origin 9.1 (OriginLab, Northampton, MA).

3. Results

Spherical PLGA microparticles were coated with layers of GA crosslinked enzyme and PEs. The resulting PLGA AP *x*PE particles were visualized by transmission electron microscopy. Uncoated PLGA particles (Figure 1A1,A2) had a regular and flat surface. The surface of these PLGA particles gradually changed after the addition of one enzyme layer and crosslinking using glutaraldehyde (Figure 1B1,B2) followed by two layers of opposite charged polyelectrolytes (Figure 1C1,C2). Particles had a uniform size and morphology. Enzymes and polyelectrolytes were deposited on the particle surface in form of clusters of plaques.

Size and size distribution of PLGA-enzyme particles were measured by DLS as summarized in Table 1. A hydrodynamic diameter of 494 ± 43 nm of a monodisperse particle population (polydispersity index (PDI) 0.16 ± 0.04) was determined for uncoated PLGA particles. Additionally, PLGA particles were analyzed by DLS after storage in water at 4 °C for 11 months. No change of particle size or PDI was observed (size 492.7 nm; PDI 0.155). An increase in size was observed after enzyme immobilization and subsequent addition of one or two layers of PEs. All PLGA AP PE particle preparations were monodisperse as shown by a PDI below 0.2. PLGA BGal PE particles showed a slightly increased PDI below 0.3. The change of zeta potential (i.e., the electrokinetic potential at the slipping/shear plane of a colloid particle) of PLGA particles after the application of subsequent opposite charged

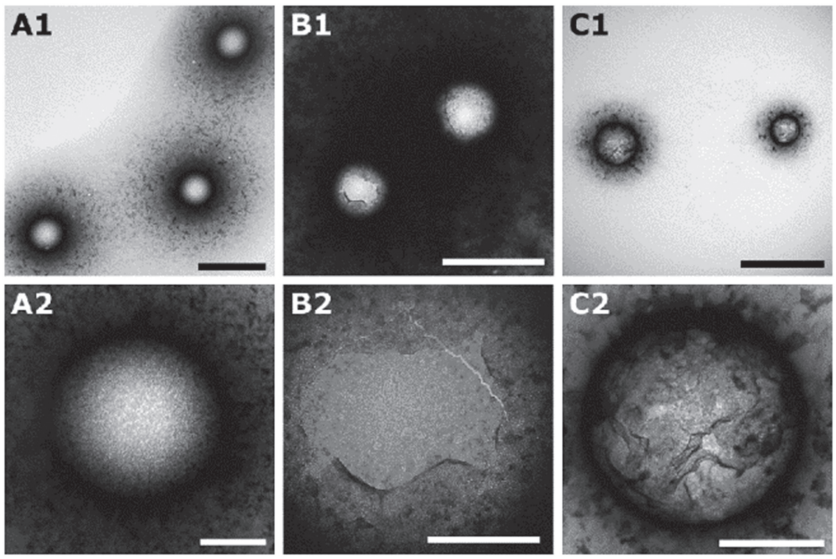

Figure 1. TEM analysis (negative staining) of uncoated PLGA particles (panels A1, A2), PLGA particles coated with acidic phosphatase (panels B1, B2), and PLGA particles coated with acid phosphatase and two layers of polyelectrolytes (panels C1, C2). Scale bars correspond to 1 μm (panels A1–C1) and 200 nm (panels A2–C2).

layers via the cLbL approach is presented in Figure 2. Bare PLGA particles showed a zeta potential around −40 mV. After addition of PAH, the zeta potential was raised to positive values. It should be noted that differences in the obtained zeta potential can be attributed to differences in molecular weight (chain length) of PAH used for the present studies (i.e., PAH of 15 000 g mol^{-1} for AP and PAH of 17 500 g mol^{-1} for BGal). Based on DLS measurements at different pH, the apparent isoelectric point of AP and BGal was estimated to be in the range of pH 4.2 and 6.4 under our assay conditions. AP and BGal are therefore negatively and positively charged at pH 4.8, respectively. Therefore, PLGA particles were layered with PAH (positively charged) or PSS (negatively charged), prior to enzyme immobilization. After enzyme immobilization, particles were coated with several layers of alternatingly charged polyelectrolytes to protect the bound enzymes. Successful layering was confirmed by the change of zeta potentials (Figure 2).

Table 1. Size and polydispersity index (PDI) of different PLGA-enzyme particles.

Enzyme	Particle	Size [nm]	PDI
–	PLGA	494.4 ± 43.2	0.156 ± 0.035
AP	PLGA AP	922.6 ± 5.4	0.175 ± 0.016
AP	PLGA AP PE	717.6 ± 18.5	0.172 ± 0.015
AP	PLGA AP 2 PE	764.9 ± 35.0	0.143 ± 0.069
BGal	PLGA BGal	635.8 ± 37.7	0.266 ± 0.017
BGal	PLGA BGal PE	648.7 ± 30.1	0.241 ± 0.012

PLGA particles carrying the two different immobilized enzymes acid phosphatase (AP) or β-galactosidase (BGal) and the indicated number of layers of polyelectrolytes (PE). Particles were analyzed using dynamic light scattering (DLS) ($n \geq 3$ experiments; values are means ± SD).

Free and immobilized enzymes were analyzed regarding their kinetic properties, which are summarized in Figure 3 and Table 2. In addition to the standard Michaelis–Menten constants, an apparent enzymatic efficiency (E_{cat}) was calculated. E_{cat} is defined as the ratio between V_{max} and K_M. In contrast to all formulations containing BGal (Table 2D–F), where no significant changes of kinetic properties were observed, formulations of AP (Table 2A–C) showed different values of K_m, V_{max}, and E_{cat}. An increased enzyme-substrate affinity was observed for both PLGA AP and PLGA AP PE as compared with free enzyme (Table 2). This was evident by a decreased K_m value. Taking into account concomitant changes of V_{max}, PLGA AP showed a 1.5 fold increased apparent enzymatic efficiency E_{cat}.

The different enzyme formulations were tested with respect to temperature and pH sensitivity, storage stability, and reusability. Immobilized AP did not show any changes regarding its temperature sensitivity when compared to free AP (Figure 4A). In contrast, immobilization of BGal on PLGA particles (Figure 4B) leads to an increased sensitivity toward elevated temperatures. Immobilized BGal did not show any improved stability against lower pH compared to free BGal (data not shown). However, the remaining activity of AP formulations increased with advanced states of immobilization after the pH of the reaction solution was reduced by one log unit. Compared with their activity at pH 4.8, the remaining activities of free AP, PLGA AP, and PLGA AP PE at pH 3.6 were 1.4% ± 0.1, 4.5% ± 0.2, and 13.0% ± 0.3, respectively. Comparing storage stability, free and immobilized formulations of AP possessed a remaining activity of around 60% after 30 d of storage irrespective of the used formulation (Figure 4C). BGal formulations retained almost 100% of their initial activity (Figure 4D). Enzymes were stored for 30 d at 4 °C. Reusability of enzymes was determined in terms of loss of activity during the course of five incubation and wash cycles (Figure 4E,F). These experiments were carried out with immobilized enzymes only since it is not possible to recover free enzyme from the incubation mix after the first activity determination. PLGA BGal particles kept around 80% of their initial activity after the fifth cycle of activity assays. A comparable result was

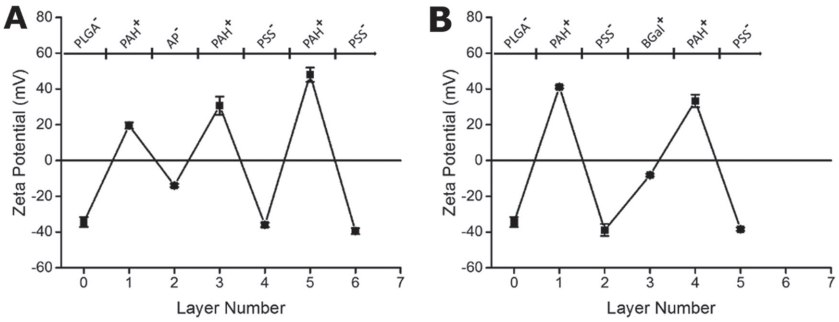

Figure 2. Alternating surface charge based on the cLbL immobilization approach of processed PLGA-enzyme particles. 0.15 mg mL^{-1} AP (panel A) or BGal (panel B) were immobilized on PLGA particles and further covered with the polyelectrolytes PAH and PSS according to the crosslinked layer-by-layer (cLbL) principle ($n \geq 3$ experiments; values are means ± SD).

obtained for PLGA AP particles, where around 65% of their initial activity was recovered.

To exclude a potential cellular toxicity of PLGA-enzyme particles, cell viability upon incubation was monitored in vitro using the HEPG2 and HUVEC cell lines. In Figure 5, the results of a 24 h 3-(4,5-dimethylthiazol-2-yl)-2,5-diphenyltertrazolium bromide (MTT) reduction assay are shown for both HEPG2 (Figure 5A) and HUVEC (Figure 5B). Up to a particle concentration of 100 μg mL^{-1} no statistically significant loss in cell viability could be seen. At the highest applied doses (250 μg mL^{-1}) of enzyme loaded particles only, a significant decrease in cell viability was observed.

The in vivo activity and stability of PLGA BGal particles was assessed in zebrafish embryos 2 d post fertilization (Figure 6). Two different staining patterns, obtained due to enzymatic formation of dark blue precipitates in vivo, were observed. Injection of free BGal resulted in a diffuse, faint and not localized color distribution whereas a dotted and localized staining pattern was obtained by injecting PLGA BGal particles. Particles seemed to accumulate within the posterior cardinal vein and the caudal vein. Zebrafish embryos were fixed and stained for BGal activity 30 min post intravenous injection of free or immobilized BGal into the Duct of Cuvier. There were no indications of acute toxicity (i.e., seizures, denaturation of tissue fluids or yolk, or heart failure) upon injection of enzyme or enzyme-loaded particles.

4. Discussion

The aim of this work was to develop and characterize an enzyme immobilization protocol (the cLbL protocol), which can be adapted to different particulate carriers and enzymes. Two our knowledge, this is the first time that different enzymes are immobilized on the surface of particles by a combination of both ionic interactions and covalent crosslinking using the same protocol. So far, combined coupling procedures were used only for industrial applications and coating of extended flat surfaces.[4] Our combined approach allowed us to immobilize enzymes by ionic interactions on PLGA particle surface and to subsequently stabilize the layered enzymes by covalent crosslinking under mild and nondestructive conditions. Loss of enzyme function (as often observed during crosslinking of enzymes using GA[13]) could be avoided, most probably

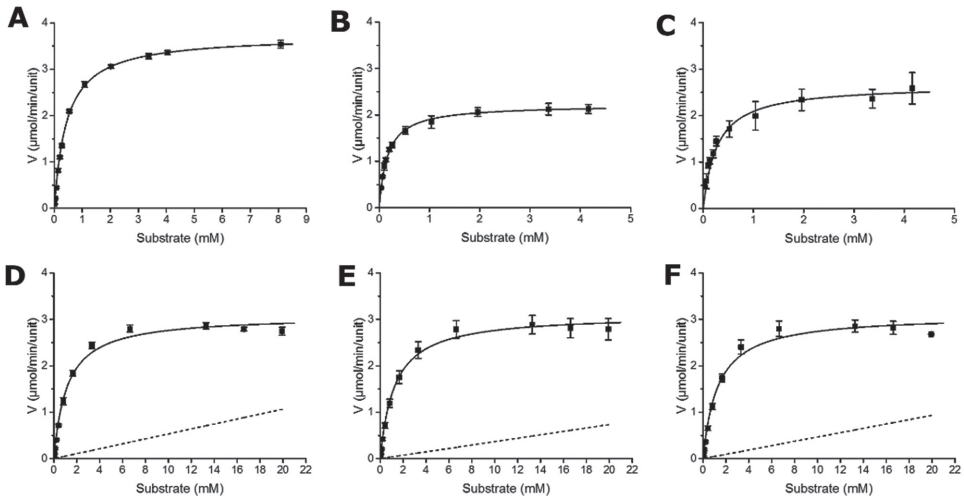

Figure 3. Enzyme kinetics of free and immobilized AP (panels A–C) and BGal (panels D–F). Michaelis–Menten enzyme kinetics of free AP (panel A), PLGA AP (panel B), PLGA AP PE (panel C), free BGal (panel D), PLGA BGal (panel E), and PLGA BGal PE (panel F). Solid lines: Fitted Michaelis–Menten kinetic model. Dotted lines: Subtracted background signal caused by unspecific conversion of educt. Values are means ± SD ($n \geq 3$).

Table 2. Michaelis–Menten kinetic parameters for free and immobilized AP and BGal.

Formulation	K_m [μM]	V_{max} [μmol min^{-1} unit^{-1}]	E_{cat} [min^{-1} unit^{-1}]
Free AP (A)	442.84 ± 28.96	3.73 ± 0.10	42.22 ± 1.62
PLGA AP (B)	165.80 ± 3.48	2.22 ± 0.12	66.84 ± 3.32
PLGA AP PE (C)	269.76 ± 17.66	2.66 ± 0.29	49.16 ± 3.15
Free BGal (D)	1151.36 ± 60.92	3.08 ± 0.07	10.73 ± 0.66
PLGA BGal (E)	1255.71 ± 16.03	3.11 ± 0.23	9.90 ± 0.75
PLGA BGal PE (F)	1361.03 ± 103.55	3.16 ± 0.20	9.33 ± 0.68

Kinetic parameters are calculated based on fitted experimental data ($n \geq 3$ experiments; values are means ± SD).

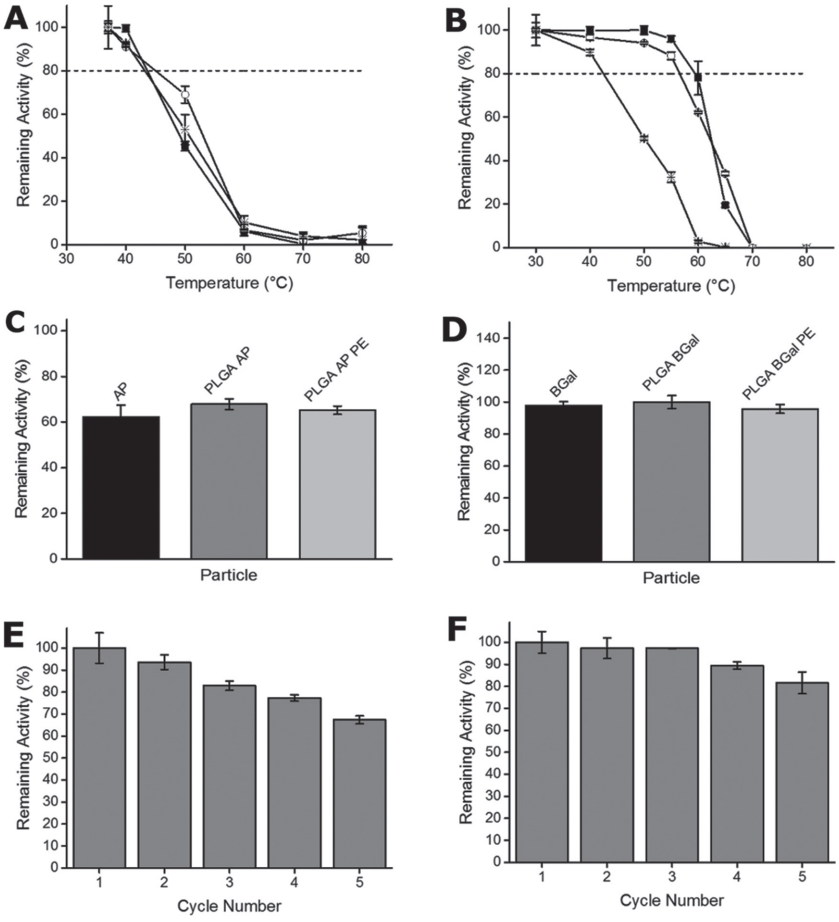

Figure 4. Stability tests of free and immobilized enzymes. Enzymatic activity of AP (panel A) and BGal (panel B) based formulations, which were kept for 10 min at the indicated temperature. Black squares: free enzyme, white circles: PLGA AP/BGal, asterisks: PLGA AP/BGal PE. Storage stability of free AP (panel C, black bar), PLGA AP (panel C, gray bar), PLGA AP PE (panel C, light gray bar), free BGal (panel D, black bar), PLGA BGal (panel D, gray bar), and PLGA BGal PE (panel D, light gray bar) after 30 d of storage at 4 °C. Reusability of PLGA AP (panel E) and PLGA BGal (panel F) as shown in terms of remaining activity after the indicated number of enzyme incubation and wash cycles. $n \geq 3$ experiments; values are means ± SD.

due to stabilization of enzymes in their active conformation prior to covalent linking. This approach can therefore be considered as a good alternative to enzyme immobilization via encapsulation, which often leads to unstable proteins.[14] Furthermore, enzyme leakage under changing pH conditions, which is one of the main drawbacks of physical enzyme adsorption,[15,16] did not occur.

The used enzymes acid phosphatase (AP) and β-galactosidase (BGal) carry opposite electrostatic charges under assay conditions demonstrating that anionic as well as cationic proteins can be immobilized by simple adjustment of the type and order of polyelectrolyte layers on the particle surface. Based on the isoelectric point and the enzymes natural working pH, the underlying particle can be layered either with an anionic or a cationic polyelectrolyte. Embedding the enzyme into polyelectrolytes provides a tridimensional network, which results in a much stronger enzyme adsorption compared to enzyme adsorption onto flat surfaces.[9] The extend of coating and thus the strength of electrostatic interactions was monitored by measuring the zeta potential of the particles. The usefulness and convenience of this analytical approach has already previously been recognized, but despite its importance there are very few protocols making use of it.[17] Adsorption of PSS always led to a surface charge of around −40 mV. PAH had a dual role: The addition of PAH to particles resulted in a strong positive surface charge[18] and the amino groups of PAH participated in crosslinking. The apparent isoelectric point of both enzymes of 4.2 and 6.4, respectively, was estimated by pH titration experiments combined with DLS size and zeta potential measurements (data not shown). Based on this result, the actual enzyme immobilization step was performed at pH 4.8 (activity assay condition for both enzymes) at which AP is negatively and BGal positively charged. The cLbL approach therefore allowed us to immobilize enzymes at their natural pH working conditions

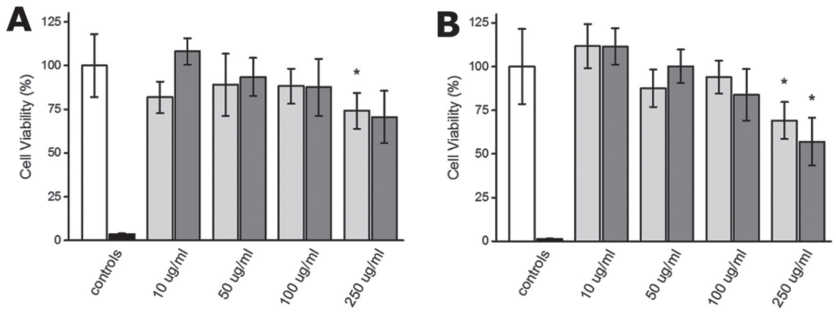

Figure 5. Cellular viability by the MTT assay. 24 h MTT viability testing for HEPG2 (panel A) and HUVEC cells (panel B) incubated with different concentrations of PLGA BGal PE (dark gray bars) and PLGA AP PE (light gray bars). Untreated cells were used as negative control (white bars, 100% viability). Positive control: 20×10^{-6} M terfenadine (black bars). Statistically significant differences as compared to 100% control are marked with an asterisk ($p > 0.05$).

where their active conformation is preserved.[19] In both cases, a change of the surface charge of carrier particles after enzyme addition was observed. Whereas the immobilization of AP completely changed the surface charge of the particle, the binding of BGal to the underlying particle was not sufficient to completely invert the zeta potential. Therefore, cationic PAH instead of anionic PSS was added on top of BGal in order to reach a positive zeta potential, which was required for addition of further PE layers.

PLGA, which is an extensively studied and Food and Drug Administration (FDA) approved polymer,[20,21] was used as the solid carrier for enzyme immobilization. PLGA particles were nonporous, monodisperse, and had a size in the sub-micrometer range. PLGA particle size was determined by DLS and TEM and a comparable diameter of around 500 nm was obtained. PLGA particle size can be tailored from a few to several thousand nanometers and therefore be adapted to the specific prerequisites of a given application.[22] From an industrial point of view, too small particles are difficult to recover from the reaction.[9] However, too big particles suffer from limited mass transport due to their decreased Brownian motion.[23] For the present study, relatively small particles were selected since they are characterized by a high surface to volume ratio resulting in a high enzyme loading capacity.[24] After the layering of AP and PEs on PLGA particles, DLS and TEM showed slightly different particle sizes. This can be explained by the dry state of the samples analyzed by TEM compared with the liquid state during DLS measurements. Whereas the solid PLGA particles are not influenced by these different states, the usually hydrated and fuzzy layers of strongly charged PEs[25] and enzymes dehydrate and therefore shrink under dry conditions.

The size of PLGA particles increased upon loading with enzymes. This is a consequence of particle aggregation due to a decrease in zeta potential from −40 mV to ≈0. Thus, the decrease in surface charge reduces electrostatic repulsion resulting in the reversible formation of particle aggregates.[26] After the addition of polyelectrolytes, however, the surface charge increased again leading (at least in the case of AP) to dismantling of aggregates.

Classic determination of kinetic parameters following the standard Michaelis–Menten kinetics was originally defined for homogenous systems ("well stirred compartments"), which is not necessarily applicable to nanoparticulate systems where phenomena such as mass diffusion limitations can occur. As a consequence, calculated K_m and V_{max} values of immobilized enzymes are approximations and cannot be compared to the corresponding parameters of free enzymes. Nevertheless, due to its simplicity and a lack of alternatives, the Michaelis–Menten model is, if properly used, still the accepted way for the comparison of kinetic parameters.[27] To validate the used enzyme assays, the activity of free AP and BGal was determined. The measured K_m values for both enzymes correspond to values published in literature.[28,29] Whereas kinetic parameters of free BGal did not change after immobilization, an improved catalytic efficiency of immobilized AP was observed. After immobilization of AP on PLGA particles, the affinity (i.e., K_M value) of AP toward its substrate 4-NPP was 2.5 fold increased and its V_{max} was slightly decreased. This resulted in an overall 1.5 fold increased apparent catalytic efficiency (E_{cat}). After covering the

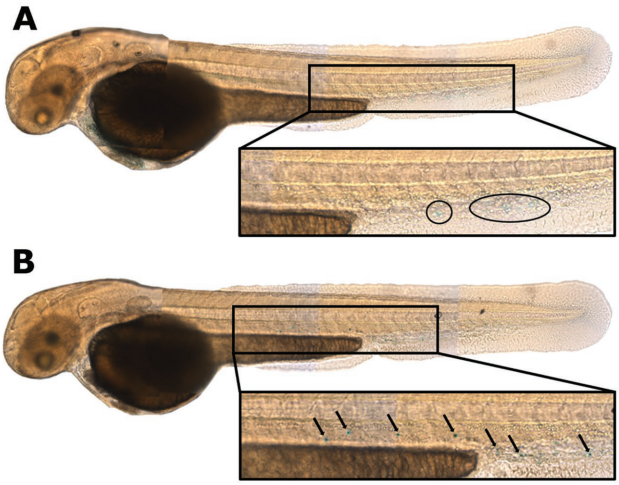

Figure 6. Enzymatic activity in vivo of PLGA BGal particles in the Zebrafish embryo. Free BGal (panel A) and PLGA BGal particles (panel B) were injected into the blood circulation of Zebrafish embryos via the Duct of Cuvier 2 d post fertilization. Arrows indicate areas of enzyme activity, which are characterized by formation of dark blue precipitates. Enzymatic activity was determined 30 min post injection.

immobilized AP with additional layers of PEs, the affinity and the V_{max} decreased but still remained on a higher level as compared to free AP. It is not uncommon to observe an increase in enzyme activity after immobilization. It has been suggested that stabilization of the active conformation or optimized orientation and exposure of the substrate binding site may be beneficial.[4,27] Substrate properties are another possible explanation for the observed changes of enzyme kinetics. 4-NPP, the substrate of AP, is zwitterionic and should therefore interact with the charged PE layer surrounding the enzyme. However, ONPG, the substrate of BGal, is not charged at assay conditions and therefore should only marginally be affected by the enzyme microenvironment.

Increased or unaltered enzyme activity does not have to go hand in hand with improved stability against elevated temperatures or changed pH conditions. BGal showed a decreased thermal stability after immobilization, which could be attributed to a decreased enzyme flexibility. This has previously been reported to be a key factor regarding thermal stability of enzymes.[30] In case of AP, an increased stability of the enzyme toward acidic reaction conditions was observed. It is tempting to speculate that PE act as a buffering system and thereby stabilize the pH of the enzyme microenvironment.[31] Both immobilized enzymes were, without any loss of activity, stored for 30 d at 4 °C and also their reuse with minor loss of activity was possible over at least five cycles of activity assays. This finding was surprising since previous reports by Ratzinger et al. indicated a 75% loss of enzyme activity when enzymes were stored under the same conditions as presented in this publication.[24] This advantage of high storage stability combined with good reusability of our novel cLBL approach is of high importance, especially regarding industrial applications.

The toxicity of PLGA enzyme PE preparations was assessed in two different cell lines. Human liver cancer cells (HEPG2) were used in order to represent the liver as the main organ of metabolism and nanoparticle accumulation. In order to assess nanoparticle safety upon injection, primary endothelial cells (HUVEC) were also incubated with increasing particle concentrations. No statistically significant effects were observed up to particle concentrations of 100 μg mL^{-1}, a dose which is accepted to represent physiologically relevant conditions.[10] Cell viability was significantly decreased only at the highest tested particle concentration of 250 μg mL^{-1}. Nevertheless, the results indicate a weak albeit potential toxicity of the tested formulations, which might be attributed to the two used polyelectrolytes PAH and PSS[8,32] or the crosslinking agent GA.

To get a first insight into stability and activity of PLGA based particles in vivo, zebrafish embryos were used as a relatively simple and easily accessible model system. Different nanoparticles such as liposomes, polystyrene beads, or PLGA have already been successfully tested in this vertebrate model.[33–35] There were no visible signs of acute toxicity upon injection. The subsequently applied staining for enzyme activity resulted in two distinct staining pattern. A diffusive blue color was obtained for free BGal whereas localized and defined blue dye precipitates resulted from PLGA BGal particles. We conclude that our particulate BGal enzyme formulation is active under in vivo conditions. The bright blue spots indicate that PLGA BGal particles remain stable and intact after injection for at least 30 min.

5. Conclusion and Outlook

During this study we developed and characterized a new and improved approach for enzyme immobilization. The described cLbL method is tunable and can be adopted to different enzymes based on their charge at a desired pH. Kinetic experiments revealed differences with respect to the apparent catalytic efficiency of the immobilized enzymes as compared to their unbound counterparts. While this parameter was unchanged or even increased for the tested enzymes, an extrapolation to other enzymes is difficult. However, the proposed test strategies offer the possibility to rapidly assess the performance of such systems. The present system shows a high stability and is therefore suited for industrial applications. In fact, stability of PLGA based particles can be adjusted from weeks to years depending on the ratio of lactic and glycolic acid.[20,36] However, future uses might as well include biomedical applications such as antigen immobilization on nanoparticulate carriers used for vaccination or immobilization of digestion enzymes like lactases or endopeptidases for the treatment of lactose intolerance or celiac disease.[37–39] Preliminary experiments in the zebrafish embryo model indeed demonstrate enzymatic activity in a biological environment (i.e., the blood circulation of a vertebrate). However, for such applications, the stability of the particulate carrier has to be reduced to ensure biotolerability. In addition, the used and potentially toxic crosslinking agent glutaraldehyde should be replaced by a biocompatible cross linking agent such as genipin.[40] Furthermore, the nonbiodegradable polymers PAH and PSS can be replaced by natural compounds such as alginates or chitosan.[41] Thus, the proposed cLbL protocol can be easily adopted for a broad range of applications.

Acknowledgements: The authors are thankful for the financial support of the "Stiftung zur Förderung des pharmazeutischen Nachwuchses in Basel" and the "Freiwillige Akademische Gesellschaft Basel," and declare no conflicts of interests. We thank the team of Prof. M. Affolter for providing zebrafish embryos.

Received: January 11, 2017; Revised: February 22, 2017; Published online: April 7, 2017; DOI: 10.1002/mabi.201700015

Keywords: crosslinking; enzyme immobilization; layer-by-layer; PLGA particles; zebrafish

[1] M. Kataoka, T. Miyakawa, S. Shimizu, M. Tanokura, *Appl. Microbiol. Biotechnol.* **2016**, *100*, 5747.
[2] Z. Grosová, M. Rosenberg, M. Rebros, M. Sipocz, B. Sedlácková, *Biotechnol. Lett.* **2008**, *30*, 763.
[3] Q. Husain, *Crit. Rev. Biotechnol.* **2010**, *30*, 41.
[4] C. Garcia-Galan, Á. Berenguer-Murcia, R. Fernandez-Lafuente, R. C. Rodrigues, *Adv. Synth. Catal.* **2011**, *353*, 2885.
[5] R. A. Sheldon, *Adv. Synth. Catal.* **2007**, *349*, 1289.
[6] S. Ding, A. A. Cargill, I. L. Medintz, J. C. Claussen, *Curr. Opin. Biotechnol.* **2015**, *34*, 242.
[7] G. Decher, J. D. Hong, J. Schmitt, *Thin Solid Films* **1992**, *210*, 831.
[8] O. S. Sakr, G. Borchard, *Biomacromolecules* **2013**, *14*, 2117.
[9] J. C. S. dos Santos, O. Barbosa, C. Ortiz, A. Berenguer-Murcia, R. C. Rodrigues, R. Fernandez-Lafuente, *ChemCatChem* **2015**, *7*, 2413.
[10] H. Kettiger, D. Sen Karaman, L. Schiesser, J. M. Rosenholm, J. Huwyler, *Toxicol. In Vitro Int. J. Publ. Assoc. BIBRA* **2015**, *30*, 355.
[11] R. L. McCall, R. W. Sirianni, *J. Vis. Exp. JoVE* **2013**, 51015, DOI:10.3791/51015.
[12] M. J. Cooney, *Methods Mol. Biol.* **2011**, *679*, 207.
[13] T. Haider, Q. Husain, *Int. J. Pharm.* **2008**, *359*, 1.
[14] W. Jiang, R. K. Gupta, M. C. Deshpande, S. P. Schwendeman, *Adv. Drug Delivery Rev.* **2005**, *57*, 391.
[15] O. Barbosa, C. Ortiz, Á. Berenguer-Murcia, R. Torres, R. C. Rodrigues, R. Fernandez-Lafuente, *RSC Adv.* **2013**, *4*, 1583.
[16] M. Hartmann, X. Kostrov, *Chem. Soc. Rev.* **2013**, *42*, 6277.
[17] J. M. Gómez, M. D. Romero, T. M. Fernández, E. Díez, *Bioprocess Biosyst. Eng.* **2012**, *35*, 1399.
[18] S. Chibowski, M. Knipa, *J. Dispersion Sci. Technol.* **2000**, *21*, 761.
[19] C. Mateo, J. M. Palomo, G. Fernandez-Lorente, J. M. Guisan, R. Fernandez-Lafuente, *Enzyme Microb. Technol.* **2007**, *40*, 1451.
[20] F. Danhier, E. Ansorena, J. M. Silva, R. Coco, A. Le Breton, V. Préat, *J. Controlled Release* **2012**, *161*, 505.
[21] H. K. Makadia, S. J. Siegel, *Polymers* **2011**, *3*, 1377.
[22] C. E. Astete, C. M. Sabliov, *J. Biomater. Sci. Polym. Ed.* **2006**, *17*, 247.
[23] H. Jia, G. Zhu, P. Wang, *Biotechnol. Bioeng.* **2003**, *84*, 406.
[24] G. Ratzinger, X. Wang, M. Wirth, F. Gabor, *J. Controlled Release* **2010**, *147*, 187.
[25] G. Decher, *Science* **1997**, *277*, 1232.
[26] J. Jiang, G. Oberdörster, P. Biswas, *J. Nanoparticle Res.* **2009**, *11*, 77.
[27] B. J. Johnson, W. Russ Algar, A. P. Malanoski, M. G. Ancona, I. L. Medintz, *Nano Today* **2014**, *9*, 102.
[28] S. Gargova, I. Pishtijski, I. Stoilova, *Biotechnol. Biotechnol. Equip.* **1995**, *9*, 47.
[29] C. Marzadori, C. Gessa, S. Ciurli, *Biol. Fertil. Soils* **1998**, *27*, 97.
[30] G. Feller, J. L. Arpigny, E. Narinx, C. Gerday, *Comp. Biochem. Physiol., Part A: Mol. Integr. Physiol.* **1997**, *118*, 495.
[31] E. Katchalski, I. Silman, R. Goldman, *Adv. Enzymol. Relat. Areas Mol. Biol.* **1971**, *34*, 445.
[32] E. Fröhlich, *Int. J. Nanomed.* **2012**, *7*, 5577.
[33] L. Evensen, P. L. Johansen, G. Koster, K. Zhu, L. Herfindal, M. Speth, F. Fenaroli, J. Hildahl, S. Bagherifam, C. Tulotta, *Nanoscale* **2016**, *8*, 862.
[34] F. Fenaroli, D. Westmoreland, J. Benjaminsen, T. Kolstad, F. M. Skjeldal, A. H. Meijer, M. van der Vaart, L. Ulanova, N. Roos, B. Nyström, *ACS Nano* **2014**, *8*, 7014.
[35] J. Yang, Y. Shimada, R. C. L. Olsthoorn, B. E. Snaar-Jagalska, H. P. Spaink, A. Kros, *ACS Nano* **2016**, *10*, 7428.
[36] T. G. Park, *Biomaterials* **1995**, *16*, 1123.
[37] S. A. Ansari, Q. Husain, *Biotechnol. Adv.* **2012**, *30*, 512.
[38] V. E. Bosio, G. A. Islan, Y. N. Martínez, N. Durán, G. R. Castro, *Crit. Rev. Biotechnol.* **2016**, *36*, 447.
[39] I. Caputo, M. Lepretti, S. Martucciello, C. Esposito, I. Caputo, M. Lepretti, S. Martucciello, C. Esposito, *Enzyme Res. Enzyme Res.* **2010**, *2010*, 2e174354.
[40] B. Manickam, R. Sreedharan, M. Elumalai, *Curr. Drug Delivery* **2014**, *11*, 139.
[41] J. Zhou, G. Romero, E. Rojas, L. Ma, S. Moya, C. Gao, *J. Colloid Interface Sci.* **2010**, *345*, 241.

Chapter IV-III

Biomimetic artificial organelles with in vitro and in vivo activity triggered by reduction in microenvironment

Tomaž Einfalt, Dominik Witzigmann, Christoph Edlinger, **Sandro Sieber**, Roland Goers, Adrian Najer, Ozana Fischer, Mariana Spulber, Jörg Huwyler, Cornelia G. Palivan

Manuscript: Nature Communications (2018) [44]

Highlights: In the future, the use of enzyme loaded biomimetic artificial organelles (AO) as cellular implants could help to treat metabolic diseases caused by deficient or mutated enzymes. This study focused on the generation of such a polymer based AOs including a protein gate to control the access of substrate to the enzyme. The stimuli sensitive opening of the protein gate as well as the AO activity upon cell uptake were shown *in vitro*. After testing the AOs under static (*in vitro*) conditions, live zebrafish embryos were used to assess the enzyme's performance under dynamic biological conditions including blood flow and the presence of plasma proteins. Due to its favorable optical properties, the zebrafish model allowed to characterize the behavior of enzyme loaded AOs *in vivo* in a relatively simple experimental set-up. This reflects an important step during the development of such sophisticated systems, since they are designed to be once used in patients.

nature COMMUNICATIONS

ARTICLE

DOI: 10.1038/s41467-018-03560-x OPEN

Biomimetic artificial organelles with in vitro and in vivo activity triggered by reduction in microenvironment

T. Einfalt[1,2], D. Witzigmann[2], C. Edlinger[1], S. Sieber[2], R. Goers[1,3], A. Najer[1], M. Spulber[1], O. Onaca-Fischer[1], J. Huwyler[2] & C.G. Palivan[1]

Despite tremendous efforts to develop stimuli-responsive enzyme delivery systems, their efficacy has been mostly limited to in vitro applications. Here we introduce, by using an approach of combining biomolecules with artificial compartments, a biomimetic strategy to create artificial organelles (AOs) as cellular implants, with endogenous stimuli-triggered enzymatic activity. AOs are produced by inserting protein gates in the membrane of polymersomes containing horseradish peroxidase enzymes selected as a model for natures own enzymes involved in the redox homoeostasis. The inserted protein gates are engineered by attaching molecular caps to genetically modified channel porins in order to induce redox-responsive control of the molecular flow through the membrane. AOs preserve their structure and are activated by intracellular glutathione levels in vitro. Importantly, our biomimetic AOs are functional in vivo in zebrafish embryos, which demonstrates the feasibility of using AOs as cellular implants in living organisms. This opens new perspectives for patient-oriented protein therapy.

[1] Department of Chemistry, University of Basel, Klingelbergstrasse 80, CH-4056 Basel, Switzerland. [2] Department of Pharmaceutical Sciences, Division of Pharmaceutical Technology, University of Basel, Klingelbergstrasse 50, CH-4056 Basel, Switzerland. [3] Department of Biosystems Science and Engineering, ETH Zürich, Mattenstrasse 26, CH-4058 Basel, Switzerland. Correspondence and requests for materials should be addressed to C.G.P. (email: Cornelia.Palivan@unibas.ch)

Mimicking biological processes by engineering biomimetic nanostructures represents an elegant strategy for addressing problems in various scientific fields, including materials science, chemistry, electronics and medicine[1–3]. By applying a bottom-up biomimetic design (i.e. arranging molecules at the nanoscale via self-assembly), it is possible to combine individual biological units, known for their sophisticated structure and activity (e.g. proteins, lipids, DNA), with robust synthetic materials (e.g. polymers, porous silica surfaces, nanoparticles). This serves to develop nanoscale biomimics with enhanced properties and functionalities[2,4–8] with potential for a wide range of applications (sensitive biosensing, patient tailored therapeutics, detoxification of environmental pollutants, etc.)[6,9–12].

Of particular interest are two different concepts that are currently the main focus in this research field: (i) artificial organelles (AOs) based on an essential need to offer efficient solutions for improved therapy and diagnostics[13] and (ii) protocell systems intended to provide simple models of cells for understanding various internal processes[2,14]. These concepts are complementary, one is essential for advancing medical applications (AOs) whereas the second concept mimics cell behaviour based on very simple systems (protocells). Similarly, as in nature, the sizes of the compartments are completely different: while AOs have nanometre range sizes, protocells reach the micrometre range. Even though protocells represent the first archetypes of an artificial cell, they still inherently lack the material variety and responsiveness found in the most basic cellular structures, and have not yet been investigated in vivo to determine whether they preserve their functionality. AOs are particularly attractive nanoscale biomimics because they can provide a required compound/signal, detoxify harmful compounds, or change cellular conditions and reactions. AOs are based on compartmentalisation of active compounds (enzymes, proteins, catalysts, mimics) within artificial nanoassemblies that reach and function in the intracellular environment, and thus serve as simplified mimics of nature's own organelles. Various examples of systems with potential to act as AOs have been developed based on liposomes, porous silica nanoparticles and polymer compartments (polymersomes) in combination with biomacromolecules[13–16]. However, very few have been evaluated in vitro to assess their in situ cellular functionality[6,15–18], and to the best of our knowledge, none has been assessed in vivo. In vivo functionality of such AOs is a crucial factor that is necessary to demonstrate that the concept of AOs is feasible in living organisms, and thus AOs can act as cellular implants.

Notably, natural organelles have membranes, since inside cells compartmentalisation is essential to provide confined reaction spaces for complex metabolic reactions. Therefore, an AO should preserve the compartmentalisation as a key factor in mimicking natural organelles. In this respect, polymer compartments, named polymersomes, are ideal candidates for the creation of AOs, because of their hollow spherical structure with a membrane serving as a border for an inner cavity and their greater mechanical stability than lipid-based compartments, i.e. liposomes[19,20]. In addition, the chemical nature of the copolymers provides the possibility of controlling their properties (e.g. size, stability biocompatibility, flexibility, stimuli-responsiveness)[2,21]. Polymersomes have been shown to serve either as carriers for biomolecules and mimics[1,2,21,22], or more recently for development of nanoreactors and even the generation of AOs[2,6,11,23]. A key factor for supporting in situ reactions[20,24] is to render the polymersome membranes permeable for substrates and products. An elegant approach bioinspired from the cell membrane is to incorporate biopores and membrane proteins[25–27]. Selective membrane permeability towards protons and ions is achieved by inserting small pore forming peptides[27], while membrane proteins induce size-dependent cut-off permeability[26,28–30] or even mediate the diffusion of specific molecules[10,31]. The few reported AOs exhibit enzymatic reactions either inside porous polymersomes[6,16,32] or inside polymersomes equipped with channel porins[17], with the aim of emulating cellular pathways (e.g. reactive oxygen species detoxification or glucose oxidation).

Another essential factor for tuning AO functionality is a triggered response to its environment, as, for example, the redox state of the cell, which regulates various processes involved in cellular signalling pathways[33,34]. While there are a few reported examples of polymersomes with a stimuli-responsive permeable membrane based on the incorporation of genetically or chemically modified membrane proteins[35], only two of them have served for the design of catalytic nanocompartments[36,37], and none has been used to control reactions inside AOs. Activation of the AO by a specific endogenous stimulus inside cells represents a challenging step in development of functional AOs in vivo. The design of AOs with triggered activity and the demonstration of their in vivo functionality represent necessary steps towards the creation of cell implants, and the provision of smart solutions for personalised medicine by a straightforward change of the biomolecules inside the AOs.

Here, we present a strategy for designing AOs with an in situ enzymatic reaction that is triggered by the presence of an intracellular stimulus, and demonstrate in vitro and in vivo functionality. Genetically modified outer membrane protein F (OmpF) porins were incorporated into polymersomes to induce redox responsiveness to the membrane, and horseradish peroxidase (HRP) simultaneously encapsulated inside their cavity to provide a source of the AO functionality. Such AOs with functionality triggered by intracellular changes represent an advance in mimicking that of nature's own organelles, especially those that are involved in the redox equilibrium of the cellular homoeostasis. Amphiphilic block copolymers poly(2-methyloxazoline)-*block*-poly(dimethylsiloxane)-*block*-poly(2-methyloxazoline) ($PMOXA_m$-$PDMS_n$-$PMOXA_m$) were used to self-assemble into polymersomes, because such copolymers have already been shown to form membranes in which biopores and membrane proteins can be successfully inserted[36–38], and to be taken up and to be non-toxic to various cell lines[17]. Once inserted in the polymersome membrane, the modified OmpF porins act as protein gates independent of the insertion direction, i.e. orientation in the membrane[36,37,39,40], and trigger the in situ HRP enzymatic reaction when a stimulus is present in the cellular environment. HRP was selected as model enzyme, because peroxidases play a significant role in the redox homoeostasis of cells and cell apoptosis[41]. This strategy of providing stimuli-responsiveness to polymersome membranes neither affects the membrane integrity, as for stimuli-responsive synthetic membranes of compartments[42], nor the size and structure of the polymersomes. Crucial steps were the evaluation of AO toxicity and functionality in human epithelial tumour cells (HeLa cells), and once these were established in vivo tolerability, preservation of the AO structure, and in situ regulation of the activity of the encapsulated enzyme in the vertebrate zebrafish embryo (ZFE) model.

Results

Bioengineering protein gates by modification of channel porins. The key factors in the design of AOs with activity triggered by changes in environmental conditions are on-demand permeability of the compartment towards enzymatic substrates/products and structural integrity of the polymersome, which mimics that of natural organelles. Therefore, our biomimetic strategy

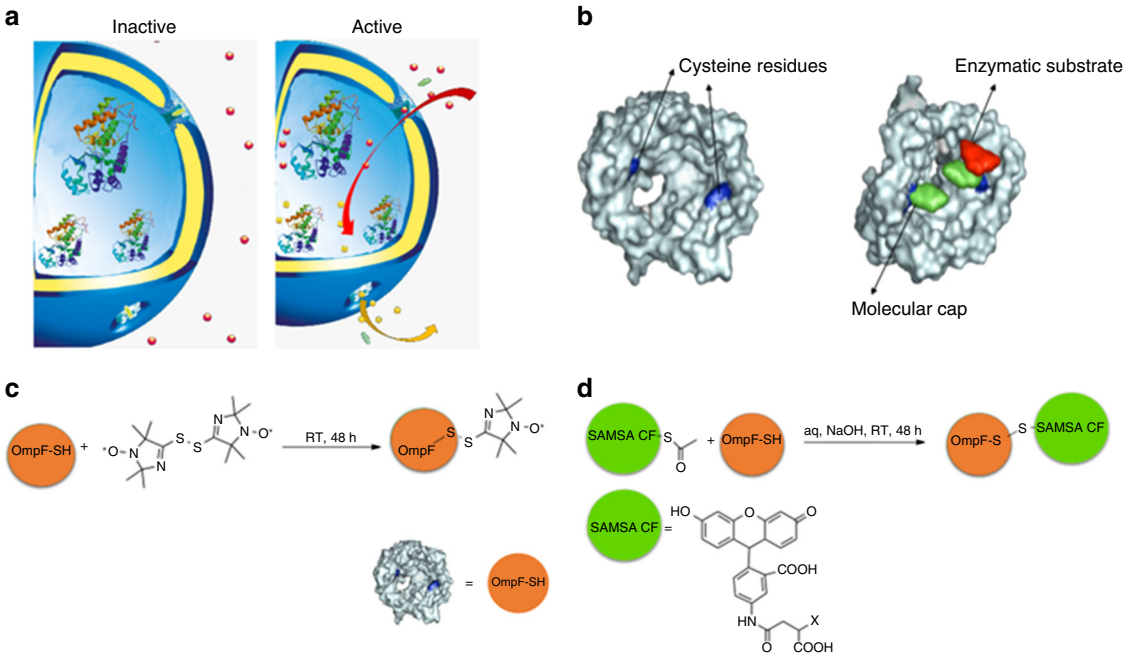

Fig. 1 Engineering stimuli-responsive OmpF. **a** Schematic representation of modified OmpF acting as a gate in catalytic nanocompartments. **b** Molecular representation of the OmpF-M cysteine mutant[37]. **c** Chemical modification of OmpF-M cysteine mutant with the spin probe bis-(2,2,5,5-tetramethyl-3-imidazoline-1-oxyl-4-yl) disulphide. **d** Chemical modification of OmpF-M cysteine mutant with the fluorophore SAMSA-CF

aimed to equip $PMOXA_6$-$PDMS_{44}$-$PMOXA_6$ polymersome membranes with protein gates that are responsive to changes in glutathione (GSH) concentrations in intracellular environments, while preserving the structure of the nanocompartment (Fig. 1a).

It has been shown very recently that chemical modifications of amino acid residues at key locations of the OmpF porin backbone influence the translocation of substrates through the pore in a pH-responsive manner[36]. Here we go one step further by using a double mutant of OmpF[37] to attach molecular caps to genetically introduced cysteine residues that serve to block/unblock the OmpF pore upon changes in redox potential, which occur when the system enters the intracellular microenvironment (Fig. 1b). In contrast to polymersomes with membranes containing OmpF genetically modified to release a payload in reductive conditions[35], our system controls the overall functionality of the AOs. We chose a cysteine double mutant of OmpF (OmpF-M) because cysteine residues, replacing the amino acids K89 and R270, were expected to form reduction-sensitive disulphide bonds with molecules selected to serve as molecular caps. These molecular caps remain attached in mildly oxidising environments and block substrate diffusion through the pore, whereas in the presence of reducing agents, such as intracellular GSH, their cleavage restores normal passage of small molecular weight molecules (<600 Da) through the OmpF pores. This approach mimics pathways of metabolism regulation, where proteins within the membranes of natural cell organelles are irreversibly activated or deactivated on demand[43,44]. In addition, we were interested in developing an irreversible protein gate in order to be able to rapidly evaluate the functionality of the organelle in vivo.

The ability of the cysteine residues of OmpF-M to form disulphide bonds with thiol groups of small molecular weight molecules was examined by two complementary assays, one using a suitable spin probe (bis-(2,2,5,5-tetramethyl-3-imidazoline-1-oxyl-4-yl) disulphide) and the second using the fluorescent dye SAMSA fluorescein (SAMSA-CF) (Fig. 1c, d).

Coupling reaction of the molecular caps with the cysteine residues of OmpF-M resulted in the formation of OmpF conjugates (OmpF-S-S-CF for OmpF conjugated with SAMSA-CF, and OmpF-S-S-NO for OmpF conjugated with bis-(2,2,5,5-tetramethyl-3-imidazoline-1-oxyl-4-yl) disulphide), respectively.

Binding of the thiol reactive spin probe to the protein was evaluated by a combination of LC-MS-MS and electron paramagnetic resonance (EPR). Upon in-gel digestion of the porin[45], LC-MS-MS analysis of the peptide fragments indicated a very high labelling efficiency of the spin probe to cysteine residues of the OmpF-M (96 ± 4%). Standard deviation is based on three measurements. The EPR spectrum of the bis-(2,2,5,5-tetramethyl-3-imidazoline-1-oxyl-4-yl) disulphide in phosphate-buffered saline (PBS) at 298 K consists of an isotropic triplet pattern (Supplementary Figure 1) with a hyperfine coupling a_N value of 15.8 G that is similar to reported values for analogous nitroxide probes where no aggregation was present[46,47]. In contrast, OmpF-S-S-NO gave a broad anisotropic EPR spectrum with no isotropic component, and is similar to that reported for 5-DSA in lipid bilayers or cholesterol aqueous solutions[48]. This EPR spectrum indicates hindered rotation of the nitroxide probe[49] after binding to the OmpF mutant (OmpF-S-S-NO), and demonstrates successful binding of the bis-(2,2,5,5-tetramethyl-3-imidazoline-1-oxyl-4-yl) disulphide to the modified OmpF mutant (Fig. 2a).

After exposure of OmpF-S-S-NO to 10 mM DTT an isotropic EPR spectrum (a_N value of 15.9 G) characteristic of the freely rotating spin probe was observed (Fig. 2b). This clearly demonstrates that the nitroxide spin probe that is bound to thiol groups of the OmpF-M under oxidative conditions is cleaved in a reductive environment.

SAMSA-CF (Thermo Fischer Scientific) was selected as a molecular cap because its size (molecular weight 521.49 Da) was expected to block the OmpF-M pore, and because of its ability

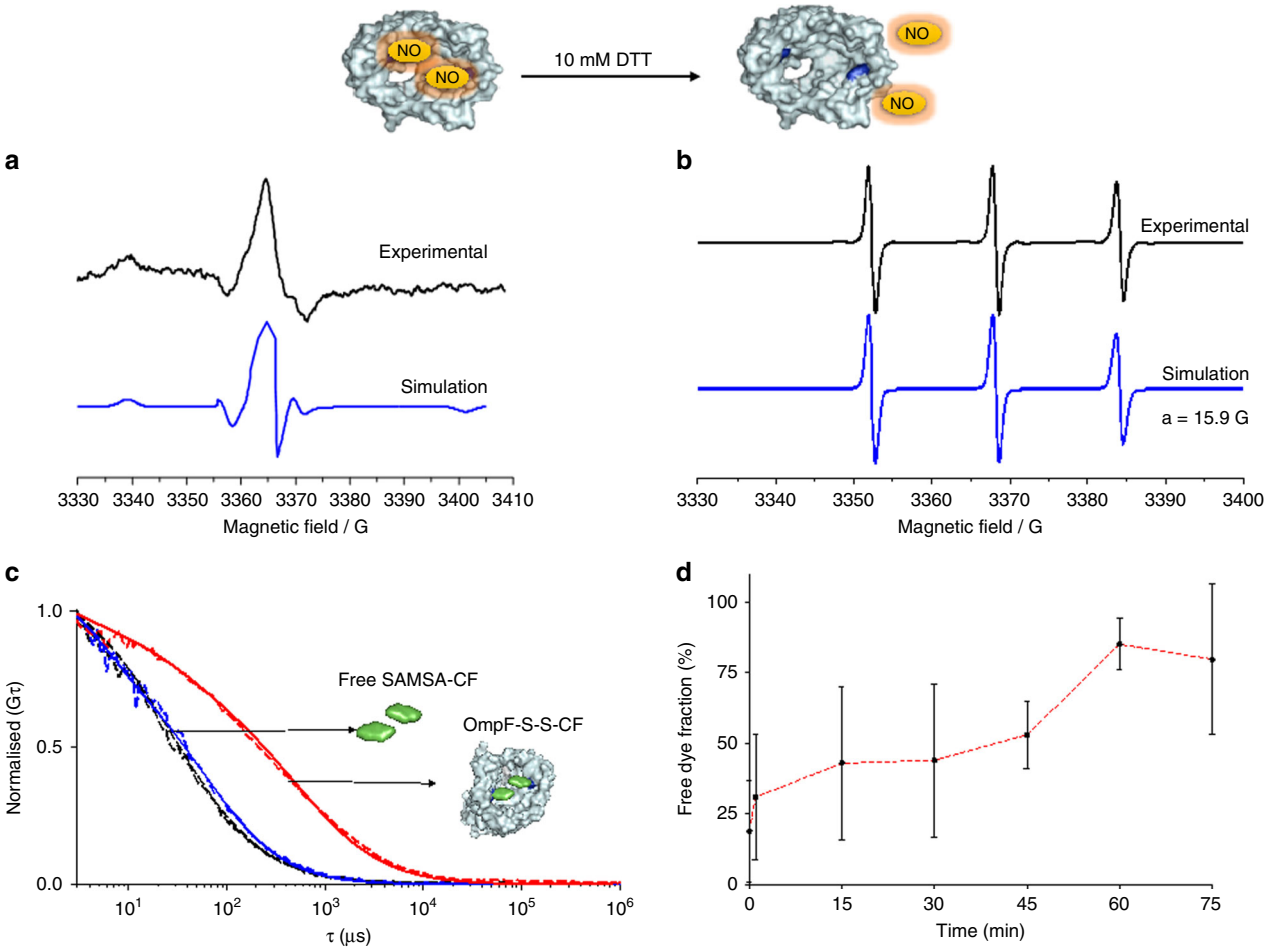

Fig. 2 Characterisation of stimuli-responsive OmpF Panel. **a** EPR spectra of bis-(2,2,5,5-tetramethyl-3-imidazoline-1-oxyl-4-yl) disulphide-labelled OmpF-M experimental (black) and simulated (blue) and **b** bis-(2,2,5,5-tetramethyl-3-imidazoline-1-oxyl-4-yl) disulphide-labelled OmpF-M in 1% OG incubated with 10 mM DTT experimental (black) and simulated (blue). **c** Normalised FCS autocorrelation curves for SAMSA-CF in PBS (black), SAMSA-CF in 1% OG (blue) and OmpF-S-S-CF in 1% OG (Red). Dotted line—experimental autocorrelation curves, full line—fit. **d** SAMSA-CF release kinetics from OmpF-M in 30 mM GSH, 1% OG, as measured by FCS and analysed with a two-component fit. Error bars show standard deviations from 60 measurements

to form cleavable disulphide bonds[50]. Thus, attachment of SAMSA-CF to OmpF-M introduces a stimuli-responsiveness to the pore, and therefore to the polymersome membrane when OmpF-S-S-CF is inserted. In addition, the fluorescent properties of SAMSA-CF allow pore modification to be analysed by a combination of sodium dodecyl sulfate polyacrylamide gel electrophoresis (SDS-PAGE) and fluorescence correlation spectroscopy (FCS).

LC-MS-MS analysis of the peptide fragments indicated a high labelling degree of OmpF-M (81 ± 31%). In addition, a fluorescent band appeared in the SDS-PAGE gel when SAMSA-CF was conjugated to OmpF-M, whereas the OmpF wild type did not interact with the fluorophore; this fluorescent band supports the formation of OmpF-S-S-CF (Supplementary Figure 2). To mimic the intracellular reductive environment, where the GSH concentration is kept at a constantly high level (10 mM GSH) by cytosolic enzymes[51], such as glutathione reductase, we studied the behaviour of the reduction-responsive molecular caps in a similar environment. Because of the absence of a steady-state concentration and constant regeneration of GSH, we used 30 mM GSH to mimic the intracellular steady state of GSH. In SDS-PAGE the fluorescent band disappeared when the OmpF-S-S-CF was mixed with GSH, indicating successful cleavage of the molecular cap under reductive conditions (Supplementary Figure 2).

The binding of SAMSA-CF to OmpF-M cysteine residues was also evaluated by FCS, because it allows the determination of diffusion coefficients, which are correlated to possible interactions of the fluorescent molecules with supramolecular assemblies, such as polymersomes, liposomes and nanoparticles in the pico- to nanomolar concentration region[9,21,47–52]. We compared the molecular brightness and diffusion times of SAMSA-CF in PBS (pH 7.4), SAMSA-CF in 1% OG PBS (pH 7.4) and SAMSA-CF bound to OmpF (OmpF-S-S-CF) in 1% OG PBS (pH 7.4) (Fig. 2c). A labelling efficiency of an average of two SAMSA-CF molecules per monomer was calculated by comparing the molecular brightness (counts per molecule, CPM in kHz) of SAMSA-CF (2.2 ± 0.7 kHz) with that of protein bound to SAMSA-CF (4.8 ± 0.6 kHz) (Fig. 2c). Standard deviations in molecular brightness are based on individual measurements of the same probe ($n = 60$). In contrast, wild-type OmpF treated similarly to the cysteine mutant OmpF-M, did not present any fluorescence after purification, and there was therefore no binding of SAMSA-CF to OmpF-WT. To determine the kinetics of OmpF pore opening, we used FCS to evaluate the cleavage of SAMSA-CF from labelled OmpF-M upon addition of 30 mM GSH at pH

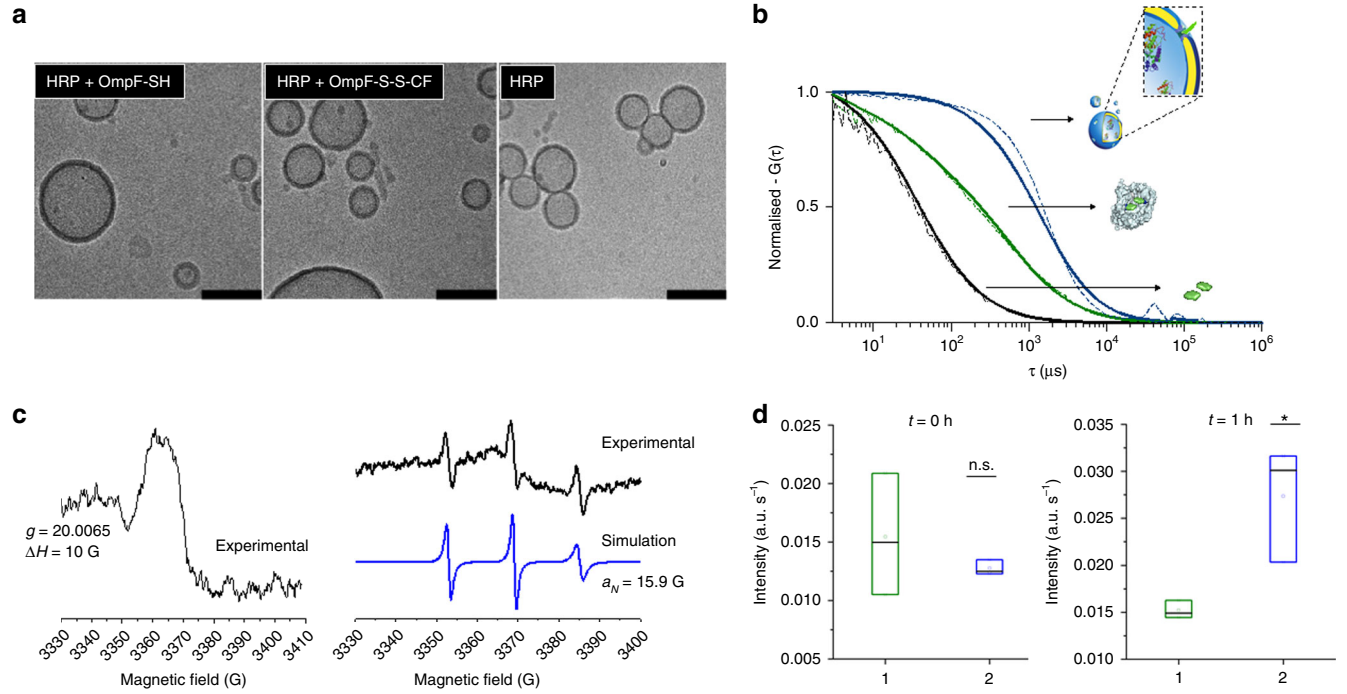

Fig. 3 Characterisation of stimuli-responsive catalytic nanocompartments. **a** Cryo-TEM micrographs of: (left) polymersomes loaded with HRP and equipped with OmpF-SH, (middle) polymersomes loaded with HRP and equipped with OmpF-S-S-CF, and (right) polymersomes loaded with HRP without OmpF. Scale bar = 100 nm. **b** Normalised FCS autocorrelation curves of SAMSA-CF in PBS (black) and OmpF-S-S-CF in the membrane of polymersomes (blue). Dotted line = experimental autocorrelation curves, solid line = fitted curve. Curves normalised to 1 to facilitate comparison. **c** Left panel: EPR spectrum of bis-(2,2,5,5-tetramethyl-3-imidazoline-1-oxyl-4-yl) disulphide-labelled OmpF reconstituted in PMOXA-PDMS-PMOXA polymersomes (black line). **c** Right panel: bis-(2,2,5,5-tetramethyl-3-imidazoline-1-oxyl-4-yl) disulphide-labelled OmpF reconstituted in PMOXA-PDMS-PMOXA polymersomes and incubated with 10 mM DTT experimental (black line) and simulated (blue line). **d** Amplex Ultra Red conversion of HRP-loaded polymersomes: immediately after addition of 30 mM GSH (left), and 1 h after addition of 30 mM GSH (right). OmpF-S-S-CF equipped HRP-loaded polymersomes (green) and OmpF-SH equipped HRP-loaded polymersomes (blue). Error bars present standard deviations in activity between three separately prepared catalytic nanocompartments ($n = 3$)

7.4 by FCS, and analysed the results by a two-component fit. Due to cleavage of the disulphide bonds between the dye and the OmpF-M, the percentage of the free dye increased over time to 85 ± 9%, with a plateau after 1 h (Fig. 2d, Supplementary Figure 3). Standard deviations in the percentage of the free dye are based on individual measurements of the same probe ($n = 60$) during a set time point.

Catalytic enzyme-polymersome nanocompartments with protein gates. The effect of different concentrations of individual components on the functionality of the final system has already been reported for the insertion of OmpF wild type into PMOXA-PDMS-PMOXA polymersomes and enzyme encapsulation within the inner cavity[53]. Here we used the optimised conditions and adapted them for the modified OmpF and our AOs. $PMOXA_6$-$PDMS_{44}$-$PMOXA_6$ copolymers spontaneously self-assembled in the presence of HRP, HRP and OmpF-S-S-CF, or HRP and OmpF-S-S-NO, and hollow spherical compartments were identified by cryo-TEM (Fig. 3a, Supplementary Figure 4). These spherical polymer assemblies were demonstrated by light scattering to be polymersomes with: R_H of 99 ± 2 nm for HRP-loaded polymersomes containing OmpF-S-S-CF, R_H of 89 ± 4 nm for polymersomes loaded with HRP and equipped with OmpF-SH, and R_H of 101 ± 1 nm for HRP-loaded polymersomes (Supplementary Tables 1 and 2). Standard deviations were determined based on Pearson's coefficient of the correlation function and the Guinier fitted one. The polymersome architecture was not affected by 30 mM GSH, with structural parameters ρ ($\rho = R_G/R_H$) values in the range 0.90–0.96, which confirmed a hollow sphere morphology[54] (Supplementary Tables 1 and 2). HRP-loaded polymersomes, HRP-loaded polymersomes equipped with OmpF-SH, and HRP-loaded polymersomes equipped with OmpF-S-S-CF all preserved their size and did not aggregate after 2 weeks storage at 4 °C in the dark (Supplementary Figures 5–7).

Insertion of channel proteins into enzyme-loaded $PMOXA_6$-$PDMS_{44}$-$PMOXA_6$ polymersomes is critical for in situ activity of the encapsulated enzyme, because the channels allow substrates and products of the enzymatic reaction to pass through the membrane. As OmpF is a pore protein, its functionality is independent of its orientation inside the membrane, and the channel porin mediates the flow of molecules up to 600 Da.

We evaluated OmpF-S-S-CF and OmpF-S-S-NO insertion into the polymersome membrane using FCS and EPR, respectively. A diffusion time of $\tau_d = 2573 \pm 960$ μs was obtained by FCS for polymersomes with reconstituted OmpF-S-S-CF, indicating that the modified protein gates were successfully inserted into the polymer membranes (free OmpF-S-S-CF in 1% OG has $\tau_d = 588 \pm 261$ μs). Standard deviation of the diffusion times is acquired from individual measurements ($n = 60$). By comparing the molecular brightness of the free fluorophore (CPM = 2.2 ± 0.7 kHz) and the OmpF-S-S-CF equipped polymersomes (CPM = 18.9 ± 11.1 kHz), it was calculated that there were five OmpF-S-S-CF porins/polymersome; these values are similar to those reported previously for wild-type OmpF[36] (Fig. 3b).

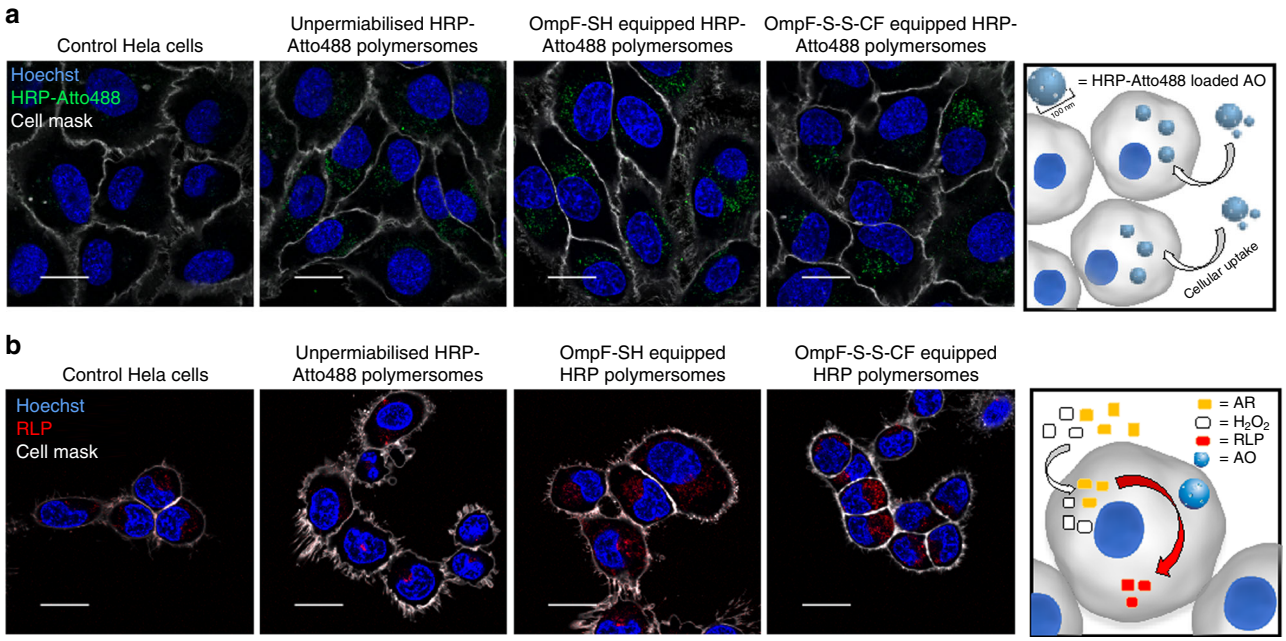

Fig. 4 Cellular uptake and intracellular activation of AOs. **a** Confocal fluorescence micrographs of HeLa cells showing cellular uptake of fluorescently labelled HRP-loaded polymersomes and AOs loaded with fluorescently labelled HRP. Scale bar: 10 µm. **b** Cellular uptake and intracellular activation of fluorescently labelled HRP-loaded polymersomes and fluorescently labelled HRP-loaded AOs. Blue signal: Hoechst 33342 nucleus stain. Grey signal: CellMask Deep Red Plasma membrane stain. Green signal: Atto488 HRP. Red signal: resorufin-like product (RLP). Scale bar 20 µm

HRP-loaded polymersomes containing OmpF-S-S-NO produced a broad EPR spectrum (Fig. 3c), indicative of low mobility, a result similar to that reported for 5-DSA and 16-DSA inserted in polymersomes membranes[55]. However, when these HRP-loaded polymersomes containing OmpF-S-S-NO were exposed to reductive conditions (10 mM DTT), an isotropic EPR spectrum ($a_N = 15.9$ G) was observed superimposed on the broad peak, indicating successful cleavage of some of the nitroxide spin probe from the OmpF (Fig. 3c).

Stimuli-responsiveness of the catalytic nanocompartments. The effect of an external stimulus on the functionality of the HRP-loaded polymersomes equipped with OmpF-S-S-CF was evaluated by their response to the addition of 30 mM GSH. The fluorescent signal associated with formation of a resorufin-like product (RLP) during the in situ enzymatic reaction in the presence of Amplex Ultra Red (AR) as a substrate for HRP was measured spectroscopically[56]. Enzymatic turnover of the AR substrate was significantly lower with HRP-loaded polymersomes equipped with OmpF-S-S-CF (by up to 36±4%) compared to HRP-loaded polymersomes equipped with OmpF-SH, suggesting that the molecular cap is sufficient to reduce the passage of small molecules through the pore. Note that the very low activity of HRP-loaded polymersomes without inserted OmpF was taken into account for background correction. Standard deviation is based on three measurements of separately prepared catalytic nanocompartments. Addition of 30 mM GSH to the system increased the activity of HRP-loaded polymersomes equipped with OmpF-S-S-CF up to that of HRP-loaded polymersomes equipped with OmpF-SH. This indicates that reduction of the disulphide bridge between the attached SAMSA-CF cap and cysteine residues of the OmpF-M successfully restored the OmpF-M pore permeability for the substrate of the enzyme by releasing the molecular cap (Fig. 3d, Supplementary Figures 8 and 9).

Nanocompartments as stimuli-responsive AOs. Here we have gone a step further by developing stimulus-triggered AOs, whose functionality is modulated by the responsiveness of modified OmpF porins inserted in the membrane of the catalytic nanocompartments. Previously designed AOs successfully overcame the first barrier of cell membranes and escaped from endosomes[17]. As PMOXA-PDMS-PMOXA polymersomes are stable at acidic pH[27,36], we consider that this will favour a successful lysosomal/endosomal escape during the recycling of lysosomes and endosomes.

Possible internalisation mechanisms of various PMOXA-PDMS-PMOXA-based polymersomes and their high cytocompatibility in various cell lines have already been reported[17,57–59]. Here, we evaluated the cytocompatibility of the biomimetic AOs by testing their cellular toxicity using the 3-(4,5-dimethylthiazol-2-yl)-5-(3-carboxymethoxyphenyl)-2-(4-sulphophenyl)-2H-tetrazolium (MTS) assay before studying their intracellular activation and enzymatic activity. Notably, their biocompatibility at the cellular level was shown by the absence of any decrease in viability in HeLa cells even after 48 h (i.e. polymer concentration ranging from 0.25 to 0.75 mg ml^{-1}) (Supplementary Figure 10).

In order to study cellular internalisation and intracellular localisation, we first conjugated HRP with Atto488 (HRP-Atto488) and Atto647 (HRP-Atto647), respectively (Supplementary Figure 11). Then we encapsulated labelled-HRP inside the cavity of polymersomes, polymersomes equipped with OmpF-S-S-CF, and polymersomes equipped with OmpF-SH. Cellular uptake assays in HeLa cells indicated successful internalisation resulting in a particulate intracellular staining pattern with increasing intensity in a time-dependent manner from 8 to 24 h (Fig. 4a, Supplementary Figures 12 and 13). The quantitative analysis indicates that after 24 h AOs did not co-localise with early endosomes or lysosomes, confirming successful intracellular endosomal escape (Supplementary Figure 14)[17]. Localised HRP-Atto488 signals confirmed the intracellular integrity of the polymersomes. In sharp contrast, if cells were treated with a

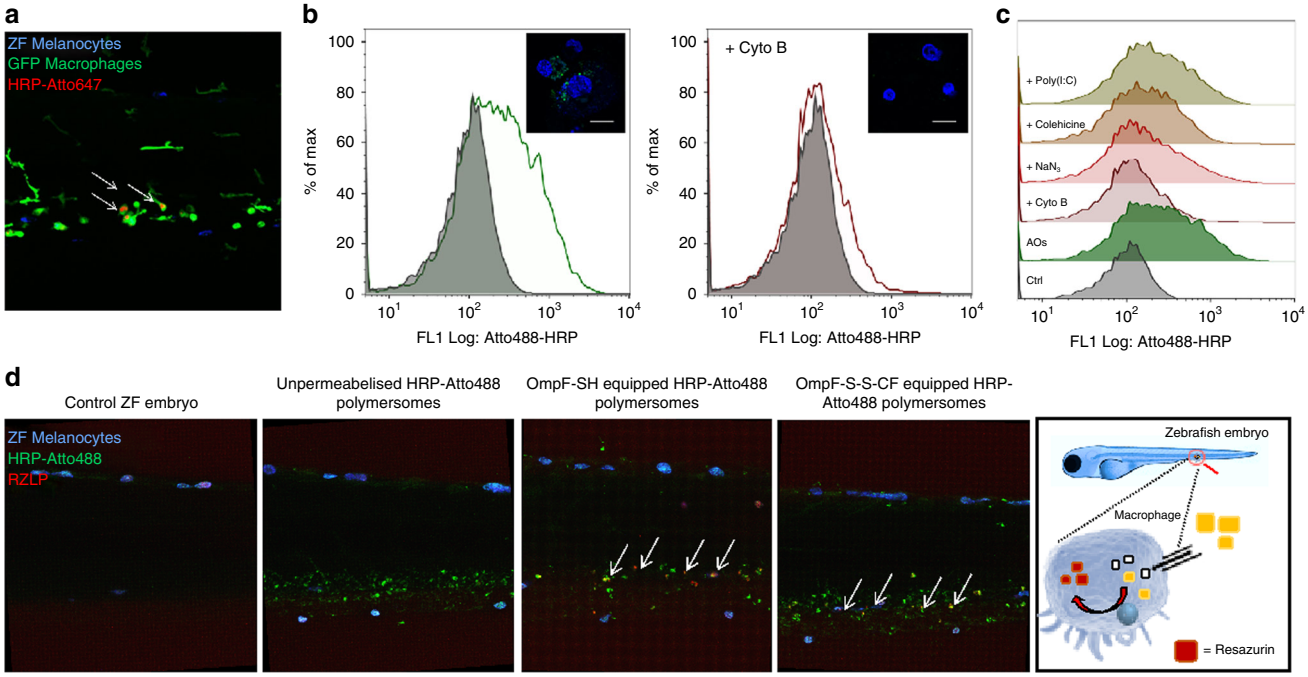

Fig. 5 Internalisation and activity of AOs in macrophages in vitro and in vivo. **a** Localisation of AOs in ZFE. Lateral view of the ZFE injected with HRP-Atto647-loaded AOs equipped with OmpF-S-S-CF. Arrowheads: Localisation of AOs. Blue signal: ZFE melanocytes. Green signal: GFP macrophages. Red signal: Atto647-loaded AOs. **b** Phagocytosis of AOs by human macrophage differentiated THP-1 cells in vitro. Qualitative (inset) and quantitative analysis of macrophage differentiated THP-1 cells incubated with AOs loaded with Atto488-labelled HRP without addition of inhibitors (left), and in the presence of phagocytosis inhibitor cytochalasin B (Cyto B) (right). Blue signal: Hoechst 33342 nucleus stain. Green signal: Atto488 HRP. Scale bar inset 20 µm. **c** Quantification of AOs in the presence of different pharmacological pathway inhibitors by flow cytometry: polyinosinic acid (Poly(I:C)), colchicines, cytochalasin B (Cyto B) and sodium azide (NaN_3). **d** In vivo ZFE biodistribution and activity of AOs—lateral view of the ZFE cross-section. Blue signal: ZFE melanocytes. Green signal: HRP-Atto488. Red signal: Resazurin-like product (RZLP). Arrows show regions of enzymatic activity of AOs

membrane disrupting agent (i.e. 0.1% saponin) (Supplementary Figure 15), polymersome membranes were affected and resulted in an intracellular cytoplasmic distribution of HRP-Atto488.

The capacity of the AOs to act within target cells in a stimuli-responsive manner was investigated by using a combination of confocal laser scanning microscopy (CLSM) and flow cytometry to evaluate their potential to respond to increased intracellular GSH levels. HeLa cells were incubated with HRP-loaded polymersomes without OmpF or with HRP-loaded polymersomes equipped with either OmpF-S-S-CF (AOs) or with OmpF-SH. Extracellular polymersomes were removed by washing before imaging the intracellular activity of AOs. Cells were incubated with a 1:1 substrate mixture of H_2O_2 and AR to allow the intracellular deposition, and finally conversion of AR into its RLP by AOs. Note that both hydrogen peroxide and AR pass through the cellular membrane via passive partitioning, while they do not penetrate the membrane of polymersomes (Supplementary Figure 9). In contrast to untreated cells, or those incubated with HRP-loaded polymersomes without OmpF, a significant increase of intracellular fluorescence was observed with AOs equipped with OmpF-S-S-CF or OmpF-SH (Fig. 4b, Supplementary Figure 16). A similar trend was observed when AR turnover was quantified by flow cytometry (Supplementary Figure 17). The strong fluorescent signal for AOs based on HRP-loaded polymersomes equipped with OmpF-S-S-CF confirmed successful intracellular cleavage of the molecular cap attached to OmpF-M, and subsequent activation of the AOs within the intracellular environment of the HeLa cells (Supplementary Figure 17).

In vivo activity of stimuli-responsive AOs. As a step further to obtaining insight into their safety, tolerability and performance in vivo, AOs were studied in a ZFE model. ZFEs were selected, because of their recognition as a complementary vertebrate animal model for applications, such as compound screening in drug discovery, toxicological studies and recombinant disease models[60–62]. Compared to rodent in vivo models, the ZFE offers unique advantages: (i) high reproducibility, (ii) low costs, (iii) high level of genetic homology to humans, (iv) availability of transgenic lines and (v) most importantly for the evaluation of AO, optical transparency. Due to their optical transparency, ZFE provide the possibility of imaging fluorescently-tagged objects and fluorescent processes in vivo at a high resolution over time[63] (Supplementary Figure 18). Our approach offers the possibility of gaining detailed insight into the circulation behaviour of AOs and subsequent enzymatic reactions as we reported recently for nano-particulate drug delivery systems in vivo[64]. In order to follow the biodistribution of AOs, we injected intravenously via the duct of Cuvier HRP-Atto488-loaded polymersomes with membranes equipped with OmpF-S-S-CF or with OmpF-SH, respectively. No acute toxicity, such as change in behaviour i.e. mobility, seizures, heart failure or other toxic effects such as malformations, denaturation of tissue fluids or yolk mass was observed in ZFE injected with AOs after 24 h. ZFE analysed 2 h post intravenous injection of all types of AOs containing Atto488 conjugated HRP showed a distinct fluorescent staining pattern (Supplementary Figure 19) in the posterior cardinal vein region, and we hypothesise that polymersomes are recognised by the ZFE early immune system and

are subsequently taken up by macrophages[65]. The remarkable recognition of polymersome-based AOs by the ZFE immune system was confirmed by the colocalisation of AOs loaded with Atto647-conjugated HRP (Atto647-HRP) injected into transgenic ZFE specifically expressing eGFP in macrophages (Fig. 5a, Supplementary Figure 20). In strong contrast to AOs loaded with Atto647-HRP, the free Atto647-HRP enzyme did not show significant macrophage colocalisation after 24 h, even when Atto647-HRP was injected at concentrations of 0.2 mg ml^{-1} (Supplementary Figure 21). Notably, only macrophages in circulation were targeted and not tissue resident macrophages (i.e. star shaped).

Once cellular internalisation of AOs by the early immune system of ZFE was successful in vivo, we explored the uptake rate, exact intracellular localisation and internalisation mechanisms of AOs in immune cells in vitro by using human macrophage differentiated THP-1 cells. AOs internalisation started as early as 30 min, and a strong internalisation by immune cells was achieved after 3 h (Supplementary Figure 22), with increasing uptake rates at higher time points. As THP-1 cells are immature macrophages with reduced phagocytotic capacity, a higher uptake rate of AOs is possible for mature (primary) macrophages in vitro and in vivo.[66] Importantly, all macrophage uptake studies were performed in the presence of serum proteins to mimic physiological conditions in vivo because opsonisation of nanoparticles by serum proteins can highly influence their interaction with cells.[67] To obtain a mechanistic understanding of the internalisation process, THP-1 macrophages were pre-treated with different pharmacological pathway inhibitors.[67] We used inhibitors with specific inhibition profiles: (i) polyinosinic acid to block scavenger receptors, (ii) colchicine to inhibit pinocytosis, (iii) cytochalasin B as phagocytosis inhibitor and (iv) sodium azide to inhibit all energy-dependent uptake processes. Cells not incubated with Atto488 HRP-loaded AOs served as a control. A 1.28-fold increase in the mean fluorescence intensity (MFI) was observed by flow cytometry analysis of the cells incubated with Atto488 HRP-loaded AOs for 6 h, which indicates internalisation of AOs by THP-1 macrophages. The uptake of AOs by macrophages was significantly inhibited by cytochalasin B (a 0.13-fold increase in MFI) and in a lower degree by sodium azide (0.43-fold increase in MFI), which indicates an energy-dependent phagocytotic internalisation process (Fig. 5b, c). On the contrary, polyinosinic acid did not inhibit the AOs uptake, suggesting little or no involvement of the scavenger receptor in the internalisation mechanism of AOs (Fig. 5c).

The internalisation process analysed by CLSM using LysoTracker™ Red DND-99 as a reporter for the lysosomal compartments indicates that AOs co-localise with lysosomal compartments during their internalisation process (Supplementary Figure 23). Interestingly, we could not detect a lysosome signal (lysotracker) 24 h after incubation of macrophages with AOs, suggesting the presence of an intracellular lysosomal escape mechanism once the AOs are taken-up by macrophages (Supplementary Figure 23). After internalisation in macrophages, the signals associated with Atto488-HRP-loaded AOs in lysosomal compartments changed to larger intracellular vesicular signals. This suggests an expansion of the AO-bearing lysosomal compartments before the AOs are released into the cytosol. For an exact mechanism by which AOs escape the lysosomal compartment and interact with cellular membranes, further investigations are planned but they are beyond the scope of this study.

In order to assess in vivo stability, integrity and functionality of AOs when exposed to the conditions in the macrophage microenvironment, we performed a second injection of AOs together with the enzyme substrate AR. Injection of the co-substrate H_2O_2 in combination with AR was not necessary, since macrophages have the ability to produce H_2O_2. In addition, co-injection of H_2O_2 resulted in a red colouring of the whole blood volume, presumably due to haemolysis and thus interaction of AR with erythrocyte enzymes or haemoglobin[66] (Supplementary Figure 24). Distinct colocalisation within macrophages of the converted AR oxidation product was found only for HRP-Atto488-loaded AOs equipped with either OmpF-SH or OmpF-S-S-CF: the molecular cap of OmpF-S-S-CF was cleaved in vivo leading to activation of the AOs. In sharp contrast, HRP-Atto488-loaded polymersomes without OmpF remained inactive, demonstrating that the polymersome membrane is sufficiently robust to remain intact in ZFE macrophages (Fig. 5d).

Discussion

Design and development of AOs able to function inside cells and support the natural organelles is a necessary step towards the creation of cellular implants. Complementary as a concept to that of protocells, AOs respond to an essential need to offer efficient solutions for improved therapeutic and diagnostic options. Previously reported examples of AOs were based on confined spaces for reactions by compartmentalisation of enzymes inside nanoscale assemblies, but were not able to function in a stimuli-responsive manner. Here, we introduce a strategy to develop AOs with functionality that can be switched on by changes in the cellular microenvironment. These stimuli-responsive AOs are created by simultaneous encapsulation of an enzyme involved in the cellular redox homoeostasis and insertion of a genetically engineered channel porin to serve as a protein gate that triggers the enzymatic activity inside AOs.

Our AOs preserved their architecture and were activated after reaching the cellular microenvironment. More exciting, they are functional in a vertebrate ZFE model, which proves that the concept of AOs as cellular implants is feasible in vivo. Furthermore, stability, biocompatibility and low toxicity of AOs represent real advantages for medical applications compared to existing solutions for enzyme replacement, such as direct enzyme delivery and transfection[67].

We believe that in the future, the high versatility of our strategy will allow straightforward development of a large variety of AOs for specific medical applications by changing the encapsulated enzymes and/or of the stimuli-responsive property of the protein gates. However, a careful selection of substrates is required to overcome the limited ability to transit through the plasma membrane of specific substrates, which are commonly used in bulk enzymatic reactions.

This example of AOs activated by changes in cellular microenvironment and that remains functional in vivo, opens the perspective of complex in situ reactions inside AOs, and represents an important advance towards the generation of multifunctional systems that will support the development of personalised medicine.

Methods

OmpF expression and extraction. The OmpF K89 R270 cysteine mutant and the OmpF wild type were expressed in BL21 (DE3) Omp8 *Escherichia coli* cells; detailed procedure is described in Supplementary Methods.[42] The extracted fraction was analysed by a 4–15% Mini-PROTEAN® TGX™ Precast SDS (Bio-Rad Laboratories, USA) gel to confirm the protein purity and the protein concentration was determined using a BCA assay kit (Pierce Chemical Co, Rockford, USA). OmpF was stored at 4 °C in 3% OG at a concentration of 1.2 mg ml^{-1} for several weeks.

OmpF modification with SAMSA fluorescein (OmpF-S-S-CF). The OmpF K89 R270 double cysteine mutant was modified by disulphide binding of SAMSA fluorescein to the free cysteine residues. The same reaction was also performed in

the presence of OmpF wild type in 3% octyl-glucopyranoside (OG) (Anatrace, USA) and 3% OG in order to serve as controls. Twenty microlitres of 959 µM SAMSA-CF (5-((2-(and-3)-*S*-(acetylmercapto) succinoyl) amino) fluorescein) (Thermo Fischer Scientific) dissolved in 5% DMSO, 1% OG in PBS buffer was added to 400 µl of 0.4 mg ml^{-1} OmpF. The mixture was shaken in dark conditions for 30 min, when deprotection of SAMSA-CF was initiated by adjusting the pH of the solution to 8.5 with 0.5 M NaOH. The reaction mixture was incubated and shaken in the absence of light for 24 h at room temperature, after which another 5 µl of 959 µM SAMA fluorescein was added. Twenty-four hours after the second addition of SAMSA fluorescein the protein was purified from the reaction mixture by washing 25 times with 1% OG in PBS pH 7.4 in Amicon Ultra-0.5 ml centrifugal filters for protein purification and concentration, molecular cut-off: 30 kDA (Millipore) (10 min at 13,000 RPM). The volume was adjusted to 475 µl with PBS pH 7.4, and the protein concentration was determined by UV-Vis spectroscopy. Forty microlitres of the purified protein fraction was taken for FCS analysis and SDS gel electrophoresis. The volume was adjusted to 500 µl and the protein was dialysed against 1 l of 0.05 % OG in PBS for 16 h and twice against PBS for 2 h using 14 kDa Membra-Cel^{TM} (Carl Roth, Germany) dialysis membranes. The protein concentration was verified by UV-VIS (A280) (Thermo Fischer Scientific, Switzerland).

OmpF modification with (bis-(2,2,5,5-tetramethyl-3-imidazoline-1-oxyl-4-yl) disulphide) (OmpF-S-S-NO*). The OmpF K89 R270 double cysteine mutant was modified by disulphide binding of (bis-(2,2,5,5-tetramethyl-3-imidazoline-1-oxyl-4-yl) disulphide) (Noxygen, Germany) to the free cysteine residues. The same reaction was also done in presence of OmpF wild type in 3% OG PBS and 3% OG PBS in order to serve as controls for unspecific binding of (bis-(2,2,5,5-tetramethyl-3-imidazoline-1-oxyl-4-yl) disulphide) to wild-type OmpF and unspecific interactions with OG micelles. Twenty microlitres of dissolved (bis-(2,2,5,5-tetramethyl-3-imidazoline-1-oxyl-4-yl) disulphide) (1.4 mM) in 4% DMSO, 1% OG in PBS buffer were added to 400 µl of 0.4 mg ml^{-1} OmpF and mixed. The reaction was performed as described above for OmpF-S-S-CF. Twenty-four hours after the second addition of (bis-(2,2,5,5-tetramethyl-3-imidazoline-1-oxyl-4-yl) disulphide) the conjugated protein was purified from the reaction mixture by washing it 25 times with 1% OG in PBS at pH 7.4 using Amicon Ultra-0.5 ml centrifugal filters for protein purification and concentration; molecular cut-off: 30kDA (Millipore). The volume was adjusted to 475 µl using PBS at pH 7.4, and the protein concentration was determined by UV-Vis spectroscopy. Forty microlitres of the purified protein fraction was taken for EPR analysis. The volume was adjusted to 500 µl and the protein dialysed against 1 l of 0.05 % OG in PBS for 16 h and twice against PBS for 2 h using 14 kDa Membra-Cel^{TM} (Carl Roth, Germany) dialysis membranes. The protein concentration was verified by UV–VIS (A280) (Thermo Fischer Scientific, Switzerland).

Characterisation of SAMSA fluorescein conjugated OmpF. A 4–15% Mini-PROTEAN® TGX™ Precast SDS (Bio-Rad Laboratories, USA) gel polyacrylamide gel was used, then samples were mixed with BN-PAGE loading buffer and 15 µl of the final OmpF solution was added to the gel. To show the effect of GSH, separate probes were incubated with the loading buffer supplemented with 30 mM GSH. The gels were run at 200 V for 45 min. (Supplementary Figure 2), and scanned unstained and stained with Coomasie blue.

Fluorescence correlation spectroscopy. All FCS measurements were performed using a Zeiss LSM 510-META/Confocor2 (Carl Zeiss, Jena, Germany) with an argon laser (488 nm), and ×40 water immersion C-Apochromat Objective lens. Measurements were performed at room temperature using a sample volume of 20 µl on a covered Lab-Tek Nunc® Lab-Tek® II chambered cover glass (Nalage Nunc International). Measurements were recorded over 3 s, and each measurement was repeated 60 times. The structural parameter and the diffusion time of the free dye in PBS pH 7.4 (SAMSA-CF) were determined independently. The autocorrelation function was calculated using a software correlator, and fitted with a one component fit (LSM 510 META-ConfoCor2 System). Detailed description of the FCS measurements and calculations are described in the Supplementary Methods.

Preparation of reduction-triggered catalytic polymersomes. To produce reduction-triggered catalytic PMOXA-*b*-PDMS-*b*-PMOXA nanocompartments, triblock copolymer films with different subsets of Outer membrane protein F (OmpF) were rehydrated with HRP. The detailed preparation technique and control experiments are described in the Supplementary Methods.

Characterisation of catalytic nanocompartments. The size and morphology of the stimuli-responsive catalytic nanocompartments were characterised by a combination of light scattering (SLS, DLS) and cryogenic transmission electron microscopy (Cryo-TEM). Detailed procedures are described in detail in the Supplementary Methods.

Enzymatic assay. The emission fluorescence intensity was determined using a LS 55 Fluorescence Spectrometer (Perkin Elmer). Samples were incubated with a final concentration of 30 mM GSH in PBS at pH 7.4, and the pH was kept at this value. For the measurement, 10 µl of the samples mixed with GSH were transferred to 220 µl of the reaction mixture (4.5 µM H_2O_2 and 3.4 µM AR) in PBS at pH 7.4. The reaction mixture was excited at 530 nm and the emission intensity was monitored at 590 nm. Fluorescence was expressed as relative fluorescence units and was measured at the same instrument setting in all experiments. The detailed procedure is described in the Supplementary Methods.

Cell toxicity assay. The [3-(4,5-dimethyl-2-yl)-5-(3-carboxymethoxyphenyl)-2-(4-sulphophenyl)-2H-tetrazolium (MTS) assay (Promega) was used to determine cell viability. HeLa cells were seeded in a triplicate at a density of 2.5×10^3 cells per well in a 96-well plate. Cells were cultured for 24 h in Dulbecco's modified Eagle's medium (DMEM) growth medium (supplemented with 10% foetal calf serum, penicillin (100 units ml^{-1}) and streptomycin (100 µg ml^{-1})). After 24 h, the medium 100 µl aliquots containing the corresponding concentration of samples [0.25, 0.5 and 0.75 mg ml^{-1}] were added to the cell medium. Cells incubated only in medium served as control (100%). After 24 h of incubation 20 µl of MTS solution was added to each well. The plates were incubated for 1 h at 37 °C, and absorption was measured at $\lambda = 490$ nm. The quantity of formazan product as measured by absorbance at 490 nm is directly proportional to the number of living cells in the culture. Absorption of cells where no nanoparticles were added served as 100%.

24 h uptake of catalytic nanocompartments. HeLa (epitheloid cervix carcinoma, human; ATCC, CCL-2) cells were cultured at a density of 3×10^4 cells per well in an eight-well Lab-Tek (NalgeNunc International, USA) for 24 h in DMEM growth medium supplemented with 10% foetal calf serum, penicillin (100 units ml^{-1}) and streptomycin (100 µg ml^{-1}) to allow attachment to the surface. After attachment, the medium was removed and catalytic nanocompartments were added to a final polymer concentration of 0.5 mg ml^{-1}. Cells were washed twice before being imaged at the respective time points.

Flow cytometry analysis of AO activity. HeLa (epitheloid cervix carcinoma, human; ATCC, CCL-2) cells were seeded in a well of a 24-well plate (8×10^4 cells per well) and cultured in DMEM containing 10% foetal calf serum, penicillin (100 units ml^{-1}) and streptomycin (100 µg ml^{-1})) for 24 h at 37 °C in a humidified CO_2 incubator. Then the medium was exchanged and polymersome solution was added to a final concentration of 0.5 mg ml^{-1} for another 24 h. Cells were washed three times with PBS, trypsinised, centrifuged, washed, centrifuged and then suspended in 1 ml PBS. AR/H_2O_2 was added to a final concentration of 10 µM, and after 2 h, flow cytometry analysis was performed using a BD FACSCanto II flow cytometer (BD Bioscience, USA). Doublets were excluded using FSC and SSC detectors, single cells were excited at 561 nm and the emission was detected in FL5 (586/15; Resorufin Channel). A total of 10,000 single cells for each sample were analysed, and data processed using Flow Jo VX software (TreeStar, Ashland, OR).

Intracellular stability of AO. HeLa (epitheloid cervix carcinoma, human; ATCC, CCL-2) cells were seeded at a density of 3×10^4 cells ml^{-1} onto poly-D-lysine-coated glass coverslips. Cells were cultured for 24 h in DMEM growth medium (supplemented with 10% foetal calf serum, penicillin (100 units ml^{-1}) and streptomycin (100 µg ml^{-1})). After attachment to the surface, the medium was removed and catalytic nanocompartments were added to a final polymer concentration of 0.5 mg ml^{-1}. Cells were incubated for an additional 24 h in the medium, then washed three times with PBS and fixed with 4% PFA for 15 min. After a neutralisation step using 50 mM NH_4Cl, cells were either treated with PBS (control) or 0.1% saponin for 10 min at room temperature. After additional washing steps, cell nuclei were counterstained for 10 min using Hoechst 33342 (0.5 µg ml^{-1}). Finally cells were embedded in Vectashield antifade mounting media. CLSM was performed using an Olympus FV-1000 inverted microscope (Olympus Ltd, Tokyo, Japan) equipped with a ×60 UPlanFL N oil-immersion objective (numerical aperture 1.40). Cells were excited at 405 nm (Hoechst 33342) and 488 nm (Atto488-HRP), and the fluorescence signal was collected using Kalman modus between 425 and 475 nm and 500 and 600 nm, respectively. To minimise spectral cross talk, the samples were scanned using sequential mode. The laser settings were adjusted depending on the treatment. Images were processed using the Fiji open source image processing package of ImageJ.

Intracellular localisation of AO. HeLa (epitheloid cervix carcinoma, human; ATCC, CCL-2) cells were seeded at a density of 3×10^4 cells per well onto poly-D-lysine-coated glass coverslips. Cells were cultured for 24 h in DMEM growth medium (supplemented with 10% foetal calf serum, penicillin (100 units ml^{-1}) and streptomycin (100 µg ml^{-1})) to allow attachment to the surface. After attachment, the medium was removed and catalytic nanocompartments were added to a final polymer concentration of 0.5 mg ml^{-1}. After 24 h cells were washed three times with PBS and then fixed for 15 min using 4% PFA. After a neutralisation step using 50 mM NH_4Cl, cells were incubated with either rabbit polyclonal anti-EEA1 (ab2900, Abcam) (1:1000) or anti-LAMP1 (ab24170, Abcam) antibody (1:1000) for early endosome or lysosome staining, respectively[58]. The cells were washed with PBS, followed by staining with the secondary goat anti-rabbit polyclonal

Dylight633-labelled antibody (1:1000; #35562, Thermo Fisher Scientific). Cell nuclei were counterstained for 10 min using Hoechst 33342 (0.5 μg ml^{-1}). Finally, cells were embedded in Vectashield antifade mounting media. CLSM was performed using an Olympus FV-1000 inverted microscope described above. Z-stacks were taken using Kalman modus and a step size of 450 nm. Cells were excited at 405 nm (Hoechst 33342), 488 nm (Atto488-HRP), and 633 nm (Early Endosome/Lysosome). The fluorescence signal was collected between 425 and 475, 500 and 600, and 655 and 755 nm, respectively, by scanning in the sequential mode, and processed as described above.

Colocalisation of polymersomes with markers of early endosome (EEA1) or lysosome (LAMP1) were carried out using the JaCoP plug-in in the Fiji software. Pearson's correlation coefficient (PCC), Mander's coefficients (M1/M2, using thresholds of $A = 200$ and $B = 180$), and Costes' randomisation-based colocalisation (200 randomisation rounds) were used to assess the extent of colocalisation.

In cellulo activity of AOs by CLSM. HeLa cells (epitheloid cervix carcinoma, human; ATCC, CCL-2) were cultured at a density of 3×10^4 cells per well in an eight-well Lab-Tek (NalgeNunc International, USA) for 24 h in DMEM growth medium (supplemented with 10% foetal calf serum, penicillin (100 units ml^{-1}) and streptomycin (100 μg ml^{-1}) to allow attachment to the surface. After attachment, the medium was removed and catalytic nanocompartments were added to a final polymer concentration of 0.25 mg ml^{-1}. Cells were then incubated for an additional 24 h in medium, washed twice with PBS and AR/H_2O_2 added in the ratio of 1:1 to a final concentration of 10 μM in DMEM-based growth medium. After 30 min, cells were washed three times with PBS and their nuclei counterstained for 10 min using Hoechst 33342 (0.5 μg ml^{-1}). Cells were washed twice with D-PBS and cultured in DMEM. CellMask Deep Red Plasma membrane stain (0.5 μl ml^{-1}) was added and cells were analysed after 5 min. CLSM was performed as described in the previous section. The laser settings for RLP, the photomultiplier tube gain and the pinhole settings were kept constant during the analysis. Images were processed using Olympus FluoView software (v3.1, Olympus).

In vivo activity of AOs. Standard ZFE culture medium at pH 7.4 was prepared at final concentrations of 5 mM sodium chloride, 0.25 mM potassium chloride, 0.5 mM magnesium sulphate, 0.15 mM potassium dihydrogen phosphate, 0.05 mM sodium phosphate dibasic, 0.5 mM calcium chloride, 0.71 mM sodium bicarbonate and 0.001% (w/v) methylene blue.

Collected eggs from adult ABC/TU ZFE (wild type) and EGFPs843 ZFE (GFP-macrophage line) were kept in ZFE culture medium at 28 °C. PTU (0.03 mg ml^{-1}) was added 1-day post fertilisation (dpf) in order to avoid pigment cell formation. Three different enzyme-loaded polymersomes were injected into 2-dpf ZFE according to an adapted protocol originally designed for microangiography. ZFE were anaesthetised using 0.01% tricaine (w/v) and cast into 0.3% (w/v) agarose containing the same amount of tricaine. Immobilised ZFE were injected with either with 3 nl of 0.2 mg ml^{-1} free HRP or 3 nl AO solution (5 mg ml^{-1}), removed from the agarose and kept in ZFE culture medium containing PTU for 24 h. Then, a second injection of 1 nl AR (78 μM) was performed following the same procedure. As control experiments, ZFE were injected with the enzymatic substrate AR and AR mixed with H_2O_2 without previous AO injection. Fluorescence imaging of injected ZFE was performed using an Olympus FV1000 confocal microscope (Olympus Schweiz AG, Volketswil, Switzerland). ZFE were excited at 488 nm (Atto488 HRP), 559 nm (Melanocytes) and 635 nm (Resazurin-like product) and the fluorescence signal was collected between 500 and 530, 575 and 620, and 655 and 755 nm, respectively.

Monocyte cell culture and differentiation to macrophages. THP-1 cells (ATCC, TIB 202) were cultured at a starting density of 2×10^5 cells ml^{-1} in Roswell Park Memorial Institute (RPMI-1640) medium containing 10% FCS, penicillin (100 units ml^{-1})/streptomycin (100 μg ml^{-1}), 10 mM HEPES, 1% sodium pyruvate and 0.05 mM mercaptoethanol. For uptake studies, THP-1 cells were seeded at a density of 5.5×10^4 cells per well onto poly-D-lysine-coated Ibidi 8-Well μ-Slides or 2×10^5 cells per ml into a 12-well plate (TPP, Switzerland) for CLSM or flow cytometry, respectively. Differentiation of human monocytic cell line THP-1 to macrophages was induced 24 h after seeding using 200 nM phorbol 12-myristate 13-acetate for 72 h.

Uptake study using pathway inhibitors. The uptake mechanism of Atto488-HRP-loaded polymersomes equipped with OmpF-S-S-CF into THP-1 macrophages was investigated using different pharmacological pathway inhibitors[67]. Cells were pre-incubated using 10 μg ml^{-1} cytochalasin B (phagocytosis) for 2 h, 0.1% sodium azide (energy-dependent uptake process) for 30 min, 100 μg ml^{-1} colchicine (pinocytosis) for 2 h and 2.5 μg ml^{-1} polyinosinic acid (scavenger receptor) for 30 min, and then treated with Atto488-HRP-loaded polymersomes.

Qualitative uptake of AOs observed by CLSM. Macrophage differentiated THP-1 cells were incubated with Atto488-HRP-loaded polymersomes equipped with OmpF-S-S-CF at a final polymer concentration of 0.25 mg ml^{-1} for specific time points as indicated. LysoTracker Red DND-99 (Invitrogen) was added to cells 1 h before imaging at a concentration of 50 nM when indicated. Cell nuclei were counterstained using Hoechst 33342 (2.5 μg ml^{-1}). Cell membranes were stained using CellMask Deep Red Plasma membrane stain (0.5 μl ml^{-1}) when indicated directly before imaging. Live cell imaging was performed as described in the previous section using an Olympus FV-1000 inverted microscope (Olympus Ltd, Tokyo, Japan) equipped with a ×60 UPlanFL N oil-immersion objective (numerical aperture 1.40). Orange colour indicated colocalisation of polymersomes with lysosomes (LysoTracker Red DND-99).

Quantitative uptake studies by flow cytometry. Differentiated THP-1 cells were incubated with Atto488-HRP-loaded polymersomes equipped with OmpF-S-S-CF at a final polymer concentration of 0.25 mg ml^{-1} for specific time points as indicated, or in the presence of different pharmacological pathway inhibitors for 6 h. Flow cytometry analysis was performed using a BD FACSCanto II flow cytometer (BD Bioscience, USA) as described in the previous section.

Ethical regulations. All procedures on live zebrafish embryos (Danio rerio) were carried out following the Swiss legislation on animal welfare.

Data availability. The data that support the findings of this study are included in the Supplementary Information; the remaining data are available from the corresponding author upon reasonable request.

Received: 25 May 2017 Accepted: 23 February 2018
Published online: 19 March 2018

References

1. Küchler, A., Yoshimoto, M., Luginbühl, S., Mavelli, F. & Walde, P. Enzymatic reactions in confined environments. *Nat. Nanotechnol.* **11**, 409–420 (2016).
2. Palivan, C. G. et al. Bioinspired polymer vesicles and membranes for biological and medical applications. *Chem. Soc. Rev.* **45**, 377–411 (2016).
3. Grzybowski, B. A. & Huck, W. T. S. The nanotechnology of life-inspired systems. *Nat. Nanotechnol.* **11**, 585–592 (2016).
4. Xiao, K., Wen, L. & Jiang, L. Biomimetic solid-state nanochannels: from fundamental research to practical applications. *Small* **12**, 2810–2831 (2016).
5. Yoo, J.-W., Irvine, D. J., Discher, D. E. & Mitragotri, S. Bio-inspired, bioengineered and biomimetic drug delivery carriers. *Nat. Rev. Drug Discov.* **10**, 521–535 (2011).
6. Balasubramanian, V. et al. Biomimetic Engineering Using Cancer Cell Membranes for Designing Compartmentalised Nanoreactors with Organelle-Like Functions. *Adv. Mater.* **29**, doi: https://dx.doi.org/10.1002/adma.201605375 (2017)
7. Parodi, A. et al. Synthetic nanoparticles functionalised with biomimetic leukocyte membranes possess cell-like functions. *Nat. Nanotechnol.* **8**, 61–68 (2013).
8. Brea, R. J., Rudd, A. K. & Devaraj, N. K. Nonenzymatic biomimetic remodeling of phospholipids in synthetic liposomes. *Proc. Natl. Acad. Sci. USA* **113**, 8589–8594 (2016).
9. Najer, A. et al. Nanomimics of host cell membranes block invasion and expose invasive malaria parasites. *ACS Nano* **8**, 12560–12571 (2014).
10. Zhang, X. et al. Active surfaces engineered by immobilizing protein-polymer nanoreactors for selectively detecting sugar alcohols. *Biomaterials* **89**, 79–88 (2016).
11. Baumann, P., Balasubramanian, V., Onaca-Fischer, O., Sienkiewicz, A. & Palivan, C. G. Light-responsive polymer nanoreactors: a source of reactive oxygen species on demand. *Nanoscale* **5**, 217–224 (2013).
12. Burns, J. R., Seifert, A., Fertig, N. & Howorka, S. A biomimetic DNA-based channel for the ligand-controlled transport of charged molecular cargo across a biological membrane. *Nat. Nanotechnol.* **11**, 152–156 (2016).
13. Palivan, C. G., Fischer-Onaca, O., Delcea, M., Itel, F. & Meier, W. Protein–polymer nanoreactors for medical applications. *Chem. Soc. Rev.* **41**, 2800 (2012).
14. Hammer, D. A. & Kamat, N. P. Towards an artificial cell. *FEBS Lett.* **586**, 2882–2890 (2012).
15. Thingholm, B., Schattling, P., Zhang, Y. & Städler, B. Subcompartmentalised nanoreactors as artificial organelle with intracellular activity. *Small* **12**, 1806–1814 (2016).
16. Godoy Gallardo, M., Labay, C., Jansman, M. M. T., Ek, P. K. & Hosta-Rigau, L. Intracellular microreactors as artificial organelles to conduct multiple enzymatic reactions simultaneously. *Adv. Health. Mater.* **6**, doi: https://dx.doi.org/10.1002/adhm.201601190 (2017).
17. Tanner, P., Balasubramanian, V. & Palivan, C. G. Aiding nature's organelles: artificial peroxisomes play their role. *Nano Lett.* **13**, 2875–2883 (2013).

18. Zhang, Y., Baekgaard Laursen, M. & Städler, B. Small subcompartmentalised microreactors as support for hepatocytes. *Adv. Healthc. Mater.* **6**, 1601141 (2017).
19. Discher, B. M., Hammer, D. A., Bates, F. S. & Discher, D. E. Polymer vesicles in various media. *Curr. Opin. Colloid Interface Sci.* **5**, 125–131 (2000).
20. Discher, B. M. et al. Polymerosome: though vesicles made from diblock copolymers. *Science* **284**, 1143–1146 (1999).
21. Gunkel-Grabole, G. et al. Polymeric 3D nano-architectures for transport and delivery of therapeutically relevant biomacromolecules. *Biomater. Sci.* **3**, 25–40 (2015).
22. Itel, F. et al. Molecular organisation and dynamics in polymersome membranes: a lateral diffusion study. *Macromolecules* **47**, 7588–7596 (2014).
23. Baumann, P., Spulber, M., Fischer, O., Car, A. & Meier, W. Investigation of horseradish peroxidase kinetics in an 'organelle-like' environment. *Small* **13**, doi: https://doi.org/10.1002/smll.201603943 (2017).
24. Dzieciol, A. J. & Mann, S. Designs for life: protocell models in the laboratory. *Chem. Soc. Rev.* **41**, 79–85 (2012).
25. Garni, M., Thamboo, S., Schoenenberger, C.-A. & Palivan, C. G. Biopores/membrane proteins in synthetic polymer membranes. *Biochim. Biophys. Acta* **1859**, 619–638 (2017).
26. Nardin, C., Widmer, J., Winterhalter, M. & Meier, W. Amphiphilic block copolymer nanocontainers as bioreactors. *Eur. Phys. J. E* **4**, 403–410 (2001).
27. Lomora, M. et al. Polymersomes with engineered ion selective permeability as stimuli-responsive nanocompartments with preserved architecture. *Biomaterials* **53**, 406–414 (2015).
28. Graff, A., Sauer, M., Van Gelder, P. & Meier, W. Virus-assisted loading of polymer nanocontainer. *Proc. Natl. Acad. Sci. USA* **99**, 5064–5068 (2002).
29. Kumar, M., Habel, J. E. O., Shen, Y.-X., Meier, W. P. & Walz, T. High-density reconstitution of functional water channels into vesicular and planar block copolymer membranes. *J. Am. Chem. Soc.* **134**, 18631–18637 (2012).
30. Muhammad, N., Dworeck, T., Fioroni, M. & Schwaneberg, U. Engineering of the E. coli Outer Membrane Protein FhuA to overcome the hydrophobic mismatch in thick polymeric membranes. *J. Nanobiotechnol.* **9**, 8 (2011).
31. Kumar, M., Grzelakowski, M., Zilles, J., Clark, M. & Meier, W. Highly permeable polymeric membranes based on the incorporation of the functional water channel protein Aquaporin Z. *Proc. Natl. Acad. Sci. USA* **104**, 20719–20724 (2007).
32. Peters, R. J. R. W. et al. Cascade reactions in multicompartmentalised polymersomes. *Angew. Chem. Int. Ed.* **53**, 146–150 (2013).
33. Hatori, Y. et al. Neuronal differentiation is associated with a redox-regulated increase of copper flow to the secretory pathway. *Nat. Commun.* **7**, 10640 (2016).
34. Dunnill, C. J., Ibraheem, K., Mohamed, A., Southgate, J. & Georgopoulos, N. T. A redox state-dictated signalling pathway deciphers the malignant cell specificity of CD40-mediated apoptosis. *Oncogene* **36**, 2515–2528 (2016).
35. Onaca, O. et al. Functionalised nanocompartments (Synthosomes) with a reduction-triggered release system. *Angew. Chem. Int. Ed.* **47**, 7029–7031 (2008).
36. Einfalt, T. et al. Stimuli-triggered activity of nanoreactors by biomimetic engineering polymer membranes. *Nano Lett.* **15**, 7596–7603 (2015).
37. Edlinger, C. et al. Biomimetic strategy to reversibly trigger functionality of catalytic nanocompartments by the insertion of pH-responsive biovalves. *Nano Lett.* **17**, 5790–5798 (2017).
38. Itel, F., Najer, A., Palivan, C. G. & Meier, W. Dynamics of membrane proteins within synthetic polymer membranes with large hydrophobic mismatch. *Nano Lett.* **15**, 3871–3878 (2015).
39. Nardin, C., Thoeni, S., Widmer, J., Winterhalter, M. & Meier, W. Nanoreactors based on (polymerised) ABA-triblock copolymer vesicles. *Chem. Commun.* **15**, 1433–1434 (2000).
40. Xiao, Q. et al. Bioactive cell-like hybrids coassembled from (glyco) dendrimersomes with bacterial membranes. *Proc. Natl. Acad. Sci. USA* **113**, E1134–E1141 (2016).
41. Mason, R. P. et al. Glutathione peroxidase activity is neuroprotective in models of Huntington's disease. *Nat. Genet.* **45**, 1249–1254 (2013).
42. Sun, H., Meng, F., Cheng, R., Deng, C. & Zhong, Z. Reduction-responsive polymeric micelles and vesicles for triggered intracellular drug release. *Antiox. Redox Signal* **21**, 755–767 (2014).
43. Egan, R. W., Paxton, J. & Kuehl, F. A. Mechanism for irreversible self-deactivation of prostaglandin synthetase. *J. Biol. Chem.* **251**, 7329–7335 (1976).
44. Mailloux, R. J., Jin, X. & Willmore, W. G. Redox regulation of mitochondrial function with emphasis on cysteine oxidation reactions. *Redox Biol.* **2**, 123–139 (2014).
45. Shevchenko, A., Tomas, H., Havlis, J., Olsen, J. V. & Mann, M. In-gel digestion for mass spectrometric characterisation of proteins and proteomes. *Nat. Protoc.* **1**, 2856–2860 (2006).
46. Zhou, L. & Schlick, S. Electron spin resonance (ESR) spectra of amphiphilic spin probes in the triblock copolymer EO13PO30EO13 (Pluronic L64): hydration, dynamics and order in the polymer aggregates. *Polymer* **41**, 4679–4689 (2000).
47. Beghein, N. et al. Characterisation of self-assembling copolymers in aqueous solutions using electron paramagnetic resonance and fluorescence spectroscopy. *J. Control Release* **117**, 196–203 (2007).
48. Deo, N., Somasundaran, P., Subramanyan, K. & Ananthapadmanabhan, K. P. Electron paramagnetic resonance study of the structure of lipid bilayers in the presence of sodium dodecyl sulfate. *J. Colloid Interface Sci.* **256**, 100–105 (2002).
49. Nakagawa, K. Spin-Probe investigations of head group behavior in aqueous dispersions of a nonionic amphiphilic compound. *Lipids* **42**, 457–462 (2007).
50. Serban, M. A., Yang, G. & Prestwich, G. D. Synthesis, characterisation and chondroprotective properties of a hyaluronan thioethyl ether derivative. *Biomaterials* **29**, 1388–1399 (2008).
51. Circu, M. L. & Aw, T. Y. Reactive oxygen species, cellular redox systems, and apoptosis. *Free Radic. Biol. Med.* **48**, 749–762 (2010).
52. Rigler, R., Mets, Ü., Widengren, J. & Kask, P. Fluorescence correlation spectroscopy with high count rate and low background: analysis of translational diffusion. *Eur. Biophys. J.* **22**, 169–175 (1993).
53. Ranquin, A., Versées, W., Meier, W., Steyaert, J. & Van Gelder, P. Therapeutic nanoreactors: combining chemistry and biology in a novel triblock copolymer drug delivery system. *Nano Lett.* **5**, 2220–2224 (2005).
54. Stauch, O., Schubert, R., Savin, G. & Burchard, W. Structure of artificial cytoskeleton containing liposomes in aqueous solution studied by static and dynamic light scattering. *Biomacromolecules* **3**, 565–578 (2002).
55. Wu, D. et al. Effect of molecular parameters on the architecture and membrane properties of 3D assemblies of amphiphilic copolymers. *Macromolecules* **47**, 5060–5069 (2014).
56. Siti, W. et al. An intercompartmental enzymatic cascade reaction in channel-equipped polymersome-in-polymersome architectures. *J. Mater. Chem. B* **2**, 2733–2737 (2014).
57. Kiene, K. et al. PDMS-b-PMOXA polymersomes for hepatocyte targeting and assessment of toxicity. *Eur. J. Pharm. Biopharm.* **119**, 322–332 (2017).
58. Dieu, L.-H., Wu, D., Palivan, C. G., Balasubramanian, V. & Huwyler, J. Polymersomes conjugated to 83-14 monoclonal antibodies: in vitro targeting of brain capillary endothelial cells. *Eur. J. Pharm. Biopharm.* **88**, 316–324 (2014).
59. Camblin, M. et al. Polymersomes containing quantum dots for cellular imaging. *Int. J. Nanomed.* **9**, 2287 (2014).
60. Ali, S., Champagne, D. L., Spaink, H. P. & Richardson, M. K. Zebrafish embryos and larvae: a new generation of disease models and drug screens. *Birth Defects Res. C Embryo Today* **93**, 115–133 (2011).
61. Rizzo, L. Y. et al. In vivo nanotoxicity testing using the Zebrafish embryo assay. *J. Mater. Chem. B Mater. Biol. Med.* **1**, 3918–3925 (2013).
62. MacRae, C. A. & Peterson, R. T. Zebrafish as tools for drug discovery. *Nat. Rev. Drug Discov.* **14**, 721–731 (2015).
63. Fenaroli, F. et al. Nanoparticles as drug delivery system against tuberculosis in zebrafish embryos: direct visualisation and treatment. *ACS Nano* **8**, 7014–7026 (2014).
64. Sieber, S. et al. Zebrafish as an early stage screening tool to study the systemic circulation of nanoparticulate drug delivery systems in vivo. *J. Control. Release* **264**, 180–191 (2017).
65. Torraca, V., Masud, S., Spaink, H. P. & Meijer, A. H. Macrophage-pathogen interactions in infectious diseases: new therapeutic insights from the zebrafish host model. *Dis. Model Mech.* **7**, 785–797 (2014).
66. Daigneault, M., Preston, J. A., Marriott, H. M., Whyte, M. K. B. & Dockrell, D. H. The identification of markers of macrophage differentiation in PMA-stimulated THP-1 cells and monocyte-derived macrophages. *PLoS ONE* **5**, e8668 (2010).
67. Lunov, O. et al. Differential uptake of functionalised polystyrene nanoparticles by human macrophages and a monocytic cell line. *ACS Nano* **5**, 1657–1669 (2011).

Acknowledgements

We gratefully acknowledge the financial support provided by the Swiss Nanoscience Institute, the Swiss National Science Foundation and the National Centre of Competence in Research—Molecular Systems Engineering. J.H., D.W. and S.S. acknowledge financial support from the Novartis University Basel Excellence Scholarship for Life Sciences, the NanoReg II research program of the European Union, the FAG Basel and Stiftung zur Förderung des Pharmazeutischen Nachwuchses in Basel. The authors thank Prof. W. Meier (University of Basel) for providing the polymer and constructive discussions, and Dr. I. A. Dinu (University of Basel) for synthesising the polymer. "Somersault18:24" is acknowledged for illustration templates. T. E. thanks M. Garni (University of Basel), Dr. M. Lomora (University of Basel), Dr. G. Quebatte (University of Basel) for fruitful discussions, and G. Persy (University of Basel) for

TEM-measurements. T.E. and D.W. thank Dr. S. Schenk (University of Basel) for providing valuable scientific advice in cell culture and support during their studies. We acknowledge Dr. M. Chami from the University of Basel, C-CINA, for the cryo-TEM experiments and Dr. B.A. Goodman for editing the manuscript. In addition, the authors thank Prof. Dr. M. Affolter (University of Basel) for supporting zebrafish breeding.

Author contributions

T.E. contributed to the OmpF modification and characterisation, AOs production and characterisation, in vitro and in vivo assays, and the writing of the manuscript; C.E. contributed to the double mutant of OmpF and characterisation of the OmpF modification; D.W. contributed to the in vitro and in vivo assays; S.S. contributed to the in vivo assays; R.G. contributed to characterising the enzymatic reactions; A.N. contributed to the FCS experiments; M.S. contributed to the EPR experiments; O.O.-F. contributed to the OmpF modification and characterisation; J.H. contributed to the in vitro and in vivo experiments and writing of the manuscript; and C.G.P. contributed to the AOs concept and writing of the manuscript.

Additional information

Supplementary Information accompanies this paper at https://doi.org/10.1038/s41467-018-03560-x.

Competing interests: The authors declare no competing interests.

Reprints and permission information is available online at http://npg.nature.com/reprintsandpermissions/

Publisher's note: Springer Nature remains neutral with regard to jurisdictional claims in published maps and institutional affiliations.

DISCUSSION AND OUTLOOK

In the presented PhD thesis, the zebrafish has been validated and applied as a preclinical screening model for nanomedicine formulation design and optimization under complex biological conditions. The following sections summarize all achievements of this PhD project and puts these into a larger context. For this purpose, selected points, which have also been partially discussed in the course of Chapter I-I, are mentioned within the discussion of the specific Chapters. Strengths and weaknesses of the exploited zebrafish features as well as future perspectives are discussed in each subchapter.

During nanomedicine development, formulation design and optimization followed by a thorough characterization of nanomedicine performance in biological environments is a key step. Due to high experimental costs, time consumption, and ethical considerations, a screening of dozens of different experimental nanomedicine formulations in rodent *in vivo* studies is not applicable. To this end, different model systems such as *in vitro* cell culture and the zebrafish are suitable and complementary tools to identify potentially successful nanomedicine formulations prior to rodent *in vivo* studies. Due to its unique advantageous features (i.e. optical transparency, availability in large quantities, fluorescent transgenic lines), the zebrafish can be used as an early and easy accessible *in vivo* screening model, which is able to mimic complex biological environments. As discussed in **Chapter I-I**, critical experimental parameters and resulting limitations have to be considered in order to promote reasonable applications of the newly introduced zebrafish model during nanomedicine formulation design and optimization.

Systemic Clearance Mechanisms

Upon administration, macrophages as part of the mononuclear phagocytic system (MPS) are among the first cells which are involved in the clearance of nanomedicines [45]. Nanoparticle size and surface chemistry determine the adsorption of specific plasma proteins (e.g. opsonins) initiating their recognition and phagocytosis by immune cells [46,47]. Starting with liposomes, surface modification of nanomedicines with PEG has shown to be an effective strategy to prevent this undesired clearance mechanism and has therefore become a classical concept in nanomedicine design. As a result, various

forms of PEG are included in many nanomedicine formulations, as it is also the case for the first FDA approved formulation, i.e. Doxil [19,48]. In **Chapter II-I**, the zebrafish model was validated regarding its ability to assess the influence of nanomedicine size and PEGylation using (fluorescently labelled) liposomes as a model system. Two main advantages of the model, namely its optical transparency in combination with the availability of a transgenic zebrafish line expressing Kaede (i.e. a green fluorescent protein) specifically in its macrophages were exploited. Importantly, it was possible to reproduce PEGylation effects, which have already been described for rodents such as decreased macrophage clearance with increasing PEG density and PEG molecular weight in the zebrafish model. In addition, zebrafish findings regarding the ability to compensate negative effects of increased liposome size by increasing PEG molecular weight were successfully verified in a follow up rodent biodistribution study.

Nevertheless, some questions regarding the full predictive power of this general experimental set-up have to be discussed. The used zebrafish line *Tg(mpeg1:Gal4/UAS:Kaede)* exploits the *mpeg1* promoter to drive fluorescent Kaede expression specifically in macrophages [49]. Assessing nanomedicine macrophage clearance using this line does not allow to distinguish between different macrophage polarization states (i.e. M1 or M2), which is an important but often neglected factor, as shown by MacParland et al. [50]. If desired, this issue can be overcome by using transgenic lines expressing fluorescent proteins depending on the polarization state, as presented in a publication describing the conservation of macrophage polarization states between zebrafish and mammalians [51]. Furthermore, this Gal4;UAS genetic construct showed to be stable in zebrafish embryos/larvae but suffers from somatic silencing, resulting in the absence of fluorescent spleen macrophages in adult zebrafish [49]. On the one hand, this is an important fact, since the spleen and its macrophages are one of the main nanomedicine clearance sites. On the other hand, the applicability of zebrafish embryos/larvae in (high-throughput) screenings is a main advantage of the model, which would get lost by the application of adult zebrafish. Recently, Schöttler et al. outlined that a much closer look at plasma protein adsorption and its effect on macrophage phagocytosis is required since, the presence

of specific plasma proteins seems to be necessary for the intended function of nanoparticle PEGylation [52]. In addition, protein corona formation around nanoparticles is heavily species dependent, as highlighted by Müller et al. [53]. Despite the relatively conserved plasma protein profile between zebrafish and human [54], this has to be kept in mind when performing such studies. One might argue that nanoparticles pre-incubated in human plasma followed by *in vitro* cell uptake studies could be the better model system to assess such questions. On the other hand, Hadjidemetriou et al. found striking differences regarding protein corona composition and *in vitro* cell uptake between liposomes which acquired their protein corona *in vivo* (mice injection and recovery) or by simple incubation in mouse plasma [55]. This indicates the importance of dynamic (blood circulation) instead of static conditions as it is present in live zebrafish embryos/larvae.

Beside its blood circulation time prolonging effect, nanomedicine PEGylation is known to initiate the Accelerated Blood Clearance (ABC) phenomenon upon the first injection of such a formulation [56]. This leads to an increased clearance of subsequent doses via a still not fully elucidated immune system mediated processes [12,57]. Based on the presented extensive validation of the zebrafish model to assess PEG formulation effects, the model is currently used to initially assess the *in vivo* performance of chemically synthesized PEG alternatives. In this regard, our group has assessed an alternative polymer surface modification in a preliminary study. Surprisingly, injecting this formulation into zebrafish blood circulation resulted in a completely unexpected biodistribution pattern. Instead of preventing macrophage phagocytosis, the assessed PEG alternative induced nanoparticle accumulation in macrophages having direct access to blood circulation (round shape) as well as tissue resident macrophages (star shape) (Figure 1). This unexpected result is remarkable since short circulating nanoparticles usually accumulate in macrophages which are located inside or in close proximity to the blood vasculature. The novel surface modification seems to trigger additional nanoparticle phagocytosis by tissue resident macrophages which are usually not reached by nanoparticles. Interestingly, macrophages are known to serve as niches for various pathogens such as *Mycobacterium tuberculosis* or *Salmonella* [58,59]. In addition, *Salmonella* show increasing resistance

against several antibiotics [60] and nanomedicines have shown to be a possible solution to overcome such issues [61]. Therefore, these findings will be further pursued in a collaborative project. To this end, primary investigations considering the exact targeting mechanism of this macrophage subset as well as the development of a nanomedicine based treatment will be investigated in a zebrafish infection model [62] followed by further studies in rodent *in vivo* models. This coincidental but promising finding highlights one of the major advantages of the zebrafish (embryo/larvae) model compared to rodent *in vivo* studies, namely the possibility to screen a lot of different nanomedicine formulations in a cost- and time effective manner without the need of regulatory approvals at an experimental level. In addition, the optical transparency and the availability of many transgenic zebrafish lines offer the possibility to observe such effects by straight forward fluorescence (confocal) microscopy.

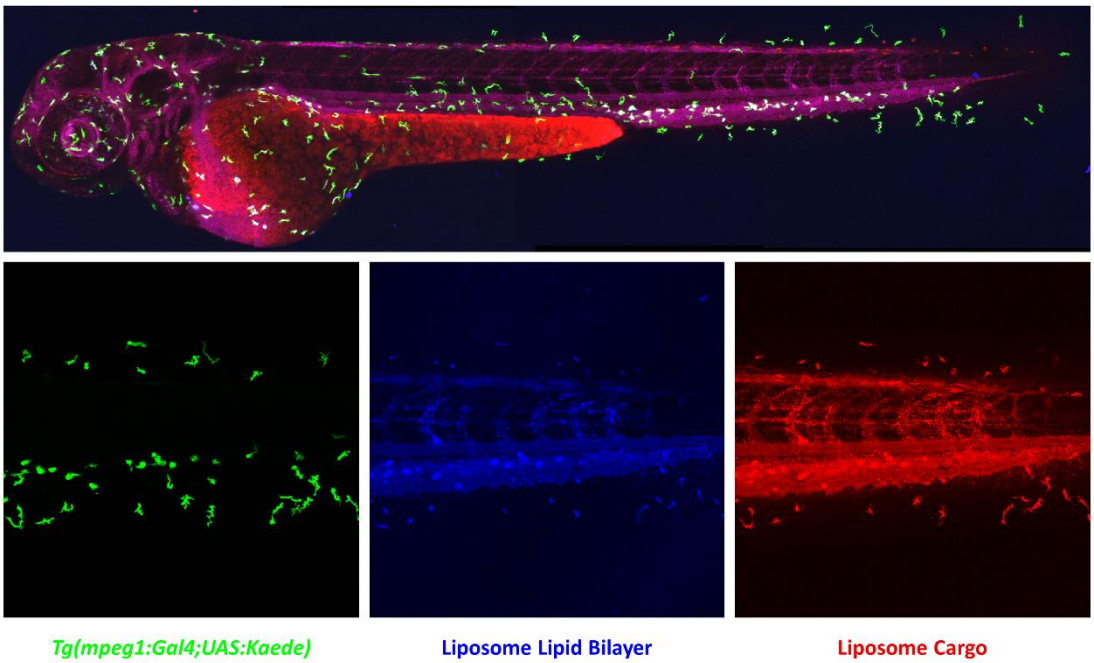

Figure 1: Targeting of macrophages located in blood circulation and tissue. Double fluorescently labelled liposomes were injected into transgenic zebrafish embryos 2 days post fertilization. Accumulation of the liposome (blue) as well as its cargo (red) in macrophages were observed 3 hours post injection, indicating the possibility to successfully deliver intact nanomedicines to the whole macrophage population.

Blood Circulation Properties

Beside surface modification (i.e. PEGylation), nanomedicine blood circulation properties can partially be controlled by further formulation design. In case of liposomes, this is connected to the transition temperature (T_m) of lipids and the amount of cholesterol incorporated into the lipid bilayer. In **Chapter II-II**, multiple (fluorescently labelled) liposome formulations composed of lipids with varying T_m and amounts of cholesterol were injected into *Tg(kdrl:EGFP)* zebrafish embryos expressing enhanced green fluorescent protein (EGFP) in their vasculature [63]. Confocal microscopy images taken after different time points were compared to published rodent pharmacokinetic data representing a classical *in vivo* study [64]. Doing so, qualitative liposome biodistribution patterns in zebrafish, which are characteristic for long or short circulating liposomes, were identified and defined. Regarding lipid T_m, short circulating liposomes (high T_m) were observed to almost immediately attach to the posterior caudal vein whereas long circulating liposomes (low T_m) showed a diffuse staining pattern, indicating their remaining presence in blood circulation. Nevertheless, these qualitative observations only allowed an accurate distinction between liposomes altered by using lipids with changing T_m. These lipids usually account for the major part of a formulation but liposomes are often composed of many additional components (i.e. cholesterol, PEGylation). In order to be able to also assess the influence of such minor formulation components, the semi-quantitative zebrafish circulation- (CF) and extravasation factor (EF) were introduced. These two zebrafish factors can be determined by image analysis using a macro which we have written for FIJI/ImageJ. These zebrafish factors subsequently were applied to all investigated nanoparticle formulations. Briefly, higher zebrafish EF and CF were observed for long circulating formulations composed of low T_m lipids or increased amount of cholesterol.

Regarding the EF, an enhanced accumulation of liposome formulations with prolonged circulation properties outside the zebrafish vasculature was observed. On the one hand, it would be tempting to speculate that an increased liposome bilayer fluidity, achieved by low T_m lipids or increased amounts of cholesterol, allows such liposome formulations to extravasate more easily in any manner. On the

other hand, this characteristic pattern showed to be independent of liposome bilayer fluidity, since also liposome surface modification with PEG resulted in the same pattern. In this respect, the zebrafish developmental stage at the time of injection (± 48 hours post fertilization (hpf)) could be a possible explanation for this observation. The zebrafish vascular morphogenesis including lumen formation is still ongoing [65,66] at this time point. Moreover, vasculature tightness during lumen formation seems to be temporally impaired, which fosters the extravasation of circulating liposomes (Figure 2). This effect is much more pronounced in case of long circulating liposomes, since short circulating liposomes are bound by the venous vasculature almost immediately after injection. Performing the zebrafish assessment at later time points at which the vasculature is further developed would be one option. On the downside, this could also interfere with the diminishing presence of the duct of Cuvier (easy accessible site of injection) and increasing regulatory requirements when exceeding developmental stages of 5 days post fertilization. Furthermore, varying extravasation patterns of different long circulating nanoparticles were observed in extended studies (data not shown). So far, different reasons such as altered nanoparticle stability or aggregation in biological environments are discussed but have to be further elucidated. With this in mind, the zebrafish extravasation factor should be applied with care, especially since the zebrafish CF has been investigated in much more detail (Chapter III-I).

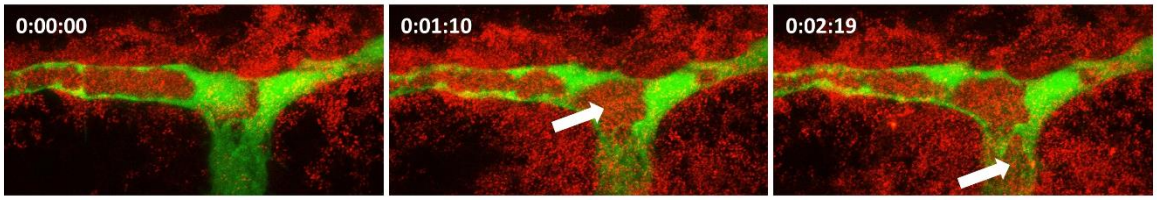

Figure 2: Time course of long circulating liposome extravasation upon zebrafish vasculature lumen formation. Transgenic zebrafish embryos expressing EGFP in their vascular endothelial cells (green) were injected with fluorescently labelled long circulating liposomes (red) at 48 hours post fertilization. Images were recorded around 1 hour post injection. Timeframe and sites of lumen formation are indicated (white arrows).

By combining the qualitative and semi-quantitative zebrafish assessment, a successful general circulation behavior prediction of a liposome formulation with so far not reported blood circulation time was possible and verified in a rodent *in vivo* study. Nevertheless, this approach always requires the comparison of a new nanomedicine formulation with at least one formulation with known

pharmacokinetic properties. Moreover, it is not possible to predict exact numerical pharmacokinetic parameters such as AUC or $t_{1/2}$ or to compare results obtained in different experimental series. Being able to provide such detailed and comparable information will be the matter of further investigations. To this end, fluorescence correlation spectroscopy (FCS) in live zebrafish embryos will be used. By this technique, changing fluorescence intensities and size dependent diffusion coefficients of nanomedicines in a defined confocal volume are measured. Based on this data and the calibration of the whole set-up, normalized pharmacokinetic parameters can be obtained. Initial experiments showed a good correlation between liposome pharmacokinetic profiles measured in zebrafish embryos by FCS or in rats generated by classical radiolabeling-blood sampling protocols (Figure 3). Beside the straightforward and adaptable (i.e. surface, membrane, or hydrophilic core dyes) fluorescent labelling, especially the possibility to start recording straight after injection and the short time intervals between single measurements can be considered as the main advantage of the suggested FCS application. Often, short circulating formulations are almost immediately removed from blood circulation after their first passage through large clearance organs such as the liver, spleen, or kidneys. Due to the time-consuming injection and blood sampling protocol, such effects can only hardly be assessed in rodent *in vivo* studies. In sharp contrast, injected zebrafish embryos can immediately be transferred to a fluorescence microscope which allows the observation of such rapid clearance effects as shown by the 10 mol% cholesterol formulation in Figure 3 (top row).

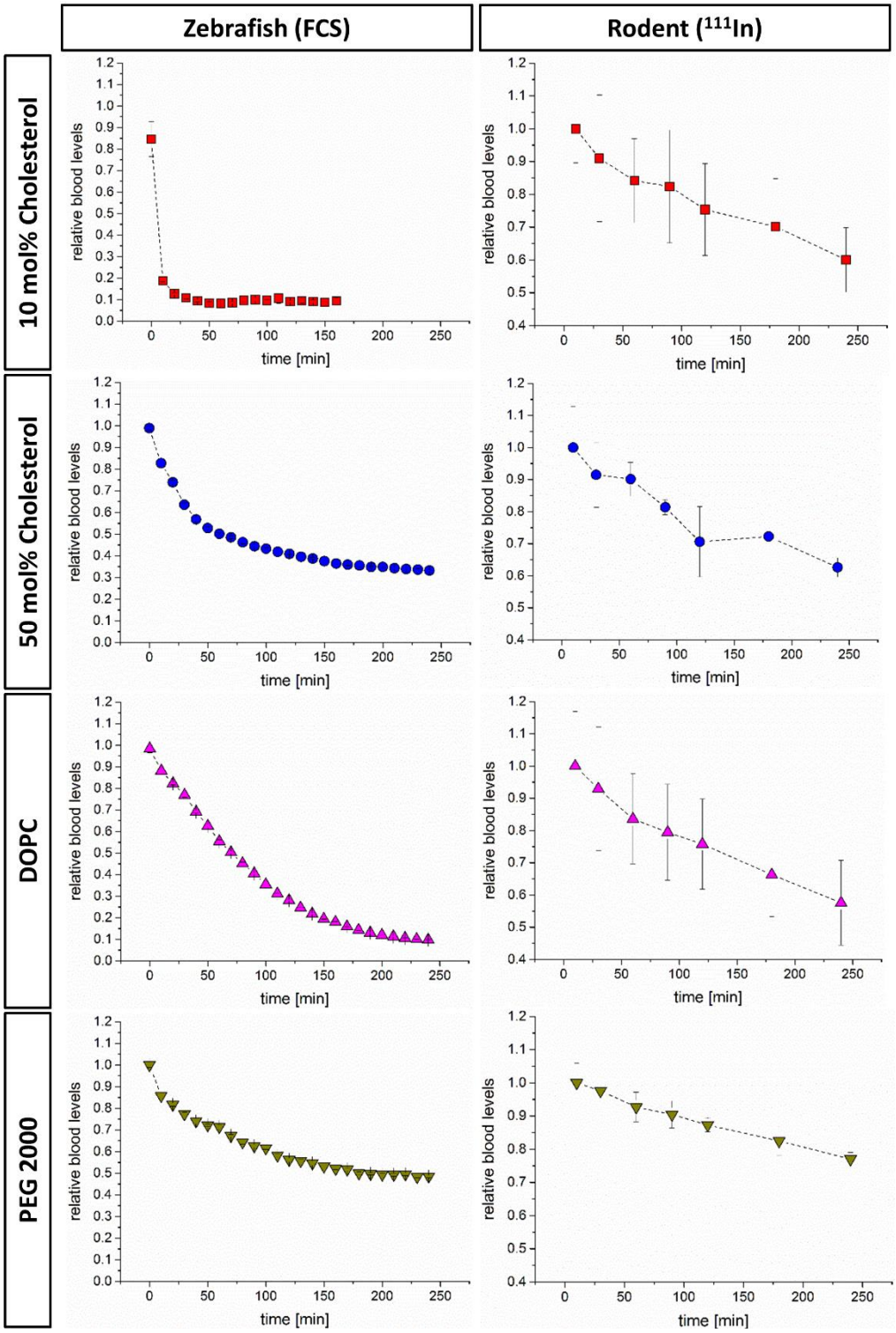

Figure 3: Liposome pharmacokinetics in zebrafish and rats. For zebrafish experiments, liposomes were fluorescently labelled and pharmacokinetic profiles were recorded by fluorescence correlation spectroscopy in live zebrafish embryos (left column). For rodent *in vivo* studies, liposomes were radiolabeled with the radionuclide ^{111}In followed by blood sampling after indicated time points (right column). All blood levels are normalized to starting concentrations.

Macromolecular Basis of Nano-Bio-Interactions

The MPS, which is located in different organs and consists of specialized macrophages (i.e. Liver Kupffer cells), is currently described as the main clearing mechanism of nanomedicines [45]. Therefore, a lot of effort has been put into the investigation of nanomedicine interactions with macrophages, as exemplary shown in Chapter II-I. Beside accumulation in macrophages, a distinct binding pattern within the caudal vein of zebrafish embryos has been observed for short circulating liposomes (Chapter II-II). As a consequence, an additional nanoparticle clearance mechanism in zebrafish embryos has been suspected and further elucidated in **Chapter III-I**. Already in 1924, Aschoff launched the concept of the reticuloendothelial system (RES), a macromolecular waste clearing system in mammalians, which not only includes macrophages but also different scavenger endothelial cells (SECs) [67]. The biggest portion of SECs are liver sinusoidal endothelial cells (LSECs), which are known to selectively express three main receptors compared to other blood vasculature endothelial cells, namely Stablilin-1 and -2 and the mannose receptor Mrc1. In the caudal vein of zebrafish embryos/larvae, the Stabilin-2 receptor was identified to scavenge nanoparticles from blood circulation. To this end, a series of injections, including short circulating liposomes, the RES vital stain lithium carmine [68], hyaluronic acid [69], and dextran sulfate [70], as well as the generation of Stabilin-2 knockout by CRISPR/Cas9, was performed. Moreover, anionic nanoparticle surface charge showed to be the predominant driver behind nanoparticle clearance via this specific receptor. Furthermore, the second scavenger receptor Stabilin-1 was shown to be involved in the clearing of smaller (< 30 nm) nanoparticles. The identification of the Stabilin-2 scavenger receptor and its localized expression was used to demonstrate targeted drug delivery to vascular endothelial cells in the caudal vein of zebrafish embryos/larvae. Therefore, a cytotoxic drug (clodronate) was encapsulated into fluorescently labelled nanoparticles which were formulated to be cleared by Stabilin-2. This resulted in a gradual loss of *kdrl:GFP*$^{+}$ endothelial cells in the caudal vein of injected *Tg(kdrl:GFP)* zebrafish embryos/larvae. Injecting clodronate loaded nanoparticles into *Tg(mpeg:GFP)* or *Tg(mpx:GFP)* did not result in an obvious loss of fluorescent macrophages or neutrophils, respectively (data not shown). Since the control injection of free clodronate did not show any effects either, it is most likely that cell

uptake via (Stabilin-2) receptor mediated endocytosis of clodronate loaded nanoparticles into vasculature endothelial cells is responsible for these observations.

The zebrafish features identified and described in Chapters II-I to III-I are summarized in Table 1. So far, the observed nanomedicine formulation effects in zebrafish and rodents showed to be conserved, making zebrafish embryos/larvae a promising model system to test and predict likely nanomedicine interactions with the RES/MPS in mammalians. Using a combination of sophisticated imaging techniques, transgenic zebrafish lines, their optical transparency, and fluorescently labelled nanoparticles allows the investigation of nanomedicine formulation effects in a live animal at a macromolecular level. As recently highlighted by Yin et al., this is of special interest for the field of nanoparticulate drug delivery [71]. Classical *in vivo* models (i.e. rodents) are a "conceptual blackbox", which does not offer the possibility to specifically reveal the effects of anatomical features, physiological processes, and molecular mechanisms on nanomedicine delivery at such high resolution. This often results in a very poor *in vitro-in vivo* translation, since a proper selection of potentially successful nanomedicine formulations under complex biological conditions is hampered [22]. Especially for therapeutic nanomedicine approaches, which require a tight control of cellular uptake and trafficking mechanisms, having the possibility to assess formulation effects in a detailed manner is of utmost importance.

Gene delivery can be considered as such while being one of the most promising future branches of therapeutic nanomedicines. Already available viral gene delivery vectors are questionable regarding their immunogenicity and in addition suffer from comparably low loading capacities. Therefore, replacing them with biocompatible nanoparticles is of great interest [72]. Nanomedicine formulation design and optimization for gene delivery is especially critical as illustrated by the "PEG dilemma" [73]. In order to fulfill their therapeutic intention, such systems need to overcome the cellular membrane, prevent/escape endosomal/lysosomal degradation, and deliver their intact gene cargo to the cytosol or the nucleus [74]. As already described, PEG is often included in nanomedicine formulations to prevent their removal from blood circulation by phagocytic cells. On the other hand, PEG is also known

to decrease nanomedicine cell uptake and to improve nanoparticle stability leading to poor endosomal/lysosomal escape resulting in gene cargo degradation under the acidic conditions in these cellular compartments. Expanding the already described features of the zebrafish model (Table 1) with *in vivo* nanomedicine cell internalization and trafficking studies will therefore be a next step which has to be well-considered. For this purpose, already available transgenic zebrafish lines expressing fluorescent proteins in endosomes [75] and/or lysosomes [76] will be of importance. As an alternative method to fluorescence based microscopy, focused ion beam scanning electron microscopy (FIB-SEM), which has already been applied on zebrafish embryos [77,78], will be evaluated to generate 3D images at isotropic resolutions in the sub-nanometer range. To this end, a nanoreactor approach, which has been described in one of our previous research projects [79], will be exploited to load the investigated nanomedicine formulations with gold nanoparticles as electron dense contrast agents.

Table 1: Zebrafish features and their applicability for nanomedicine formulation design and optimization. Relevant formulation parameters of investigated nanoparticles, time points after nanoparticle zebrafish injection or incubation, used zebrafish lines, an overview of discovered key formulation effects, and the original thesis chapter are given. The exact chemical identities of lipids and polymers are listed in the abbreviation section. In addition to the indicated compositions, all nanoparticles have been fluorescently labelled using 1 mol% of fluorescent dyes. Nanoparticle size (nm) and surface charge (mV) were measured by dynamic light scattering. hpi = hours post injection, T_m = lipid transition temperature.

Zebrafish Feature	Investigated Nanoparticles	Assessed Time Points	Zebrafish Line(s)	Effects of Formulation Parameters	Chapter
Macrophage Clearance	Liposomes: - 90 nm PEG350 3.0, 6.5, 10 mol% - 90 nm PEG750 3.0, 6.5, 10 mol% - 90 nm PEG2000 3.0, 6.5, 10 mol% - 90 nm PEG5000 3.0, 6.5, 10 mol% - 60 nm PEG350 6.5 mol% - 120 nm PEG350 6.5 mol% - 60 nm PEG2000 6.5 mol% - 120 nm PEG2000 6.5 mol%	3, 24 hpi	*Tg(kdrl:EGFP)*, *Tg(mpeg1:Gal4;UAS:Kaede)*	Decreased macrophage clearance by: - Increased PEG molecular weight - Increased PEG density - Decreased nanoparticle size Higher PEG molecular weight is able to compensate larger nanoparticle size.	II-I
	Liposomes: - 100 nm POPC, Chol (55:45 mol%) - 100 nm POPC, Chol, PEG2000 (50:41:9 mol%) - 325 nm POPC, Chol (55:45 mol%) - 464 nm POPC, Chol (55:45 mol%)	2 hpi	*Tg(mpeg:GFP)*	Decreased macrophage clearance by: - Decreased nanoparticle size - Addition of PEG	III-I
Zebrafish Circulation (CF) and Extravasation Factor (EF)	Liposomes: - DAPC 20:4 (T_m -70 °C) - DOPC (T_m -22 °C) - DMPC (T_m 23 °C) - DPPC (T_m 41 °C) - DSPC (T_m 55 °C) - DAPC 20:0 (T_m 66 °C) - DSPC, Chol (90:10 mol%) - DSPC, Chol (80:20 mol%) - DSPC, Chol (70:30 mol%) - DSPC, Chol (60:40 mol%) - DSPC, Chol (50:50 mol%) - DSPC, Chol, PEG2000 (55:40:5 mol%) - DSPC, Chol, PEG2000 (50:40:10 mol%)	1, 24 hpi	*Tg(kdrl:EGFP)*	Prolonged nanoparticle circulation (increased CF and EF) by: - Low lipid transition temperature (T_m) - Increasing amount of cholesterol (Chol) - Increasing amount of PEG2000	II-II

Stabilin-1 and -2 Clearance	Liposomes (± 110 nm): - POPC, Chol (55:45 mol%) (-16 mV) - DSPC, DSPG, Chol (53:21:26 mol%) (-34 mV) - DOTAP, DOPC (51.5:48.5 mol%) (46 mV) - DOPC ± Clodronate (-11 mV) - DSPC ± Clodronate (-3 mV) - DOPG (-37 mV) - DSPG (-46 mV) - DOTAP (36 mV) - POPC (-17 mV) Virus-like (28 nm) - 90 CCMV capsid protein dimer (-15 mV) Polymersome (83 nm) - PIP, PEG (57:43 mol%) (-24 mV) Quantum Dots (< 10 nm) (-71 mV) Latex beads (121 nm) (-51 mV)	1, 8, 24, 48 hpi	*Tg(kdrl:GFP)*, *Tg(kdrl:RFP-CAAX)*, Homozygous *stab2*^{ibl2} mutants, Heterozygous *stab2*^{ibl2} mutants, *Tg(mpx:GFP)*	Stabilin-1 and -2 clearance is independent from nanoparticle chemical identity (i.e. lipid, polymer, virus). Stabilin-2 nanoparticle clearance is an interplay of: - Nanoparticle size > 30 nm - Pronounced anionic nanoparticle surface charge < -30 mV - High transition temperature lipid but neutral nanoparticle surface charge (DSPC) Nanoparticle binding to Stabilin-2 results in receptor mediated endocytosis. Stabilin-1 nanoparticle clearance seems to be mediated by: - Nanoparticle size < 30 nm A pronounced cationic surface charge leads to nanoparticle binding to the whole zebrafish vasculature.	III-I
Toxicity	Liposomes (1, 10, 100, 1000 µM): - DOPC - DMPC - DPPC - DSPC - DAPC 20:0 - DOTAP - PEI	24, 48, 72 hours post incubation	ABC/TU	Zebrafish embryo mortality induced by: - Increasing dose (1 < 10 < 100 < 1000 µM) - Pronounced cationic surface charge (DOPC = DMPC = DPPC = DSPC = DAPC 20:0 < DOTAP < PEI)	II-II

Passive and Active Targeting

After the successful introduction, set-up, and validation of the zebrafish model in Chapters I-I to III-I, **Chapter IV-I** has been dedicated to further applications of the established model. Ligand surface modification of nanomedicines is commonly referred as active targeting and triggers the uptake into diseased cells which express specific proteins or receptors. This is often used as a complementary approach to passive targeting which relies on the EPR effect [80]. After passive accumulation, the main purpose of the targeting ligand is to retain the nanomedicine at the site of action and enhance internalization [81]. During formulation design and optimization of such actively targeted nanomedicines, the optimal ligand density on the nanoparticle surface is a key parameter which is normally evaluated *in vitro* using cells deficient or expressing the target of interest. In general, higher ligand densities usually result in increased nanomedicine cell uptake *in vitro*. Interestingly, optimal ligand densities identified *in vitro* often show poor performance *in vivo*, as observed by Shan et al. [82] and in Chapter IV-I. In order to overcome this issue, the zebrafish model was used as a complementary tool to select the nanoparticle formulation carrying the optimal ligand density for subsequent rodent *in vivo* studies. First, *Tg(kdrl:EGFP)* zebrafish embryos were used to assess the influence of ligand density on blood circulation behavior. Higher ligand densities were observed to result in nanoparticle aggregation whereas intermediate and lower ligand densities showed gradually increasing blood circulation properties (i.e. diffuse staining pattern indicating long circulation properties). Second, a comparably simple zebrafish xenograft model was generated [83] by injecting genetically modified cells, expressing the receptor of interest and green fluorescent protein (GFP) into wild type zebrafish embryos. The nanoparticle formulation modified with a medium ligand density showed the highest degree of colocalization with the targeted cells. These findings were confirmed in a subsequent rodent *in vivo* organ distribution study. The highest and medium ligand density nanoparticle formulations were observed to accumulate in the target organ (liver). However, nanoparticles bearing a high ligand density suffered from a poor liver to spleen ratio. Most probably, this is a result of nanoparticle aggregation, as shown in zebrafish studies, leading to nanoparticle phagocytosis by macrophages

expressed in the spleen. Therefore, the potential of using the zebrafish model during formulation design and optimization of actively targeted nanomedicines has been shown in this chapter.

Since decorating the surface of nanoparticle with receptor ligands is one way to increase nanomedicine cell uptake via receptor mediated endocytosis [6], the already indicated use of the zebrafish as an *in vivo* model for cell internalization and trafficking could become even more valuable. Further approaches are the use of zebrafish tumor models which include the possibility to assess EPR effects on targeted nanomedicine delivery. Upon Vascular Endothelial Growth Factor (VEGF) secreting cancer cell injection into zebrafish, Stoletov et al. demonstrated vessel remodeling and angiogenesis including the formation of vascular holes mediating vascular permeability [84]. Keeping this in mind, the generation of a zebrafish xenograft model using the approach published by Nicoli et al. [85], which strongly induces angiogenesis resulting in a completely vascularized tumor, could be a possibility to generate such an EPR mimicking zebrafish xenograft model. Importantly, a thorough characterization of the model will be of utmost importance, since the size of vasculature fenestration (holes) is known to vary between organs, tumor types [86] and to be dependent on the secretion of different endothelial growth factors by cancer cells [87].

Enzyme Activity

Enzyme immobilization on nanoparticles is envisioned for several therapeutic applications [88]. Designing artificial organelles or cells including membrane gates, which control the encapsulated enzymes access to its substrates even goes a step further and is an exciting branch of nanomedicine [89,90]. Successful delivery and therapeutic application of such systems require specific formulation properties which enable cellular internalization, a controlled biodistribution, avoidance of undesired clearance, and endosomal escape. In addition, the designed systems have to be nontoxic, biocompatible and functional under *in vivo* conditions [91]. In **Chapter IV-II**, model enzymes were immobilized on PLGA nanoparticles and injected into zebrafish embryos in order to assess their biocompatibility and stability under *in vivo* conditions. Especially the presence of free or unreacted glutaraldehyde, which has been used to crosslink enzymes with nanoparticles, was considered as

potentially critical. In general, injected zebrafish embryos were observed to be highly vulnerable to crosslinking chemicals (i.e. GA) or remaining organic solvents origin from the nanomedicine preparation process (data not shown). Nevertheless, injecting PLGA-enzyme particles did not result in acute signs of toxicity. Furthermore, performing an enzyme activity assay (formation of a colored reaction product) on injected zebrafish embryos was used to evaluate the systems stability and activity in a biological environment. As a result, injected PLGA immobilized enzymes showed a dotted and bright staining pattern whereas the colored product was diffusely distributed in case of injected free enzyme. Based on the dotted and localized staining pattern of immobilized enzymes, the stability and functionality of the presented system upon injection into a biological environment was concluded. Due to the required experimental conditions of the enzyme activity assay, the injected zebrafish embryos had to be euthanized, fixed, and permeabilized prior to the addition of the enzyme substrate. Consequently, this protocol does only allow to assess the stability and integrity of nanoparticle-enzyme systems but not their actual functionality under live *in vivo* conditions. Beside its beneficial simplicity, this reflects a severe drawback of such an experimental set-up, since the immobilized enzymes access to its substrate can be heavily affected by the presence of blood flow.

Nevertheless, this issue can be overcome by using alternative enzyme activity assays, as demonstrated in **Chapter IV-III**. In this study, polymer based artificial organelles (AO) loaded with a model enzyme (i.e. horseradish peroxidase, HRP) were developed and tested *in vitro* and *in vivo* using the zebrafish model. Importantly, the enzyme loaded nanoparticles were equipped with reduction sensitive protein gates controlling the enzyme access to its substrate. In presence of hydrogen peroxide (H_2O_2), HRP converts the enzyme substrate Amplex Ultra Red (AR) into the fluorescent resorufin-like product (RLP). *In vitro*, the designed artificial organelles were taken up by macrophages, an observation which has been confirmed by injecting them into *Tg(mpeg1:Gal4;UAS:Kaede)* zebrafish embryos. In order to assess the systems integrity and functionality under live *in vivo* conditions, the formation of RLP in AO injected live zebrafish embryos was successfully observed upon subsequent injection of the enzyme substrate AR. Coincidentally, using this specific model enzyme reaction and the accumulation of AOs

in macrophages did not require an additional injection of H_2O_2, since it is inherently produced by macrophages [92].

On the one hand, using the zebrafish for this purpose allowed an initial assessment of the performance of such sophisticated systems under live biological conditions. On the other hand, model enzymes and the resulting experimental conditions which are required for the specific enzyme activity assay are always defined. Most often, using model enzymes is only valuable during early steps of the formulation design and optimization. As soon as the therapeutic efficiency of such as system has to be tested, model enzymes have to be exchanged by the therapeutic enzyme. Therefore, model enzymes for such studies should not only be chosen based on their price, stability, or easiness to handle. Moreover, the actual enzyme properties (i.e. molecular weight, required reaction conditions) should be carefully considered. Keeping this in mind, the zebrafish is a valuable complementary tool to test immobilized and encapsulated enzyme activity under *in vivo* conditions.

CONCLUSION

During this PhD thesis, four major objectives (Chapter I to IV) had to be evaluated to set-up and validate the zebrafish as an early and easy accessible *in vivo* tool for nanomedicine development.

First, the zebrafish has demonstrated advantageous characteristics for nanomedicine formulation design and optimization including its optical transparency, the availability of transgenic lines, the relatively straight forward *in vivo* experimental set-up, and the possibility to screen large numbers of samples. These features allow an improved selection of potentially successful nanomedicine formulations for subsequent rodent *in vivo* studies under complex biological conditions. Consequently, if reasonably applied, this newly introduced model system can serve as an optimal tool to close the *in vitro* - *in vivo* gap during nanomedicine development **(Chapter I)**.

Second, the zebrafish model was further characterized and validated as a model system for nanomedicine development. Special foci were systemic macrophage clearance (i.e. a main nanomedicine clearing mechanisms in mammalians) and the identification of imaging based nanomedicine biodistribution patterns indicative for long or short blood circulation behavior. Importantly, findings in zebrafish showed a high predictive power for rodent *in vivo* experiments evaluating the effect of various nanomedicine formulation parameters such as size, PEGylation, lipid transition temperature, or cholesterol content **(Chapter II)**.

Third, a detailed follow-up study was performed evaluating additional nanomedicine clearance mechanisms. Interestingly, the Stabilin-2 scavenger receptor in the caudal vein of zebrafish embryos/larvae was identified, which is the tissue were short circulating nanomedicines accumulate. Different formulation parameters such as an anionic surface charge and a defined size range were identified to influence this clearance mechanism. Importantly, this nanomedicine scavenging process corresponds to an already well-known nanomedicine clearing mechanism by liver sinusoidal endothelial cells of mammalians. Thus, the zebrafish has been identified as a suitable and predictive model regarding the hepatic clearance of novel nanomedicine formulations (**Chapter III**).

Fourth, further applications of the zebrafish model were evaluated. During the development of actively targeted nanomedicines the zebrafish model demonstrated its superior predictive power for subsequent rodent *in vivo* studies when compared to a standard *in vitro* setting. Additionally, the biocompatibility, stability, and functionality of two nanoparticle-enzyme systems under *in vivo* conditions were tested in zebrafish. These findings successfully demonstrated the broad applicability of the zebrafish model to assess sophisticated nanomedicines under complex and dynamic biological conditions (**Chapter IV**).

Conclusively, the findings presented in this PhD thesis will hopefully increase the understanding of basic nanomedicine formulation effects and therefore foster a successful translation of further nanomedicines from bench to bedside.

ABBREVIATIONS

ABC	Accelerated Blood Clearance
AO	artificial organelle
AR	Amplex (Ultra) Red
AUC	area under the curve
CAM	chorioallantoic membrane
CCMV	Cowpea Chlorotic Mottle Virus
CF	(Zebrafish) circulation factor
Chol	cholesterol
DAPC 20:0	1,2-diarachidoyl-sn-glycero-3-phosphocholine
DAPC 20:4	1,2-diarachidonoyl-sn-glycero-3-phosphocholine
DMPC	1,2-dimyristoyl-sn-glycero-3-phosphocholine
DOPC	1,2-dioleoyl-sn-glycero-3-phosphocholine
DOPG	1,2-dioleoyl-sn-glycero-3-phospho-(1'-rac-glycerol)
DOTAP	1,2-dioleoyl-3-trimethylammonium-propane
DPPC	1,2-dipalmitoyl-sn-glycero-3-phosphocholine
DSPC	1,2-distearoyl-sn-glycero-3-phosphocholine
DSPG	1,2-distearoyl-sn-glycero-3-phospho-(1'-rac-glycerol)
EGFP	enhanced green fluorescent protein
EPR	enhanced permeability and retention effect
FCS	fluorescence correlation spectroscopy
FDA	(United States) Food and Drug Administration
FIB-SEM	focused ion beam scanning electron microscopy
GFP	green fluorescent protein
HBV	Hepatitis B Virus
hpf	hours post fertilization
hpi	hours post injection
HRP	Horseradish peroxidase
H_2O_2	hydrogen peroxide
LSECs	liver sinusoidal endothelial cells
MPS	mononuclear phagocytic system
Nanomedicines	drug or therapeutic agent loaded nanoparticles
NTCP	sodium-taurocholate cotransporting polypeptide
PEG	polyethylenglycol

PEG2000	1,2-distearoyl-sn-glycero-3-phosphoethanolamine-N-[methoxy(polyethylene glycol)-2000]
PEG350	1,2-distearoyl-sn-glycero-3-phosphoethanolamine-N-[methoxy(polyethylene glycol)-350]
PEG5000	1,2-distearoyl-sn-glycero-3-phosphoethanolamine-N-[methoxy(polyethylene glycol)-5000]
PEG750	1,2-distearoyl-sn-glycero-3-phosphoethanolamine-N-[methoxy(polyethylene glycol)-750]
PEI	polyethylenimine
PIB	polyisobutylene
PLGA	poly(lactide-co-glycolide)
POPC	1-palmitoyl-2-oleoyl-sn-glycero-3-phosphocholine
RES	reticuloendothelial system
RLP	resorufin-like product
SECs	scavenger endothelial cells
T_m	transition temperature
$t_{1/2}$	half-life
VEGF	Vascular Endothelial Growth Factor

BIBLIOGRAPHY

[1] P. Ehrlich, Experimental Researches on Specific Therapy, on Immunity with Special Relationship between Distribution and Action of Antigens, (1908).

[2] P. Grossen, D. Witzigmann, S. Sieber, J. Huwyler, PEG-PCL-based nanomedicines: A biodegradable drug delivery system and its application, J. Control. Release Off. J. Control. Release Soc. 260 (2017) 46–60. doi:10.1016/j.jconrel.2017.05.028.

[3] D. Peer, J.M. Karp, S. Hong, O.C. Farokhzad, R. Margalit, R. Langer, Nanocarriers as an emerging platform for cancer therapy, Nat. Nanotechnol. 2 (2007) 751–760. doi:10.1038/nnano.2007.387.

[4] H. Ragelle, F. Danhier, V. Préat, R. Langer, D.G. Anderson, Nanoparticle-based drug delivery systems: a commercial and regulatory outlook as the field matures, Expert Opin. Drug Deliv. 14 (2017) 851–864. doi:10.1080/17425247.2016.1244187.

[5] A. Wicki, D. Witzigmann, V. Balasubramanian, J. Huwyler, Nanomedicine in cancer therapy: challenges, opportunities, and clinical applications, J Control Release. 200 (2015) 138–157. doi:10.1016/j.jconrel.2014.12.030.

[6] J. Shi, P.W. Kantoff, R. Wooster, O.C. Farokhzad, Cancer nanomedicine: progress, challenges and opportunities, Nat. Rev. Cancer. 17 (2017) 20–37. doi:10.1038/nrc.2016.108.

[7] A.D. Bangham, R.W. Horne, NEGATIVE STAINING OF PHOSPHOLIPIDS AND THEIR STRUCTURAL MODIFICATION BY SURFACE-ACTIVE AGENTS AS OBSERVED IN THE ELECTRON MICROSCOPE, J. Mol. Biol. 8 (1964) 660–668.

[8] Y. Barenholz, Doxil®–the first FDA-approved nano-drug: lessons learned, J. Control. Release Off. J. Control. Release Soc. 160 (2012) 117–134. doi:10.1016/j.jconrel.2012.03.020.

[9] J.-C. Leroux, Editorial: Drug Delivery: Too Much Complexity, Not Enough Reproducibility?, Angew. Chem. Int. Ed. 56 (2017) 15170–15171. doi:10.1002/anie.201709002.

[10] F. Danhier, To exploit the tumor microenvironment: Since the EPR effect fails in the clinic, what is the future of nanomedicine?, J. Control. Release Off. J. Control. Release Soc. 244 (2016) 108–121. doi:10.1016/j.jconrel.2016.11.015.

[11] J.I. Hare, T. Lammers, M.B. Ashford, S. Puri, G. Storm, S.T. Barry, Challenges and strategies in anti-cancer nanomedicine development: An industry perspective, Adv. Drug Deliv. Rev. 108 (2017) 25–38. doi:10.1016/j.addr.2016.04.025.

[12] L. Belfiore, D.N. Saunders, M. Ranson, K.J. Thurecht, G. Storm, K.L. Vine, Towards clinical translation of ligand-functionalized liposomes in targeted cancer therapy: Challenges and opportunities, J. Controlled Release. 277 (2018) 1–13. doi:10.1016/j.jconrel.2018.02.040.

[13] S. Wilhelm, A.J. Tavares, Q. Dai, S. Ohta, J. Audet, H.F. Dvorak, W.C.W. Chan, Analysis of nanoparticle delivery to tumours, Nat. Rev. Mater. 1 (2016) 16014. doi:10.1038/natrevmats.2016.14.

[14] A.P. Blum, J.K. Kammeyer, A.M. Rush, C.E. Callmann, M.E. Hahn, N.C. Gianneschi, Stimuli-Responsive Nanomaterials for Biomedical Applications, J. Am. Chem. Soc. 137 (2015) 2140–2154. doi:10.1021/ja510147n.

[15] V.P. Torchilin, Multifunctional, stimuli-sensitive nanoparticulate systems for drug delivery, Nat. Rev. Drug Discov. 13 (2014) 813–827. doi:10.1038/nrd4333.

[16] M.V. Yezhelyev, X. Gao, Y. Xing, A. Al-Hajj, S. Nie, R.M. O'Regan, Emerging use of nanoparticles in diagnosis and treatment of breast cancer, Lancet Oncol. 7 (2006) 657–667. doi:10.1016/S1470-2045(06)70793-8.

[17] J.H. Ryu, S. Lee, S. Son, S.H. Kim, J.F. Leary, K. Choi, I.C. Kwon, Theranostic nanoparticles for future personalized medicine, J. Controlled Release. 190 (2014) 477–484. doi:10.1016/j.jconrel.2014.04.027.

[18] T. Lammers, F. Kiessling, M. Ashford, W. Hennink, D. Crommelin, G. Storm, Cancer nanomedicine: Is targeting our target?, Nat. Rev. Mater. 1 (2016). doi:10.1038/natrevmats.2016.69.

[19] D. Bobo, K.J. Robinson, J. Islam, K.J. Thurecht, S.R. Corrie, Nanoparticle-Based Medicines: A Review of FDA-Approved Materials and Clinical Trials to Date, Pharm. Res. 33 (2016) 2373–2387. doi:10.1007/s11095-016-1958-5.

[20] S. Behzadi, V. Serpooshan, W. Tao, M.A. Hamaly, M.Y. Alkawareek, E.C. Dreaden, D. Brown, A.M. Alkilany, O.C. Farokhzad, M. Mahmoudi, Cellular uptake of nanoparticles: journey inside the cell, Chem. Soc. Rev. 46 (2017) 4218–4244. doi:10.1039/c6cs00636a.
[21] S. Mitragotri, T. Lammers, Y.H. Bae, S. Schwendeman, S. De Smedt, J.-C. Leroux, D. Peer, I.C. Kwon, H. Harashima, A. Kikuchi, Y.-K. Oh, V. Torchilin, W. Hennink, J. Hanes, K. Park, Drug Delivery Research for the Future: Expanding the Nano Horizons and Beyond, J. Control. Release Off. J. Control. Release Soc. 246 (2017) 183–184. doi:10.1016/j.jconrel.2017.01.011.
[22] K. Paunovska, C.D. Sago, C.M. Monaco, W.H. Hudson, M.G. Castro, T.G. Rudoltz, S. Kalathoor, D.A. Vanover, P.J. Santangelo, R. Ahmed, A.V. Bryksin, J.E. Dahlman, A Direct Comparison of in Vitro and in Vivo Nucleic Acid Delivery Mediated by Hundreds of Nanoparticles Reveals a Weak Correlation, Nano Lett. (2018). doi:10.1021/acs.nanolett.8b00432.
[23] C. Nüsslein-Volhard, The Identification of Genes Controlling Development in Flies and Fishes (Nobel Lecture), Angew. Chem. Int. Ed. Engl. 35 (1996) 2176–2187. doi:10.1002/anie.199621761.
[24] C. Nüsslein-Volhard, The zebrafish issue of Development, Dev. Camb. Engl. 139 (2012) 4099–4103. doi:10.1242/dev.085217.
[25] D. Ribatti, The chick embryo chorioallantoic membrane (CAM). A multifaceted experimental model, Mech. Dev. 141 (2016) 70–77. doi:10.1016/j.mod.2016.05.003.
[26] R. Swadi, G. Mather, B.L. Pizer, P.D. Losty, V. See, D. Moss, Optimising the chick chorioallantoic membrane xenograft model of neuroblastoma for drug delivery, BMC Cancer. 18 (2018) 28. doi:10.1186/s12885-017-3978-x.
[27] C.S. Kue, K.Y. Tan, M.L. Lam, H.B. Lee, Chick embryo chorioallantoic membrane (CAM): an alternative predictive model in acute toxicological studies for anti-cancer drugs, Exp. Anim. 64 (2015) 129–138. doi:10.1538/expanim.14-0059.
[28] W.A. Sassen, R.W. Köster, A molecular toolbox for genetic manipulation of zebrafish, Adv. Genomics Genet. (2015). doi:10.2147/AGG.S57585.
[29] C.A. MacRae, R.T. Peterson, Zebrafish as tools for drug discovery, Nat. Rev. Drug Discov. 14 (2015) 721–731. doi:10.1038/nrd4627.
[30] R. White, K. Rose, L. Zon, Zebrafish cancer: the state of the art and the path forward, Nat. Rev. Cancer. 13 (2013) 624–636. doi:10.1038/nrc3589.
[31] G.J. Lieschke, P.D. Currie, Animal models of human disease: zebrafish swim into view, Nat. Rev. Genet. 8 (2007) 353–367. doi:10.1038/nrg2091.
[32] L. Evensen, P.L. Johansen, G. Koster, K. Zhu, L. Herfindal, M. Speth, F. Fenaroli, J. Hildahl, S. Bagherifam, C. Tulotta, L. Prasmickaite, G.M. Mælandsmo, E. Snaar-Jagalska, G. Griffiths, Zebrafish as a model system for characterization of nanoparticles against cancer, Nanoscale. 8 (2016) 862–877. doi:10.1039/c5nr07289a.
[33] L.D. Mayer, L.C.L. Tai, D.S.C. Ko, D. Masin, R.S. Ginsberg, P.R. Cullis, M.B. Bally, Influence of Vesicle Size, Lipid Composition, and Drug-to-Lipid Ratio on the Biological Activity of Liposomal Doxorubicin in Mice, Cancer Res. 49 (1989) 5922–5930.
[34] M.C. Woodle, K.K. Matthay, M.S. Newman, J.E. Hidayat, L.R. Collins, C. Redemann, F.J. Martin, D. Papahadjopoulos, Versatility in lipid compositions showing prolonged circulation with sterically stabilized liposomes, Biochim. Biophys. Acta. 1105 (1992) 193–200.
[35] A.A. Gabizon, Y. Barenholz, M. Bialer, Prolongation of the Circulation Time of Doxorubicin Encapsulated in Liposomes Containing a Polyethylene Glycol-Derivatized Phospholipid: Pharmacokinetic Studies in Rodents and Dogs, Pharm. Res. 10 (1993) 703–708. doi:10.1023/A:1018907715905.
[36] C. Kirby, J. Clarke, G. Gregoriadis, Effect of the cholesterol content of small unilamellar liposomes on their stability in vivo and in vitro, Biochem. J. 186 (1980) 591–598. doi:10.1042/bj1860591.
[37] C.D. Oja, S.C. Semple, A. Chonn, P.R. Cullis, Influence of dose on liposome clearance: critical role of blood proteins, Biochim. Biophys. Acta BBA - Biomembr. 1281 (1996) 31–37. doi:10.1016/0005-2736(96)00003-X.
[38] T.M. Allen, C.B. Hansen, D.E.L. de Menezes, Pharmacokinetics of long-circulating liposomes, Adv. Drug Deliv. Rev. 16 (1995) 267–284. doi:10.1016/0169-409X(95)00029-7.

[39] S. Sieber, P. Grossen, J. Bussmann, F. Campbell, A. Kros, D. Witzigmann, J. Huwyler, Zebrafish as a Preclinical In Vivo Screening Model for Nanomedicines, Adv. Drug Deliv. Rev. (2019). doi:10.1016/j.addr.2019.01.001.
[40] S. Sieber, P. Grossen, P. Uhl, P. Detampel, W. Mier, D. Witzigmann, J. Huwyler, Zebrafish as a predictive screening model to assess macrophage clearance of liposomes in vivo, Nanomedicine Nanotechnol. Biol. Med. (2019). doi:10.1016/j.nano.2018.11.017.
[41] S. Sieber, P. Grossen, P. Detampel, S. Siegfried, D. Witzigmann, J. Huwyler, Zebrafish as an early stage screening tool to study the systemic circulation of nanoparticulate drug delivery systems in vivo, J Control Release. 264 (2017) 180–191. doi:10.1016/j.jconrel.2017.08.023.
[42] F. Campbell, F.L. Bos, S. Sieber, G. Arias-Alpizar, B.E. Koch, J. Huwyler, A. Kros, J. Bussmann, Directing Nanoparticle Biodistribution Through Evasion and Exploitation of Stab2-Dependent Nanoparticle Uptake, ACS Nano. (2018). doi:10.1021/acsnano.7b06995.
[43] S. Sieber, S. Siegrist, S. Schwarz, F. Porta, S.H. Schenk, J. Huwyler, Immobilization of Enzymes on PLGA Sub-Micrometer Particles by Crosslinked Layer-by-Layer Deposition, Macromol. Biosci. 17 (2017). doi:10.1002/mabi.201700015.
[44] T. Einfalt, D. Witzigmann, C. Edlinger, S. Sieber, R. Goers, A. Najer, M. Spulber, O. Onaca-Fischer, J. Huwyler, C.G. Palivan, Biomimetic artificial organelles with in vitro and in vivo activity triggered by reduction in microenvironment, Nat. Commun. 9 (2018) 1127. doi:10.1038/s41467-018-03560-x.
[45] H.H. Gustafson, D. Holt-Casper, D.W. Grainger, H. Ghandehari, Nanoparticle uptake: The phagocyte problem, Nano Today. 10 (2015) 487–510. doi:10.1016/j.nantod.2015.06.006.
[46] M. Mahmoudi, N. Bertrand, H. Zope, O.C. Farokhzad, Emerging understanding of the protein corona at the nano-bio interfaces, Nano Today. 11 (2016) 817–832. doi:10.1016/j.nantod.2016.10.005.
[47] C.D. Walkey, J.B. Olsen, H. Guo, A. Emili, W.C.W. Chan, Nanoparticle Size and Surface Chemistry Determine Serum Protein Adsorption and Macrophage Uptake, J. Am. Chem. Soc. 134 (2012) 2139–2147. doi:10.1021/ja2084338.
[48] M.C. Woodle, Sterically stabilized liposome therapeutics, Adv. Drug Deliv. Rev. 16 (1995) 249–265. doi:10.1016/0169-409X(95)00028-6.
[49] F. Ellett, L. Pase, J.W. Hayman, A. Andrianopoulos, G.J. Lieschke, mpeg1 promoter transgenes direct macrophage-lineage expression in zebrafish, Blood. 117 (2011) e49-56. doi:10.1182/blood-2010-10-314120.
[50] S.A. MacParland, K.M. Tsoi, B. Ouyang, X.-Z. Ma, J. Manuel, A. Fawaz, M.A. Ostrowski, B.A. Alman, A. Zilman, W.C.W. Chan, I.D. McGilvray, Phenotype Determines Nanoparticle Uptake by Human Macrophages from Liver and Blood, ACS Nano. 11 (2017) 2428–2443. doi:10.1021/acsnano.6b06245.
[51] M. Nguyen-Chi, B. Laplace-Builhe, J. Travnickova, P. Luz-Crawford, G. Tejedor, Q.T. Phan, I. Duroux-Richard, J.-P. Levraud, K. Kissa, G. Lutfalla, C. Jorgensen, F. Djouad, Identification of polarized macrophage subsets in zebrafish, ELife. 4 (2015) e07288. doi:10.7554/eLife.07288.
[52] S. Schöttler, G. Becker, S. Winzen, T. Steinbach, K. Mohr, K. Landfester, V. Mailänder, F.R. Wurm, Protein adsorption is required for stealth effect of poly(ethylene glycol)- and poly(phosphoester)-coated nanocarriers, Nat. Nanotechnol. 11 (2016) 372–377. doi:10.1038/nnano.2015.330.
[53] L.K. Müller, J. Simon, C. Rosenauer, V. Mailänder, S. Morsbach, K. Landfester, The Transferability from Animal Models to Humans: Challenges Regarding Aggregation and Protein Corona Formation of Nanoparticles, Biomacromolecules. (2017). doi:10.1021/acs.biomac.7b01472.
[54] C. Li, X.F. Tan, T.K. Lim, Q. Lin, Z. Gong, Comprehensive and quantitative proteomic analyses of zebrafish plasma reveals conserved protein profiles between genders and between zebrafish and human, Sci. Rep. 6 (2016) 24329. doi:10.1038/srep24329.
[55] M. Hadjidemetriou, Z. Al-Ahmady, M. Mazza, R.F. Collins, K. Dawson, K. Kostarelos, In Vivo Biomolecule Corona around Blood-Circulating, Clinically Used and Antibody-Targeted Lipid Bilayer Nanoscale Vesicles, ACS Nano. 9 (2015) 8142–8156. doi:10.1021/acsnano.5b03300.

[56] P. Laverman, M.G. Carstens, O.C. Boerman, E.T.M. Dams, W.J.G. Oyen, N. van Rooijen, F.H.M. Corstens, G. Storm, Factors Affecting the Accelerated Blood Clearance of Polyethylene Glycol-Liposomes upon Repeated Injection, J. Pharmacol. Exp. Ther. 298 (2001) 607–612.
[57] J. Szebeni, Complement activation-related pseudoallergy: A stress reaction in blood triggered by nanomedicines and biologicals, Mol. Immunol. 61 (2014) 163–173. doi:10.1016/j.molimm.2014.06.038.
[58] A.M. Cadena, S.M. Fortune, J.L. Flynn, Heterogeneity in tuberculosis, Nat. Rev. Immunol. 17 (2017) 691–702. doi:10.1038/nri.2017.69.
[59] J.R. Kurtz, J.A. Goggins, J.B. McLachlan, Salmonella infection: Interplay between the bacteria and host immune system, Immunol. Lett. 190 (2017) 42–50. doi:10.1016/j.imlet.2017.07.006.
[60] J.A. Crump, M. Sjölund-Karlsson, M.A. Gordon, C.M. Parry, Epidemiology, Clinical Presentation, Laboratory Diagnosis, Antimicrobial Resistance, and Antimicrobial Management of Invasive Salmonella Infections, Clin. Microbiol. Rev. 28 (2015) 901–937. doi:10.1128/CMR.00002-15.
[61] R.S. Santos, C. Figueiredo, N.F. Azevedo, K. Braeckmans, S.C. De Smedt, Nanomaterials and molecular transporters to overcome the bacterial envelope barrier: Towards advanced delivery of antibiotics, Adv. Drug Deliv. Rev. (2017). doi:10.1016/j.addr.2017.12.010.
[62] M. Varas, A. Fariña, F. Díaz-Pascual, J. Ortíz-Severín, A.E. Marcoleta, M.L. Allende, C.A. Santiviago, F.P. Chávez, Live-cell imaging of Salmonella Typhimurium interaction with zebrafish larvae after injection and immersion delivery methods, J. Microbiol. Methods. 135 (2017) 20–25. doi:10.1016/j.mimet.2017.01.020.
[63] S.-W. Jin, D. Beis, T. Mitchell, J.-N. Chen, D.Y.R. Stainier, Cellular and molecular analyses of vascular tube and lumen formation in zebrafish, Development. 132 (2005) 5199–5209. doi:10.1242/dev.02087.
[64] S.C. Semple, A. Chonn, P.R. Cullis, Influence of cholesterol on the association of plasma proteins with liposomes, Biochemistry (Mosc.). 35 (1996) 2521–2525. doi:10.1021/bi950414i.
[65] E. Ellertsdóttir, A. Lenard, Y. Blum, A. Krudewig, L. Herwig, M. Affolter, H.-G. Belting, Vascular morphogenesis in the zebrafish embryo, Dev. Biol. 341 (2010) 56–65. doi:10.1016/j.ydbio.2009.10.035.
[66] L. Herwig, Y. Blum, A. Krudewig, E. Ellertsdottir, A. Lenard, H.-G. Belting, M. Affolter, Distinct Cellular Mechanisms of Blood Vessel Fusion in the Zebrafish Embryo, Curr. Biol. 21 (2011) 1942–1948. doi:10.1016/j.cub.2011.10.016.
[67] L. Aschoff, Das reticulo-endotheliale System, in: Ergeb. Inn. Med. Kinderheilkd., Springer, Berlin, Heidelberg, 1924: pp. 1–118. doi:10.1007/978-3-642-90639-8_1.
[68] Y. Kawai, B. Smedsrød, K. Elvevold, K. Wake, Uptake of lithium carmine by sinusoidal endothelial and Kupffer cells of the rat liver: new insights into the classical vital staining and the reticulo-endothelial system, Cell Tissue Res. 292 (1998) 395–410. doi:10.1007/s004410051069.
[69] B. Zhou, J.A. Weigel, L. Fauss, P.H. Weigel, Identification of the Hyaluronan Receptor for Endocytosis (HARE), J. Biol. Chem. 275 (2000) 37733–37741. doi:10.1074/jbc.M003030200.
[70] E.N. Harris, P.H. Weigel, The ligand-binding profile of HARE: hyaluronan and chondroitin sulfates A, C, and D bind to overlapping sites distinct from the sites for heparin, acetylated low-density lipoprotein, dermatan sulfate, and CS-E, Glycobiology. 18 (2008) 638–648. doi:10.1093/glycob/cwn045.
[71] B. Yin, K.H.K. Li, L.W.C. Ho, C.K.W. Chan, C.H.J. Choi, Toward Understanding in Vivo Sequestration of Nanoparticles at the Molecular Level, ACS Nano. (2018). doi:10.1021/acsnano.8b00141.
[72] E. Keles, Y. Song, D. Du, W.-J. Dong, Y. Lin, Recent progress in nanomaterials for gene delivery applications, Biomater. Sci. 4 (2016) 1291–1309. doi:10.1039/C6BM00441E.
[73] H. Hatakeyama, H. Akita, H. Harashima, A multifunctional envelope type nano device (MEND) for gene delivery to tumours based on the EPR effect: a strategy for overcoming the PEG dilemma, Adv. Drug Deliv. Rev. 63 (2011) 152–160. doi:10.1016/j.addr.2010.09.001.
[74] P.R. Cullis, M.J. Hope, Lipid Nanoparticle Systems for Enabling Gene Therapies, Mol. Ther. 25 (2017) 1467–1475. doi:10.1016/j.ymthe.2017.03.013.

[75] B.S. Clark, M. Winter, A.R. Cohen, B.A. Link, Generation of Rab-based transgenic lines for in vivo studies of endosome biology in zebrafish, Dev. Dyn. 240 (2011) 2452–2465. doi:10.1002/dvdy.22758.
[76] K. Ellis, J. Bagwell, M. Bagnat, Notochord vacuoles are lysosome-related organelles that function in axis and spine morphogenesis, J Cell Biol. 200 (2013) 667–679. doi:10.1083/jcb.201212095.
[77] J. Silvent, A. Akiva, V. Brumfeld, N. Reznikov, K. Rechav, K. Yaniv, L. Addadi, S. Weiner, Zebrafish skeleton development: High resolution micro-CT and FIB-SEM block surface serial imaging for phenotype identification, PLOS ONE. 12 (2017) e0177731. doi:10.1371/journal.pone.0177731.
[78] N.L. Schieber, P. Machado, S.M. Markert, C. Stigloher, Y. Schwab, A.M. Steyer, Chapter 4 - Minimal resin embedding of multicellular specimens for targeted FIB-SEM imaging, in: T. Müller-Reichert, P. Verkade (Eds.), Methods Cell Biol., Academic Press, 2017: pp. 69–83. doi:10.1016/bs.mcb.2017.03.005.
[79] D. Witzigmann, S. Sieber, F. Porta, P. Grossen, A. Bieri, N. Strelnikova, T. Pfohl, C. Prescianotto-Baschong, J. Huwyler, Formation of lipid and polymer based gold nanohybrids using a nanoreactor approach, 5 (2015) 74320–74328. doi:10.1039/C5RA13967H.
[80] N. Bertrand, J. Wu, X. Xu, N. Kamaly, O.C. Farokhzad, Cancer nanotechnology: The impact of passive and active targeting in the era of modern cancer biology, Adv. Drug Deliv. Rev. 66 (2014) 2–25. doi:10.1016/j.addr.2013.11.009.
[81] J. Reineke, Terminology matters: There is no targeting, but retention, J. Controlled Release. 273 (2018) 180–183. doi:10.1016/j.jconrel.2018.01.016.
[82] D. Shan, J. Li, P. Cai, P. Prasad, F. Liu, A.M. Rauth, X.Y. Wu, RGD-conjugated solid lipid nanoparticles inhibit adhesion and invasion of α<Subscript>v</Subscript>β<Subscript>3</Subscript> integrin-overexpressing breast cancer cells, Drug Deliv. Transl. Res. 5 (2015) 15–26. doi:10.1007/s13346-014-0210-2.
[83] J. Yang, Y. Shimada, R.C.L. Olsthoorn, B.E. Snaar-Jagalska, H.P. Spaink, A. Kros, Application of Coiled Coil Peptides in Liposomal Anticancer Drug Delivery Using a Zebrafish Xenograft Model, ACS Nano. 10 (2016) 7428–7435. doi:10.1021/acsnano.6b01410.
[84] K. Stoletov, V. Montel, R.D. Lester, S.L. Gonias, R. Klemke, High-resolution imaging of the dynamic tumor cell vascular interface in transparent zebrafish, Proc. Natl. Acad. Sci. U. S. A. 104 (2007) 17406–17411. doi:10.1073/pnas.0703446104.
[85] S. Nicoli, M. Presta, The zebrafish/tumor xenograft angiogenesis assay, Nat. Protoc. 2 (2007) 2918–2923. doi:10.1038/nprot.2007.412.
[86] M. Gaumet, A. Vargas, R. Gurny, F. Delie, Nanoparticles for drug delivery: The need for precision in reporting particle size parameters, Eur. J. Pharm. Biopharm. 69 (2008) 1–9. doi:10.1016/j.ejpb.2007.08.001.
[87] R. Cao, A. Eriksson, H. Kubo, K. Alitalo, Y. Cao, J. Thyberg, Comparative Evaluation of FGF-2–, VEGF-A–, and VEGF-C–Induced Angiogenesis, Lymphangiogenesis, Vascular Fenestrations, and Permeability, Circ. Res. 94 (2004) 664–670. doi:10.1161/01.RES.0000118600.91698.BB.
[88] V.E. Bosio, G.A. Islan, Y.N. Martinez, N. Duran, G.R. Castro, Nanodevices for the immobilization of therapeutic enzymes, Crit. Rev. Biotechnol. 36 (2016) 447–464. doi:10.3109/07388551.2014.990414.
[89] R.J.R. W. Peters, I. Louzao, J.C.M. van Hest, From polymeric nanoreactors to artificial organelles, Chem. Sci. 3 (2012) 335–342. doi:10.1039/C2SC00803C.
[90] T.M.S. Chang, Therapeutic applications of polymeric artificial cells, Nat. Rev. Drug Discov. 4 (2005) 221–235. doi:10.1038/nrd1659.
[91] Tanner Pascal, Egli Stefan, Balasubramanian Vimalkumar, Onaca Ozana, Palivan Cornelia G., Meier Wolfgang, Can polymeric vesicles that confine enzymatic reactions act as simplified organelles?, FEBS Lett. 585 (2011) 1699–1706. doi:10.1016/j.febslet.2011.05.003.
[92] E. Le Moal, G. Juban, A.S. Bernard, T. Varga, C. Policar, B. Chazaud, R. Mounier, Macrophage-derived superoxide production and antioxidant response following skeletal muscle injury, Free Radic. Biol. Med. 120 (2018) 33–40. doi:10.1016/j.freeradbiomed.2018.02.024.

ACKNOWLEDGMENT

I would like to begin with my doctoral advisor **Prof. Dr. Jörg Huwyler**. He always had time to answer my questions, was open for many project ideas, and was supportive far beyond what you can expect of a PhD supervisor. His enthusiasm for science was contagious and motivating which altogether turned my PhD more into a hobby than a profession. I am looking forward to my PostDoc in his lab tackling further scientific challenges together with him.

I would like to thank **Prof. Dr. Markus Affolter** for his co-referee and for unselfishly sharing his zebrafish facility with our group. In this context I would also like to thank **Dr. Heinz Georg Belting** and the whole **Fish Club** for sharing their enormous knowledge and giving me inspiring insights into their research.

I would like to thank the **Stiftung zur Förderung des pharmazeutischen Nachwuchses in Basel** and the **Freiwilligen Akademischen Gesellschaft Basel (FAG)** for their generous financial support of this PhD project.

Furthermore, a great "thank you" goes to **Prof. Dr. Alexander Kros**, **Dr. Jeroen Bussmann**, and **Dr. Fred Campbell** and their whole group for welcoming me as a guest at the University of Leiden. Their hospitality allowed me to start my work with the zebrafish, which has been crucial for the further development of my PhD.

I would like to thank all collaborators who contributed to any part of this thesis. In particular, I would like to thank my initial supervisor **Dr. Fabiola Porta**, my master students **Stéphanie Schwarz** and **Salome Siegfried**, **Dr. Tomaz Einfalt**, **Prof. Dr. Cornelia G. Palivan**, **Dr. Pascal Detampel, Prof. Dr. Walter Mier**, **Dr. Philipp Uhl, Matthias Voigt, Prof. Dr. Mark Helm, Etienne Schmelzer, and Niels Schellinx.**

I would like to thank **Dr. Dominik Witzigmann,** who has always been a role model in and outside the lab. Already during my master thesis, he started supervising my projects which turned out to be a stroke of luck. He was always willing to share his enormous knowledge, and his passion for science

motivated me to do this PhD. His guidance and experience resulted in many excellent publications and I am looking forward to further fruitful collaboration. I am sure and hope he will get rewarded for all he has done so far for many young scientists. I would also like to thank **Dr. Philip Grossen** and **Dr. Stefan Siegrist**, who have been in the lab during my whole PhD. Their open minds and willingness to collaborate created a great working environment. Furthermore, I really appreciated their mental support during all the usual up and downs and their shared enthusiasm for after work activities.

I would like to thank **Dr. Susanne Schenk** for her honest and valuable scientific inputs and for always supporting me. Of course I would also like to thank the whole group of **Pharmaceutical Technology** for so much support and the great working environment which allowed me to enjoy being at work. It has been a pleasure to collaborate and/or talk about science and private stuff. A special thanks to my colleagues teaching the practical course of solid dosage forms for having so much fun together during practicals. I am looking forward to further occasions “abusing” the lab equipment.

I would like to thank all my friends from home and Basel for always being there even if I did not always have a lot of time for them. I hope you know how much I appreciate each of you! I would especially like to thank my two roommates **Selim** and **Ben** with whom I have shared a flat for the past nine years. Their personal way of doing or seeing things differently often inspired me and helped me to relax in stressful situations. Thanks for the great time and the unforgettable moments!

A great thank goes to my parents **Hansjörg** and **Bea Sieber**. They always supported me in what I have been doing and backed me up whenever I needed it. Without their steady support, it would not have been possible to pursue my dreams in such a lighthearted manner. Furthermore, I would like to thank **Dario Sieber** for not only being a brother but also a friend, which means a lot to me.

Finally, I would like to thank my girlfriend **Melanie Haag**. She had to stand all my moods, flaws, and little “neuroses” to the greatest extend and did it with almost endless patience. I am extremely thankful for her tolerance and support during the whole time and for having her by my side. I am looking forward to many years to come.

Sandro Sieber

St.Alban-Anlage 19, 4052 Basel, Switzerland
M: sandro.sieber@hotmail.de T: +41 79 946 75 74

As a scientist and skydiver, I am fascinated by new challenges and used to perform in demanding situations.

Professional Experience

2014 - present **Scientist,** University of Basel

- Implementing and validating the zebrafish experimental facility in the group of Pharmaceutical Technology including evaluation an acquisition of the required equipment
- Design and development of nanomaterial based drug delivery systems including the optimization of manufacturing processes with respect to up-scaling
- Organizing and guiding international collaborations with academic and industrial partners (Universities of Mainz, Freiburg, and Leiden, Hoffmann La-Roche)
- Publishing in peer-reviewed journals and presenting scientific results at international conferences (e.g. CLINAM Basel, ILS/LRD Athens)
- Active contribution to patenting processes and marketing of generated intellectual property
- Supervising practical courses for bachelor students and representing the university and the department at public events (Maturandeninfotag, Masterinfoabend, Schülerbesuche)

07 2018 **Visiting scientist,** Mount Desert Island Biological Laboratory

- Evaluating the killifish as a model for renal drug clearance

2016 - 2018 **Member of the AVUBA association board**

- Representing PhD's and Postdoc's interests at the university senate
- Negotiating new job descriptions for university assistants

08 2015 - 10 2015 **Visiting scientist,** University of Leiden

- Acquiring technical and practical know-how working with zebrafish

05 2013 - 10 2013 **Internship Manufacturing Science and Technology,** Hoffmann-La Roche

- Supporting the daily business of the GMP subunit in the production of solid dosage forms focusing on cleaning validation
- Identifying and weighing risk factors for cross contamination by performing a Multi-Product Risk Assessment
- Troubleshooting of an in-process product loss by performing a Root Cause Analysis

Trainings and Qualifications

Software	Microsoft Office, Stavex, Origin Pro, Adobe Illustrator, ImageJ, GIMP
Languages	German (native), English (C1/C2), French (A2/B1)
Additional courses	Project Management for new PhDs Leadership Basics LTK Module 20 Course in Laboratory Animal Science Creating Scientific Posters

Education

2014 - 2018	PhD Pharmaceutical Sciences, University of Basel
2012 - 2014	Master of Pharmaceutical Sciences, University of Basel
2009 - 2012	Bachelor of Pharmaceutical Sciences, University of Basel
2004 - 2008	Matura with a major in economics and law, Kantonsschule Heerbrugg (SG)

Honors and Awards

Research Grant	Grant supporting my PhD project (CHF 72'000) awarded by the Stiftung zur Förderung des pharmazeutischen Nachwuchses in Basel
Travel Grant	Grant for staying at the University of Leiden (CHF 7'600) awarded by the Freiwilligen Akademischen Gesellschaft (FAG) Basel
Cover Story	Selected for the cover story of the Journal of Controlled Release (October 2017) including an editorial by the editor in chief
Invited Speaker	Presenting our zebrafish model at the Leiden Cell Symposium 2018
Presentation Award	3rd best Talk during the PhD Retreat 2016

Activities and Interests

Handball	JS licensed U9 handball coach HBBB Binningen
Skydiving	

Bibliography of Publications

- D. Witzigmann, S. Sieber, F. Porta, P. Grossen, A. Bieri, N. Strelnikova, T. Pfohl, C. Prescianotto-Baschong, J. Huwyler, Formation of lipid and polymer based gold nanohybrids using a nanoreactor approach, RSC Advances (2015)
- S. Sieber, S. Siegrist, S. Schwarz, F. Porta, S.H. Schenk, J. Huwyler, Immobilization of Enzymes on PLGA Sub-Micrometer Particles by Crosslinked Layer-by-Layer Deposition, Macromol Biosci. (2017)
- P. Grossen, D. Witzigmann, S. Sieber, J. Huwyler, PEG-PCL-based nanomedicines: A biodegradable drug delivery system and its application, J Control Release. (2017)
- S. Sieber, P. Grossen, P. Detampel, S. Siegfried, D. Witzigmann, J. Huwyler, Zebrafish as an early stage screening tool to study the systemic circulation of nanoparticulate drug delivery systems in vivo, J Control Release. (2017)
- F. Campbell, F.L. Bos, S. Sieber, G. Arias-Alpizar, B.E. Koch, J. Huwyler, A. Kros, J. Bussmann, Directing Nanoparticle Biodistribution through Evasion and Exploitation of Stab2-Dependent Nanoparticle Uptake, ACS Nano (2018)
- T. Einfalt, D. Witzigmann, C. Edlinger, S. Sieber, R. Goers, A. Najer, M. Spulber, O. Onaca-Fischer, J. Huwyler, C.G. Palivan, Biomimetic artificial organelles with in vitro and in vivo activity triggered by reduction in microenvironment, Nat Commun. (2018)
- S. Sieber, P. Grossen, J. Bussmann, F. Campbell, A. Kros, D. Witzigmann, J. Huwyler, Zebrafish as a Preclinical In Vivo Screening Model for Nanomedicines, Advanced Drug Delivery Reviews (2019)
- S. Sieber, P. Grossen, P. Uhl, P. Detampel, W. Mier, D. Witzigmann, J. Huwyler, Zebrafish as a predictive screening model to assess macrophage clearance of liposomes in vivo, Nanomedicine: Nanotechnology, Biology and Medicine (2019)
- M. Sedighi, S. Sieber, F. Rahimi, M.-A. Shahbazi, A.H. Rezayan, J. Huwyler, D. Witzigmann, Rapid optimization of liposome characteristics using a combined microfluidics and design-of-experiment approach, Drug Delivery and Translational Research (2019)